A STATOR TURN FAULT DETECTION METHOD AND A FAULT-TOLERANT OPERATING STRATEGY FOR INTERIOR PM SYNCHRONOUS MOTOR DRIVES IN SAFETY-CRITICAL APPLICATIONS

A Dissertation

Presented to

The Academic Faculty

by

Youngkook Lee

In Partial Fulfillment

of the Requirements for the Degree

Doctor of Philosophy in the

School of Electrical and Computer Engineering

Georgia Institute of Technology

August 2007

A STATOR TURN FAULT DETECTION METHOD AND A FAULT-TOLERANT OPERATING STRATEGY FOR INTERIOR PM SYNCHRONOUS MOTOR DRIVES IN SAFETY-CRITICAL APPLICATIONS

Approved by:

Dr. Thomas G. Habetler, Advisor
School of Electrical and Computer Engineering
Georgia Institute of Technology

Dr. Ronald G. Harley
School of Electrical and Computer Engineering
Georgia Institute of Technology

Dr. Deepakraj M. Divan
School of Electrical and Computer Engineering
Georgia Institute of Technology

Dr. Ayanna M. Howord
School of Electrical and Computer Engineering
Georgia Institute of Technology

Dr. Dean J. Patterson
School of Electrical Engineering
University of Nebraska

Date Approved: June 29, 2007

To My Parents,

My Loving Wife, Dukehee,

and My daughters, Hyungi and Seohee.

ACKNOWLEDGEMENTS

Although a doctoral dissertation is considered to a personal accomplishment, I realize it would not have been possible without the encouragement, trust, and support of many people.

First of all, I would like to express my most sincere gratitude to my advisor Dr. Thomas G. Habetler. He has been a wise and trusted advisor throughout the entire process. His guidance and training have helped me to solve engineering problems and improve my communication skills as an engineer. If it has not been for his vision, encouragement, and his confidence in my ability, much of this work would not have been completed.

I would also like to express my gratitude to Dr. Ronald G. Harley and Dr. Deepakraj M. Divan for their suggestions and guidance on my research work. I am also indebted to Dr. Ayanna M. Howard and Dr. Dean J. Patterson for being my dissertation committee members.

I would like to acknowledge Hyundai Motor Company for providing the chance of my study here, Georgia Institute of Technology and financial support necessary to conduct this research. I would like to especially thank Dr. Ho-Gi Kim, Dr. Jin-Hwan Jung, Mr. Hyoung-Bin Ihm, Mr. Tae-Hoon Lee, and Mr. Sang-Hyun Moon for their encouragement and support.

It was encouragement of my best friend, Dr. Byoung-Kuk Lee that motivated me to pursue a higher degree. I truly appreciate his sincere friendship. I am also indebted to

my friends, Dr. Jin Hur, Dr. Dong-Myoung Lee, and Jae-Hyeoung Seo for their encouragement and support.

I would also like to thank all of my fellow graduate students of the lab for their friendship and support over the last four years of endeavor. Among them, I wish to especially thank Dr. Zhi Gao, Dr. Long Wu, Dr. Bin Lu, Dr. Salman Mohagheghi, Aristidis Zachas, Wei Zhou, Wei Qiao, Yi Yang, Hajeet Zhodal, and Jean Carlos Hernandez Mejia.

Most of all, I owe the greatest debt of gratitude to my family. I would like to thank my parents and my brothers for a lifetime of support, encouragement, and education. I am also thankful to my parent-in-laws for their love and support. Lastly, I would like to thank my wife Dukehee whose love and support has helped to make everything I have accomplished possible.

TABLE OF CONTENTS

LIST OF TABLES

LIST OF FIGURES

GLOSSARY OF SYMBOLS

Symbol	Definition	Unit
Definition of Electrical and Magnetic Symbols		
i	: Instantaneous current	A
I	: rms current	Arms
$\tilde{i}$	: Current vector	A
v	: Instantaneous voltage	V
V	: rms voltage	Vrms
$\tilde{v}$	: Voltage vector	V
p	: Instantaneous power	W
P	: Number of poles of an electric machine	-
R	: Resistance	ohm
L	: Inductance	H
M	: Mutual inductance	H
C	: Capacitance	F
Z	: Impedance	ohm
λ	: Instantaneous flux linkage	Wb
B	: Flux density	T
T	: Torque	Nm
ω	: Angular velocity in radian per second	rad/sec
f	: Frequency in hertz	Hz
θ	: Angle (rotating position)	rad
Definition of Thermal Symbols		
P	: Power loss	W
R	: Thermal resistance	$^{\circ}C/W$
C	: Thermal capacitance	$J/^{\circ}C$
θ	: Temperature	$^{\circ}C$

Symbol	Definition	Unit

Definition of Subscripts

a,b,c	: *abc* reference frame	-
q,d	: *qd* reference frame	-
P,N,Z	: Sequence components	-
s	: Stator	-
r	: Rotor	-
PM	: Permanent magnet	-
n	: Motor neutral point	-
o	: Mid point of the dc-link of an inverter	-
m	: Magnetizing	-

Definition of Superscripts

s	: Stationary reference frame	-
e	: Synchronously (rotor-aligned) rotating reference frame	-
*	: Reference	-

Definition of Reference Axis

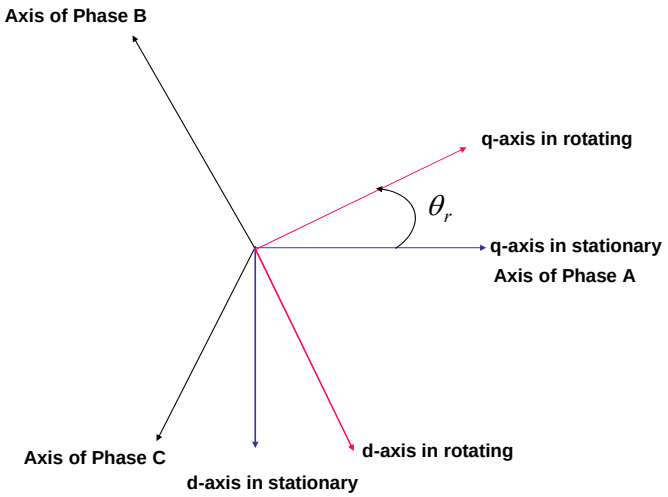

Figure N.1. Definition of axis in various reference frames

Definition of Transformation

- Transformation from variables in the *abc* reference frame from to the *qd* stationary reference frame and vice versa.

$$\begin{bmatrix} f_q^s \\ f_d^s \end{bmatrix} = \frac{2}{3}\begin{bmatrix} 1 & -\frac{1}{2} & -\frac{1}{2} \\ 0 & -\frac{\sqrt{3}}{2} & \frac{\sqrt{3}}{2} \end{bmatrix}\begin{bmatrix} f_a \\ f_b \\ f_c \end{bmatrix}, \quad \begin{bmatrix} f_a \\ f_b \\ f_c \end{bmatrix} = \begin{bmatrix} 1 & 0 \\ -\frac{1}{2} & -\frac{\sqrt{3}}{2} \\ -\frac{1}{2} & \frac{\sqrt{3}}{2} \end{bmatrix}\begin{bmatrix} f_q^S \\ f_d^S \end{bmatrix}$$

- Transformation from variables in the *qd* stationary reference frame to the *qd* synchronously rotating reference frame and vice versa.

$$\begin{bmatrix} f_q^e \\ f_d^e \end{bmatrix} = \begin{bmatrix} \cos\theta_e & -\sin\theta_e \\ \sin\theta_e & \cos\theta_e \end{bmatrix}\begin{bmatrix} f_q^S \\ f_d^S \end{bmatrix}, \quad \begin{bmatrix} f_q^S \\ f_d^S \end{bmatrix} = \begin{bmatrix} \cos\theta_e & \sin\theta_e \\ -\sin\theta_e & \cos\theta_e \end{bmatrix}\begin{bmatrix} f_q^e \\ f_d^e \end{bmatrix}$$

- Transformation from phase variables into sequence components.

$$\boldsymbol{T} = \frac{1}{3}\begin{bmatrix} 1 & a & a^2 \\ 1 & a^2 & a \\ 1 & 1 & 1 \end{bmatrix}, \text{ where } a = e^{j\frac{2\pi}{3}}$$

SUMMARY

A stator turn fault in a symmetrical three-phase AC motor can result in complete failure and shutdown of the machine unless the fault is detected early and evasive action is taken. This consequence can become catastrophic in safety-critical drive applications wherein an abrupt interruption in the drive's operation can result in injury or death. It is therefore imperative to maintain uninterrupted drive's operation under a stator turn fault condition in a safety-critical application. However, it is much challenging to maintain the availability of an interior permanent magnet synchronous motor (IPMSM) drive under a stator turn fault condition because of the presence of the spinning rotor magnets. This makes many engineers hesitant to employ IPMSMs in safety-critical drive applications, despite the IPMSM's excellent performance characteristics.

The scope of this work is to increase the stator turn fault tolerance of IPMSM drives in safety-critical applications. The objective is achieved by an on-line turn fault detection method and a simple turn fault-tolerant operating strategy.

In developing a turn fault detection scheme or a turn fault-tolerant operating strategy, a clear understanding of the characteristics of stator turn faults is a prerequisite. In addition, a reliable test bench for evaluating any method is absolutely required because even a minor deficiency in the method can result in critical failures. For these reasons, this work begins with developing a simulation model of an IPMSM drive with stator turn faults.

Even though the characteristics of stator turn faults have been explored intensively, the question of the time it takes for a turn fault to propagate to the adjacent turns or the

entire winding remains unanswered. Research on this issue is crucial to the development of a turn fault-tolerant operating strategy, since a method to predict the remaining life of the faulty motor or to establish an alarm level for the safe operation in the presence of the fault is desired. For this purpose, a thermal model of an IPMSM with stator turn faults is developed in this work.

Investigations into the characteristics of stator turn faults, using the developed simulation model, reveal that a turn fault in a current-controlled voltage source inverter (CCVSI)-driven machine leads to a reduced fundamental positive sequence component of the voltage references as compared to the machine without a fault for a given torque reference and rotating speed. In addition, it is also observed that the difference in the fundamental positive sequence components of the voltage references can be more easily observed in a synchronously (rotor-aligned) rotating reference frame. On the basis of these findings, an on-line turn fault detection method is developed. The method does not require calculation of sequence components and importantly, does not require measurements of the machine terminal voltages.

The investigations reveal another important fact that the amplitude of the circulating current in the shorted turns is nearly proportional to the amplitude of the stator line-neutral voltage, and thus can be significantly reduced by appropriately adjusting the stator line-neutral voltage. Based on this principle, a stator turn fault-tolerant operating strategy is proposed. This strategy does not result in the complete loss of availability of the drive in the presence of a stator turn fault. Additionally, the strategy can be implemented without any change in the standard drive configuration.

In addition, it is found that the same principle of the proposed turn fault-tolerant operating strategy can be applied to any type of electric machine drive that utilizes the rotor flux to generate the developed torque. To verify the generality of the principle, a stator turn fault-tolerant operating strategy for induction motor drives is also developed.

All the proposed models and methods are verified through simulations and experiments.

CHAPTER 1

INTRODUTION

1.1 Overview

Owing to their excellent performance characteristics, including high power density, large constant-power speed ratio (CPSR), and high efficiency, interior permanent magnet synchronous motors (IPMSMs) have been highlighted as one of the more attractive candidates for electric actuating systems in a wide variety of industrial and transit applications. These applications include safety-critical ones where an abrupt interruption in the drive's operation could result in a serious accident. For this reason, electric motor drives with a high degree of fault tolerance are required for these applications. One concern, however, with employing IPMSM drives in safety-critical applications is their unmanageable behavior under fault conditions resulting from the presence of the spinning rotor magnets that cannot be turned off at will. This clear weak point has made engineers hesitant to employ IPMSMs in safety-critical applications [1], and clearly makes the research on how to increase the fault tolerance of IPMSM drives crucial.

According to the survey in [2], 35-40 % of induction motor failures are related to the stator winding insulation and core. Moreover, it is generally believed that a large portion of stator winding-related failures are initiated by insulation failures in several turns of a stator coil within one phase. This type of fault is referred to as a "stator turn fault" [3], [28]. A stator turn fault in a symmetrical three-phase AC machine causes a large circulating current to flow and subsequently generates excessive heat in the shorted

turns. Without limiting the heat that is proportional to the square of the circulating current, the fault generally results in complete motor failure [4]. However, the worst consequence of a stator turn fault in a safety-critical application would be a serious accident involving loss of human life resulting from an abrupt shutdown of the drive's operation. The main theme of this work is to increase the stator turn fault tolerance of an IPMSM drives in safety-critical applications.

1.2 Fault Tolerance

The simplest definition of fault tolerance is that a fault in a component or sub-system does not cause the overall system to malfunction [5]. The fault tolerance of a given system can be quantified in terms of reliability and availability. Generally, reliability means an attribute of components and systems that will not need to be repaired and is often measured in terms of mean time to failure (MTTF). Availability is simply measured in terms of the expected proportion of time that the system will be available for use [5]. Highly conservative design and redundancy are commonly applied in improving the fault tolerance of electric motor drives. Overly conservative design is based on the idea that the chances of operating close to the failure limit can be reduced by over-sizing the system's capacity. The concept of redundancy is well understood: if part of a system fails, there is an extra or spare that is able to operate in place of the failed unit such that the operation of the system is uninterrupted [5]. Although these two approaches are the surest ways to increase the fault tolerance of an electric motor drive, they *greatly* increase the cost and complexity of the system. Moreover, redundancy may not be practical for an application that has a severe restriction on the installation space, such as in the case of

traction drives in electric or hybrid-electric vehicles. As alternatives to these approaches, fault diagnosis and fault-tolerant operating strategies have been proposed. The purpose of a condition monitoring tool is to detect a certain failure from its point of inception so as to prevent it from developing into the catastrophic phase. Fault-tolerant operating strategies are based on the concept that a faulty system can maintain its uninterrupted operation with the assistance of a modified topology or control algorithm. To implement such approaches as practical entities, it is desired to design a motor drive which carries out the following tasks [6]:

(1) Fault detection or identification

(2) Fault isolation if possible

(3) Remedial (Emergency) actions after fault detection

1.3 Stator Winding Insulation Failures

The organic materials used for insulation in electric machines are subjected to deterioration from a combination of thermal overloading and cycling, transient voltage stresses on the insulating material, mechanical stresses, and contaminations. Among the possible causes, thermal stresses are the main reason for the degradation of the stator winding insulation. Generally, stator winding insulation thermal stresses are categorized into three types: aging, overloading, and cycling [7]. Even the best insulation will fail quickly if operated above its temperature limit. As a rule of thumb, the life of insulation is reduced by 50 % for every $10^{\circ}C$ increase above the stator winding temperature limit [8]. It is thus necessary to monitor the stator winding temperature so that an electric machine will not operate beyond its thermal capacity. For this purpose, many techniques

have been reported in [9]-[12]. However, the inherent limitation of these techniques is their inability to detect a localized hot spot at its initial stage.

A few mechanical problems that accelerate insulation degradation include movement of a coil, vibration resulting from rotor unbalance, loose or worn bearings, air-gap eccentricity, and broken rotor bars [7]. The current in the stator winding produces a force on the coils that is proportional to the square of the current. This force is at its maximum under transient overloads, causing the coils to vibrate at twice the synchronous frequency with movement in both the radial and the tangential direction. This movement weakens the integrity of the insulation system [7]. Mechanical faults, such as broken rotor bar, worn bearings, and air-gap eccentricity, may be a reason why the rotor strikes the stator windings. Therefore, such mechanical failures should be detected before they fail the stator winding insulation [13]-[15].

Electrical stresses, mainly related to the machine terminal voltages, also cause insulation degradation. Among the various electrical stresses, partial discharges (PDs) in the windings and transient voltages at the machine terminals are considered the major stresses. Partial discharge, referred to as corona in the past, is not only a cause, but also a symptom of insulation degradation. Insulation failure detection methods monitoring a change in the pattern of PD have been proposed in [16]-[18]. With the increased emphasis of energy conservation and high performance motor control, the use of pulse width-modulated voltage source inverters (PWM-VSIs) has grown at an exponential rate. This has made the stator windings open to higher electrical stresses. For example, PD may not yield a severe problem on the stator winding insulation in low voltage mains-fed applications, while in PWM-VSI-driven applications, PDs have been found in the

machines operating at voltages much lower than 5 kV [19]. Furthermore, high speed PWM operations introduce high rate of rise of transient voltages at the machine terminals. For these reasons, many researchers have paid much attention to the effects of PWM operations on the stator winding insulation [19]-[21].

Contaminations due to foreign materials can lead to adverse effects on the stator winding insulation. The presence of foreign material can lead to a reduction in heat dissipation or create harmful reagents in the presence of PD [22]. It is thus very important to keep the motors clean and dry, especially when the motors operate in a hostile environment.

Regardless of the causes, stator winding-related failures can be divided into the following five groups: turn-to-turn, coil-to-coil, line-to-line, line-to-ground, and single or multi-phase windings open-circuit faults as presented in Figure 1.1.

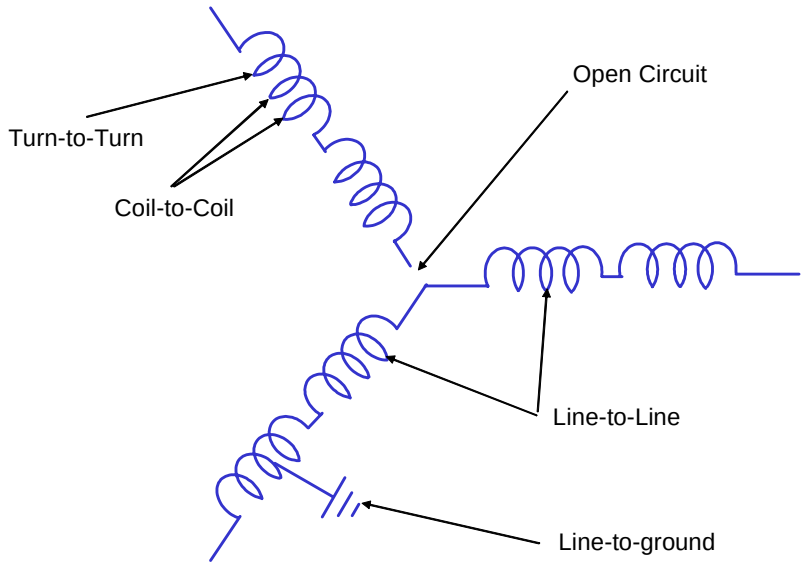

Figure 1.1. Possible failure modes in wye-connected stator windings [7].

Among the five failure modes, turn-to-turn faults (stator turn fault) have been considered the most challenging one since the other types of failures are usually the consequences of turn faults. Furthermore, turn faults are very difficult to detect at their initial stages. To solve the difficulty in detecting turn faults, a lot of methods have been developed [4], [23]-[39]. As a result, tremendous advances have been achieved in the area of turn fault diagnosis. Nonetheless, the question about the delay time between a turn fault and other severe failures still remains to be answered. However, it is believed that the delay time is not instantaneous, and estimated to be between a third of a second and several minutes or longer [27], [30]. This implies an important fact that if a stator turn fault is detected at its initial stage, the fault can be prevented from developing into the catastrophic phase with aid from an appropriate remedial action.

1.4 Stator Turn Fault Diagnosis

A stator turn fault induces a large circulating current, which leads to excessive heat generation in the shorted turns. The heat, which is proportional to the square of the circulating current, expedites the severity of the fault to a destructive phase [4]. Because of the destructive nature, an early detection of a turn fault is imperative to prevent the complete loss of the motor or drive system. However, conventional temperature monitoring functions cannot be used for this purpose because the monitoring functions are too slow to detect a localized hot spot induced by a turn fault that has a much faster and larger rise in the temperature than those of lumped thermal bodies. Furthermore, the exact position of a stator turn fault is unpredictable. Fortunately, intensive investigations on stator turn faults revealed that the faults introduce specific changes in the electric

properties of the machines. This has driven a great deal of effort to develop methods for an early detection of a turn fault [4], [23]-[39].

During the past years, off-line periodic insulation tests were commonly performed to monitor the winding insulation. All of the off-line methods check the response to a dc, ac, or surge signal injected into the motor after taking the motor off line [23], [24]. However, all the off-line methods have an inherent limitation, which is the requirement of having to take the motor out of service. To overcome the inherent disadvantage of off-line insulation testing, a large number of on-line turn fault detection methods have been proposed in [4], [25]-[39]. Almost all the proposed methods try to detect a change in the unbalance in the motor using indicators such as the second-order harmonic in the instantaneous power [25] or in the air-gap torque [26]; negative sequence current [27]; negative sequence impedance [28]; zero sequence voltage [33]; mismatches in the sequence impedance matrix [4], [29]. However, most of the methods consider turn faults in mains-fed induction motor applications, while the research on a turn fault detection method for current-controlled voltage source inverter (CCVSI)-driven IPMSM applications still remains unexplored territory. Only a few turn fault detection methods for CCVSI-driven induction motor applications have been proposed in [32]-[39].

Almost all IPMSMs in industry applications are driven by CCVSIs, which introduce difficulties in detecting a stator turn fault. The presence of the controller actions may abate the effectiveness of some of the fault indicators employed in mains-fed applications. The drives' non-stationary operation may result in unsatisfactory performance of methods based on conventional sequence decomposition, which work best when signals are at quasi-steady state or steady-state conditions. Actually, every

motor drive system is not perfectly symmetric, but has inherent asymmetries. These inherent asymmetries influence the sensitivity of a turn fault detection method.

Turn fault detection methods, which employ negative and zero sequence components at the machine terminal voltages as the fault indicators, are proposed in [32] and [33]-[35], respectively. Although they have the ability to detect a turn fault without being affected by the controller actions, they require voltage sensors, which are a critical drawback. Furthermore, the turn fault detection method monitoring the zero sequence voltage can be only applied to wye-connected stator windings with an accessible floating neutral point.

The second-order harmonic in the *d*-axis current in the synchronously rotating reference frame (i_{ds}^{e}) is used as the turn fault indicator for an induction motor drive in [36]. But, this method is viable only when the *d*-axis current reference (i_{ds}^{e*}) remains nearly constant. In controlling an IPMSM, maximum torque per ampere (MTPA) operation is commonly applied. Under this operation, the *d*-axis current reference varies depending on the required developed torque. Thus, the idea adapted in [36] may not be effective for detecting turn faults in IPMSM drives.

In [37], the statistical distribution of the six active switching states of a VSI is proposed as the turn fault indicator for CCVSI-driven induction motor applications. Although the characteristics of a VSI are properly taken into account, the authors did not pay much attention to the fact that an uneven distribution of the six active switching states can also be caused by oscillatory loads or a non-linearity in the inverter and its controller.

A turn fault detection method injecting a high-frequency carrier signal into the machine terminal voltages is proposed in [38]. This method uses the resultant high-frequency negative sequence current (or alternatively the negative sequence impedance) for turn fault detection. Although the method is highly insensitive to non-idealities in a drive, it is very complicated and requires a large computational effort.

In [39], a data adaptation technique, which observes a time-varying signal in the space vector domain, is proposed. The proposed technique is based on the idea that every frequency component in a time-varying signal is observed as a dc-component in the reference frame that rotates at the corresponding frequency in either the clockwise or counter-clockwise direction. This principle provides a simple way to extract a specific frequency component in a time-varying signal.

To compensate for the inherent asymmetries in a given drive, look-up table and neural network-based methods are commonly applied [29], [32]. These two methods can improve the sensitivity of a turn fault detection method to the inherent drive asymmetries. However, intensive data over the entire motor operating ranges is generally required in the stage of training neurons or generating look-up tables.

1.5 Stator Turn Fault-Tolerant Operating Strategy

Since abruptly interrupting the operation of a drive can result in a serious accident in safety-critical applications, it is imperative to maintain the drive's uninterrupted operation even in the presence of a stator turn fault, at least until the drive can be stopped safely. Generally, reducing the likelihood of a stator turn fault can be achieved by designing a machine and its insulation system conservatively. But achieving a longer

availability in the presence of a stator turn fault is a much more challenging issue. Since it has been generally accepted that there is no way to prevent stator turn faults in an IPMSM from developing into the catastrophic phase except for stopping the faulty machine completely, redundancy-based evasive actions have been considered as the only possible way to maintain the availability of an IPMSM drive under a stator turn fault condition. For this reason, little work has been done on this issue and can be categorized in the following three areas: redundancy [40], special operating modes for stopping the fault motor without further damage [1], [41], and fault-tolerant machines [42]-[44].

Even though redundancy is the surest way to maintain the availability of an IPMSM drive with a stator turn fault, it is not a panacea. Redundancy approaches greatly increase the cost and complexity of the drive, and greatly increase size and weight. For these reasons, redundancy approaches can be justified only in few specific applications.

In [1] and [41], a post turn fault operating strategy is proposed. This strategy can reduce the circulating current in the shorted turns, and is named symmetrical short-circuit operation. Although the circulating current in the shorted turns can be significantly reduced by activating symmetrical short-circuit operation, the controls over the speed and torque of the faulty motor are no longer available under this operation.

Another way to increase the stator turn fault tolerance of an electric motor drive is to develop a fault-tolerant machine. From the standpoint of fault tolerance, switched reluctance motors (SRMs) are generally regarded to have the best performance [42]. However, SRMs are not preferred in certain applications that require high efficiency and accurate control because of their low efficiency, large acoustic noise, and vibration. A new configuration of PM motor that combines the advantages of SRMs and PMSMs is

proposed and named “modular fault-tolerant PM machine” in [42]-[44]. Because of the presence of the magnetic coupling between the stator windings and permanent magnets, even this configuration is still open to damage resulting from the circulating current in the shorted turns. Furthermore, the new configuration requires a more complicated and expensive converter than the standard two-level VSI because each phase requires a separated H-bridge converter.

1.6 Problem Statement

From the previous discussion, it can be seen that a turn fault in an IPMSM drive in a safety-critical application should be detected at its initial stage in an on-line fashion, and the drive’s operation, even after the early detection of the fault, should be maintained in order to prevent a potentially serious accident involving loss of human life. The scope of this work is to increase the stator turn fault tolerance of IPMSM drives in safety-critical applications. This objective is to be achieved by developing a complete solution for high turn fault tolerance that includes an electrical model and a thermal model of an IPMSM with stator turn faults, a turn fault detection method, and a turn fault-tolerant operating strategy.

To provide an accurate description of the behaviors of a turn fault in an IPMSM drive and a reliable test bench for evaluating any method for turn fault detection or fault-tolerant operating strategy, a model of an IPMSM with stator turn faults is derived and integrated with a current-controlled inverter model. In the derivation of the machine model, an equivalent circuit based approach is adapted for a faster simulation speed. In addition, the machine model is represented in terms of phase variables to describe the

asymmetry caused by a turn fault more effectively. Moreover, this approach provides a distinct feature that *qd*-variable models cannot have. Phase-variable based machine models can be easily modified to be applicable to either case where the phase winding consists of coils connected in series or parallel. By exploiting this feature, the model of an IPMSM with stator turn faults is developed so that it is applicable to either type of coil connection. For more realistic simulations, magnetic non-linearity is also considered in the model.

A prediction of the remaining life of the motor or an establishment of an alarm level for the safe operation in the presence of a stator turn fault would be a valuable contribution in the area of turn fault-tolerant operating strategy. To realize this, an intensive investigation on the thermal behaviors of a stator turn fault is indispensable. In spite of the criticality, research on the issue has not been carried out, thus far. In this work, a thermal model of an IPMSM with stator turn faults is developed through a lumped parameter-based approach. Since the focus of the thermal modeling is to estimate the temperatures at the shorted turns and other turns in the stator windings, the proposed approach can provide an appealing means to achieve the stated goal of continuing to operate in the presence of a fault. The importance of the proposed thermal model of an IPMSM with stator turn faults is evident during the development of the turn fault-tolerant operating strategy.

The on-line turn fault detection method for an IPMSM drive begins with a thorough evaluation of the state of the art turn fault detection methods for CCVSI-driven applications. A voltage reference-based turn fault detection is proposed in this work. The basis of the proposed method is that the change in the asymmetry of the motor

caused by a turn fault in a CCVSI-driven application should be reflected into the voltage references because of the presence of the current-controller actions. The use of voltage reference for turn fault detection gives distinct benefits over conventional current- and voltage-based turn fault detection methods. The proposed approach can solve the problem of current-based turn fault detection methods resulting from the controller actions. In addition, no voltage sensor and no additional burden to the control tasks is required to obtain the voltage references, which are readily available in any CCVSI-driven application.

The turn fault-tolerant operating strategy for IPMSM drives begins with a thorough evaluation of the state of the art. The review will clearly show that all the previous strategies have unsatisfactory performance characteristics with respect to cost, efficiency, and availability. To overcome the drawbacks of the previous methods, a simple turn fault-tolerant operating strategy is proposed. The theoretical foundation of the strategy comes from a finding that the amplitude of the circulating current in the shorted turns is nearly proportional to the amplitude of the stator line-neutral voltage. The finding implies that the circulating current can be reduced significantly with an appropriate adjustment to the stator line-neutral voltages. As a result, the propagation speed of the turn fault can be significantly reduced. It is worth emphasizing that the proposed strategy does not require any hardware modification to the standard drive configuration and more importantly, it does not result in the complete loss of availability of a drive in the presence of a stator turn fault. Another important contribution of the proposed strategy is that the same principle can be applied to any type of electric machine that develops

electromagnetic torque. The generality of the principle is verified through simulations and experiments using a 5 HP induction motor.

All the proposed models and schemes in this work are verified through simulations and experiments on a 10 kW IPMSM drive, which is used in a hybrid-electric vehicle traction system.

1.7 Dissertation Outline

The background and motivation of this work has been introduced in this chapter. A summary and evaluation of the state of the art turn fault detection methods for CCVSI-driven applications is presented in Chapter 2. In Chapter 3, previous work on stator turn fault-tolerant operating strategy is reported. A simulation model of an IPMSM drive with stator turn fault is derived in Chapter 4. A model to investigate the thermal behavior of a stator turn fault in an IPMSM is developed in Chapter 5. In Chapter 6, an on-line turn fault detection method that is suitable for IPMSM drives is proposed. A simple stator turn fault-tolerant operating strategy, which can reduce the propagation speed of a stator turn fault significantly, is introduced in Chapter 7. Experimental setup and implementation of various tests are presented in Chapter 8. The simulation and experimental result verifying all the proposed models and schemes are provided in Chapters 9, 10, 11, and 12, respectively. In Chapter 13, a stator turn fault-tolerant operating strategy for induction motor drives is proposed and verified. The conclusions and contributions of this work are presented in Chapter 15. Recommendations for future work are also presented in this chapter.

CHAPTER 2

SUMMARY OF PREVIOUS WORK ON STATOR TURN FAULT DETECTION

2.1 Overview

Tremendous advances have been achieved in the area of stator turn fault diagnosis as illustrated by the numerous on-line turn fault detection methods in the literature [4], [25]-[39]. However, most of the methods focus on detecting turn faults in mains-fed induction motors, while the research on turn fault detection for CCVSI-driven IPMSMs still remains an unexplored area. Only a few methods consider turn fault detection for CCVSI-driven induction motors [32]-[39].

The presence of the controller actions in a CCVSI makes the inverter act as a controlled current source, while the power supply of a mains-fed machine acts as a voltage source. In addition, the variable speed, non-stationary operation of the drive changes the fundamental frequency continuously. Finally, the drive's inherent asymmetries have been an obstacle to more reliable turn fault detection. These reasons are the main causes leading to difficulties in detecting turn faults in CCVSI-driven machines. These difficulties can be overcome only by proper selections of fault indicators, data adaptation or signal processing technique, and the fault decision algorithm, all based on the characteristics of the particular drive system.

In this chapter, previously proposed turn fault detection methods for CCVSI-driven machines are summarized and evaluated in terms of their particular fault indicator, data adaptation technique, and fault decision algorithm.

2.2 Fault Indicators

A distinct difference of CCVSI-driven applications from mains-fed applications is the presence of the controller action. Since the machine currents are being controlled, the effectiveness of current-based turn fault detection method will be abated in CCVSI-driven machines. This means that a turn fault indicator for CCVSI-driven applications should be selected such that it is strongly dependent on turn faults, but quite independent of the controller actions. In this section, previously proposed fault indicators to attenuate the adverse effects of controller actions on turn fault detection are introduced and evaluated.

2.2.1 Fundamental Negative Sequence Voltage

A stator turn fault in a symmetrical three-phase AC machine results in a phase imbalance of the machine. This imbalance induces fundamental negative sequence components in the stator line-neutral voltages and line currents [27], [28]. The interaction between the fundamental positive sequence voltage and the fundamental negative sequence current or vice versa introduces second-order harmonics in the instantaneous power, developed torque, and rotating speed [25], [26].

A CCVSI tries to regulate the line currents so as to follow their references by adjusting the output voltages. If the current references are perfectly balanced, and the

performances of the current controllers are perfect, then no fundamental negative sequence current will be observed even under a stator turn fault condition, but a fundamental negative sequence component will appear in the inverter output voltage because the CCVSI injects the required negative sequence voltage to maintain the symmetry of the line currents. However, this is valid only in the ideal situation.

A practical speed controller has limited performance. Furthermore, speed (position) information, which has a second-order harmonic resulting from a turn fault, is used as one of the inputs to the speed controller. If the speed controller cannot remove the second-order harmonic from the output of the controller (torque reference), the symmetry of the current references will be distorted. Furthermore, the speed (position) information is used for converting variables from the stationary *abc* reference frame to the synchronously rotating *qd* reference frame and vice versa. In addition, the performances of a practical current controller are non-ideal. For these practical reasons, a negative sequence current can still be observed when a CCVSI-driven application has a turn fault in spite of its controller actions. However, it can be inferred that the degree of the negative sequence current caused by a turn fault would be affected by the performance of the speed and current controllers in a CCVSI-driven application. If the bandwidth of the speed controller is well below the frequency of the second-order harmonic in the rotating speed, the output of the speed controller (torque reference) will be nearly dc, and the fundamental negative component in the machine terminal voltages will be dominant in the line currents. On the other hand, if the torque reference (current reference) contains the second-order harmonic, then the fundamental negative sequence component is dispersed in both the inverter output voltages and line currents. On the basis of these

observations, a negative sequence voltage based turn fault detection method is proposed in [32]. Although the proposed method is effective to detect a stator turn fault in CCVSI-driven machines, it requires voltage sensors that are rarely installed in ordinary drives. This is the main drawback of the method.

2.2.2 Fundamental Zero Sequence Voltage

A phase impedance variation (or imbalance) is introduced when a turn fault occurs in any of the stator phase, and this variation will induce a fundamental zero sequence voltage in a wye-connected electric machine. Turn fault detection methods based on this phenomenon are proposed in [33]-[35]. The basic ideas of the methods are identical, but the difference lies only in the number of voltage sensors used.

When considering only the fundamental component of electrical excitation, the sum of the stator line-neutral voltages is given by

$$\tilde{V}_{sum} = \tilde{V}_{an} + \tilde{V}_{bn} + \tilde{V}_{cn} = Z_a \tilde{I}_a + Z_b \tilde{I}_b + Z_c \tilde{I}_c , \tag{2.1}$$

where $\tilde{V}$, $\tilde{I}$, and Z represent the phasors of stator line-neutral voltage, current, and impedance, respectively, the subscripts a, b, and c represent the phases, and the subscript, n, denotes the floating neutral point of the stator windings.

For a balanced machine, the three-phase sequence impedances are

$$Z_a = Z_b = Z_c , \tag{2.2}$$

In a wye-connected stator windings, the sum of the phase currents must be

$$\tilde{I}_a + \tilde{I}_b + \tilde{I}_c = 0 . \tag{2.3}$$

The above relationships imply that for a balanced machine,

$$\begin{aligned} &\tilde{V}_{sum} = \tilde{V}_{an} + \tilde{V}_{bn} + \tilde{V}_{cn} = 0 \quad \text{and} \\ &v_{sum}(t) = v_{an}(t) + v_{bn}(t) + v_{bn}(t) = 0, \end{aligned} \tag{2.4}$$

where $v(t)$ represents the instantaneous voltage. Thus, any deviation from (2.4), where

$$v_{sum}(t) \neq 0 \tag{2.5}$$

reveals potential phase imbalance caused by turn faults.

The use of fundamental zero sequence voltage as a fault indicator can enhance the reliability of turn fault detection for CCVSI-driven machines since no zero sequence voltage will be observed in a balanced machine. Furthermore, the degree of the fundamental zero sequence voltage is quite independent of the controller actions. Despite these distinct advantages, zero sequence voltage-based turn fault detection methods have several critical limitations in practice. First, the methods can only be used for wye-connected machines because no zero sequence voltage can be observed in delta-connected machines. Secondly, the wye-connected machines should have an accessible floating neutral point because zero sequence voltage cannot be measured in the line-line voltages. Lastly, the machine terminal voltages must be measured.

2.2.3 Second Order Harmonic in the *d*-axis Current in the Synchronously Rotating Reference Frame

When an induction motor drive operates in the constant flux (or constant torque) region, the *d*-axis current reference in the synchronously rotating reference frame (i_{ds}^{e*}) is constant, while the *q*-axis current reference in the same reference frame (i_{qs}^{e*}) is

determined by the output of the speed controller (torque reference). This implies that i_{ds}^{e*} remains constant in constant-flux region even under a stator turn fault condition, while i_{qs}^{e*} will be affected by the second-order harmonic in the rotating speed caused by the fault.

As discussed in section 2.1.1, the fundamental negative sequence current caused by a turn fault is still observable in a CCVSI-driven application. Furthermore, the induced negative sequence current will be distributed in both the *q*-axis current (i_{qs}^{e}) and the *d*-axis current (i_{ds}^{e}). In the synchronously rotating reference frame, the fundamental negative sequence current is observed to be a component rotating at the synchronous frequency in a direction opposite to the rotating reference frame, while the fundamental positive sequence component current is observed to be a stationary. Thus, the fundamental negative sequence current would be observed as a second-order harmonic in the time domain, while the fundamental positive sequence current would be seen as a dc-component. Therefore, i_{ds}^{e*} and i_{ds}^{e} will have different magnitudes in their second-order harmonics under a turn fault condition, and the difference would be a good turn fault indicator for CCVSI-driven induction motors. Also this difference in i_{ds}^{e*} and i_{ds}^{e} is quite independent of the controller actions. Based on this reasoning, a detection method for stator turn faults in CCVSI-driven induction motor applications is proposed in [36]. Although the proposed method is effective in detecting stator turn faults in CCVSI-driven induction motor applications, the method is only viable when the induction motor operates in the constant flux region, wherein i_{ds}^{e*} remains constant. In controlling an IPMSM, maximum torque per ampere (MTPA) operation is commonly applied, and i_{ds}^{e*}

under this operation varies depending on the required developed torque. This means that the use of second-order harmonic in i_{ds}^{e*} as a turn fault indicator is not a good choice for detecting turn faults in CCVSI-driven IPMSM applications.

2.2.4 Uneven Distribution of Inverter Switching States

The output voltages of a two-level VSI are generated through eight different switching states: six active and two zero states. As discussed earlier, a stator turn fault in a CCVSI-driven machine induces a negative sequence component in the inverter output voltages. As a result, an uneven distribution of the six active switching states will be induced during a single or multiples of the fundamental electrical period.

In [37], an on-line detection method based on monitoring the statistical distribution of the active switching states is proposed. The proposed method simply counts how often each active switching state is applied to the machine during the period of observation. The hexagon diagram of the inverter switching states is illustrated in Figure 2.1 where $\overline{u}$ represents a switching state, H denotes the counted number of a switching state during the period of observation, the subscript, p, represents the period of observation, and each integer number from zero to seven represents the index of each switching state.

To detect machine asymmetries, the symmetric mean value, $H_{m(p)}$ is calculated by

$$H_{m(p)} = \frac{\sum_{n=1}^{6} H_{n(p)}}{6}. \tag{2.6}$$

The absolute values of $H_{n(p)}$ vary with the point of operation as well as with the period of observation.

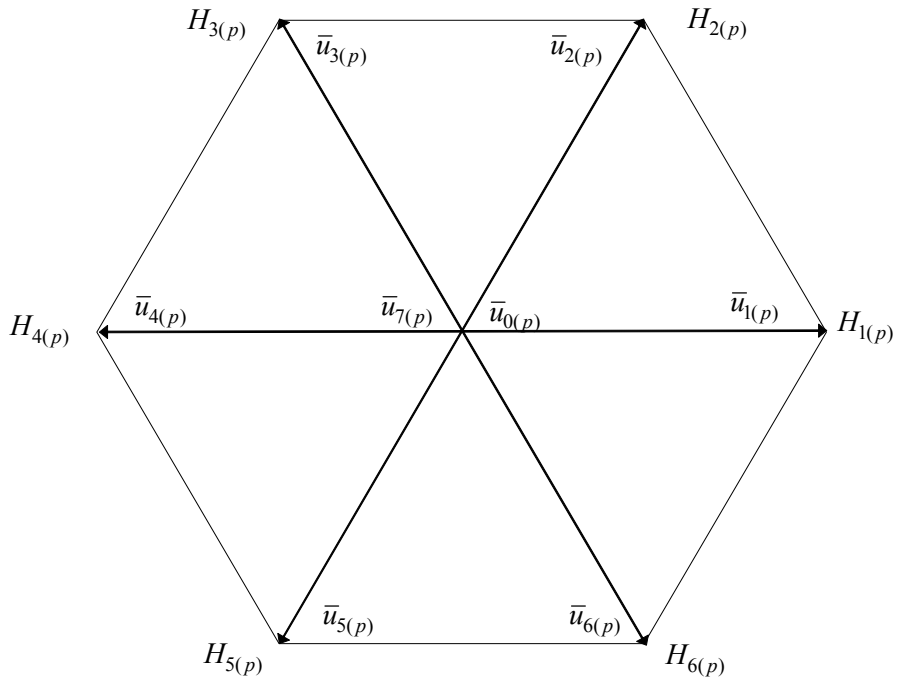

Figure 2.1. Hexagon diagram of the switching states of a two-level VSI.

Thus, the relative deviation from the actual mean value for the switching state, u_1, is calculated as,

$$h_{1(p)} = \frac{H_{n(p)} - H_{m(p)}}{H_{m(p)}} \times 100[\%]. \tag{2.7}$$

The relative deviation from the actual mean value defined in (2.7) cannot only tell the occurrence of a stator turn fault, but also can tell which phase winding has the fault. Although the proposed method is based on a proper understanding of the characteristics of CCVSIs, the authors of [37] did not pay much attention to the fact that an uneven distribution of the active switching states can be caused by other factors, such as oscillatory loads, fluctuating rotating speeds, and fluctuations in the dc-link voltage.

2.2.5 Negative Sequence Current (or Impedance) in High Frequency Carrier Signal

A reliable turn fault detection method for CCVSI-driven machines is proposed in [38], which injects a high-frequency carrier signal into the machine terminal voltages. The resultant high-frequency negative sequence current (or alternatively the negative sequence impedance) is then used for turn fault detection. Although the method is based on similar principles as that of the negative sequence impedance- and sequence impedance-based methods [4], [29], this method has distinct advantages over the fundamental excitation based techniques.

When excited by balanced three-phase high frequency carrier signal voltage, given by (2.8), which is substantially faster than the stator dynamics, the motor can be adequately modeled using only the stator transient inductance.

$$v^s_{qds\_c} = V_c e^{j\omega_c t}, \tag{2.8}$$

In this case, the high-frequency machine model is expressed as

$$v^s_{qds\_c} \cong j\omega_c L_{\sigma s} i^s_{qds\_c}, \tag{2.9}$$

where V_c represents the amplitude of the high-frequency carrier signal, ω_c represents the carrier frequency, $L_{\sigma s}$ represents the stator transient inductance, and the subscript, c, denotes a variable resulting from the high-frequency carrier signal injection.

If there is an unbalance in the machine's leakage inductance, the interaction between the carrier-signal voltage and the unbalance in the leakage inductance will

produce a carrier-signal current consisting of both positive and negative sequence components. This is represented by,

$$i^s_{qds\_c} = i^s_{qds\_cp} + i^s_{qds\_cn} = I_{cp}e^{j\omega_c t} + jI_{cn}e^{j(h\theta_A - \omega_c t)}, \tag{2.10}$$

where

$$I_{cp} = \frac{V_c}{\omega_c}\left(\frac{\sum L_{\sigma s}}{\sum L^2_{\sigma s} - \Delta L^2_{\sigma s}}\right) \text{ and } I_{cp} = \frac{V_c}{\omega_c}\left(\frac{\Delta L_{\sigma s}}{\sum L^2_{\sigma s} - \Delta L^2_{\sigma s}}\right) \tag{2.11}$$

represent the amplitudes of the positive and negative carrier-signal currents, θ_A is the angular position of the saliency in electrical radians, h represents the harmonic order of saliency, $L_{\sigma qs}$ and $L_{\sigma ds}$ are the *q*- and *d*-axis stator transient inductances in the saliency synchronously reference frame, $\sum L_{\sigma s} = \frac{L_{\sigma qs} + L_{\sigma ds}}{2}$ represents the average stator transient inductance, and $\Delta L_{\sigma s} = \frac{L_{\sigma qs} - L_{\sigma ds}}{2}$ represents the differential stator transient inductance.

The positive sequence carrier-signal current is proportional to the average stator transient inductance and contains no saliency spatial information. The negative sequence carrier-signal current is proportional to the differential stator transient inductance and contains saliency spatial location information of the phase. Thus, a stator turn fault can be detected by monitoring the negative sequence carrier-signal current (or the negative sequence carrier-impedance). The proposed method superimposed on the fundamental excitation voltage, provides interesting advantages when compared to fundamental excitation based techniques. First, the measured high-frequency negative sequence impedance or current will be shown to be independent of operating conditions of the

machine as the fault develops, *i.e.,* independent of the flux level, load level, and fundamental excitation frequency. Secondly, a high-frequency carrier-signal voltage will noticeably reduce the influence of the controller actions on the negative sequence current. Finally, the carrier-signal voltage, which is independent of the fundamental voltages, is injected using an inverter. This dramatically decreases the sensitivity to supply voltage imbalances. Despite the clear advantages, the method is too complicated and requires a large computational effort. In addition, the frequency of the injected carrier signal should be selected carefully such that the frequency is not so close to other harmonics such as stator slot harmonics and PWM-related sub-harmonics. .

2.3 Data Adaptation (Signal Processing) Techniques

The non-stationary operations of a drive change the fundamental frequency continuously. This makes conventional sequence decomposition, which yield the best performance when signals are at quasi-steady or steady-state conditions, ineffective for turn fault detection. To analyze a time-varying signal, several signal processing techniques based on two dimensional time-frequency domain representation have been proposed. Among them, the short-time Fourier transform (STFT) and wavelet transform (WT) have been commonly applied for machine fault diagnosis. In this section, the two techniques are discussed briefly. In addition, another approach to analyzing signals containing multi-frequency components and suitable for stator turn fault diagnosis, is introduced.

2.3.1 Short Time Fourier Transform (STFT)

The standard method for analyzing time-varying signals is the STFT. The STFT applies the Fourier Transform to a windowed signal to obtain the energy distribution of the different frequency components at the time corresponding to the center of the window [46]. The STFT of a continuous-time signal $x(t)$ is defined as,

$$STFT(\tau, f) = \int_{-\infty}^{\infty} x(t)w(t-\tau)e^{-j2\pi ft}dt\,, \tag{2.12}$$

where $w(t)$ is the window function whose position is translated in time by τ. The discrete form of (2.12) is,

$$STFT(k, m) = \sum_{n=0}^{N-1} x(n)w(n-m)e^{-j\frac{2\pi kn}{N}}\,, \tag{2.13}$$

where $w(n)$ is the sliding window.

When the variation of a time varying signal under analysis is relatively slow, it can be assumed that the signal is stationary throughout the calculation of the STFT. The number of STFT calculations required depends on the signal sample length and the size of the time window used to partition the signal. Despite its simplicity in implementation and reasonable performance, a limitation of this method is caused by the fact that the length of the window influences on the frequency resolution. Though increasing the window length leads to improvement in frequency resolution, but it also means that the non-stationarities occurring during the interval of the window will be smeared in time and frequency. This inherent relationship between the time and frequency resolutions becomes more critical when the STFT deals with signals whose frequency content is

continuously changing. Thus, a compromise in the frequency and time resolutions has to be made in an implementation.

2.3.2 Wavelet Transform (WT)

To solve the trade-off between time and frequency resolutions of the STFT, the wavelet transform (WT) has been developed [47]. In contrast to the STFT, the WT uses short windows at high frequencies and long windows for low frequencies. Using the WT, the time-varying spectra of non-stationary signals can also been obtained in form of scalograms defined as the squared modulus of the WT [47]. The continuous wavelet transform (CWT) of a signal, $x(t)$ depends on two variables: scale (frequency) parameter (a), and time parameter (τ). It is given by,

$$CWT(a,\tau) = \frac{1}{\sqrt{a}} \int_{-\infty}^{+\infty} x(t) g(\frac{t-\tau}{a}) dt \,. \tag{2.14}$$

Although the WT partially solves the practical problems of the STFT, but it has a restriction on the choice of $g(t)$, the base function. The base function must have a zero average value and should be short duration, which, in mathematical terms, is called the admissibility condition on $g(t)$ [48]. The performance of the WT depends on the selection of base function. In [49], a practical implementation of the WT for detecting broken rotor bar and stator turn faults in an induction motor is introduced.

2.3.3 Space Vector Decomposition in Multiple Reference Frames

In analyzing non-stationary signals, the STFT and WT are the commonly used methods. These two transforms ideally decompose all the contained frequency

components in a time-varying signal. However, they may be somewhat inefficient for turn fault detection because the observation of only one or two frequency components (fundamental or negative sequence component) would be enough for the purpose. Another possible way for decomposing frequency components from a non-stationary signal is to represent the signal in the space vector domain. As mentioned earlier, every frequency component in a non-stationary signal can be observed as a stationary component in a reference frame rotating at the corresponding frequency in either the clockwise or counter-clockwise direction. This means that the fundamental negative sequence component caused by a stator turn fault will be seen as a stationary component in the reference frame rotating at the synchronous frequency but in a direction opposite to the synchronously rotating reference frame. A turn fault detection method, which monitors the fundamental positive sequence current using this idea, is proposed in [39].

2.4 Fault Decision Algorithms

In practice, any electric motor drive is not perfectly balanced, and has non-idealities. These non-idealities are due to such causes as inverter non-linearities, motor inherent asymmetry, and current or speed measuring errors. The non-idealities in a drive influence the sensitivity of a turn fault detection method because the physical consequences of them are easily confused with those of the asymmetry resulting from a turn fault. This makes it critical to compensate for the effects of non-idealities for more reliable turn fault detection. But, the compensation is somewhat challenging because the non-idealities vary depending on operating conditions in a non-linear manner. To solve

this problem, several pattern identification algorithms have been applied. Among them, look-up table and artificial neural network-based methods have been commonly used.

2.4.1 Look-Up Table-Based Methods

The basic concept of a look-up table-based turn fault detection method is straight-forward. The selected fault indicator is obtained over the entire drive operating range when the motor is healthy, and stored in tables. Then the influence of the non-idealities in the drive can be compensated for by comparing the actual values of the fault indicator with the stored data.

Although the concept is simple, the practicality of a look-up table-based turn fault detection method is not easy to achieve because of its inherent limitations. The reliability of a look-up table-based method is strongly dependent on the look-up table resolution. In other words, the more accurate turn fault detection requires a higher look-up table resolution. This leads to the requirements of more extensive experiments and larger memory space for storing the data. In addition, it is very difficult or even impossible to generate a look-up table where all possible causes of non-idealities are considered.

An implementation of look-up table-based turn fault detection method for a mains-fed induction motor is proposed in [29]. Trutt, *et. al* selected the positive or negative voltage resulting from a turn fault as the fault indicator, taking into account the inherent motor asymmetry and power supply unbalance. However, this method does not consider the slip dependency of the inherent motor asymmetry, which can lead to inaccurate turn fault detection in an induction motors.

2.4.2 Artificial Neural Network-Based Methods

As discussed in section 2.3.1, a look-up table-based turn fault detection method is difficult to implement with considering all possible causes of non-idealities in a drive system. To overcome this difficulty, other techniques, which are effective for recognizing specific patterns in data clusters that have non-linear relationships with a large input space, have been developed [50]. These techniques include expert systems, artificial neural networks (ANNs), and fuzzy-logic systems. Among them, ANNs have been commonly applied in the area of machine fault diagnosis since they are general nonlinear-function approximators. Basically, these approximations are achieved using a suitable network of artificial neurons, which are connected by appropriate weights. However, neural networks must be trained under various combinations of the input elements before an acceptable approximation is achieved.

A neural network based on off-line training should be trained under all operating conditions that are expected to occur in practice. But it is not practically possible to obtain data over the entire drive operating range prior to turn fault monitoring, which can result in inaccurate turn fault detection when the input space changes significantly. To solve this problem, several self-commissioning training algorithms are proposed in [51], where the weights of a feed-forward neutral network are retrained whenever the input space is changed.

In [32], a turn fault detection method for a CCVSI-driven induction motor is proposed by applying a feed-forward NN (FFNN) technique. The schematic of the proposed method is presented in Figure 2.2. In the learning stage, the NN is trained with the sequence components of currents and positive sequence voltages under various

excitation frequencies and load conditions, to predict the negative sequence voltage for a healthy machine. Then, in the monitoring phase, the difference between the measured and estimated negative sequence voltages is monitored to detect the asymmetries resulting from a turn fault. As indicated in Figure 2.2, the proposed method can reduce the possibility of inaccurate fault detection when the input space is changed significantly since the weights of the feed-forward NN are retained in an on-line fashion. The proposed method significantly increases the reliability of turn fault detection for CCVSI-driven machines. However, the method is complicated, requires much computation, and requires additional voltage sensors and cabling.

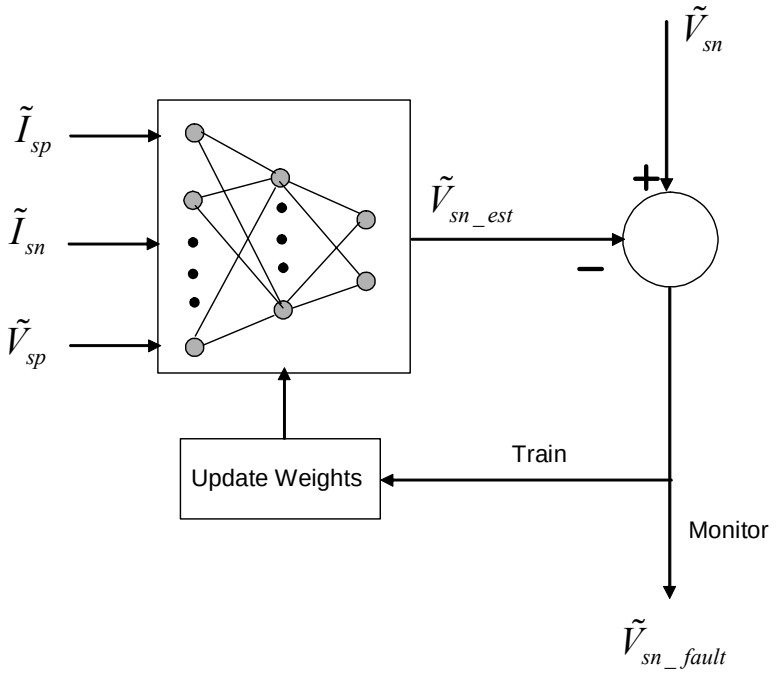

Figure 2.2. Schematic of FFNN-based turn fault detection for induction motor drives [32].

2.5 Chapter Summary

The state of the art on-line turn fault detection methods for CCVSI-driven machines have been summarized and evaluated to cover the main issues in the area of stator turn fault diagnosis.

As mentioned earlier, CCVSIs are indispensable for variable speed operations and high performances, but they lead to difficulties in detecting turn faults. To solve the difficulties, several methods have been developed. However, none of them can be used as a universal method that yields good performance for every type of machine drive. This suggests that a fully understanding of the characteristics of the concerned drive system should be the starting point of the development of a turn fault detection method. Then fault indicator, data adaptation technique, and fault decision algorithm should be properly selected for reliable turn fault detection.

Since almost all CCVSIs have their own controller hardware and built-in current sensors, it would be desirable that a turn fault detection method for CCVSI-driven machines should be implemented in the same controller hardware without any additional sensors and any degradation in control performances.

The review in this chapter also indicates that previously proposed methods mainly consider turn faults in induction motors, while the research on turn fault detection for IPMSM drives still remains an unexplored area. However, the usage of IPMSM drives is rapidly increasing in a wide variety of industrial and transit applications. Thus, the demand for a reliable turn fault detection method for IPMSM drives is increasing.

CHAPTER 3

SUMMARY OF PREVIOUS WORK ON STATOR TURN FAULT-TOLERANT OPERATING STRATEGY

3.1 Overview

In an application where safety is not a critical issue, just stopping the drive's operation when a stator turn fault is detected would be enough. On the contrary, in a safety-critical application, it is imperative to maintain uninterrupted drive operation under a stator turn fault condition. This is more challenging for any type of permanent magnet synchronous motor (PMSM) drive because of the presence of the spinning permanent magnets. In spite of the need to resolve this issue, the research on how to maintain the availability of an electric motor drive under a stator turn fault condition still remains an unexplored area. The small amount of work on this issue has been performed mainly in three ways: redundancy, remedial actions to stop the faulty motor without further damage, and development of fault-tolerant machines. This lack of research is due to the pre-conceived notion that it is impossible to prevent a turn fault from progressing to the catastrophic phase when the faulty machine is operating. A summary and evaluation of previously proposed wok on increasing the stator turn fault tolerance, especially the availability, of motor drives are presented in this chapter.

3.2 Redundancy-Based Approach

The circulating current in the shorted turns resulting from a turn fault is generated by the interaction between these turns and the rotating air-gap magnetic flux. This means that the circulating current can be extinguished only by isolating the shorted turns from the rotating air-gap magnetic flux. However, in a conventional symmetrical three-phase AC machine, it is impossible to isolate only the shorted turns from the rotating air-gap magnetic flux. Thus, removing the rotating air-gap magnetic flux is the only way to extinguish the circulating current. However, no torque will be developed by removing the magnetic flux. If the drive system has an extra motor that can take place of the faulty motor, the uninterrupted drive's operation can be maintained. However, the faulty motor should be electrically and magnetically separable from the redundant motor. Furthermore, in the case of a PMSM drive, the faulty motor should also be mechanically separable from the load system as well as the extra motor because the rotating air-gap magnetic flux of the faulty motor can be quenched when the motor stop rotating completely.

A possible configuration of a fault-tolerant PMSM drive system with redundancy is presented in Figure 3.1 [40]. The drive system in Figure 3.1 consists of two separated drives, each acting as the redundant part when the other fails to operate properly. The mechanical components for mechanically isolating from the motors from the drive system are also found in the drive system. However, these mechanical components will not be necessary for induction motor drives with a stator turn fault.

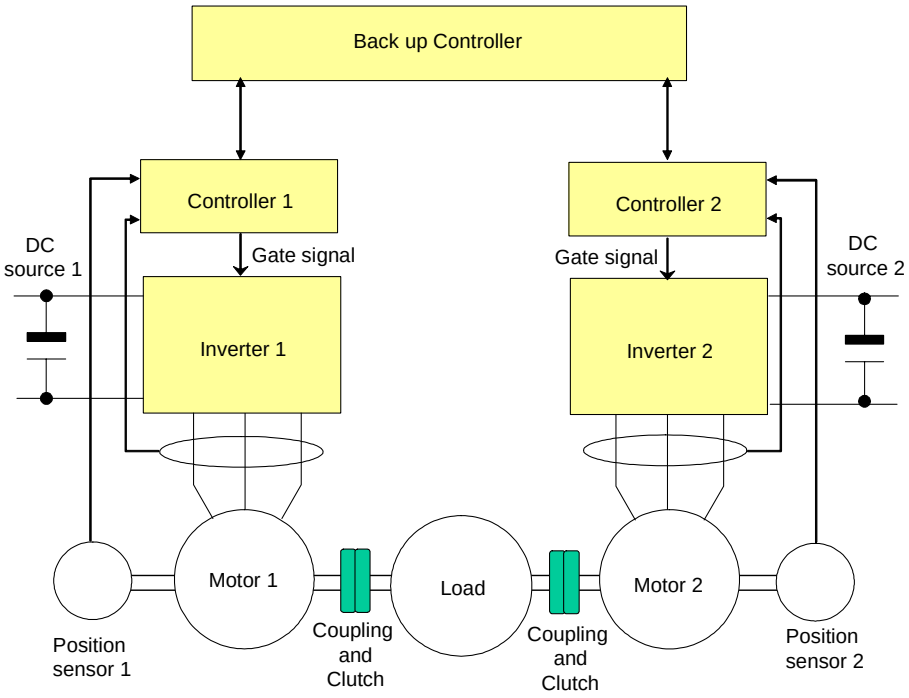

Figure 3.1. A possible configuration of a fault-tolerant PMSM drive with redundancy.

Although a redundancy-based approach can provide a much higher fault tolerance to an electric motor drive without any performance degradation, it increases the cost and complexity of the system significantly. Moreover, redundancy-based approaches may not be practical for applications that have severe restrictions on the installation space and mechanical structure, such as in the case for traction drives in electric vehicles. For these reasons, the use of redundancy-based approaches can be justified only in a few applications.

3.3 Drive Operating Modes for Stopping Machine Safely

In an application where the driving force to the load system is supplied from a combination of two or more actuators, the continuous supply of driving force can be

maintained even though the driving force from one of the actuators is no longer available. When a stator turn fault is detected in such an application, the main concern would be to stop the faulty machine without further damage. For this purpose, two types of operations can be used, namely, free-running and symmetrical short-circuit operation.

3.3.1 Free-Running Operation

When the stator currents are cut off, an electric machine will either decelerate automatically by consuming the store mechanical energy or will be forced to rotate by a mechanical counterpart connected to it. In general, this operating mode is referred to as free-running operation. In an induction motor, the rotating air-gap magnetic flux decays to zero under free-running operation. Therefore, the circulating current resulting from a turn fault can be completely extinguished under this operation. However, the scenario in the case of PMSMs is quite different because of the presence of the rotating permanent magnets. Although the stator currents are switched off, the shorted turns in a PMSM continue to link with the rotating magnetic flux contributed by the permanent magnets until the motor completely stops rotating. This implies that a stator turn fault in PMSMs cannot be prevented from thermally progressing even under free-running operation if the operation is maintained for a sufficiently long time. For this reason, free-running operation is not an effective post-turn fault operating mode for a PMSM. And this limitation will be more critical for applications where the electric machines are directly coupled to the mechanical counterparts or loads, such as power train systems of hybrid electric vehicles. However, it should be mentioned that control over the machine is completely lost under free-running operation regardless of the type of the machine.

3.3.2 Symmetrical Short-Circuit Operation

It was shown in the previous section that free-running operation is not an allowable post turn fault operating mode for PMSM drives. However, this is not the only limitation of the operation.

Once free-running operation is commenced, the PMSM drive becomes a three-phase diode rectifier with a PM generator. If the PMSM rotates at high speed where the rotor-induced voltage, the so called back-emf voltage, exceeds the dc-link voltage, then unregulated power from the PMSM charges the dc-link because field-weakening operation is no longer available under free-running operation. If the dc-link is unable to absorb the unregulated power, the dc-link would undergo severe stress, and in the worst case, the dc-link could fail. Reference [52] provides a systematic investigation of the PMSM drive's operation in this situation, referred to as uncontrolled generator operation (UCG). To avoid the undesirable stress on the dc-link resulting from unregulated power, an operating mode, referred to as symmetrical short-circuit operation, is employed in [41]. This operating mode is activated by turning on the pair of the top or bottom switching devices in a six-switch inverter.

The schematics of a PMSM drive under UCG operation and symmetrical short-circuit operation are presented in Figure 3.2(a) and (b), respectively. As shown in Figure 3.2(b), the output poles of the inverter are clamped to the positive or negative dc-link junction under symmetrical short-circuit operation; therefore, no power flows between the motor and the dc-link. Thus, the possible damage to the dc-link component resulting from excessive generated power is not a concern.

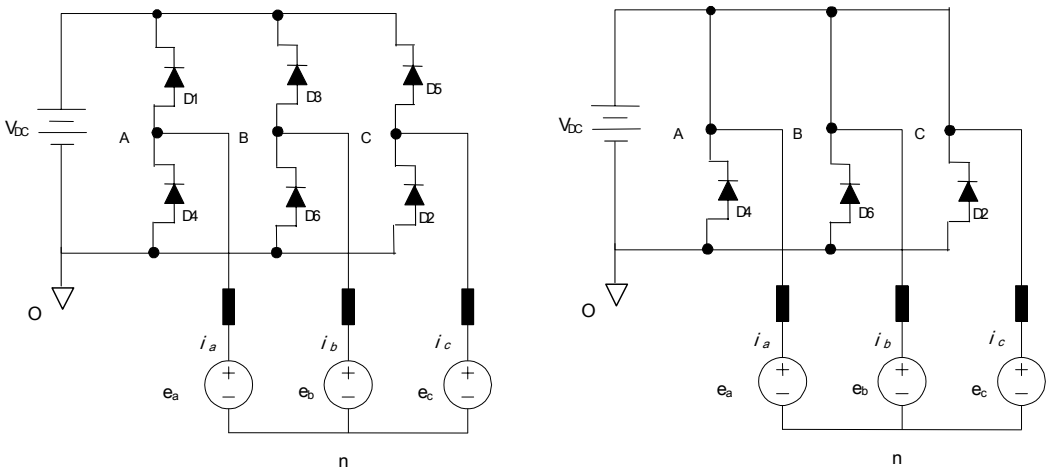

(a) UCG operation **(b) Symmetrical short-circuit operation**

Figure 3.2. Schematics of a PMSM drive under UCG and symmetrical short-circuit operation.

Symmetrical short-circuit operation is an effective post fault operating mode in the presence of an inverter failure, especially in the case of switching device short-circuit failure [41]. In addition, this operating mode works as a good post turn fault operating mode for PMSM drives. All three machine terminals are shorted at the positive or negative dc-link junction through the inverter switching devices under symmetrical short-circuit operation. Consequently, the line-line machine terminal voltages get close to zero. In this situation, the rotating air-gap magnetic flux produced by the stator currents acts against the rotating air-gap magnetic flux contributed by the permanent magnets in such a way that the resultant air-gap magnetic flux would be close to zero. This phenomenon can be seen in the equivalent circuits in terms of the *qd*-variables in the synchronously rotating reference frame.

The equivalent circuits of an IPMSM under symmetrical short-circuit operation are presented in Figure 3.3.

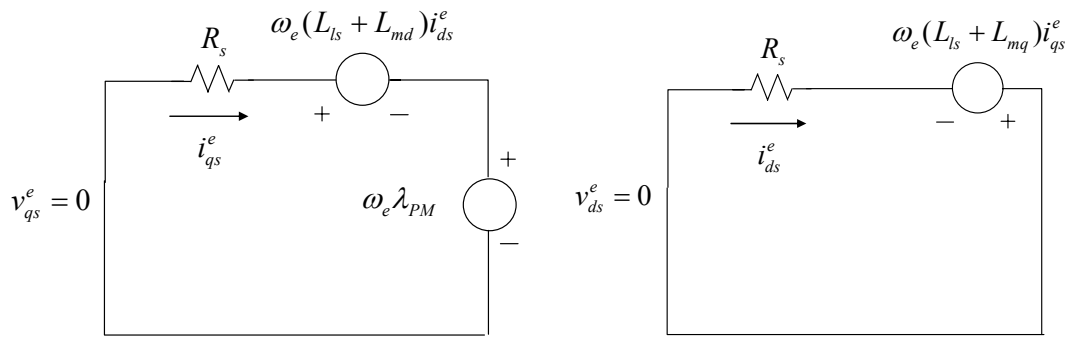

(a) *q*-axis **(b) *d*-axis**

Figure 3.3. The *qd*-axis equivalent circuits of an IPMSM in the synchronously rotating reference frame under symmetrical short-circuit operation.

The representations of the *q*- and *d*-axis voltages and currents under symmetrical short-circuit operation are given, respectively by,

$$\begin{bmatrix} v^e_{qs} \\ v^e_{ds} \end{bmatrix} = \begin{bmatrix} 0 \\ 0 \end{bmatrix} = \begin{bmatrix} R_s i^e_{qs} + \omega_e (L_d i^e_{ds} + \lambda_{PM}) \\ R_s i^e_{ds} - \omega_e L_q i^e_{qs} \end{bmatrix}, \tag{3.1}$$

$$\begin{bmatrix} i^e_{qs} \\ i^e_{ds} \end{bmatrix} = -\frac{1}{R_s^2 + \omega_e^2 L_q L_d} \begin{bmatrix} R_s \omega_e \lambda_{PM} \\ \omega_e^2 L_q \lambda_{PM} \end{bmatrix}, \tag{3.2}$$

where the subscripts, *q* and *d* designate variables in the *q*- and *d*-axis, respectively; the subscript, *s,* designates a stator variable; the superscript, *e*, represents a variable in the synchronous reference frame; R represents a resistance; L represent a inductance; ω_e represents the synchronous frequency in radian per second; λ_{PM} represents the flux linkage contributed by the permanent magnets. From (3.1) and (3.2), the developed torque in symmetrical short-circuit operation can be obtained as,

$$T_{e\_sym} = \frac{3}{2}\frac{P}{2} R_s \lambda_{PM}^2 \left[\frac{-\omega_e}{R_s^2 + \omega_e^2 L_q L_d} + (L_d - L_q)\frac{L_q \omega_e^3}{(R_s^2 + \omega_e^2 L_q L_d)^2}\right], \tag{3.3}$$

where P is the number of poles of the machine.

Equations (3.2) and (3.3) imply several interesting phenomena under the symmetrical short-circuit operation. Symmetrical short-circuit operation induces a *d*-axis current that produces a magnetic flux opposing λ_{PM}, whose amplitude is almost the same as the ratio of λ_{PM} to L_d i.e., $\frac{\lambda_{PM}}{L_d}$, referred to as the characteristic current of the IPMSM. Furthermore, this operation induces a small negative *q*-axis current. As a result, a small braking torque is developed, whose amplitude is maximized at a certain rotating speed, *i.e.*, $\omega_e = R_s \Big/ \sqrt{L_d L_q}$ [41]. Although a braking torque (generating torque) is developed in the symmetrical short-circuit operation, the rotating air-gap magnetic flux that linkages the stator windings can be significantly reduced. This implies that the circulating current in the shorted turns resulting from a stator turn fault can be significantly reduced under the symmetrical short-circuit operation. The effectiveness of the operation as a post-turn fault operation for PMSM drives is investigated in [1] and [53]. In this work, symmetrical short-circuit operation is singled out, and detailed analysis of the performance is given in Chapter 12. However, it should be noted that the critical limitation of this operating mode is that control over the machine under symmetrical short-circuit operation is no longer available.

3.4 Development of Turn Fault-Tolerant Electric Machine

Generally, reducing the likelihood of a stator turn fault can be achieved by designing a machine conservatively; however, this is not cost-effective. Another way for a higher stator turn fault tolerance of an electric machine is to provide inherent turn fault

tolerance to the machine by adapting specific design configurations. In this section, several machine design configurations (or approaches) for this purpose are discussed.

3.4.1 Fault-Tolerant Machines

In general, stresses related to motor failures do not act on a specific spot or part but on the entire motor. Moreover, any excessive stress generated by a faulty part impacts other healthy components. Thus, to make a motor more fault tolerant, the coupling effects of stresses between the components should be minimized. An electric machine that has less coupling effects between the parts can be realized if the following requirements are satisfied [42], [44]:

(1) Complete electrical isolation between phases

(2) Implicit limiting of fault currents

(3) Magnetic isolation between phases

(4) Physical isolation between phases

(5) More than three-phases

Considering the structure of conventional electric machines, only switched reluctance motors (SRMs) come close to achieving the above requirements. SRMs have inherent high stator turn fault tolerance. This is due to the fact that only opening the faulty winding can eliminate the circulating current in the shorted turns while maintaining the uninterrupted operation. Despite this clear advantage, SRMs are not preferred in certain applications that require high efficiency and accurate control because of their low efficiency, large acoustic noise, and vibration. One possible way to reduce the vibrations resulting from a large torque pulsation is to increase the number of phases; thus, SRMs

have generally more than three phases. For operating a SRM, the asymmetrical half-bridge converter topology is generally applied, and the converter topology is compared with that of a conventional symmetrical three-phase AC machine in Figure 3.4. As shown in Figure 3.4(b), each phase winding in a SRM is electrically and magnetically isolated from the other phases; thereby, high fault tolerance is inherently given to the machine. However, this feature makes it necessary to sense all the phase currents for controlling the machine. For this reason, a more complicated and expensive converter will be required for a SRM that has more than three phases.

Several researchers have proposed a specific configuration of permanent magnet machines that combines the advantages of SRMs and PMSMs. This configuration is called modular fault-tolerant PM machine or hybrid stepping motor [43], [44]. The cross-sectional view of an eight-pole and six-phase modular fault-tolerant PM machine is illustrated in Figure 3.5.

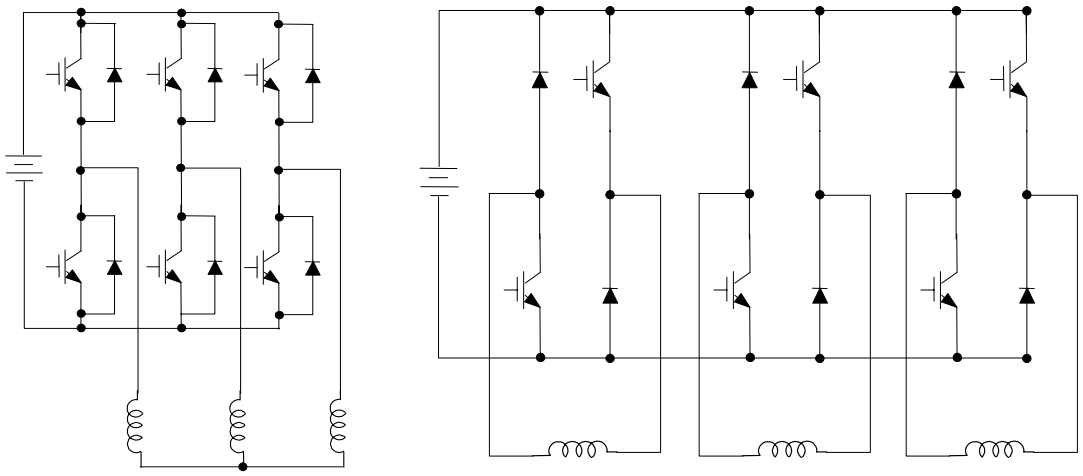

(a) three-phase symmetrical machine **(b) three-phase SRM**

Figure 3.4. Schematics of the converters for a three-phase symmetrical machine and SRM.

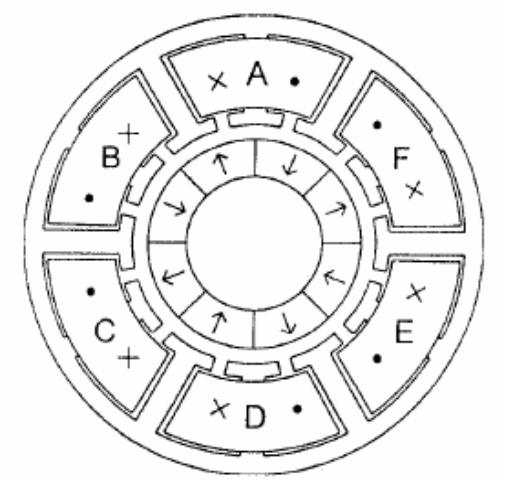

Figure 3.5. Cross sectional view of an eight-pole and six-phase modular fault-tolerant machine.

The stator winding structure of this type of machine is the same as that of a SRM, and the rotor structure is the same as that of a surface mounted PM synchronous motor (SPMSM). Therefore, electrical and magnetic isolations between the phase windings are achieved. However, even in this type of machine, the magnetic couplings between the stator windings and rotor magnets still exist. Thus, when a stator turn fault occurs, the circulating current in the shorted turns will flow since the shorted turns link with the rotating magnetic flux contributed by the permanent magnets. This means that a stator turn fault in even a modular fault-tolerant PM machine is subjected to progress to the catastrophic phase.

Mecrow *et al.* [43] proposed an operating mode to reduce the circulating current without interrupting the operation. However, the proposed operating mode has the exact same theoretical foundation as the symmetrical short-circuit. When a stator turn fault in a phase winding is detected in a modular fault-tolerant PM machine, the two ends of the faulty winding are shorted through the converter switching devices at the negative and

positive dc-link junctions, respectively. Even in this situation, the other healthy phases continue to generate propulsion for the load because the phase windings are electrically and magnetically decoupled from each other. However, a modular fault-tolerant machine has a distinct disadvantage. Since the phase currents in a modular fault-tolerant PM motor should flow bi-directionally, a more complicated and expensive converter topology is required for the motor. The block diagram of the converter topology for a modular fault-tolerant PM motor is presented in Figure 3.6. As shown in the figure, each phase of a modular fault-tolerant PM motor requires a separated H-bridge converter. This means that the numbers of required H-bridges and current sensors are the exactly same as the number of phases of the motor.

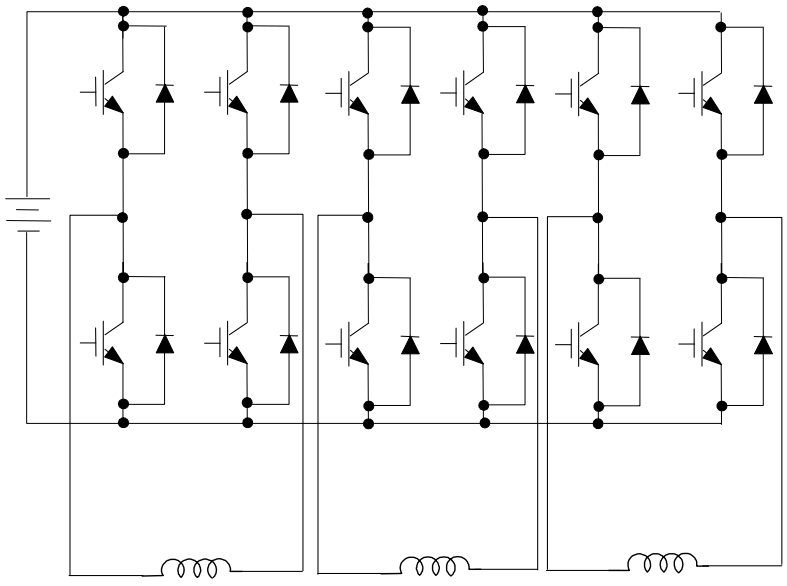

Figure 3.6. Schematic of the converter for a three-phase modular fault-tolerant PM motor.

3.4.2 Winding Structures for Higher Turn Fault Tolerance

It was shown in the previous section that a higher stator turn fault tolerance can be achieved by fault-tolerant machines that have quite different configurations from those of the conventional symmetrical three-phase AC machines. But these configurations have trade-offs, such as low efficiency and requirement of a complicated and expensive converter topology. However, specific winding configurations can yield a better turn fault tolerance in a conventional symmetrical three-phase AC machine. Two typical approaches for this purpose are discussed as follows.

3.4.2.1 Concentrated Winding Configuration

The use of windings concentrated around the teeth in electric machines can offer several advantages over overlapped windings. Concentrated windings are simpler and more cost-effective than lap windings. Furthermore, the volume of copper used in the end-windings in a concentrated winding configuration can be reduced in significant proportions, particularly when the axial length of the machine is smaller than the radial length (a disk-type motor). This leads to some reduction in the stator copper loss [54], [55]. Furthermore, concentrated windings can provide some degree of thermal isolation between the different phase windings. On the contrary, rotor core losses in a concentrated winding configuration can be slightly larger because the winding configuration generally has larger slot openings and harmonics in the rotating magnetomotive forces (MMF) than those of a lap winding configuration [55]. However, the most critical problem is that even a concentrated winding cannot provide any help for the prevention of a turn fault from spreading to the adjacent turns or entire winding.

3.4.2.2 Form Winding Configuration

Electrical stresses nowadays have become a major cause of insulation degradation resulting from the wide applications of VSIs and PWM schemes. However, electrical stresses can influence on the winding insulation with different severities depending on their structures. In terms of arrangement of individual turns in the stator slots, the stator windings are generally divided into two types: form and random windings. The cross-sectional views of these two types of windings are presented in Figure 3.7 [57].

In a form winding, individual turns are arranged in precise locations with respect to each other, that is, turn one is always next to turn two, turn two is always next to turn three, and so on. While in a random winding, turns are randomly distributed and can be in close proximity to a number of other turns. Furthermore, wires can migrate during manufacturing and take new positions with respect to other coils. When migration occurs, the electrical stresses between turns increase, and this condition will be compounded by voltage source inverters. For example, in a coil having four turns wound randomly with a peak turn-to-turn voltage of 38 V, if turn one and turn four are touching, the peak turn-to-turn voltage can be as high as 114 V; furthermore, this can be amplified by a voltage source inverter (VSI). A similar form-coil design would have a peak voltage of only 38 V because turns one and four would never be next to each other [57]. However, the possibility of an occurrence of a turn fault is not completely removed even in a form winding configuration. Moreover, even a form winding configuration cannot prevent a turn fault from aggravating.

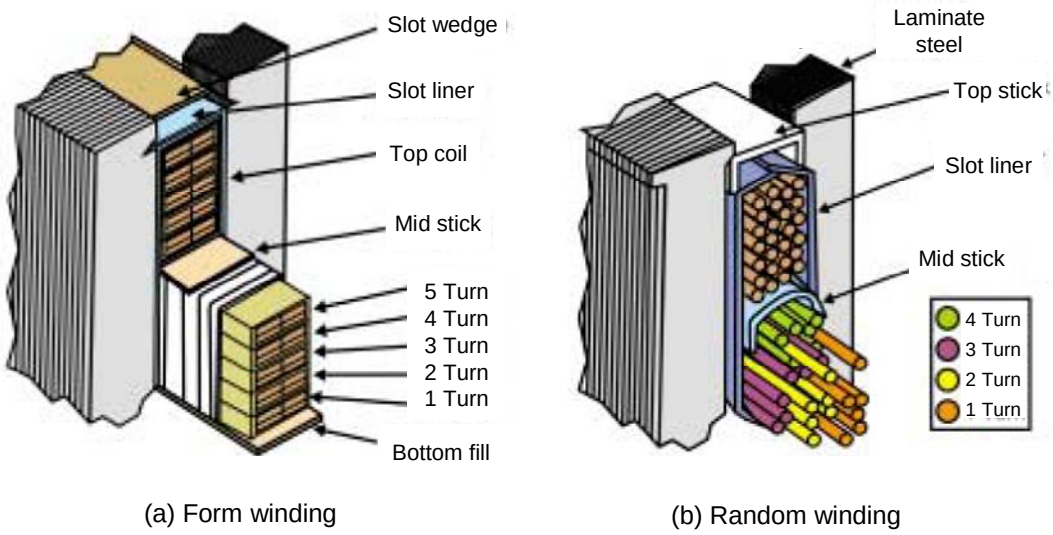

Figure 3.7. Cross sectional views of form and random windings [57].

3.5 Chapter Summary

In this chapter, previously proposed approaches for a higher stator turn fault tolerance of electric machine drives have been summarized and evaluated.

It has been pointed out that the most desirable property of a stator turn fault-tolerant operating strategy for an electric motor drive in a safety-critical application is to maintain its uninterrupted operation without any performance degradation. Unfortunately, this can be achieved only by a redundancy-based approach, which can be justified in few specific applications.

Two operating modes for stopping an electric machine with a turn fault safely have been investigated. But they have an inherent limitation: control over the faulty machine is lost under the operation.

Also, two different machine configurations that provide inherent turn fault tolerance were discussed. Although they have a clear advantage in the aspect of turn fault tolerance, they have trade-offs such as low efficiency and requirement of a complicated and expensive converter topology. Two winding configurations have been presented that can reduce the possibility of an occurrence of turn fault. However, they cannot provide any help for preventing the fault from spreading to other healthy turns.

Although IPMSMs have an inherent drawback of high turn fault tolerance, the application of IPMSMs is increasing rapidly because they have attractive features that the other types of electric machines do not have. This situation makes it critical to develop a turn fault-tolerant operating strategy for IPMSM drive that does not result in the complete loss of the availability of the drives in the presence of a turn fault, and additionally, does not require any hardware modification to the standard drive configuration.

CHAPTER 4

MODELING OF IPMSM DRIVES WITH STATOR TURN FAULTS

4.1 Overview

Modeling of electric machines with stator turn faults is one of the essential tasks in developing a turn fault detection scheme or a fault-tolerant operating strategy. Obviously, a more accurate model will be the better for the purpose. However, it is theoretically impossible to model all the non-idealities in a real situation. Thus, the accuracy of a model needs to be compromised with the complexity of the model. Anyway, models of electric machines for stator turn fault diagnosis or fault-tolerant operating strategies should be able to describe the behavior of a turn fault and to account for the effects of the fault.

Generally, finite element analysis (FEA) provides accurate information on electromagnetic field inside of a machine directly based on its geometry and material properties. This has driven many researchers to use FEA for electric machine design and machine fault study. A FEA-based model of a brushless dc motor (BLDC) with stator turn fault in proposed in [58]. However, the long time for simulation mitigates the attractiveness of FEA; furthermore, FEA requires detailed machine specifications that are unusually available to application engineers. An equivalent circuit-based machine model has a simpler from and fast simulation speed, but a poorer accuracy than an FEA-based model. Equivalent circuit-oriented induction motor and IPMSM models with stator turn

faults are derived in terms of phase variables in [59] and [60], respectively. Although they have a reasonable accuracy with a fast simulation speed, the proposed models consider only the case where the phase winding consists of coils or turns connected in series; furthermore, the magnetic non-linearity is not considered.

In this work, an equivalent circuit-based model of an IPMSM with stator turn faults is derived in terms of phase variables. The use of equivalent circuit-based approach yields a fast simulation speed, which is important for extensive investigations under various operating conditions. A phase-variable based approach provides a more appropriate way to represent the asymmetry resulting from a turn fault than a *qd*-variable based approach whose basic assumption is the perfect balance of a machine. In addition, the phase-variable model is derived to be applicable to either case where the phase winding consists of coils connected in series or parallel. For more accurate simulations, the magnetic non-linearity of an IPMSM is considered in the derived model. Since almost all IPMSM applications utilize current-controlled inverters, the derived machine model is integrated with a CCVSI model to investigate the behavior of a turn fault in an IPMSM while taking the operation of a CCVSI into account.

4.2 Series and Parallel Windings

In general, coils in a phase winding can be connected in three different ways: all coils in series (series winding), all coils in parallel (parallel winding), and combinations of coils in series and coils in parallel (series-parallel winding). In a series winding, the coil currents in a phase are identical even though the coils are not identical. On the contrary, non-identical coils in a phase of a parallel or series-parallel winding induce an

uneven distribution of the coil currents; consequently, uneven I^2R losses will be generated in the coils [61]. For this reason, series windings are common in electric machines. However, parallel windings are frequently required for multi-pole and high torque density low voltage PMSMs. In this work, the two types of coil connections, series and parallel windings, are considered in the derivation of a model of an IPMSM with stator turn faults.

Before deriving the model, the relationships between the coil parameters and the per-phase equivalent parameters in a series and parallel windings are investigated. For the sake of simplicity, it is assumed that a phase winding consists of identical *m* coils connected in series or parallel. With this assumption, it can be said that the voltages at the coils in the series winding are identical, while the coil currents in the parallel winding are identical. The relationships between the coil and per-phase equivalent parameters in the two cases are given by, respectively,

- In the case of a series winding:

$$\begin{aligned} R_s &= mR_{s\_coil}, \quad L_{ls} = mL_{ls\_coil}, \\ L_M &= m^2 L_{M\_coil}, \quad M_{ij} = m^2 M_{ij\_coil}, \end{aligned} \tag{4.1}$$

- In the case of a parallel winding:

$$\begin{aligned} R_s &= \frac{R_{s\_coil}}{m}, \quad L_{ls} = \frac{L_{ls\_coil}}{m}, \\ L_M &= L_{M\_coil}, \quad M_{ij} = M_{ij\_coil}, \end{aligned} \tag{4.2}$$

where R_s represent the per-phase equivalent resistance; L_{ls}, L_M, and M_{ij} represent the per-phase equivalent uncoupled leakage, self-magnetizing inductances, and mutual inductance between different phases, respectively; R_{s_coil} is the coil resistance; L_{ls_coil}, L_{M_coil}, and M_{ij_coil} are the coil, self-magnetizing inductances, and mutual inductance between coils in different phases, respectively.

4.3 Machine Equations of a Healthy IPMSM

Regardless of the type of coil connection, the stator line-neutral voltages and developed torque of a fault-free IPMSM are identically represented in terms of per-phase equivalent parameters, respectively as [62], [63],

$$\boldsymbol{v}_{sn} = \boldsymbol{R}_s \boldsymbol{i}_s + \frac{d\boldsymbol{\lambda}_s(\boldsymbol{i}_s, \boldsymbol{\lambda}_{sr}, \theta_r)}{dt} = \boldsymbol{R}_s \boldsymbol{i}_s + \boldsymbol{L}_s(\theta_r)\frac{d\boldsymbol{i}_s}{dt} + \omega_e \frac{d\boldsymbol{L}_s(\theta_r)}{d\theta_r}\boldsymbol{i}_s + \omega_e \frac{d\boldsymbol{\lambda}_{sr}(\theta_r)}{d\theta_r}, \tag{4.3}$$

$$T_e = \frac{P}{2}\left[\frac{1}{2}\boldsymbol{i}_s^T \frac{d\boldsymbol{L}_s(\theta_r)}{d\theta_r}\boldsymbol{i}_s + \boldsymbol{i}_s^T \frac{d\boldsymbol{\lambda}_{sr}(\theta_r)}{d\theta_r}\right], \tag{4.4}$$

where $\boldsymbol{v}_{sn} = \begin{bmatrix} v_{an} & v_{bn} & v_{cn} \end{bmatrix}^T$ and $\boldsymbol{i}_s = \begin{bmatrix} i_a & i_b & i_c \end{bmatrix}^T$ represent the stator line-neutral voltage and phase current matrices, respectively; $\boldsymbol{\lambda}_s(\theta_r) = \begin{bmatrix} \lambda_{ar}(\theta_r) & \lambda_{br}(\theta_r) & \lambda_{cr}(\theta_r) \end{bmatrix}^T$ represents the matrix of the per-phase equivalent magnetic flux linkages contributed by the permanent magnets; $\boldsymbol{R}_s = diag\begin{bmatrix} R_s \end{bmatrix}$ and $\boldsymbol{L}_s(\theta_r)$ denote the per-phase equivalent stator resistance and inductance matrices, respectively; θ_r represents the rotor position in electrical radians, ω_e represents the synchronous frequency in electrical radians per second; P represents the number of poles. The general form of the flux linkage contributed by the permanent magnets is given by [62]-[64],

$$\boldsymbol{\lambda}_{sr}(\theta_r) = \sum_{k=1}^{\infty} \lambda_{2k-1} \begin{bmatrix} \sin\left[(2k-1)\theta_r\right] \\ \sin\left[(2k-1)\left(\theta_r - 2\pi/3\right)\right] \\ \sin\left[(2k-1)\left(\theta_r + 2\pi/3\right)\right] \end{bmatrix}, \tag{4.5}$$

where k is a positive integer number; $2k-1$ represents the order of space harmonic component resulting from non-sinusoidal stator winding and rotor magnet distributions;

λ_{2k-1} represents the magnitude of each harmonic component. The self and mutual inductances in $\boldsymbol{L}_s(\theta_r)$ are generally represented, respectively as,

$$\begin{aligned}
L_{aa}(\theta_r) &= L_{ls} + L_{am}(\theta_r) = L_{ls} + L_1 - \sum_{h=1}^{\infty} L_{2h}\cos(2h\theta_r) \\
L_{bb}(\theta_r) &= L_{ls} + L_{bm}(\theta_r) = L_{ls} + L_1 - \sum_{h=1}^{\infty} L_{2h}\cos\left[2h\left(\theta_r - 2\pi/3\right)\right], \\
L_{cc}(\theta_r) &= L_{ls} + L_{cm}(\theta_r) = L_{ls} + L_1 - \sum_{h=1}^{\infty} L_{2h}\cos\left[2h\left(\theta_r - 4\pi/3\right)\right]
\end{aligned} \tag{4.6}$$

$$\begin{aligned}
M_{ab}(\theta_r) &= M_{ba}(\theta_r) = -\frac{1}{2}L_1 - \sum_{h=1}^{\infty} L_{2h}\cos\left[2h\left(\theta_r - \pi/3\right)\right] \\
M_{bc}(\theta_r) &= M_{cb}(\theta_r) = -\frac{1}{2}L_1 - \sum_{h=1}^{\infty} L_{2h}\cos\left[2h\left(\theta_r + \pi\right)\right] \\
M_{ca}(\theta_r) &= M_{ac}(\theta_r) = -\frac{1}{2}L_1 - \sum_{h=1}^{\infty} L_{2h}\cos\left[2h\left(\theta_r + \pi/3\right)\right]
\end{aligned} \tag{4.7}$$

where h is a positive integer number, L_1 represents the component of the inductances that is independent of the rotor position, and L_{2h} represents the magnitude of a rotor position-dependent magnetizing inductance resulting from the rotor saliency [62]-[64].

4.4 Machine Equations with a Stator Turn Fault in a Series Winding

Practically, a stator turn fault can occur within one coil, between two coils of the same phase, or between two different phases. Since the first case is most common, and generally occurs first, only the first case is considered in this work. First, the machine equations of an IPMSM with stator turn faults in a series winding are derived, and the derived representations are extended to the case of a parallel winding.

Figure 4.1 illustrates the schematic of three-phase wye-connected windings with a stator turn fault on a single coil in the *a*-phase winding, where each phase winding consists of coils connected in series. As shown in the figure, the fault splits the faulty phase winding into two parts: healthy turns (as_1) and shorted turns (as_2). In the figure, the symbols, *a, b,* and *c* denote the three phases, respectively; *n* denotes the floating neutral point of the windings; i_a, i_b, and i_c represent the three phase currents; i_f represents the circulating current in the shorted turns; R_f represents a possible external impedance between the shorted turns, referred to as fault impedance and assumed to be resistive. However, in most cases with low voltage machines, a stator turn fault occurs with zero fault impedance, i.e., $R_f = 0$ (bolted turn faults). The severity of the stator turn fault is referred to as fault fraction, which is denoted by the symbol, μ_{se}. This is defined as the ratio of the number of turns shorted to the number of turns per phase.

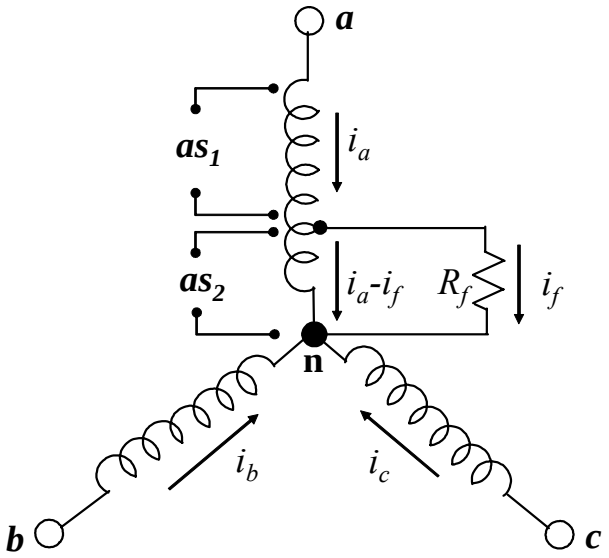

Figure 4.1. Schematic of wye-connected three-phase windings with a stator turn fault on a single coil in a series winding.

The schematic diagram in Figure 4.1 implies that regardless of the number of coils in a single phase winding, a series winding machine with a turn fault can be interpreted as a four winding machine where the windings are mutually coupled each other [60]. It can also be inferred that the resistance, leakage inductance, mutual inductance, and back-emf voltage of each winding are proportional to the number of turns in the winding, while the self-magnetizing inductance is proportional to the square of the number of turns. Based on this inference, the voltage at the windings and the developed torque of a series winding IPMSM with a turn fault on the *a*-phase winding are represented in terms of per-phase equivalent variables, respectively as [60],

$$\boldsymbol{v}'_{\boldsymbol{sn}} = \boldsymbol{R}'_s \boldsymbol{i}'_s + \frac{d\boldsymbol{\lambda}'_s(\boldsymbol{i}'_s, \boldsymbol{\lambda}'_{sr}, \theta_r)}{dt} = \boldsymbol{R}'_s \boldsymbol{i}'_s + \boldsymbol{L}'_s(\theta_r)\frac{d\boldsymbol{i}'_s}{dt} + \omega_e \frac{d\boldsymbol{L}'_s(\theta_r)}{d\theta_r}\boldsymbol{i}'_s + \omega_e \frac{d\boldsymbol{\lambda}'_{sr}(\theta_r)}{d\theta_r}, \tag{4.8}$$

$$T_e = \frac{P}{2}\left[\frac{1}{2}\boldsymbol{i}'^{T}_s \frac{d\boldsymbol{L}'_s(\theta_r)}{d\theta_r}\boldsymbol{i}'_s + \boldsymbol{i}'^{T}_s \frac{d\boldsymbol{\lambda}'_{sr}(\theta_r)}{d\theta_r}\right], \tag{4.9}$$

where $\boldsymbol{v}'_{sn} = \begin{bmatrix} v_{as1} & v_{as2} & v_{bn} & v_{cn} \end{bmatrix}^T$; $\boldsymbol{\lambda}'_{sr}(\theta_r) = \begin{bmatrix} (1-\mu_{se})\lambda_{ar} & \mu_{se}\lambda_{ar} & \lambda_{br} & \lambda_{cr} \end{bmatrix}^T$; $\boldsymbol{i}'_s = \begin{bmatrix} i_a & i_a - i_f & i_b & i_c \end{bmatrix}^T$;

$\boldsymbol{R}'_s = diag\begin{bmatrix}(1-\mu_{se})R_s & \mu_{se}R_s & R_s & R_s\end{bmatrix}$;

$$\boldsymbol{L}'_s = \begin{bmatrix} (1-\mu_{se})L_{ls} + (1-\mu_{se})^2 L_{am} & \mu_{se}(1-\mu_{se})L_{am} & (1-\mu_{se})M_{ab} & (1-\mu_{se})M_{ac} \\ \mu_{se}(1-\mu_{se})L_{am} & \mu_{se}L_{ls} + \mu_{se}^2 L_{am} & \mu_{se}M_{ab} & \mu_{se}M_{ab} \\ (1-\mu_{se})M_{ba} & \mu_{se}M_{ba} & L_{ls} + L_{bm} & M_{bc} \\ (1-\mu_{se})M_{ca} & \mu_{se}M_{ca} & M_{cb} & L_{ls} + L_{cm} \end{bmatrix}.$$

Expanding and rearranging (4.8) and (4.9) yield

$$\begin{aligned} \boldsymbol{v}_{sn} = {} & \boldsymbol{R}_s \boldsymbol{i}_s + \boldsymbol{L}_s(\theta_r)\frac{di_s}{dt} + \omega_e \frac{d\boldsymbol{L}_s(\theta_r)}{d\theta_r}\boldsymbol{i}_s + \omega_e \frac{d\boldsymbol{\lambda}_{sr}(\theta_r)}{d\theta_r} \\ & -\mu_{se}\left\{\begin{bmatrix} R_s \\ 0 \\ 0 \end{bmatrix} i_f + \begin{bmatrix} L_{aa}(\theta_r) \\ M_{ab}(\theta_r) \\ M_{ac}(\theta_r) \end{bmatrix}\frac{di_f}{dt} + \omega_e \frac{d}{d\theta_r}\begin{bmatrix} L_{aa}(\theta_r) \\ M_{ab}(\theta_r) \\ M_{ac}(\theta_r) \end{bmatrix} i_f \right\}, \end{aligned} \tag{4.10}$$

$$T_e = \frac{P}{2}\begin{bmatrix} \left(\frac{1}{2}\mathbf{i}_s^T \frac{d\mathbf{L}_s(\theta_r)}{d\theta_r}\mathbf{i}_s + \mathbf{i}_s^T \frac{d\boldsymbol{\lambda}_{sr}(\theta_r)}{d\theta_r}\right) + \frac{1}{2}\mu_{se}^2 \frac{dL_{aa}(\theta_r)}{d\theta_r} i_f^2 - \mu_{se} i_f \left(\frac{d\lambda_{ar}(\theta_r)}{d\theta_r}\right) \\ -\mu_{se} i_f \left(i_a \frac{dL_{aa}(\theta_r)}{d\theta_r} + i_b \frac{dL_{ab}(\theta_r)}{d\theta_r} + i_c \frac{dL_{ac}(\theta_r)}{d\theta_r}\right) \end{bmatrix}. \tag{4.11}$$

The voltages at as_1 and as_2 can be obtained from (4.8), respectively as,

$$\begin{aligned} v_{as1} = &(1-\mu_{se})\left[R_s i_a + \mathbf{L}_a(\theta_r)\frac{d\mathbf{i}_s}{dt} + \omega_e \frac{d\mathbf{L}_a(\theta_r)}{d\theta_r}\mathbf{i}_s + \omega_e \frac{d\lambda_{ar}(\theta_r)}{d\theta_r}\right], \\ &-\mu_{se}(1-\mu_{se})\left[L_{am}(\theta_r)\frac{di_f}{dt} + \omega_e \frac{dL_{am}(\theta_r)}{d\theta_r} i_f\right] \end{aligned} \tag{4.12}$$

$$\begin{aligned} v_{as2} &= R_f i_f \\ &= \mu_{se}\left[R_s i_a + \mathbf{L}_a(\theta_r)\frac{d\mathbf{i}_s}{dt} + \omega_e \frac{d\mathbf{L}_a(\theta_r)}{d\theta_r}\mathbf{i}_s + \omega_e \frac{d\lambda_{ar}(\theta_r)}{d\theta_r}\right], \\ &-\mu_{se}\left[R_s i_f + L_{ls}\frac{di_f}{dt} + \mu_{se}\left(L_{am}(\theta_r)\frac{di_f}{dt} + \omega_e \frac{dL_{am}(\theta_r)}{d\theta_r} i_f\right)\right] \end{aligned} \tag{4.13}$$

where $\mathbf{L}_a(\theta_r) = \left[L_{aa}(\theta_r)\ M_{ab}(\theta_r)\ M_{ac}(\theta_r)\right]$.

When a stator turn fault is involved with a small number of μ_{se}, the resultant asymmetry in the stator voltages generally has a small effect on the overall stator voltages. Thus, equations (4.13) can be rewritten as,

$$v_{an} \approx \left[\frac{R_f}{\mu_{se}} + R_s i_f + \mu_{se}\omega_e \frac{dL_{am}(\theta_r)}{d\theta_r}\right] i_f + \left[L_{ls} + \mu_{se} L_{am}(\theta_r)\right]\frac{di_f}{dt}. \tag{4.14}$$

The sum of the stator line-neutral voltages (zero sequence voltage) of a perfectly balanced three-phase wye-connected electric machine is always zero. However, a stator turn fault breaking the symmetry of the machine induces a fundamental zero sequence

component of the stator line-neutral voltages. The resultant fundamental zero sequence voltage can be obtained by summing the stator line-neutral voltage in (4.10) as,

$$v_z = \frac{1}{3}\left(v_{an} + v_{bn} + v_{cn}\right) = -\frac{\mu_{se}}{3}\left(R_s i_f + L_{ls}\frac{di_f}{dt}\right). \tag{4.15}$$

4.5 Machine Equations with a Stator Turn Fault in a Parallel Winding

The schematic diagram of three-phase wye-connected windings, where each phase winding consists of two coils connected in parallel, with a stator turn fault on a coil in the *a*-phase winding, is presented in Figure 4.2. In the figure, i_{a1} and i_{a2} represent the currents flowing through a_1 and a_2 coils in the *a*-phase winding, respectively, and this is same for the other phases.

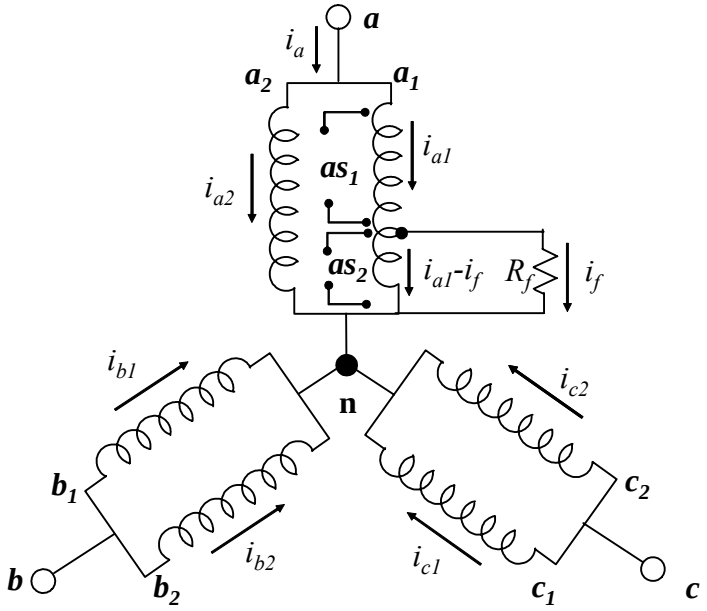

Figure 4.2. Schematic of wye-connected three-phase windings with a stator turn fault on a single coil in a parallel winding.

As shown in Figure 4.2, the stator turn fault divides the faulty coil (a_1 coil) into two parts: healthy turns (as_1) and shorted turns (as_2), while the other coils remain unchanged. Thus, the machine in this situation can be interpreted as having seven coils that are mutually coupled each other. This can be readily generalized for case where a phase winding consists of m coils connected in parallel such that the machine can be interpreted as having $3m+1$ coils that are mutually coupled each other. The fault fraction of the turn fault in the machine is defined, similarly to that in a series winding machine, as the ratio of the number of turns shorted to the number of turns per coil. And this is denoted by the symbol, μ_{pa}.

When a stator turn fault occurs on a coil in the *a*-phase winding where m coils are connected in parallel, the following relationships should be satisfied:

$$\begin{aligned} &v_{an} = v_{a1} = v_{as1} + v_{as2} = v_{a2} = \cdots = v_{am}, \quad v_{an} = \frac{1}{m}\sum_{j=1}^{m} v_{aj} \\ &v_{bn} = v_{b1} = v_{b2} = \cdots = v_{bm}, \qquad\qquad v_{bn} = \frac{1}{m}\sum_{j=1}^{m} v_{bj} \\ &v_{cn} = v_{c1} = v_{c2} = \cdots = v_{cm}, \qquad\qquad v_{cn} = \frac{1}{m}\sum_{j=1}^{m} v_{cj} \end{aligned} \quad , \tag{4.16}$$

$$\begin{aligned} &i_a = \sum_{j=1}^{m} i_{aj}, \quad i_{a1} \neq i_{a2} = i_{a3} = \cdots = i_{am} \\ &i_b = \sum_{j=1}^{m} i_{bj}, \quad i_{b1} = i_{b2} = i_{b3} = \cdots = i_{bm} \\ &i_c = \sum_{j=1}^{m} i_{cj}, \quad i_{c1} = i_{c2} = i_{c3} = \cdots = i_{cm} \end{aligned} \quad , \tag{4.17}$$

where m represents the number of coil connected in parallel in a phase winding, the subscript, j, represents the individual coil number. By applying the same inference for a series winding and the relationships presented in (4.16) and (4.17), the stator line-neutral

voltages and developed torque under the fault condition can be represented in terms of per-phase equivalent parameters, respectively as,

$$\begin{aligned}\boldsymbol{v}_{sn} &= \boldsymbol{R}_s\boldsymbol{i}_s + \boldsymbol{L}_s(\theta_r)\frac{di_s}{dt} + \omega_e\frac{d\boldsymbol{L}_s(\theta_r)}{d\theta_r}\boldsymbol{i}_s + \omega_e\frac{d\boldsymbol{\lambda}_{sr}(\theta_r)}{d\theta_r} \\ &\quad -\mu_{pa}\left\{\begin{bmatrix}R_s\\0\\0\end{bmatrix}i_f + \begin{bmatrix}L_{aa}(\theta_r)\\M_{ab}(\theta_r)\\M_{ac}(\theta_r)\end{bmatrix}\frac{di_f}{dt} + \omega_e\frac{d}{d\theta_r}\begin{bmatrix}L_{aa}(\theta_r)\\M_{ab}(\theta_r)\\M_{ac}(\theta_r)\end{bmatrix}i_f\right\},\end{aligned} \tag{4.18}$$

$$T_e = \frac{P}{2}\begin{bmatrix}\left(\frac{1}{2}\boldsymbol{i}_s^T\frac{d\boldsymbol{L}_s(\theta_r)}{d\theta_r}\boldsymbol{i}_s + \boldsymbol{i}_s^T\frac{d\boldsymbol{\lambda}_{sr}(\theta_r)}{d\theta_r}\right) + \frac{1}{2}\mu_{pa}^2\frac{dL_{aa}(\theta_r)}{d\theta_r}i_f^2 - \mu_{pa}i_f\left(\frac{d\lambda_{ar}(\theta_r)}{d\theta_r}\right)\\ -\mu_{pa}i_f\left(i_a\frac{dL_{aa}(\theta_r)}{d\theta_r} + i_b\frac{dL_{ab}(\theta_r)}{d\theta_r} + i_c\frac{dL_{ac}(\theta_r)}{d\theta_r}\right)\end{bmatrix}. \tag{4.19}$$

The voltages at as_1 and as_2 in a_1 coil can be obtained, respectively as,

$$\begin{aligned}&v_{as1} = \\ &(1-\mu_{pa})\left[m\left(R_s i_{a1} + L_{ls}\frac{di_{a1}}{dt}\right) + \boldsymbol{L}_{am}(\theta_r)\frac{d\boldsymbol{i}_s}{dt} + \omega_e\frac{d\boldsymbol{L}_a(\theta_r)}{d\theta_r}\boldsymbol{i}_s + \omega_e\frac{d\lambda_{ar}(\theta_r)}{d\theta_r}\right], \\ &-(1-\mu_{pa})\mu_{pa}\left[L_{am}(\theta_r)\frac{di_f}{dt} + \omega_e\frac{dL_{am}(\theta_r)}{d\theta_r}i_f\right]\end{aligned} \tag{4.20}$$

$$\begin{aligned}&v_{as2} = R_f i_f = \\ &\mu_{pa}\left[m\left(R_s i_{a1} + L_{ls}\frac{di_{a1}}{dt}\right) + \boldsymbol{L}_{am}(\theta_r)\frac{d\boldsymbol{i}_s}{dt} + \omega_e\frac{d\boldsymbol{L}_a(\theta_r)}{d\theta_r}\boldsymbol{i}_s + \omega_e\frac{d\lambda_{ar}(\theta_r)}{d\theta_r}\right], \\ &-\mu_{pa}\left[m\left(R_s i_f + L_{ls}\frac{di_f}{dt}\right) + \mu_{pa}L_{am}(\theta_r)\frac{di_f}{dt} + \mu_{pa}\omega_e\frac{dL_{am}(\theta_r)}{d\theta_r}i_f\right]\end{aligned} \tag{4.21}$$

where $\boldsymbol{L}_{am}(\theta_r) = \left[L_{am}(\theta_r)\ \ M_{ab}(\theta_r)\ \ M_{ac}(\theta_r)\right]$.

Also, the fundamental component in the sum of the line-neutral voltages resulting from the fault can be obtained in terms of per-phase equivalent parameters as,

$$v_z = \frac{1}{3}\left(v_{an} + v_{bn} + v_{cn}\right) = -\frac{\mu_{pa}}{3}\left(R_s i_f + L_{ls}\frac{di_f}{dt}\right). \tag{4.22}$$

4.6 Implementation of Drive-Integrated Simulation Model

Having derived the mathematical representations of an IPMSM with stator turn faults, this section discusses the issue of implementing a drive-integrated simulation model. The drive-integrated simulation model composed of five functional blocks is implemented in Matlab Simulink™. The block diagram of the developed model is presented in Figure 4.3. In the diagram, the superscript, *, denotes the reference of a variable, the subscript, *so,* represents the quantity of a stator variable referred to the mid-point of the dc-link, and the subscript, *s,* represents the quantity of a stator variable referred to the floating neutral point of the machine.

4.6.1 IPMSM with Stator Turn Faults

The values of machine parameters are indispensable to specify the derived machine model. If the magnetic system of the machine is linear, the per-phase equivalent machine parameters would be constant. But all electric machines have non-linear magnetic systems.

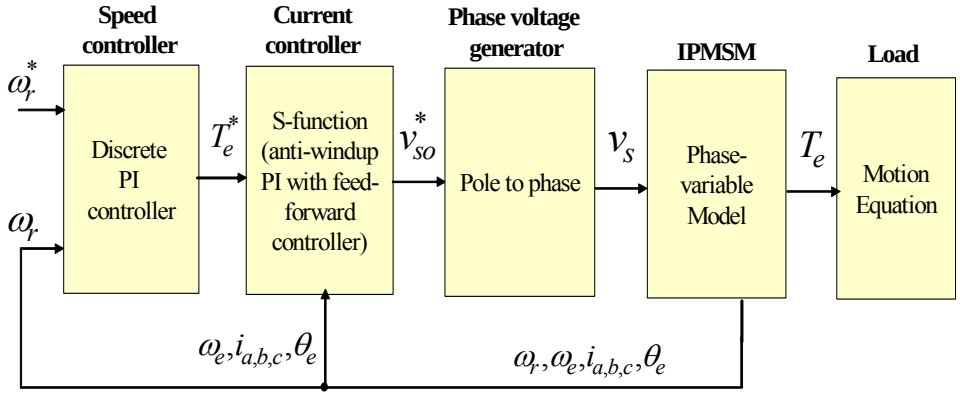

Figure 4.3. Block diagram of the developed simulation model.

Especially, in an IPMSM, the magnetic non-linearity leads to significant variations in the flux-related machine parameters, specifically, self-magnetizing and mutual inductances. For a more realistic model, the effects of the non-linearity should be considered. These non-linear effects are included in the developed model. The way how to consider them will be discussed in a later section.

Once the per-phase equivalent parameters are determined, the state-space equation of the currents are obtained using equations (4.10) or (4.18), as,

$$\boldsymbol{i}_s^{'} = \frac{1}{\boldsymbol{L}_s^{'}(\theta_r)} \int (\boldsymbol{v}_{sn}^{'} - \boldsymbol{r}_s^{'} \boldsymbol{i}_s^{'} - \omega_e \frac{d\boldsymbol{\lambda}_{sr}^{'}}{d\theta_r}) dt \ . \tag{4.23}$$

For example, the implemented blocks of the healthy turns and the shorted turns in the *a*-phase winding in a series winding IPMSM are presented in Figure 4.4(a) and (b), respectively.

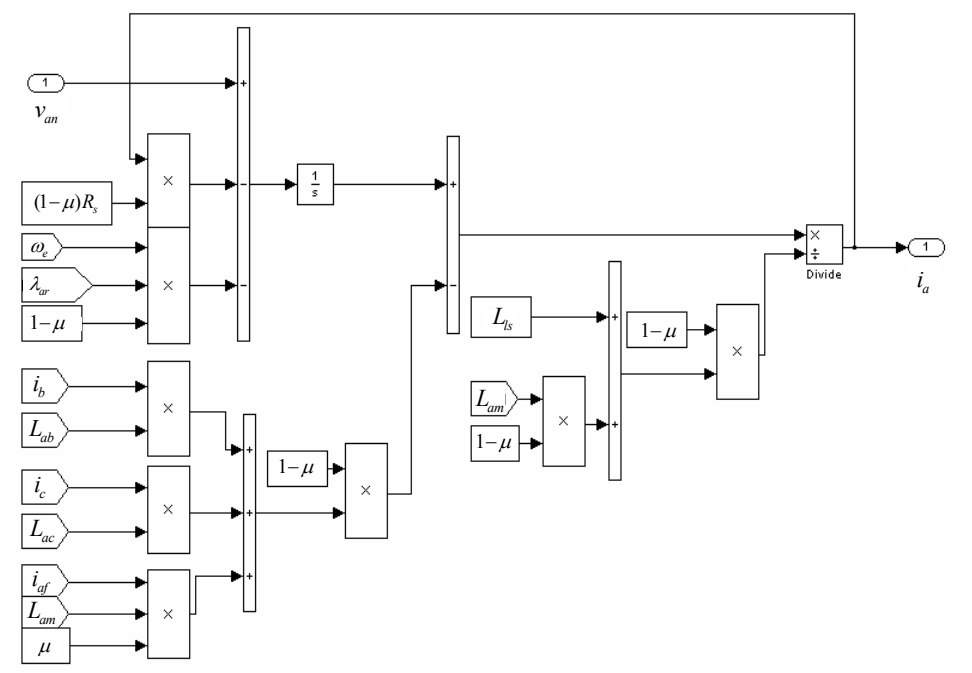

(a) Healthy turns

Figure 4.4. Simulink block diagrams of the faulty phase winding.

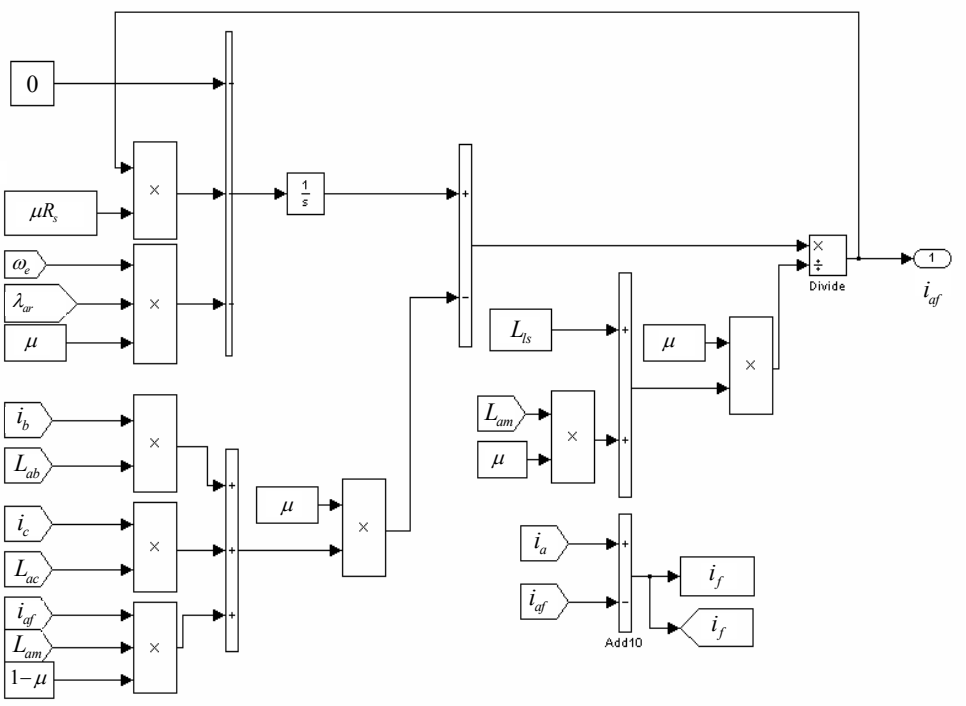

(b) Shorted turns

Figure 4.4. Simulink block diagrams of the faulty phase winding.

4.6.2 Speed and Current Controllers

Owing to the advances in micro-processor technology, digitally controlled inverters are widely used in industry applications. To model a digitally controlled inverter as closely as an actual one, the effects of control and sampling rates should be taken into account, in other words, a real-time simulation model is required. In Matlab, real-time simulation can be realized using an s-function block. In this work, the main functions of a CCVSI, which include speed and current controls, and PWM generation, are implemented in an s-function.

The speed controller is implemented with an anti-windup proportional-integral compensator (PI compensator) and updates the torque reference at every speed control

period. The *q*- and *d*-axis currents are regulated through synchronous anti-windup PI compensators with feed-forward [63]; consequently, the *q*- and *d*-axis voltage references are generated from the current controllers. Maximum torque per ampere (MTPA) and field-weakening operation are also implemented [65], [66]. The references of the pole voltages (inverter output voltages referred to the mid-point of the dc-link) are generated from the *q*- and *d*-axis voltage references through space vector PWM (SVPWM) scheme.

The main feature of the CCVSI model is that it is implemented in an s-function converted from a C-language source code, which is directly applicable to a real drive. With this property, any method for fault detection or fault-tolerant operating strategy can be fully evaluated before its application to a real system.

4.6.3 Stator Line-Neutral Voltage Generator

Generally, in an electric motor drive, there is no physical connection between the machine neutral point and the inverter neutral point, for which the mid-point of the dc-link is generally used. Furthermore, the two neutral points are assumed to have the same potential for the fundamental voltage. However, this assumption is only valid under perfectly balanced conditions [35]. When the machine has a stator turn fault, but the inverter has no fault, a fundamental zero sequence voltage appears in the stator line-neutral voltages, while no fundamental zero sequence voltage will be introduced in the inverter pole voltages (inverter output voltages referred to the mid-point of the dc-link). As a result, a fundamental component will appear in the voltage difference between the two neutral points.

In a phase-variable drive model where the machine stator voltages are represented referred to the machine neutral point, the voltage difference between the machine and

inverter neutral points should be considered to model the zero sequence component in the stator line-neutral voltage resulting from a turn fault. This consideration can be realized by the mathematical manipulations that follow.

The stator line-neutral voltages are expressed in terms of the inverter pole voltages and the voltage difference between the mid-point of the dc-link and the machine neutral point by

$$\begin{bmatrix} v_{an} \\ v_{bn} \\ v_{cn} \end{bmatrix} = \begin{bmatrix} v_{ao} - v_{no} \\ v_{bo} - v_{no} \\ v_{co} - v_{no} \end{bmatrix}, \tag{4.24}$$

where the subscript, o, denotes the mid-point of the dc-link.

Summing the rows of (4.24) yields

$$v_{no} = \frac{1}{3}[(v_{ao} + v_{bo} + v_{co}) - (v_{an} + v_{bn} + v_{cn})], \tag{4.25}$$

By inserting (4.25) into (4.24), the following equation can be obtained:

$$\begin{bmatrix} v_{an} \\ v_{bn} \\ v_{cn} \end{bmatrix} = \frac{1}{3}\begin{bmatrix} 2v_{ao} - (v_{bo} + v_{co}) + (v_{an} + v_{bn} + v_{cn}) \\ 2v_{bo} - (v_{ao} + v_{co}) + (v_{an} + v_{bn} + v_{cn}) \\ 2v_{co} - (v_{ao} + v_{bo}) + (v_{an} + v_{bn} + v_{cn}) \end{bmatrix}, \tag{4.26}$$

Inserting (4.15) or (4.22), which is representing the summation of the stator line-neutral voltages under a stator turn fault, into (4.26) yields

$$\begin{bmatrix} v_{an} \\ v_{bn} \\ v_{cn} \end{bmatrix} = \frac{1}{3}\begin{bmatrix} 2v_{ao} - (v_{bo} + v_{co}) - \mu(R_s i_f + L_{ls} \, di_f / dt) \\ 2v_{bo} - (v_{ao} + v_{co}) - \mu(R_s i_f + L_{ls} \, di_f / dt) \\ 2v_{co} - (v_{ao} + v_{bo}) - \mu(R_s i_f + L_{ls} \, di_f / dt) \end{bmatrix}. \tag{4.27}$$

The stator line-neutral voltage generator block applies the calculated voltages according to (4.27) to the machine terminals. By doing this, the zero sequence component in the stator line-neutral voltages resulting from a turn fault can be modeled.

4.6.4 Load

The driven load can be modeled using the mechanical equation.

$$T_L = J\frac{d\omega_r}{dt} + A\omega_r^2 + B\omega_r + T_{fri}, \tag{4.28}$$

where T_L represents the overall load torque, ω_r represents the rotating speed, J denotes the equivalent inertia of the motor and load, A denotes the coefficient of the load component proportional to the square of the rotating speed, B denotes the equivalent viscous coefficient of the motor and load, T_{fri} represents the load component not depending on the rotating speed.

4.7 Consideration of Magnetic Non-Linearity

The magnetic circuit in any electric machine is non-linear, and particularly in IPMSMs, the magnetic non-linearity leads to significant variations in the flux-related machine parameters. Furthermore, stator turn faults add another degree to the non-linearity because the large circulating current in the shorted turns produces an additional magnetic flux that does not exist under fault-free conditions. The effects of the non-linearity should therefore be considered in order to make the machine model more realistic.

The issue of how to take into account the variations of the machine parameters, especially the inductances, has been studied for a long time. For more accurate and stable control of an electric machine, the exact knowledge of the values of the inductances is indispensable. This has driven extensive research on this issue [67]-[73].

The two main causes of the variations of the inductances are magnetic saturation and cross-magnetization effects. The effects of magnetic saturation on the inductances can be easily understood when a typical *B*-*H* curve of a magnetic material is considered [67]. The consequence of magnetic saturation on the inductances is reductions in the inductances. On the contrary, cross-magnetization is associated with more complicated characteristics of the magnetic systems. Simply, cross-magnetization encompasses the magnetic behavior of a saturable machine when the vector of the main magnetomotive force (MMF) is applied in a direction that is not geometrically or analytically favored in the magnetic structure of the machine; furthermore, various influencing factors on cross-magnetization in an electric machine exist [70]. Armature reaction in a DC motor is a good example of a cross-magnetization. The flux generated by the armature current leads to a distortion of the flux contributed by the field current. This means that the armature current influences the magnitude and direction of the field flux. In other words, the two flux components are not completed decoupled. In a symmetrical three-phase AC machine, cross-magnetization can be easily explained along the *q* and *d* axes. Many studies on the effects of cross-magnetization in three-phase AC machines are found in the literature, [71]-[73].

In general, the effects of magnetic saturation and cross-magnetization can be included in a phase-variable model through two approaches: FEA [74], [75] and physical

experiments. In either case, it takes quite a long time to obtain the inductance profiles which take the effect of the magnetic non-linearity into account. In this work, the second approach is adapted for this purpose. Since a *qd* variable-based approach is easier than a phase variable-based approach in obtaining the inductance profiles experimentally, the *q*- and *d*-axis inductance profiles are obtained, and then the obtained inductance profiles are converted into phase inductance profiles. The detailed procedure for this is as follows.

Once the *q*- and *d*-axis flux linkages in the synchronously rotating reference frame are extracted from the measured currents, voltages, and rotating speed with using the voltage equations, the flux linkages can be expressed as [72],

$$\begin{aligned} \lambda_q^e &= L_{qq} i_q^e + M_{qd} i_d^e, \\ \lambda_d^e &= L_{dd} i_d^e + M_{dq} i_q^e + \lambda_{PM}, \end{aligned} \quad (4.29)$$

where the superscript e designates variables in the synchronously rotating reference frame, the subscript, *q*- and *d* designate variables in the *q*- and *d*-axes, respectively, L_{qq} and L_{dd} represent the *q*- and *d*-axis self-inductances, respectively, M_{qd} and M_{dq} represent the *q*- and *d*- axis cross-coupling inductances, respectively.

The self- and cross-coupling inductances in (4.29) can be determined by the following partial derivatives as,

$$\begin{aligned} L_{qq} &= \frac{\partial \lambda_q^e}{\partial i_q^e} = L_{ls} + L_{mq}, \quad M_{qd} = \frac{\partial \lambda_q^e}{\partial i_d^e}, \\ L_{dd} &= \frac{\partial \lambda_d^e}{\partial i_d^e} = L_{ls} + L_{md}, \quad M_{dq} = \frac{\partial \lambda_d^e}{\partial i_q^e}, \end{aligned} \quad (4.30)$$

where, L_{mq} and L_{md} are the *q*- and *d*-axis self-magnetizing inductances.

Assuming that the *qd*-magnetic fields are orthogonal to each other, and the *q*-axis in a synchronously rotating reference frame is aligned to the *a*-axis at the initial rotor

position, then the self- and mutual- inductances of the phase windings in (4.6) and (4.7) will be modified by applying the transformation from the *qd*-synchronous rotating reference frame to the *abc*- stationary reference frame, respectively as,

$$\begin{aligned}
L_{aa}(\theta_r) &= L_{ls} + L_1 - L_2\cos(2\theta_r) + M_1\sin(2\theta_r) \\
L_{bb}(\theta_r) &= L_{ls} + L_1 - L_2\cos\left(2\theta_r - 4\pi/3\right) + M_1\sin\left(2\theta_r - 4\pi/3\right), \\
L_{cc}(\theta_r) &= L_{ls} + L_1 - L_2\cos\left(2\theta_r - 2\pi/3\right) + M_1\sin\left(2\theta_r - 2\pi/3\right)
\end{aligned} \tag{4.31}$$

$$\begin{aligned}
M_{ab}(\theta_r) &= -\frac{1}{2}L_1 - L_2\cos\left(2\theta_r - 2\pi/3\right) + M_1\sin\left(2\theta_r - 2\pi/3\right) + M_2 \\
M_{ac}(\theta_r) &= -\frac{1}{2}L_1 - L_2\cos\left(2\theta_r + 2\pi/3\right) + M_1\sin\left(2\theta_r + 2\pi/3\right) - M_2 \\
M_{ba}(\theta_r) &= -\frac{1}{2}L_1 - L_2\cos\left(2\theta_r - 2\pi/3\right) + M_1\sin\left(2\theta_r - 2\pi/3\right) - M_2 \\
M_{bc}(\theta_r) &= -\frac{1}{2}L_1 - L_2\cos(2\theta_r) + M_1\sin(2\theta_r) + M_2 \\
M_{ca}(\theta_r) &= -\frac{1}{2}L_1 - L_2\cos\left(2\theta_r + 2\pi/3\right) + M_1\sin\left(2\theta_r + 2\pi/3\right) + M_2 \\
M_{cb}(\theta_r) &= -\frac{1}{2}L_1 - L_2\cos(2\theta_r) + M_1\sin(2\theta_r) - M_2
\end{aligned}, \tag{4.32}$$

where $L_1 = \frac{L_{md} + L_{mq}}{3}, L_2 = \frac{L_{md} - L_{mq}}{3}$, $M_1 = \frac{M_{dq} + M_{qd}}{3}$, $M_2 = \frac{\sqrt{3}(M_{dq} - M_{qd})}{6}$.

Using the relationships in (4.31) and (4.32), the phase inductance profiles that include the effects of saturation and cross-magnetization can be determined.

In IPMSMs, where permanents magnets whose permeability is almost same as that of air, are buried inside of the rotor, the effective air-gap length of the *d*-axis is much longer than that of the *q*-axis. Hence, the *d*-axis inductance is much smaller than the *q*-axis inductance, and the *d*-axis magnetic field will not be easily saturated. Furthermore, in a recent rotor design where permanent magnets are buried with multi-layered, the

cross-magnetization effects are insignificant [68]. Under this particular condition, the flux models in (4.29) and (4.30) can be simplified, respectively as,

$$\begin{aligned} \lambda_q^e &= L_q i_q^e, \\ \lambda_d^e &= L_d i_d^e + \lambda_{PM}, \end{aligned} \quad , \tag{4.33}$$

$$\begin{aligned} L_d &\approx \text{constant}, \\ L_q &= \frac{\partial L_{q0}}{\partial i_{qs}} + L_{q0}, \end{aligned} \quad , \tag{4.34}$$

where L_{q0} is the unsaturated q-axis inductance.

As mentioned earlier, the large circulating current resulting from a turn fault can add two additional sources of non-linearity to the magnetic system. First, the current flowing through the shorted turns generates a magnetic field that acts against the main air-gap flux. In the worst case, the permanent magnets can be demagnetized. Secondly, the circulating current in the shorted turns may lead to an increase in the local leakage flux, particularly slot leakage. This can change the saturation condition of tooth-tip region [76]. However, when a small number of turns are involved in a turn fault, the induced flux linkage resulting from the turn fault will not be large enough to demagnetize the permanent magnets. Moreover, the increased slot leakage will not be strong enough to lead to a significant change in the magnetic saturation in tooth-tip region. In addition, the leakage inductance is not easily saturated [77], [78]. For these reasons, the effects of the non-linearity in the magnetic system resulting from a turn fault can be ignored in this work.

4.8 Chapter Summary

In this chapter, a phase variable-based model of an IPMSM with stator turn faults has been developed and integrated with a CCVSI model. This model is applicable to a single phase winding consisting of coils connected in either series or parallel. For more realistic simulations, magnetic non-linearity has also been considered in the derived model. Owing to these distinct features, the developed model can be used as a powerful tool for investigating the characteristics of a stator turn fault in IPMSM drives. However, this is not the only contribution of this model. It can save time and money by pointing out even a minor deficiency in any tested method for turn fault diagnosis or fault-tolerant operating strategy since the model provides a reliable test bench for evaluating the method before its application to a real drive system. The developed model is verified through simulations and experiments, which are detailed in Chapter 9.

Actually, the excessive heat in the shorted turns propagates a stator turn fault to the other healthy turns. Thus, the investigation of the thermal behavior of a stator turn fault is also critical. For this investigation, a thermal model of an IPMSM with stator turn fault is derived in the next chapter.

CHAPTER 5

THERMAL MODEL OF AN IPMSM WITH STATOR TURN FAULTS

5.1 Overview

A stator turn fault generates excessive heat in the shorted turns, and the heat promulgates the severity of the fault until it reaches a destructive stage. Therefore, it is crucial to investigate the thermal behavior of a turn fault in order to predict the remaining life of the faulty motor or to establish an alarm level for the safe operation in the presence of the fault. However, there is little research to date in this area. Previous works have shown that the delay time between a turn fault and other severe failures is not instantaneous, and estimated to be between a third of a second and several minutes or longer. The uncertainty in this area is due to the lack of a methodology to investigate the thermal behavior of a turn fault. This methodology should not result in any further damage to a machine or a drive system and should make it possible to examine the behavior under various operating conditions. Such a methodology is proposed in this chapter.

The method described in this work aims at building a thermal model of an electric machine with stator turn faults, whose thermal parameters are determined experimentally. However, it should be noted that the experimental conditions are set so that the temperature at the shorted turns does not result in further insulation failures. In this

chapter, an implementation of the methodology for the case of an IPMSM is introduced. The validation of the proposed method is presented in Chapter 10.

5.2 Methodology for Investigating the Thermal Behavior of a Turn Fault

The first step in the proposed method is to build a thermal model of a fault-free machine, which is then modified for turn fault conditions. With the resultant thermal model, the thermal behavior of a turn fault is investigated under various operating conditions. In the methodology, the parameters of the thermal models are determined using the temperature measurements from the thermal sensors installed at various locations in the machine, and an approximate power loss model. The flowchart of the proposed method is shown in Figure 5.1.

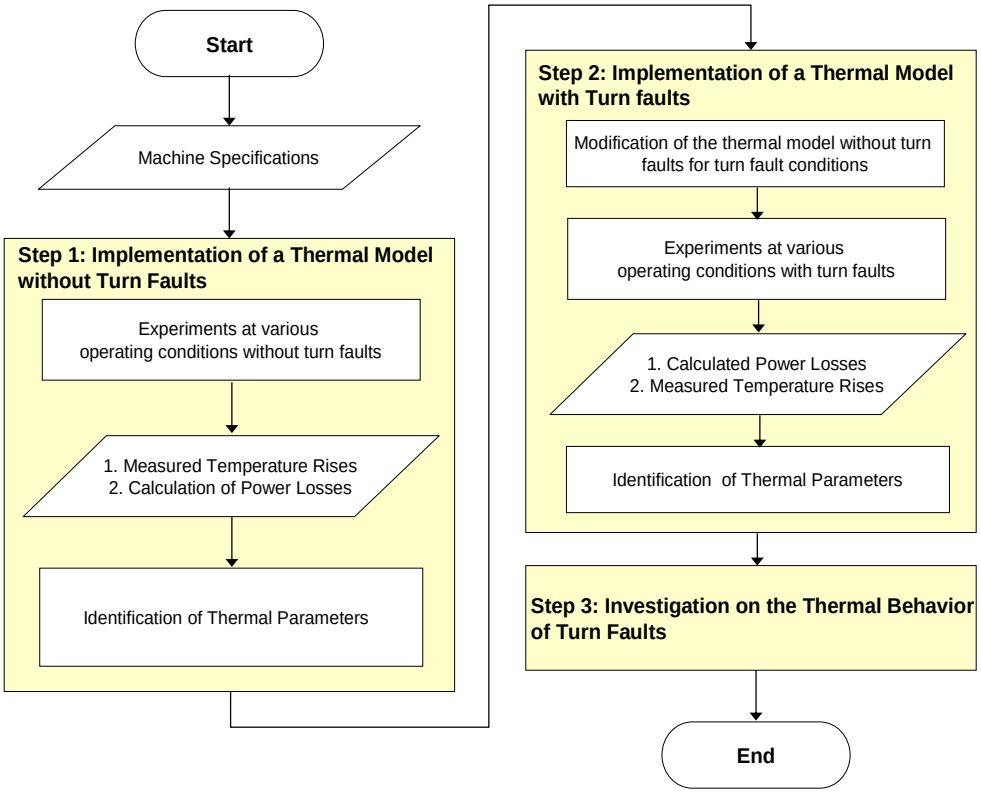

Figure 5.1. Flowchart of the proposed method for investigating the thermal behavior of a turn fault.

5.3 Approaches for Thermal Modeling of an Electric Machine

Generally, thermal models of electric machines are classified into two categories: (1) finite element analysis (FEA)-based and (2) lumped-parameter thermal models. FEA-based models are more accurate, but highly computational intensive. A lumped-parameter thermal model is equivalent to a thermal network that is composed of thermal resistances, capacitances, and the corresponding power losses. The accuracy of the model is generally dependent on the number of thermally homogenous bodies used in the model. The parameters of a lumped-parameter model are usually determined in two ways. The first is by using comprehensive knowledge of the motor's physical dimensions and construction materials [79]-[81]. The second is to identify the parameters from extensive temperature measurements at different locations in the motor [82]-[84].

Even though an electric machine is made of various materials that have different thermal characteristics, the machine can be assumed to consist of several thermally homogenous lumped bodies. Based on this assumption, simplified thermal models of an induction motor and a PMSM consisting of two lumped thermal bodies are proposed in [82], [83] and [84], respectively. It has been verified that the models provide an adequate and convenient means of estimating the key temperatures inside an electric machine.

In this work, a lumped-parameter based approach is adopted. This approach will be sufficient for the thermal modeling in this work since the focus of the modeling is to estimate the temperatures of the shorted turns and other turns under a stator turn fault condition.

5.4 Losses in IPMSMs

In developing a thermal model, a clear understanding of the characteristics and mechanisms of power losses in the motor is important. Power losses in an electric machine consist of copper, core, stray, windage, and friction losses [85], [86]. Among these, copper, core, and friction (bearing loss) losses mainly contribute to the rise in temperature of the machine. The contributions of stray and windage losses to the machine temperature are usually negligible, even though they play a role in machine efficiency.

Core losses of mains-fed induction motors are usually assumed constant because the excitation frequency is fixed. Furthermore, core losses are much smaller than copper losses under loaded conditions. For this reason, only copper losses are generally considered when the temperature of an induction motor is estimated. On the other hand, the elimination of rotor windings and the presence of permanent magnets make core losses form a larger portion of the total losses in a PMSM as compared to that of an induction motor [86], [87]. In addition, core losses in a CCVSI-driven PMSM significantly change with operating condition. Furthermore, core losses can be larger than copper losses under lightly loaded conditions. For these reasons, the contribution of the core losses to machine temperature rise cannot be ignored when a thermal model of a PMSM is derived. Copper losses can be easily determined since they are proportional to the square of the current, while the determination of core losses is much more difficult because of their strong dependency on machine geometry, material properties, power supply, control method, and so on. This has driven a great deal of research on the estimation of core losses in PMSMs [86]-[98].

5.4.1 Classification of Core Loss

Core losses arise from the variations in the magnetic flux density throughout the magnetic material. Core losses are often divided into hysteresis and eddy-current losses [85], [86]. Eddy-current loss can be further divided into two components: (1) classical loss and (2) anomalous or excess loss. Classical loss is associated with the currents induced from variations of the flux density in a magnetic material and a finite conductivity of the magnetic material. Anomalous loss is caused by the induced eddy current concentration around moving magnetic domain walls due to continuous rearrangements of the domain configuration [88], [89]. The general representation of the three types of core losses in a magnetic material is presented as [86]-[88],

$$p_{core} = k_h f B_m^{\alpha} + \frac{k_e}{2\pi^2}\left(\frac{dB}{dt}\right)_{rms}^2 + \frac{k_{exc}}{(2\pi^2)^{3/4}}\left(\frac{dB}{dt}\right)_{rms}^{1.5} \quad [W/kg], \tag{5.1}$$

where, p_h, p_e, and p_{exc} represent hysteresis, eddy-current, and excess loss densities, respectively; f is the fundamental excitation frequency; B_m represents the peak value of flux density; k_h, k_e, and k_{exc} represent the hysteresis, eddy-current, and excess loss constants, respectively; $\left(dB/dt\right)_{rms}$ is the rms value of the rate of change of the flux density. The Steinmetz constant, α, is usually in the range of 1.8~2.2.

As presented in (5.1), hysteresis loss can be determined somewhat easily since it depends only on the peak value of flux density when minor loops are ignored. On the other hand, eddy-current losses are quite difficult to estimate since the eddy-currents in a magnetic material are associated with all frequency components in the flux density [91]-[94]. This makes it necessary to identify all the harmonics as well as the fundamental

component in the magnetic flux density for a more accurate estimation. These harmonics are caused by non-sinusoidal distribution of permanent magnetic flux, stator slot, non-sinusoidal stator current, and PWM operation.

5.4.2 Locations of Core Loss

Core losses of a CCVSI-driven PMSM are generated in the stator core, the rotor core, and the permanent magnets. Since the fundamental air-gap field rotates in synchronism with the rotor in a PMSM, the fundamental flux density does not contribute to the rotor and permanent magnet losses. The space harmonics in the flux density caused by the permanent magnets generate losses in the stator core, not in the rotor core and permanent magnets [90]. On the other hand, the stator slot harmonics generate losses only in the rotor core and permanent magnets. But the PWM-related harmonics contribute to the losses both in the stator and rotor cores [90]. Generally, the rotor and permanent magnet losses are much smaller than the stator core losses. Furthermore, the permanent magnet losses are small enough to ignore when the magnets are subdivided into several pieces (*i.e.*, segmented) [94]. However, the amount of the rotor core loss is strongly influenced by the waveform of the stator current. The work carried out in [91]-[93] verified the above-mentioned statement by showing that a rectangular stator current generates much more rotor core loss than a sinusoidal current.

5.4.3 Core Loss Models

FEA has been considered the most reliable approach to modeling core losses because of its detailed use of machine geometry and material properties, [90], [92], and [94]. However, FEA-based models are complicated and time consuming. For faster

estimation, analytical approaches based on (5.1) have been introduced in [86]-[88], albeit with some loss in estimation accuracy. Although equation (5.1) seems straight-forward for core loss estimation, the detailed machine specifications and identification of all frequency components in the flux density are still important for an accurate core loss prediction. Furthermore, the dependency of the loss coefficients, k_h, k_e, and k_{exc}, on the level of induction and the excitation frequency makes the estimation significantly more complicated [95].

5.5 Lumped-Parameter Thermal Model of a Fault-Free IPMSM

The authors of [82] and [83] assumed that an induction motor consists of two lumped thermal bodies: the stator and rotor. Measurements of the stator and rotor temperatures were used to identify the parameters of the proposed models.

The stator temperature of an electric machine can be measured using a contact-type thermal sensor, while the rotor temperature is difficult to measure with a contact-type thermal sensor since the rotor is moving. To overcome the difficulty in measuring the rotor temperature, an infrared sensor is used in [83]. In [82], the rotor temperature is estimated by employing the rotor resistance as the temperature indicator. A resistance-based method cannot be used for PMSMs, however, since the rotor windings are eliminated. Although the strength of the permanent magnets is related to the rotor temperature, it is not a good rotor temperature indicator.

Although the rotor temperature can be measured using an infrared sensor, the models proposed in [82] and [83] have another difficulty when they are applied to a CCVSI-driven machine. In the thermal models, the heat transfer between the stator and

rotor across the air-gap is modeled with a contact thermal resistance. However, this heat transfer is affected by the rotating speed. This implies that the thermal contact resistance between the stator and rotor in a mains-fed induction motor can be assumed constant because the rotating speed is nearly constant, while the contact thermal resistance in a CCVSI-driven machine will not remain constant since the speed changes randomly. However, as discussed earlier, rotor core losses in a PMSM are much smaller than stator core losses when the stator currents are controlled to be sinusoidal. Furthermore, the heat transfer between the rotor core and frame is much smaller than the heat transfer between the stator core and frame. For these reasons, the contribution of rotor core losses to temperature rises at the stator and frame can be safely ignored. Using this reasoning, a thermal model of a PMSM is proposed in [84], which consists of only two thermal bodies: the stator and frame. The basic structure of the thermal model can be applied to this work without resulting in a significant inaccuracy since the focus of this work is to estimate the stator winding temperatures under turn fault conditions.

5.5.1 Simplified Thermal Model of a Fault-Free IPMSM

The simplified thermal model of a fault-free IPMSM used in this work is presented in Figure 5.2. In the figure, the quantities, θ_S and θ_F are temperature rises [$^\circ C$] above ambient temperature (θ_a) at the stator winding and frame, respectively. The current sources, P_{SW} and P_{SC} [W], represent the power losses in the stator winding and core, respectively. The thermal resistance, R_1 [$^\circ C/W$], represents the heat dissipation capability of the stator to the ambient through the combined effects of heat conduction and convection; R_2 [$^\circ C/W$] is associated with the heat dissipation capability of the frame

to the ambient; the contact thermal resistance, R_3 $[^\circ C/W]$ is associated with the heat transfer between the stator and frame. The thermal capacitance, C_1 $[J/^\circ C]$, is the thermal capacity of the stator, while C_2 $[J/^\circ C]$ is the combined thermal capacity of the frame.

According to the definition of thermal capacitance, C_1 and C_2 are fixed once a motor is manufactured. On the contrary, the thermal resistances, R_1, R_2, and R_3 are dependent on the environmental air flow conditions. If a motor is installed at a moving station, the moving speed of the station will strongly affect the heat dissipation of the motor. Moreover, an impaired cooling condition results in a significant increase in the thermal resistances. However, it is assumed in this work that the environmental conditions and cooling capacity of an IPMSM are fixed.

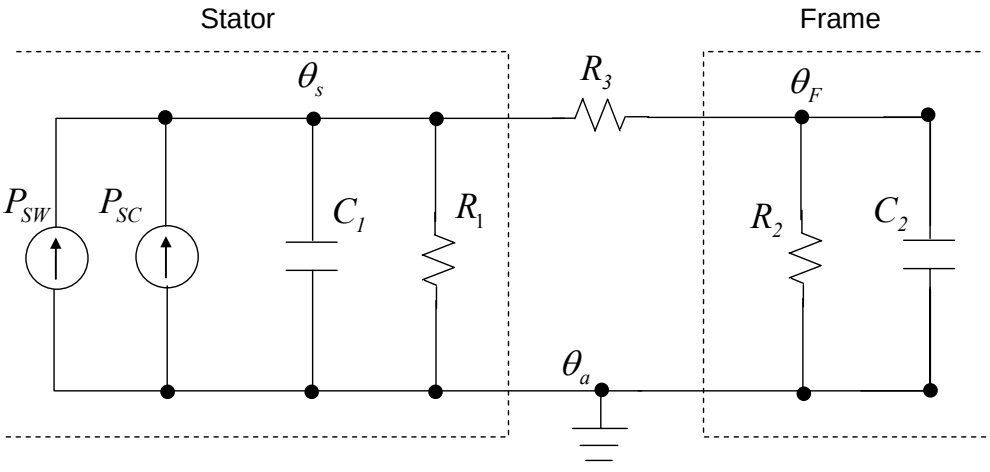

Figure 5.2. Schematic of the simplified thermal model of a fault-free IPMSM.

5.5.2 Simplified Power Loss Model

As indicated in Figure 5.2, the rotor and permanent magnet losses are ignored in the proposed model, and only the stator copper and core losses are considered. This approximation will not yield significant inaccuracy in temperature estimation, as discussed earlier. The approximate loss model of an IPMSM used in this work is introduced in this section.

5.5.2.1 Stator Copper Loss

PWM operation of a CCVSI induces harmonic components in the stator currents, and consequently increases the stator copper loss, but only slightly [97], [98]. This harmonic effect will be ignored here since the currents are nearly sinusoidal.

The stator winding resistance increases as the winding temperature increases. The stator copper loss, taking into account the effect of the stator winding temperature, can be expressed as,

$$P_{SW} = 3R_s(\theta_a)\left[1+\delta\theta_s\right]\left(\frac{i_s}{\sqrt{2}}\right)^2 = \frac{3R_s(\theta_a)\left[1+\delta\theta_s\right]}{2}\left[(i_{qs}^e)^2+(i_{ds}^e)^2\right], \tag{5.2}$$

where $R_s(\theta_a)$ is the per-phase stator resistance at ambient temperature θ_a, δ is the temperature coefficient, θ_s represents temperature rise above ambient temperature at the stator winding, i_{qs}^e and i_{ds}^e represent the *q*- and *d*-axis currents in the synchronously rotating reference frame.

5.5.2.2 Stator Core Losses

In order to approximate the stator core loss, the following assumptions are made: (1) the magnetic flux density is evenly distributed throughout the stator core, (2) only the fundamental flux density is considered, (3) anomalous eddy-current loss is negligible, and (4) the loss coefficients are constant.

The first assumption makes the stator core a lumped core loss source, which consequently allows the core loss to be represented in terms of the magnetic flux linkage. On the basis of the assumptions, the stator core losses can be represented as,

$$P_{SC} = k_h \hat{\lambda}_e^2 \omega_e + k_e \hat{\lambda}_e^2 \omega_e^2 \qquad [W], \tag{5.3}$$

where, k_h and k_e are the hysteresis and eddy-current loss coefficients, respectively, $\hat{\lambda}_e$ is the amplitude of the fundamental flux linkage, and ω_e represents the synchronous frequency in electrical radians per second. However, it should be noted that the loss coefficients, k_h and k_e, are determined experimentally. The procedure for this will be discussed in a later section.

The fundamental flux linkage can be determined in terms of *qd*-variables by the following equation [96]:

$$\hat{\lambda}_e = \sqrt{(L_{mq} i_{qs}^e)^2 + (L_{md} i_{ds}^e + \lambda_{PM})^2} \tag{5.4}$$

where, L_{mq} and L_{md} represent the *q*- and *d*- axis magnetizing inductances, respectively, and λ_{PM} represents the fundamental flux linkage contributed by the permanent magnets.

The magnetic flux density in the stator core is not evenly distributed throughout the stator core. As a result, the core loss densities (estimated in W/kg) at different locations in the stator core will be different. However, a location with a larger flux density will have a smaller surface area; consequently, will have less weight. For this reason, the effects of different flux densities in various locations on the core losses can be partly compensated for in the lumped representation (estimated in W) in terms of flux linkage. The frequency of each space harmonic flux linkage is the multiplication of the fundamental frequency by the order of the harmonic, while its amplitude is generally the multiplication of the fundamental flux linkage by the inverse of the harmonic order (h). Thus, the following approximation can be made:

$$\begin{aligned} \hat{\lambda}_h^2 \omega_h &\approx \frac{1}{h} \hat{\lambda}_e^2 \omega_e \\ \hat{\lambda}_h^2 \omega_h^2 &\approx \hat{\lambda}_e^2 \omega_e^2 \end{aligned}, \tag{5.5}$$

where $\hat{\lambda}_h$ and ω_h represent the amplitude and frequency of a space harmonic flux linkage. It can be inferred from (5.5) that the contributions of the space harmonics to the core losses can be included in the approximate model presented in (5.3) when the core loss coefficients are determined experimentally.

5.5.3 Identification of Thermal Parameters

To identify the parameters of the proposed thermal model of a fault-free IPMSM, the measured stator winding and frame temperature rises under three different operating conditions are used. The procedure for this is discussed in this section.

5.5.3.1 Analysis of the Thermal Model

Assuming that P_{SW} and P_{SC} are the inputs, and θ_S is the output, the state space equations governing the thermal model of Figure 5.2 is represented as,

$$\begin{bmatrix} \frac{d\theta_s}{dt} \\ \frac{d\theta_F}{dt} \end{bmatrix} = \boldsymbol{A}\begin{bmatrix} \theta_S \\ \theta_F \end{bmatrix} + \boldsymbol{B}\begin{bmatrix} P_{SW} + P_{SC} \\ 0 \end{bmatrix}$$
$$= \begin{bmatrix} -\frac{1}{C_1}(\frac{1}{R_1}+\frac{1}{R_3}) & \frac{1}{R_3}\frac{1}{C_1} \\ \frac{1}{R_3}\frac{1}{C_2} & -\frac{1}{C_2}(\frac{1}{R_2}+\frac{1}{R_3}) \end{bmatrix}\begin{bmatrix} \theta_S \\ \theta_F \end{bmatrix} + \begin{bmatrix} \frac{1}{C_1} & 0 \\ 0 & 0 \end{bmatrix}\begin{bmatrix} P_{SW} + P_{SC} \\ 0 \end{bmatrix}, \quad (5.6)$$

$$y = \boldsymbol{C}\begin{bmatrix} \theta_S \\ \theta_F \end{bmatrix} = \begin{bmatrix} 1 & 0 \end{bmatrix}\begin{bmatrix} \theta_S \\ \theta_F \end{bmatrix}. \quad (5.7)$$

The Laplace transform of (5.6) and (5.7) is obtained as

$$Y(s) = \frac{b_1 s + b_0}{a_2 s^2 + a_1 s + a_0} P_S(s), \quad (5.8)$$

where $P_S = P_{SW} + P_{SC}$, $a_0 = R_1 + R_2 + R_3$, $a_1 = R_1R_2C_1 + R_1R_3C_1 + R_1R_2C_2 + R_2R_3C_2$, $a_2 = R_1R_2R_3C_1C_2$, $b_1 = R_1R_2R_3C_2$, and $b_0 = R_1R_2 + R_1R_3$.

At a steady-state condition, θ_S and θ_F are expressed, respectively as,

$$\theta_s(t)\big|_{t=\infty} = \frac{R_1(R_2+R_3)}{R_1+R_2+R_3} P_S = K_S P_S$$
$$\theta_F(t)\big|_{t=\infty} = \frac{R_2}{R_2+R_3}\frac{R_1(R_2+R_3)}{R_1+R_2+R_3} P_S = K_F K_S P_S = K_F\, \theta_s(t)\big|_{t=\infty} \quad (5.9)$$

For convenience, $K_S = \dfrac{R_1(R_2+R_3)}{R_1+R_2+R_3}$ and $K_F = \dfrac{R_2}{R_2+R_3}$ are referred as to the stator temperature gain and the frame temperature gain in the henceforth analysis, respectively.

5.5.3.2 Stator Temperature Gain and Power Loss Coefficients

To identify the stator temperature gain, K_S, and the two core loss coefficients, k_h and k_e, θ_S is measured under three different operating conditions. Also, the stator currents and rotating speeds are measured to determine the corresponding stator copper losses and fundamental flux linkages. With applying the measured or calculated values to the relationship presented in the first low of (5.9), K_S, k_h, and k_e, can be identified as,

$$\begin{bmatrix} K_S \\ K_S k_h \\ K_S k_e \end{bmatrix} = \begin{bmatrix} P_{SW1} & \hat{\lambda}_{e1}^2 \omega_{e1} & \hat{\lambda}_{e1}^2 \omega_{e1}^2 \\ P_{SW3} & \hat{\lambda}_{e2}^2 \omega_{e2} & \hat{\lambda}_{e2}^2 \omega_{e2}^2 \\ P_{SW3} & \hat{\lambda}_{e3}^2 \omega_{e3} & \hat{\lambda}_{e3}^2 \omega_{e3}^2 \end{bmatrix}^{-1} \begin{bmatrix} \theta_{s1}(t)\big|_{t=\infty} \\ \theta_{s2}(t)\big|_{t=\infty} \\ \theta_{s3}(t)\big|_{t=\infty} \end{bmatrix}, \tag{5.10}$$

where the subscripts, 1, 2, and 3, represent the three different operating conditions, respectively.

Even though the identifications of K_S, k_h, and k_e look straight-forward, accurate temperature measurements are required because a negative value of K_S, k_h, or k_e can result from inaccurate temperature measurements.

5.5.3.3 Thermal Resistance and Capacitance of the Frame

The thermal resistance, R_2, and capacitance, C_2, of the frame can be approximated using the information of the frame geometry.

Since the heat from the frame to the ambient is mainly transferred through heat convection, R_2 can be approximated by [79],

$$R_2 = \frac{1}{h_C A_F}, \tag{5.11}$$

where h_C represents the contact thermal coefficient and A_F is the surface area of the frame in contact with the cooling air.

The thermal capacitance, C_2, can be approximated with the relationship of a total thermal capacity of a cylindrical body as [79],

$$C_2 = \rho c_p \pi (r_1^2 - r_2^2), \tag{5.12}$$

where ρ is the density of the frame material, c_p represents the specific heat of the frame material, r_1 and r_2 represents the outer and inner radii of the frame.

5.5.3.4 Contact Thermal Resistance between the Stator and Frame

With applying the identified R_2 to the relationship presented in the second low of (5.9), the contact thermal resistance, R_3, can be simply identified as,

$$R_3 = R_2 \left(\frac{\theta_s(t)\big|_{t=\infty}}{\theta_F(t)\big|_{t=\infty}} - 1 \right). \tag{5.13}$$

5.5.3.5 Thermal Resistance and Capacitance of the Stator

Once K_S, R_2, and R_3 are identified, then the thermal resistance of the stator, R_1, can be identified using

$$K_S = \frac{R_1 (R_2 + R_3)}{R_1 + R_2 + R_3}. \tag{5.14}$$

From (5.14), R_1 is obtained as,

$$R_1 = \frac{K_S(R_2 + R_3)}{R_2 + R_3 - K_S}. \tag{5.15}$$

The thermal capacitance of the stator, C_1, can be identified by applying a curve fitting method to the measured stator temperature rises. Since the other thermal parameters are already determined, the curve fitting can be performed without any difficulty. However, C_1 will be of the same order of magnitude of C_2, but will have somewhat larger value than C_2 due to the design of the motor.

5.6 Simplified Thermal Model of an IPMSM with Stator Turn Faults

It is obvious that a stator turn fault divides the stator windings into two parts: the shorted turns and healthy turns. Furthermore, it can be easily seen that the turns close to the shorted turns will have a larger rise in temperature than the turns relatively far away from the shorted turns. This means that the healthy turns physically adjacent to the shorted turns would be most vulnerable to insulation failure. Based on this reasoning, it is assumed that a stator turn fault divides the stator windings into the following three parts: (1) the shorted turns, (2) the turns adjacent to the shorted turns, and (3) the turns relatively far away from the shorted turns. For convenience, the turns adjacent to the short and the turns far away from the shorted turns are referred to here as the adjacent turns and the healthy turns, respectively. When a small number of turns are involved in a stator turn fault, the flux density resulting from the circulating current in the shorted turns

(i_f) would be negligible compared to the overall flux density. Therefore, the core losses contributed by i_f can be safely ignored.

Based on the above discussion, the thermal model of a fault-free IPMSM can be modified into that presented in Figure 5.3 under a turn fault condition. In the figure, the quantities, θ_T, θ_A, and θ_H are the temperature rises [$^\circ C$] above the ambient temperature (θ_a) at the shorted turns, adjacent turns, and healthy turns, respectively. The current sources, P_{TW}, P_{AW}, and P_{HW} [W], represent the copper losses at the three parts of the stator winding, respectively. The current source, P_{SC}, represents the total stator core loss. However, it should be noted that the stator core losses do not change as a result of the turn fault. The thermal resistances, R_T, R_A, and R_H [$^\circ C/W$], represent the heat dissipation capabilities of the three parts of the stator winding to the ambient, respectively. The thermal capacitances, C_T, C_A, and C_H [$J/^\circ C$], represent the thermal capacities of the three parts, respectively. The contact thermal resistances, R_{TA} and R_{AH} [$^\circ C/W$], are associated with the heat transfer between the shorted and adjacent turns and between the adjacent turns and healthy turns, respectively.

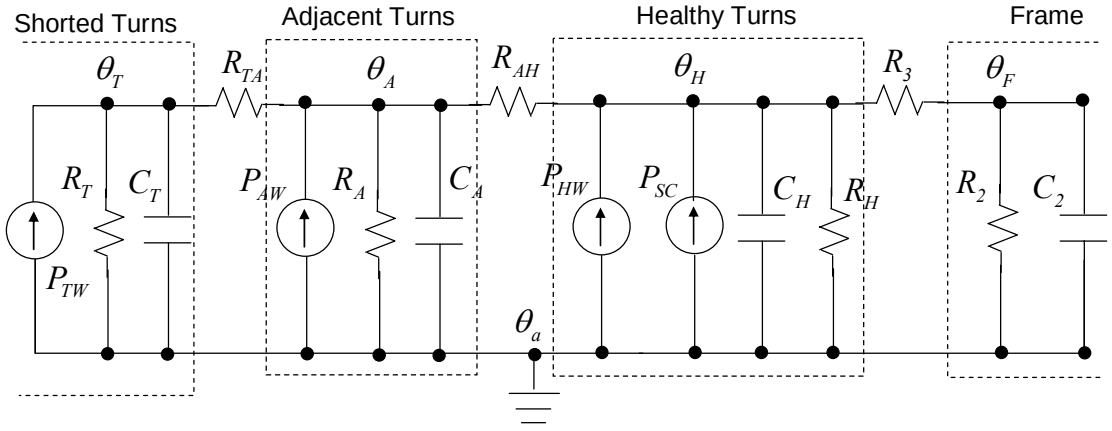

Figure 5.3. Schematic of the simplified thermal model of an IPMSM with a turn fault.

5.6.1 Power Loss Model

Since the contribution of i_f to the stator core losses is ignored, the calculated stator core loss under fault-free conditions can also be used for estimating the stator core losses under turn fault conditions. However, the copper losses, P_{TW}, P_{AW}, and P_{HW} $[W]$, need to be recalculated for the faulty case. To accomplish this, the resistance and the current in each of the three parts of the stator windings must be determined.

The resistance of a single turn at the ambient temperature, θ_a, can be obtained as,

$$R_{Turn}(\theta_a) = R_S(\theta_a)\frac{m}{N_{Turn}}, \tag{5.16}$$

where m represents the number of coils connected in parallel in a phase winding, and N_{Turn} represents the number of turns per phase in a series winding or the number of turn per coil in a parallel winding.

Defining the numbers of shorted turns and adjacent turns as N_T and N_A, respectively, the resistances of the three parts can be determined by the following equations.

$$R_{TW}(\theta_T + \theta_a) = N_T R_{Turn}(\theta_a)\left[1 + \delta\theta_T\right], \tag{5.17}$$

$$R_{AW}(\theta_A + \theta_a) = N_A R_{Turn}(\theta_a)\left[1 + \delta\theta_A\right], \tag{5.18}$$

$$R_{HW}(\theta_H + \theta_a) = \left(3mN_{Turn} - N_T - N_A\right) R_{Turn}(\theta_a)\left[1 + \delta\theta_H\right], \tag{5.19}$$

where $R_{TW}(\theta_T + \theta_a)$, $R_{AW}(\theta_A + \theta_a)$, and $R_{HW}(\theta_H + \theta_a)$ represent the resistances of the three parts of the stator windings at the corresponding temperatures, respectively.

The currents flowing through the adjacent turns and healthy turns are identical to the per-coil current and are given by,

$$i_A = i_H = i_{coil} = \frac{i_s}{m} = \frac{\sqrt{\left(i_{qs}^e\right)^2 + \left(i_{ds}^e\right)^2}}{m}, \tag{5.20}$$

where i_A and i_H represent the currents flowing through the adjacent turns and healthy turns, respectively, i_{coil} is the per-coil current, and i_s is the per-phase current.

As investigated in Chapter 4, the actual current flowing through the shorted turns (i_T) is

$$i_T = i_{coil} - i_f . \tag{5.21}$$

Although the representation in (5.21) is simple, the rms value of i_T is difficult to obtain because i_{coil} and i_f have a phase angle difference that varies depending on operating conditions. This means that the phase angle difference should be considered to estimate the copper loss in the shorted turns more accurately. The details for the determination of the phase angle difference between i_{coil} and i_f are discussed in Chapter 10.

As investigated in Chapter 4, the amplitude of i_f is strongly influenced by the resistance of the shorted turns. Since the resistance is temperature dependent, the amplitude of i_f is also dependent on the temperature of the shorted turns. Taking the effect of temperature into account, the representation of i_f can be modified from (4.14) or (4.21) as,

$$i_f \approx \frac{\mu v_s}{\mu\{mR_s(\theta_T + \theta_a) + j\omega_e[mL_{ls} + \mu(L_1 - 3L_2)]\}}. \tag{5.22}$$

Once the phase angle difference between i_{coil} and i_f ($\alpha_{i_{coil}-i_f}$) is given, then i_T can be represented as,

$$i_T = \hat{i}_{coil}\cos\left(\omega_e t + \alpha_{i_{coil}-i_f}\right) - \hat{i}_f \cos\left(\omega_e t\right), \tag{5.23}$$

where $\hat{i}_{coil}$ and $\hat{i}_f$ represent the magnitudes of i_{coil} and i_f, respectively.

From (5.31), the rms value of i_T is determined by,

$$I_T = \frac{1}{\sqrt{2}}\sqrt{\left[\hat{i}_f - \hat{i}_{coil}\cos\left(\alpha_{i_{coil}-i_f}\right)\right]^2 + \left[\hat{i}_{coil}\sin\left(\alpha_{i_{coil}-i_f}\right)\right]^2}. \tag{5.24}$$

Now, the copper losses, P_{TW}, P_{AW}, and P_{HW} [W], can be calculated by the following equations:

$$P_{TW} = N_T R_{Turn}(\theta_a)\left[1 + \delta\theta_T\right] I_T^2, \tag{5.25}$$

$$P_{AW} = N_A R_{Turn}(\theta_a)\left[1 + \delta\theta_A\right] I_{coil}^2, \tag{5.26}$$

$$P_{HW} = (3mN_{Turn} - N_T - N_A) R_{Turn}(\theta_a)\left[1 + \delta\theta_H\right] I_{coil}^2, \tag{5.27}$$

where I_{coil} is the rms value of i_{coil}.

5.6.2 Identification of Thermal Parameters

Actually, every single turn in the stator windings forms an individual thermal network that consists of a thermal resistor, thermal capacitor, and power source. The individual thermal networks are connected through contact thermal resistors. In Figure

5.4, the single-turn thermal network including a contact thermal resistor is illustrated. The lumped-parameter thermal model of a fault-free IPMSM, presented earlier, is based on the assumption that the single-turn thermal networks are identical, and form the lumped-stator thermal network when connected in parallel. Under this assumption, it can be said that the single-turn thermal networks have the same rise in temperature and the same thermal time constant as those of the lumped-stator thermal network. If the temperatures are the same, then no heat transfer will occur between the single-turn thermal networks. In other words, the contact thermal resistance, R_{II} in Figure 5.4, will have no effect on the thermal characteristics. From this discussion, the heat dissipation capability, R_I, and the thermal capacity, C_I, of the single turn thermal network can be determined using the corresponding lumped-stator thermal parameters.

$$R_I = 3mN_{Turn}R_1, \tag{5.28}$$

$$C_I = \frac{C_1}{3mN_{Turn}}. \tag{5.29}$$

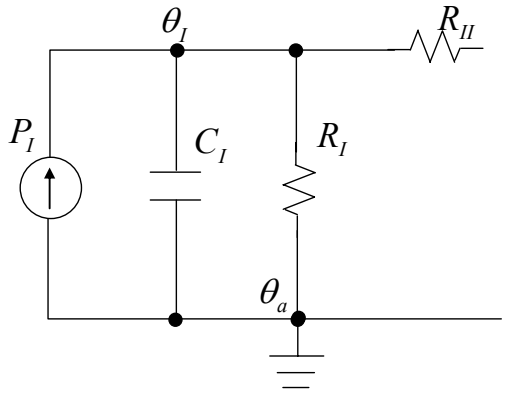

Figure 5.4. An individual thermal network forming the lumped-stator thermal body.

5.6.2.1 Thermal Resistances and Capacitances in the Three Parts of the Stator Windings

The relationships presented in (5.28) and (5.29) are applicable in identifying the heat dissipation capacities and thermal capacities of the three parts of the stator windings. The application results are,

$$R_T = R_l \frac{3mN_{Turn}}{N_T},\ R_A = R_l \frac{3mN_{Turn}}{N_A}, \text{ and } R_H = R_l \frac{3mN_{Turn}}{3mN_{Turn} - N_T - N_A}, \tag{5.30}$$

$$C_T = C_l \frac{N_T}{3mN_{Turn}},\ C_A = C_l \frac{N_A}{3mN_{Turn}}, \text{ and } C_H = C_l \frac{3mN_{Turn} - N_T - N_A}{3mN_{Turn}}. \tag{5.31}$$

5.6.2.2 Contact Thermal Resistances between the Three Parts of the Stator Windings

Under fault-free conditions, it is assumed that there is no heat transfer between the single-turn thermal networks. However, with a turn fault condition, heat transfer between the three parts of the stator will occur because the temperature rises are not identical.

The contact thermal resistances, R_{TA} and R_{AH} in Figure 5.3, are associated with the heat transfer between the shorted and adjacent turns, and between the adjacent and the other healthy turns, respectively. These two contact thermal resistances can be determined using the measured temperatures at the three parts of the stator windings. For this, the following equations can be used:

$$R_{TA} = \frac{\theta_T(t)\big|_{t=\infty} - \theta_A(t)\big|_{t=\infty}}{P_{TW}(t)\big|_{t=\infty} - \dfrac{\theta_T(t)\big|_{t=\infty}}{R_T}} \tag{5.32}$$

$$R_{AH} = \frac{\theta_A(t)\big|_{t=\infty} - \theta_H(t)\big|_{t=\infty}}{P_{AW}(t)\big|_{t=\infty} - \dfrac{\theta_A(t)\big|_{t=\infty}}{R_A} - \left(\dfrac{\theta_A(t)\big|_{t=\infty} - \theta_T(t)\big|_{t=\infty}}{R_{TA}} \right)} \tag{5.33}$$

As indicated in (5.32) and (5.33), the accuracies in the approximations of R_{TA} and R_{AH} are strongly dependent on the accuracy of the temperature measurements. However, more accurate approximations could be achievable with more extensive temperature measurements under various operating conditions.

5.7 Chapter Summary

In this chapter, a useful approach for investigating the thermal behavior of a machine with a stator turn fault has been proposed. The proposed methodology not only makes it possible to examine the thermal behavior of a stator turn fault under various operating conditions, it also provides a way to predict the remaining life or establish an alarm level for the safe operation of the motor in the presence of a turn fault. This represents an important tool in the development of a reliable turn fault-tolerant operating strategy.

Based on the proposed methodology, a thermal model of an IPMSM with stator turn faults has also been derived. The validation of the proposed thermal model is provided through simulations and experiments in Chapter 10. In addition, the contribution of the proposed thermal model in the area of turn fault-tolerant operating strategy is verified in Chapter 12.

CHAPTER 6

AN ON-LINE TURN FAULT DETECTION METHOD FOR IPMSM DRIVES

6.1 Overview

The use of CCVSIs in drive systems increases the complexity of detecting stator turn faults. This is due to the presence of controller actions, the non-stationary operation of the drive, and the drive's non-idealities. To overcome these difficulties, several methods have been developed. However, all these methods have trade-offs or limitations. Current-based turn fault detection methods may be ineffective for CCVSI-driven machines because the current controllers try to maintain the symmetry of the currents. Even though voltage-based turn fault detection methods have reasonable performance, they require additional voltage sensors and cables.

In fact, every type of drive system has different characteristics and requirements. This suggests that it is impossible to develop a universal turn fault detection method that works reliably in every type of drive system. A clear understanding of the characteristics of the concerned drive system is a prerequisite in developing a turn fault detection method. As reported in Chapter 2, almost all of the previous turn fault detection methods consider turn faults in CCVSI-driven induction motors. No method has been developed for detecting turn faults in CCVSI-driven IPMSMs.

In this work, an on-line stator turn fault detection method for CCVSI-driven IPMSMs is proposed. In addition, the method overcomes some of the limitations in

conventional current- and voltage-based turn fault detection methods. Also, a discussion on both the theoretical and the practical issues in implementing the method is presented. The developed turn fault detection method is validated through simulations and experiments, detailed in Chapter 11.

6.2 Theoretical Foundations

In most low voltage machines, a stator turn fault occurs with zero external impedance between the shorted turns, *i.e.*, *a bolted turn fault*. In this situation, the faulty winding (or coil) will have a fewer number of effective turns than the other healthy windings (or coils). This reduction in the number of turns in the faulty winding results in changes in the sequence components of the machine impedances and rotor-induced voltages (back-emf voltages). These changes are reflected into the machine voltages and currents. However, the manner of the reflection will be different depending on the type of power supply feeding the machine.

6.2.1 Simplified Model of an IPMSM with Stator Turn Faults

Although the phase variable model, presented in Chapter 4, accurately describes the operating characteristics of an IPMSM with stator turn faults, the model is somewhat complicated to show the effects of turn faults on the machine parameters intuitively. In this section, a simplified model is presented for this purpose. To carry out this simplified analysis, it is assumed that a series winding IPMSM has a bolted turn fault in the *a*-phase winding. Under a bolted turn fault condition, the voltage at the shorted turns becomes nearly zero. As a result, the voltage can be neglected in the faulty phase winding voltage.

The contributions of the circulating current in the shorted turns to the machine terminal voltages are negligible when a small number of turns are involved in the bolted turn fault. However, the contributions of the circulating current to the machine terminal voltages increase as the fault gets worse, while increasing the machine asymmetry. This means that when a large number of turns are shorted, the changes in the sequence components of the machine impedances and rotor-induced voltages are more significant. The leakage flux is also negligible, since the leakage inductance is generally much smaller than the magnetizing inductance. Based on this discussion, the stator line-neutral voltages of a series winding IPMSM with a bolted turn fault on the *a*-phase winding are expressed as,

$$\begin{bmatrix} v_{an} \\ v_{bn} \\ v_{cn} \end{bmatrix} = \begin{bmatrix} \eta R & 0 & 0 \\ 0 & R & 0 \\ 0 & 0 & R \end{bmatrix} \begin{bmatrix} i_a \\ i_b \\ i_c \end{bmatrix} + \begin{bmatrix} \eta^2 L & -\eta\frac{L}{2} & -\eta\frac{L}{2} \\ -\eta\frac{L}{2} & L & -\frac{L}{2} \\ -\eta\frac{L}{2} & -\frac{L}{2} & L \end{bmatrix} \frac{d}{dt} \begin{bmatrix} i_a \\ i_b \\ i_c \end{bmatrix} + \begin{bmatrix} \eta E_{an} \\ E_{bn} \\ E_{cn} \end{bmatrix}, \tag{6.1}$$

where the symbol, η, denotes the ratio of the number of healthy turns to the number of turns per phase ($\eta = 1-\mu$) and E represents the rotor induced voltage (back-emf voltage). Since zero sequence current is always zero in a wye-connected three-phase system, the sequence component voltage equation of (6.1) is represented as,

$$\begin{aligned} \begin{bmatrix} V_P \\ V_N \\ V_Z \end{bmatrix} &= \frac{1}{3} \begin{bmatrix} \eta R + 2R & (\eta-1)R \\ (\eta-1)R & \eta R + 2R \\ (\eta-1)R & (\eta-1)R \end{bmatrix} \begin{bmatrix} I_P \\ I_N \end{bmatrix} \\ &+ \frac{1}{3} j\omega_e \begin{bmatrix} (\eta^2+2)L + \frac{L}{2}(2\eta+1) & (\eta^2-1)L + L(\eta-1) \\ (\eta^2-1)L + L(\eta-1) & (\eta^2+2)L + \frac{L}{2}(2\eta+1) \\ (\eta^2-1)L + \frac{L}{2}(1-\eta) & (\eta^2-1)L + \frac{L}{2}(1-\eta) \end{bmatrix} \begin{bmatrix} I_P \\ I_N \end{bmatrix} + \frac{1}{3} \begin{bmatrix} (\eta+2)E_{an} \\ (\eta-1)E_{an} \\ (\eta-1)E_{an} \end{bmatrix} \end{aligned}, \tag{6.2}$$

There are several important observations that can be drawn from the simplified analysis. Since η is a positive real number less than one, and decreases as the fault gets worse, it can be concluded that a bolted turn fault reduces the positive sequence components of the machine impedances and back-emf voltages, while increasing the negative sequence and coupling terms in the impedance matrix. This simplified model is sufficient to show the effects of a bolted turn fault on the machine parameters.

6.2.2 Effects of Controller Actions

Since the negative sequence current resulting from a stator turn fault is much smaller than the positive sequence current [59], the contribution of the coupling terms to the positive sequence voltage is much smaller than those of the reduced positive sequence components of the machine impedances and back-emf voltages. For this reason, positive sequence current slightly increases under a stator turn fault condition in a mains-fed application where the power supply is a fixed voltage source [59]. In a CCVSI-driven application, the inverter controls the line currents so as to follow their references by introducing negative sequence voltage and reducing positive sequence voltage under a stator turn fault condition. Since the inverter output voltages are produced according to the voltage references that are generated through the current controllers, the variations in the machine parameters will be reflected into the voltage references. This implies that for a given rotating speed and current references (or alternatively, torque reference), the presence of a stator turn fault results in a reduced positive sequence component and an increased negative sequence component of the voltage references as compared to a machine without a turn fault. Thus, it can be concluded that the differences in positive and negative sequence components of the voltage references, for a given torque reference

and rotating speed, under a stator turn fault and fault-free conditions can indicate the occurrence of a stator turn fault. This is the basic concept of the stator turn fault detection method proposed in this work. The use of voltage reference for turn fault detection provides distinct advantages over conventional voltage-based methods. Measurements of the machine terminal voltages, which lead to additional cost and the inconvenience of installing voltage sensors, are not required for the proposed method. Furthermore, no additional computation for obtaining voltage references is required since the generation of voltage references is one of the existing tasks in CCVSI-driven applications.

6.2.3 Observation in the Synchronously (Rotor-Aligned) Rotating Reference Frame

As mentioned earlier, conventional sequence decomposition is not an optimal choice for dealing with handling time-varying signals. The STFT and WT are powerful tools for analyzing time-varying signals, but they are somewhat inefficient for stator turn fault diagnosis where the observation of one or two frequency components is sufficient. One approach that can overcome the disadvantages of the fore-mentioned methods is to observe signals in a rotating reference frame. It is a well-known theory [62], [63] that variables in a three-phase system can be transformed into space vectors in a two-axis, q and d, system where the axes are orthogonal to one other. Once the reference frame rotates at a certain frequency in either the clockwise or counter-clockwise direction, then a space vector is decomposed into a stationary component and other rotating components in either the clockwise or counter-clockwise direction. Furthermore, the stationary component is observed as a dc component in the time domain, while the rotating

components are seen as ac components. Thereby, the dc-component can be easily extracted by just filtering out the ac components. This is the basic idea of the data adaptation technique employed for the proposed turn fault detection method.

In the rotor-aligned (synchronously) rotating reference frame, the fundamental positive sequence voltage reference is always observed as a stationary component, while the fundamental negative sequence voltage reference is seen as a component that rotates at the synchronous frequency in the opposite direction. Thus, the fundamental positive and negative sequence voltage references in the rotor-aligned rotating reference frame are observed as a dc component and a second-order harmonic in the time domain, respectively. Figure 6.1 provides a graphical representation which compares the voltage references for a given torque reference and rotating speed under both stator turn fault and fault-free conditions in (a) the space vector domain and (b) the time domain, respectively.

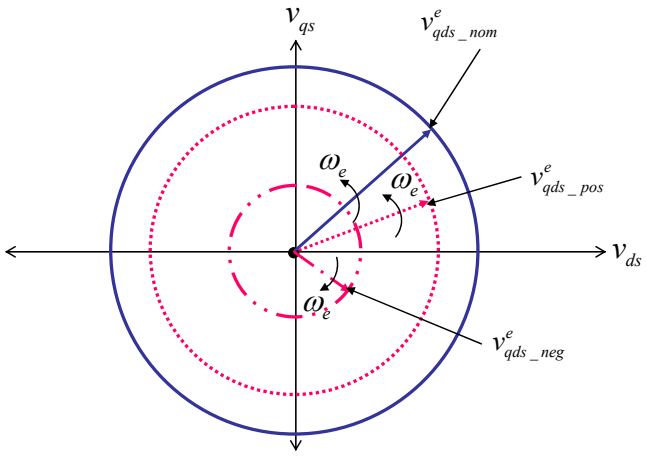

(a) In the space vector domain

Figure 6.1. Voltage references under fault-free and turn fault conditions.

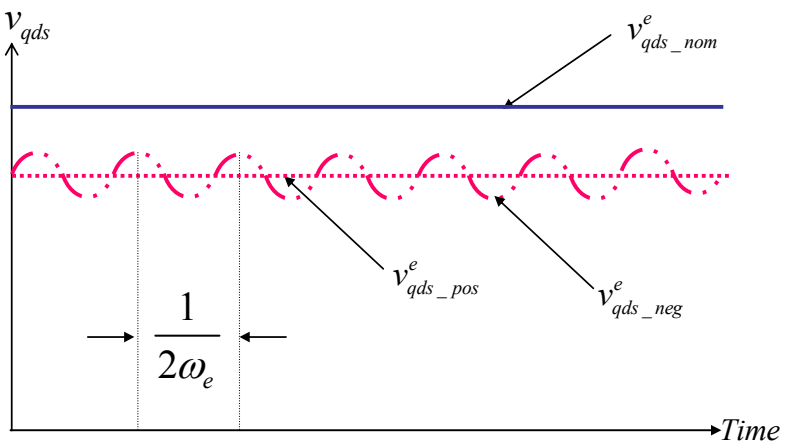

- Blue solid line : Stator voltage under fault-free condition
- Red dashed line : Positive sequence voltage with stator turn faults
- Red long-dashed line: Negative sequence voltage with stator turn faults

(b) In the time domain

Figure 6.1. Voltage references under fault-free and turn fault conditions.

Either a reduction in the fundamental positive sequence voltage reference or an increase in the fundamental negative sequence voltage reference can be employed as a turn fault indicator. However, the fundamental negative sequence voltage reference in the rotor-aligned (synchronously) rotating reference frame is observed as a second-order harmonic in the time domain whose frequency varies corresponding to the synchronous frequency. This means that a variable band-pass filter is required when the fundamental negative sequence voltage reference is selected as the fault indicator. Although the fundamental negative sequence voltage reference can be observed as a stationary component in the reference frame that rotates at the synchronous frequency but in the opposite direction to the synchronously rotating reference frame, this transformation is not necessary for controlling an electric machine. This means that additional computation for the transformation is required. In contrast, a simple low-pass filter is required when the fundamental positive sequence voltage reference is assigned as the

fault indicator. Furthermore, the generation or representation of voltage references in the rotor-aligned (synchronously) rotating reference is already one of the essential tasks in an ordinary electric motor drive. Thus, it can be concluded that the selection of fundamental positive sequence voltage reference as a turn fault indicator would be a better choice since the selection does not require additional burden to the drive's control tasks except for simple low-pass filtering.

6.3 Implementation

Figure 6.2 presents the basic concept of the proposed turn fault detection method. As indicated in the figure, an IPMSM drive, which is operated with rotor-field oriented vector control incorporating MTPA operation, is considered.

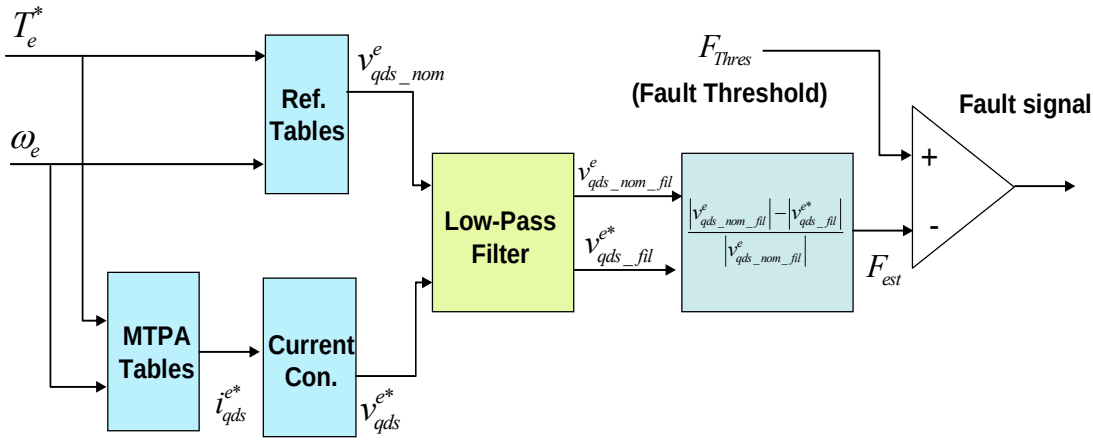

Figure 6.2. Basic concept of the proposed turn fault detection method.

The proposed turn fault detection method can be divided into the following four steps: (1) obtaining the actual voltage references for a given torque reference and rotating speed through the current controllers, (2) estimating the voltage references for the same torque reference and rotating speed from the pre-defined look-up tables, (3) filtering the actual and estimated voltage references through a low-pass filter, (4) comparing the low-pass filtered quantities.

6.3.1 Voltage Reference Tables Obtained from a Fault-Free Motor

To realize the proposed idea, the reference data of the voltage references obtained from a fault-free drive are required to compare with the actual voltage references. These reference data can be updated via an on-line machine model or can be stored in look-up tables from off-line experiments or from on-line measurements during a fault-free initialization period. Although a model-based approach does not require extensive experiments and additional memory space in the control hardware, this approach is very sensitive to the drive's non-idealities and variations in the machine parameters.

The presence of rotor saliency in an IPMSM leads to a characteristic feature that non-salient PM machines do not have. The developed torque of an IPMSM consists of two torque components: magnetic aligned torque (electromagnetic torque) and reluctance torque components. Therefore, many combinations of the two torque components for a given developed torque exist. Furthermore, there will always exist a specific combination that requires the least amplitude of the stator currents. Nowadays, a control method exploiting this feature of an IPMSM, the so called maximum torque per ampere (MTPA) operation, is gaining popularity because it can minimize the stator copper loss. However, specific trajectories of the q- and d-axis currents for MTPA operation must be

determined to realize this operation. Generally, these trajectories are obtained experimentally, and stored in look-up tables with torque reference and rotating speed as the indices because the accuracy of the trajectories is strongly influenced by the magnetic non-linearity. During the same experimental stage used to obtain the MTPA tables, the reference data of the *q*- and *d*-axis voltage references can also be obtained and stored in look-up tables whose sizes will be exactly the same as those of the MTPA tables. When compared to a model-based method, this experiment-based approach provides a distinct advantage. Since the voltage reference tables are built through experiments, the non-idealities of the given motor are taken into consideration in the reference data.

From this discussion, it can be said that an experiment-based method (look-up table-based method) would be superior to a model-based method for an IPMSM drive operated with the MTPA rule.

6.3.2 Obtaining Voltage References from an Operating Motor

In an ordinary vector-controlled drive, the voltage references are generated in terms of the *qd*-variables in the synchronously rotating reference frame, and are transformed back into three-phase (*abc*) voltage references. The *qd*-voltage references are generally generated from proportional-integral (PI) current controllers with feed-forward. The general form of the current controllers for an IPMSM is given by,

$$\begin{bmatrix} v_{qs}^{e*} \\ v_{ds}^{e*} \end{bmatrix} = K_P \begin{bmatrix} e_{qs}^{e} \\ e_{ds}^{e} \end{bmatrix} + K_I \int \begin{bmatrix} e_{qs}^{e} \\ e_{ds}^{e} \end{bmatrix} dt + \omega_e \begin{bmatrix} 0 & L_d \\ -L_q & 0 \end{bmatrix} \begin{bmatrix} i_{qs}^{e*} \\ i_{ds}^{e*} \end{bmatrix} + \omega_e \begin{bmatrix} \lambda_{PM} \\ 0 \end{bmatrix}, \tag{6.3}$$

where K_P and K_I represent the proportional and integral gains, respectively, and the symbol, *e*, represents the error between the reference and actual value.

As shown in (6.3), at steady-state, the voltage references will be almost constant, while the voltage references under transient conditions will contain high-frequency components. However, if the voltage references are filtered through low-pass filters whose cut-off frequencies are much lower than the synchronous frequency, the high frequency components will be removed.

6.3.3 Fault Decision

The estimated and calculated *q*- and *d*-axis voltage references for a given torque reference and rotating speed are applied to low-pass filters to extract the fundamental positive sequence voltage references. To increase the accuracy of the extraction, the cut-off frequency of the low-pass filters should be properly adjusted, proportional to the synchronous frequency. However, the adjustment of the cut-off frequency is only required when the rotor rotates at an extremely low speed. A fixed value of cut-off frequency can be used without any performance degradation at any other speed. Roughly speaking, a cut-off frequency of less than one half of the synchronous frequency will be sufficient for the purpose.

After filtering the estimated and calculated voltage references, a normalized quantity, F_{est}, referred to as the fault estimation, is calculated as,

$$F_{est} = \frac{\left|v^{e}_{qds\_nom\_fil}\right| - \left|v^{e*}_{qds\_fil}\right|}{\left|v^{e}_{qds\_nom\_fil}\right|}, \tag{6.4}$$

where $v^{e}_{qds\_nom\_fil}$ and $v^{e}_{qds\_fil}$ represent the low-pass filtered quantities of the estimated and calculated voltage references, respectively. If F_{est} exceeds the preset fault threshold (F_{Thres}), the detector will send out the fault signal.

It is easily seen that the sensitivity of the proposed turn fault detection is strongly related to the setting of F_{Thres}. If F_{Thres} is selected tightly, then the detection will be very sensitive. When F_{Thres} is selected with too wide a range, then the accuracy of detection will be undermined. It can be also inferred that the magnitude of the change in the voltage references is dependent on the rotating speed and applied load; therefore, F_{est} will be different at different operating conditions, even under the same turn fault condition. Moreover, the circulating current in the shorted turns also affects the asymmetries in the machine variables. For these reasons, F_{Thres} should be selected or tuned carefully.

6.4 Practical Issues

The advantages of the proposed turn fault detection method were clearly explained in the previous section. However, several practical issues should be considered to enhance the performance of the proposed method. In this section, these practical issues are discussed.

6.4.1 Motor Inherent Asymmetry and Non-linearity

Since the reference tables of voltage references are obtained experimentally, the inherent asymmetry and non-linearity of the tested motor are already taken into account in the reference tables. However, the degrees of inherent asymmetry and non-linearity of individual motors are different even though they have the same specifications; this can impair the generality of the proposed turn fault detection method. The differences in

inherent asymmetry and non-linearity of individual motor can be compensated for by updating the reference tables from on-line measurements or tuning F_{Thres} during a fault-free initialization period. For tuning F_{Thres}, an artificial intelligence (AI) technique is a good choice. Such techniques are described in [50] and [51].

6.4.2 Inverter Non-linearity

Generally, inverter non-linearity is caused by two factors: blanking time and variations in the dc-link voltage. In a two-level VSI where the top and bottom switching devices in an inverter-leg operate complimentary to one other, a blanking time is introduced between the instant when a switching device turns off and the instant when the complementary switching device turns on. This blanking time, sometimes referred to as dead time, should be sufficiently long so as to prevent a critical failure. Although the blanking time is indispensable for safe operation, it introduces non-linearity to the inverter output voltages, and consequently, it affects the current control performance. This has driven considerable research on the compensation for the effects of blanking time [100], [101]. One of the effects of blanking time is the discrepancy between the voltage references and inverter output voltages (machine terminal voltages), and this can influence the sensitivity of the proposed turn fault detection method. The voltage references are transformed into the corresponding duty ratios (or switching times) of the top switching devices in the three inverter legs. However, the duration of an inverter pole voltage is always less than the equivalent switching time of the corresponding voltage reference by the duration of the blanking time unless the blanking time is properly compensated for. In other words, the actual machine terminal voltage is always smaller

than the voltage reference by the equivalent voltage of the blanking time. The equivalent voltage of the blanking time of a VSI can be determined by,

$$v_{T\_Blank} = \frac{T_{Blank}}{T_{SW}} \cdot V_{DC}, \tag{6.5}$$

where T_{Blank} represents the duration of the blanking time, T_{SW} represents the switching period, and V_{DC} represents the dc-link voltage. As shown in (6.5), the equivalent voltage of a blanking time is a function of the duration of the blanking time and amplitude of the dc-link voltage. In every VSI, the blanking time is fixed. Hence, the equivalent voltage lead to a constant offset in the voltage references regardless of the operation conditions as long as the dc-link voltage is constant. This means that if the dc-link voltage remains constant, the blanking time has no effect on the sensitivity of the proposed turn fault detection method. However, the sensitivity of the proposed method will be affected when the dc-link voltage fluctuates. If the blanking time is properly compensated [100], [101], the variation in the offset voltage in the voltage references can also be effectively compensated.

6.4.3 Operating Temperature

All of the machine parameters are dependent on the operating temperature. The stator winding resistance and the strength of the permanent magnets have a somewhat stronger dependency on the operating temperature than the other machine parameters. The stator winding resistance increases as the temperature rises, while the residual flux density and intrinsic coercivity of permanent magnets decreases with increasing temperature [105]. These two characteristics result in variations in the voltage

references. Thus, it necessary to consider the effects of the operating temperature on the voltage references for a higher reliability of the proposed method. The winding resistance and the residual flux density of permanent magnet taking into account the operating temperature can be written as, [61], [105],

$$R(\theta) = R(\theta_0)\left[1 + \delta\left(\theta - \theta_0\right)\right], \tag{6.6}$$

$$B_r(\theta) = B_r(\theta_0)\left[1 + s\left(\theta - \theta_0\right)\right], \tag{6.7}$$

respectively, where $R(\theta_o)$ and $B_r(\theta_o)$ are the resistance and residual flux density at temperature θ_o, and δ and s are constants.

Although the representations, (6.6) and (6.7), are given, it is very difficult to estimate the variations in voltage references as a result of the change in operating temperature accurately. More intensive work on this issue remains as future work in this area.

6.4.4 Non-Stationary Operations and Performance Characteristics of Controllers

Non-stationary operations result in fluctuations in the torque reference and rotating speed; consequently, resulting in fluctuations in the voltage references. When a small amount of fluctuation occurs in a non-stationary operation, the resultant fluctuation in the voltage references can be effectively filtered out owing to the presence of a low pass-filter whose cut-off frequency is near to dc in the proposed turn fault detection method. When a non-stationary operation occurs with a rapid change in the torque or speed reference, the voltage references also change rapidly. In this situation, the fault detection can be influenced by the regulation performances of the current controllers since large

differences, such as overshoots, in the current references and actual currents can be introduced. For a more reliable detection, current controllers that have faster step responses and less overshoots are desirable.

6.4.5 Inverter and Permanent Magnet Failures

In CCVSI-driven applications, the asymmetries introduced by the fault-free inverters are negligible since essentially balanced voltages are applied to the healthy machine. However, any inverter failure increases the asymmetries in the machine variables. The common inverter failures are those in the switching devices and current sensors. These failures can be readily identified because the switching device failures introduce specific patterns in the line currents [102], and the failures in current sensors result in large errors in the current control [103]. However, it should be mentioned that theses failures are also critical in CCVSI-driven applications.

Both demagnetization and deformation of the permanent magnets result in a reduced positive sequence component of the machine terminal voltages. Therefore, the effects of the failures on the voltage references will be almost the same as those of a stator turn fault. For this reason, it may be difficult to differentiate a stator turn fault from failure in the permanent magnets. However, the failures in permanent magnets introduce specific harmonic components, generally sub-harmonics of the mechanical rotating speed, in the line currents [13], [104]. By monitoring these specific sub-harmonics, the failures in the permanent magnets can be identified.

6.5 Chapter Summary

In this chapter, an on-line stator turn fault detection method for IPMSM drives has been proposed. The method is based on monitoring a change in the fundamental positive sequence voltage reference. Practical issues in the implementation of the proposed method have also been discussed.

As pointed out in this chapter, the proposed method has several distinct advantages over previously proposed methods. The selection of voltage references as the fault indicator makes it unnecessary to measure the machine terminal voltages. The observation of the fault signature in the synchronously rotating reference frame significantly attenuates the effects of non-stationary operations; furthermore, does not add any additional burden to the machine control tasks except for simple low-pass filtering. In addition, the proposed scheme is immune to the inherent asymmetries in a given motor since these asymmetries are already taken into account in the reference data obtained experimentally under fault-free conditions. The validation of the proposed method through simulations and experiments is provided in Chapter 11.

In many cases, an early detection of a stator turn fault followed by an interruption in the drive's operation can minimize the financial loss due to the fault. However, it is imperative to maintain uninterrupted drive operation in safety-critical applications in order to prevent a serious accident involving the loss of human life. To provide a solution for maintaining the drive's availability under stator turn fault conditions, a simple turn fault-tolerant operating strategy for IPMSM is proposed in the next chapter.

CHAPTER 7

A STATOR TURN FAULT-TOLERANT OPERATING STRATEGY FOR IPMSM DRIVES

7.1 Overview

In the previous chapter, a simple on-line turn fault detection method for IPMSM drives was proposed. However, as recognized in this work, an IPMSM drive in a safety-critical application does not only require a reliable turn fault detection method, but also imperatively requires a proper remedial action that can maintain the drive's uninterrupted operation.

The most desirable characteristic of a remedial action is to maintain the drive's uninterrupted operation without any degradation in the performance characteristics of the drive in the presence of a stator turn fault. Unfortunately, this is very difficult to achieve, short of using redundancy-based approaches. But these approaches can be justified in specific applications. In transit applications such as traction drives, uninterrupted operation during a short period of time, even with a "limp home" mode, can prevent injury or death.

In this work, a simple stator turn fault-tolerant operating strategy for IPMSM drives that does not require any hardware modification to the standard drive configuration is proposed. Additionally, this strategy does not result in the complete loss of availability of the drive. The theoretical foundations of the strategy are provided in this chapter, and the validation of the strategy is carried out in Chapter 12.

7.2 Theoretical Foundations

In this analysis, it is assumed that a stator turn fault on the *a*-phase winding is detected correctly in its initial stage, and the fault fraction (μ) is small enough so that the turn fault does not break the symmetry of the machine significantly. It is also assumed that the faulty IPMSM is still operated by the rotor field-oriented vector control.

The basic concept of the proposed strategy is to reduce the propagation speed of the turn fault by reducing the circulating current in the shorted turns (i_f). This concept is applicable to any type of coil connections (series or parallel windings). Thus, a stator turn fault in a series winding machine is only considered in developing the proposed turn fault-tolerant operating strategy.

7.2.1 Relationship between Circulating Current and Stator Voltage

The basic idea of the proposed fault-tolerant operating strategy comes from the representation of the voltage at the shorted turns (as_2) in the faulty winding. Rearranging (4.12) yields

$$\frac{R_f}{\mu} i_f + \left\{ R_s i_f + \left[L_{ls} + \mu L_{am}(\theta_r) \right] \frac{di_f}{dt} + \mu \omega_e \frac{dL_{am}(\theta_r)}{d\theta_r} i_f \right\} = v_{as}^0 , \tag{7.1}$$

where $L_{am}(\theta_r) = L_1 - L_2 \cos(2\theta_r)$ represents the self-magnetizing inductance of the *a*-phase winding, and v_{as}^0 represents the instantaneous value of the *a*-phase-neutral voltage.

Noting that θ_r equals $\omega_e t$ in any synchronous machine, the complex variable forms of i_f, $L_{am}(\theta_r)$, and v_{as}^0 in a steady-state condition can be defined respectively as,

$$\tilde{i}_f = I_f e^{j(\omega_e t + \rho_I)}, \quad \tilde{L}_{am} = L_1 - L_2 e^{j(2\omega_e t)}, \quad \tilde{v}_{as}^0 = V_{as}^0 e^{j(\omega_e t + \rho_V)}, \tag{7.2}$$

where I_f and V_{as}^0 represents the amplitudes of i_f and v_{as}^0, respectively, ρ_I and ρ_V represent the phase angle differences referred to the rotor induced voltage (back-emf voltage), respectively. By inserting the complex variables defined in (7.2) into (7.1), the following equations can be obtained.

$$\tilde{i}_f \left\{ \frac{R_f}{\mu} + R_s + j\omega_e \left[L_{ls} + \mu\left(L_1 - 3\tilde{L}_2 \right) \right] \right\} = \tilde{v}_{as}^0, \tag{7.3}$$

$$\left| \tilde{i}_f \right| = \frac{\left| \tilde{v}_{as}^0 \right|}{\left| \frac{R_f}{\mu} + r_s + j\omega_e \left[L_{ls} + \mu\left(L_1 - 3\tilde{L}_2 \right) \right] \right|}. \tag{7.4}$$

Generally, the asymmetry in the stator voltages resulting from a stator turn fault has a very small effect on the overall stator voltage. Therefore, the amplitude of the faulty phase voltage is almost the same as that of the complex stator voltage vector ($\tilde{v}_s^e$) in the synchronously rotating reference frame. Consequently, equation (7.4) can be rewritten as,

$$\left| \tilde{i}_f \right| \approx \frac{\left| \tilde{v}_s^e \right|}{\left| \frac{R_f}{\mu} + r_s + j\omega_e \left[L_{ls} + \mu\left(L_1 - 3\tilde{L}_2 \right) \right] \right|}. \tag{7.5}$$

Equation (7.5) suggests how to reduce i_f and as a result, reduce the propagation speed of the fault. There are three possible ways to reduce i_f: (1) increase R_f, (2) increase the leakage inductance and resistance of the stator winding, and (3) reduce the stator line-neutral voltage. The external impedance between the shorted turns (R_f) is not a controllable variable. Furthermore, a stator turn fault in a low voltage machine is generally a bolted fault, i.e., $R_f = 0$. For these reasons, the first way has no meaning.

The second way can be implemented during the machine design stage. However, a larger leakage inductance and resistance of the stator windings will yield a poorer efficiency. Thus, this option is absolutely unattractive. The last way is to reduce the stator voltage vector, which is a controlled variable in CCVSIs. Reducing the stator voltage prevents the fault from spreading to the entire machine winding *without* resulting in the loss of the drive's availability.

7.2.2 Development of a Stator Turn Fault-Tolerant Operating Strategy

The stator voltages and developed torque of a fault-free IPMSM in a steady-state condition are expressed in terms of the *qd*-variables in the synchronously rotating reference frame respectively as,

$$\begin{bmatrix} v_{qs}^e \\ v_{ds}^e \end{bmatrix} = \begin{bmatrix} R_s i_{qs}^e + \omega_e \left(L_d i_{ds}^e + \lambda_{PM} \right) \\ R_s i_{ds}^e - \omega_e L_q i_{qs}^e \end{bmatrix}, \tag{7.6}$$

$$T_e = \frac{3}{2}\frac{P}{2}[\lambda_{PM} i_{qs}^e + \left(L_d - L_q \right) i_{ds}^e i_{qs}^e]. \tag{7.7}$$

The presence of reluctance torque in an IPMSM yields a peculiar characteristic. Namely, there are many combinations of *q*- and *d*-axis currents (i_{qs}^e and i_{ds}^e) for a given developed torque. Nowadays, in the control of IPMSMs, this characteristic is exploited to achieve maximum torque per ampere (MTPA) [65], [66]. However, it can be inferred that a specific combination which makes the stator voltage smallest, should exist. *This implies that an appropriate selection of q- and d-axis currents for a given operating condition can reduce the stator voltage significantly. Consequently, a significant reduction in* i_f *is achievable while maintaining the given operating condition*.

If a negative i_{ds}^{e} is applied with the requirement of maintaining the same rotating speed (ω_{e0}) and developed torque (T_{e0}) as before, then using (7.7), the corresponding i_{qs}^{e} can be determined by a function of the newly applied negative *d*-axis current (i_{ds1}^{e}) as,

$$i_{qs1}^{e} = \frac{T_{e0}}{\frac{3}{2}\frac{P}{2}\left[\lambda_{PM} + \left(L_d - L_q\right) i_{ds1}^{e}\right]} = \frac{C_1}{C_2 + i_{ds1}^{e}}, \tag{7.8}$$

where C_1 and C_2 are constants dependent on the machine parameters and T_{e0}.

By inserting (7.8) back into (7.5), the amplitude of the circulating current in the shorted turns ($\left|\tilde{i}_f\right|$) is represented as,

$$\left|\tilde{i}_f\right| = \sqrt{\frac{\left[R_s \frac{C_1}{C_2 + i_{ds1}^{e}} + \omega_{e0}\left(L_d i_{ds1}^{e} + \lambda_{PM}\right)\right]^2 + \left[-R_s i_{ds1}^{e} + \omega_{e0} L_q \frac{C_1}{C_2 + i_{ds1}^{e}}\right]^2}{\left(R_s + \frac{R_f}{\mu}\right)^2 + \omega_{e0}^2\left[L_{ls} + \mu\left(L_1 - 3\tilde{L}_2\right)\right]^2}}. \tag{7.9}$$

As shown in (7.9), the amplitude of i_f at a given operating condition is a function of i_{ds1}^{e}. The specific i_{ds}^{e}, which minimizes i_f, can be determined by solving,

$$\frac{\partial\left|\tilde{i}_f\right|}{\partial i_{ds1}^{e}} = 0. \tag{7.10}$$

However, the solution of (7.10) is not achievable because the denominator of (7.9) is a function of an unknown quantity, the fault fraction (μ). However, the denominator is not a function of the *d*-axis current. Therefore, the specific combinations of i_{qs}^{e} and i_{ds}^{e}, which minimizes i_f at all possible operating conditions, can be determined by solving,

$$\frac{\partial\left|\tilde{v}_s^{e}\right|^2}{\partial i_{ds}^{e}} = \frac{\partial}{\partial i_{ds}^{e}}\left[R_s \frac{C_1}{C_2 + i_{ds}^{e}} + \omega_e\left(L_d i_{ds}^{e} + \lambda_{PM}\right)\right]^2 + \left[-R_s i_{ds}^{e} + \omega_e L_q \frac{C_1}{C_2 + i_{ds1}^{e}}\right]^2 = 0. \tag{7.11}$$

The mathematical formulations, which explain the basic concept of the proposed turn fault tolerant operating strategy, seem somewhat complicated. The basic concept can be explained more intuitively using a circle diagram. An example showing how the proposed strategy works is illustrated in Figure 7.1. With the assumption that the voltage drop across the stator resistance is negligible, the circle of the stator current vector and the ellipse of the stator voltage vector at a steady-state condition can be drawn using the following relationships:

$$\left|\tilde{i}_s\right|^2 = i_{qs}^{e\ 2} + i_{ds}^{e\ 2}, \tag{7.12}$$

$$\left(\frac{\left|\tilde{v}_s\right|}{\omega_e}\right)^2 = \left(L_d i_{ds}^e + \lambda_{PM}\right)^2 + \left(L_q i_{qs}^e\right)^2, \tag{7.13}$$

where $\tilde{i}_s$ represents the stator current vector.

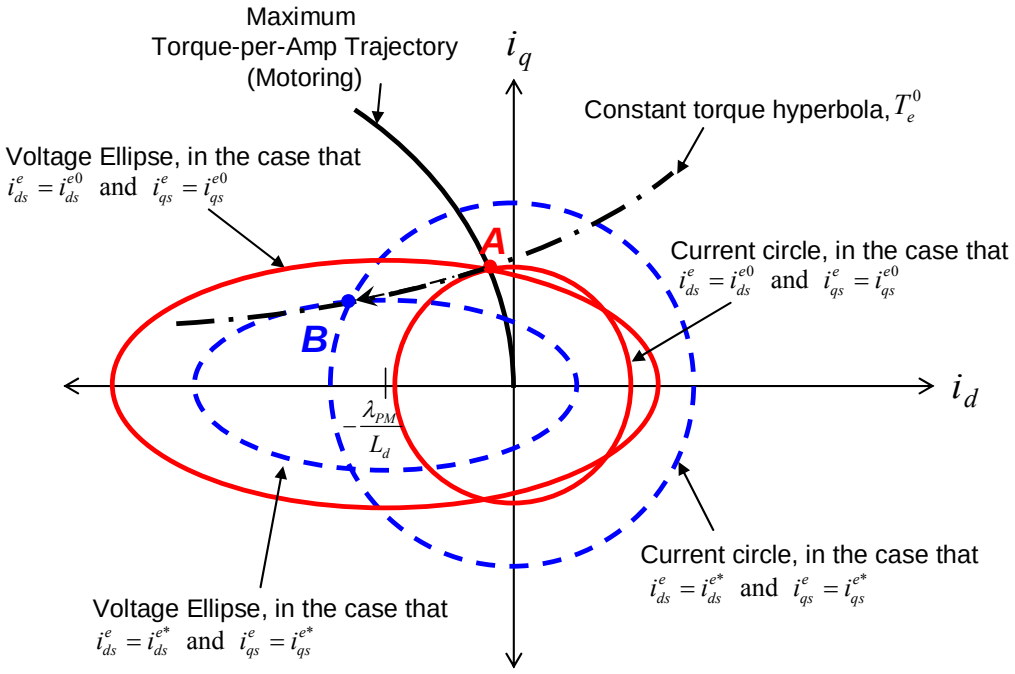

Figure 7.1. Circle diagram showing how the proposed strategy works.

The radius of the circle of the stator current vector is limited by the maximum current rating of the drive, and the radius of the ellipse of the stator voltage vector is restricted by the maximum amplitude of the inverter output voltage. Another important feature of an IPMSM implied in the circle diagram is that while the center of the circle of stator current vector is located at the origin, the ellipse of the stator voltage vector is centered at the characteristic current of the IPMSM.

The combinations of i_{qs}^{e} and i_{ds}^{e} yielding a given developed torque form a hyperbola in the circle diagram. Furthermore, it can be inferred that a specific combination, which minimizes the radius of the circle, should exist. Therefore, the MTPA operation trajectory can be obtained by connecting the specific combination minimizing the radius at every developed torque condition.

Assuming that a stator turn fault is detected when the motor is working at operating point *A* in Figure 7.1, the proposed fault strategy will start to function to minimize the radius of the ellipse of the stator voltage vector while maintaining the given developed torque and rotating speed. If operating point *B* satisfies this requirement in Figure 7.1, the operating point of the IPMSM will move from *A* to *B*.

7.3 Practical Issues

Even though the theoretical foundations of the proposed turn fault-tolerant operating strategy is straight-forward, there are several practical issues to be considered to enhance the performance of this strategy.

7.3.1 Machine Specifications

Simply stated, the basic idea of the proposed strategy is to reduce the stator line-neutral voltage by reducing the rotating magnetic flux. But this should be done while maintaining the required torque and speed and consequently, the required power. This means that the stator current under the proposed strategy will be larger than that prior to activating the strategy. As a result, a larger stator copper loss will be generated when compared to the fault free operation. If the increased copper loss results in the stator winding temperature exceeding the critical temperature, the operation under the proposed strategy should be terminated. However, temperature rise at the stator winding under the proposed strategy is not instantaneous. The temperature will rise to some critical level with a certain time constant. This implies that the operating area and duration under the proposed strategy must be restricted, and the restriction is related to the physical parameters of the machine. It can be also inferred that the allowable area and duration under the proposed strategy is strongly related to the amplitude of the required stator current. The baseline of the proposed strategy is to reduce the rotating magnetic flux and to compensate the reduction in the electromagnetic torque by increasing the reluctance torque. If an IPMSM has a smaller value of characteristic current and larger rotor saliency, the proposed strategy can be operated with a smaller stator current. One encouraging aspect of applying the proposed strategy is that a number of IPMSM designs, whose characteristic current is around the rated current, have been introduced to have a better field-weakening performance [1], [52]. This type of machine is called a "one-per-unit-inductance" machine. Another influencing factor on the required stator current for the proposed strategy is the allowable maximum $|i_f|$ which does not result in

insulation failure between the shorted and adjacent turns. It would not be necessary to minimize $|i_f|$ at every operating point as long as the limit is not exceeded. However, the determination of the allowable $|i_f|$ is very difficult, and can only be established through investigation of the thermal behavior of a stator turn fault. This issue is further investigated in Chapter 12.

7.3.2 Magnetic Non-linearity

In the development of the proposed turn fault-tolerant operating strategy, the magnetic system is assumed to be linear. However, the *q*- and *d*- axis inductances (L_q and L_d) vary depending on operating condition because of magnetic saturation and cross-coupled magnetization effects. In Chapter 4, the variations in L_q and L_d were discussed. Using the experimentally obtained L_q and L_d profiles, the effects of the magnetic non-linearity can be compensated in the trajectories of i_{qs}^e and i_{ds}^e for the proposed strategy.

7.3.3 Suitable Applications

The proposed fault-tolerant operating strategy is applicable in any application that mandates high stator turn fault tolerance. However, the strategy can yield greatly increased fault tolerance in specific applications that require the faulty machine to keep rotating in spite of some degradation in performance. From this perspective, a traction drive in a mild-hybrid vehicle or pure electric vehicle is a very suitable application for the proposed strategy. The general configuration of the power-train system in a mild hybrid

vehicle is presented in Figure 7.2. As shown in the figure, since the electric machine is connected directly to the internal combustion engine and the transmission, it is very difficult or even impossible to isolate the electric machine from its mechanical counterparts while the vehicle is moving. Thus, even though the faulty machine is not required to generate any propulsion, the machine must continue to rotate because of its mechanical connections to the internal combustion engine and the transmission. Because of the presence of the permanent magnets, the circulating current in the shorted turns cannot be extinguished by simply cutting off the stator currents. In this situation, the proposed strategy can ideally reduce the circulating current to be much less than the rated current by nulling the q-axis flux and controlling the q-axis current to be zero.

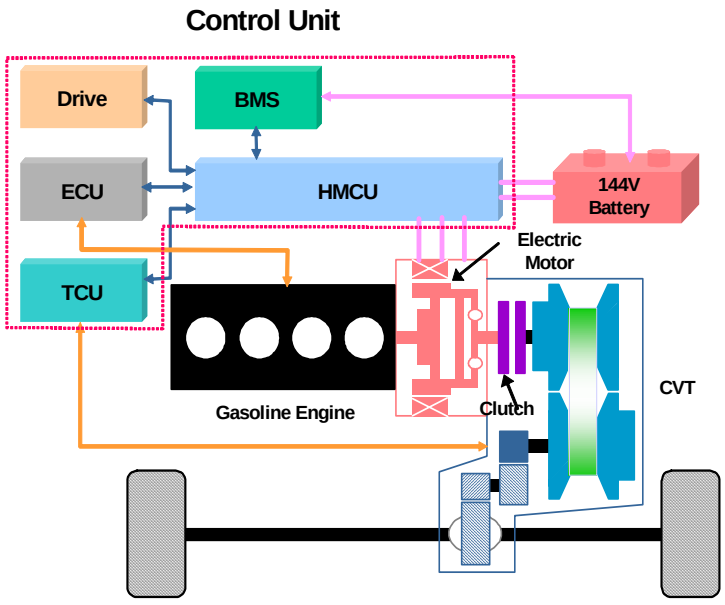

Figure 7.2. Configuration of the power train system in a mild-type parallel hybrid electric vehicle.

7.4 Chapter Summary

The theoretical foundations of a stator turn fault-tolerant operating strategy for IPMSM drives in safety-critical applications have been discussed in this chapter. The basic concept of the strategy is to reduce the stator line-neutral voltages and consequently, the amplitude of the circulating current resulting from a turn fault. It has been shown that this simple principle can reduce the propagation time of a turn fault without requiring any hardware modification to the standard drive configuration. Additionally, it has been shown that the strategy does not result in the complete loss of the availability of the drives in the presence of a turn fault. However, the most valuable contribution of the proposed strategy is that it can prevent a serious accident involving the loss of human life due to the abrupt shutdown of the drive's operation.

Several practical issues for enhancing the performances of the proposed strategy are also discussed. The validation of the proposed strategy is provided in Chapter 12.

CHAPTER 8

EXPERIMENTAL SETUP AND IMPLEMENTATION OF A STATOR TURN FAULT

8.1 Overview

An electrical model and a thermal model of an IPMSM with stator turn faults, turn fault detection method, and fault-tolerant operating strategy were proposed in the previous four chapters, respectively. In this chapter, the experimental setup and the implementations of various tests are discussed.

8.2 Experimental Setup

The experimental setup consists of four main subsystems: the tested drive, load, drive user interface, and data acquisition systems. The overall experimental setup is illustrated in Figure 8.1.

8.2.1 Tested Drive System

In this work, an eight-pole 10 kW IPMSM with a rated speed of 2450 rpm and a rated torque of 40 Nm driven by a current-controlled inverter is considered. The key specifications of the tested IPMSM and inverter are summarized in Table 8.1 and Table 8.2, respectively. The front views of the tested IPMSM and inverter are presented in Figure 8.2.

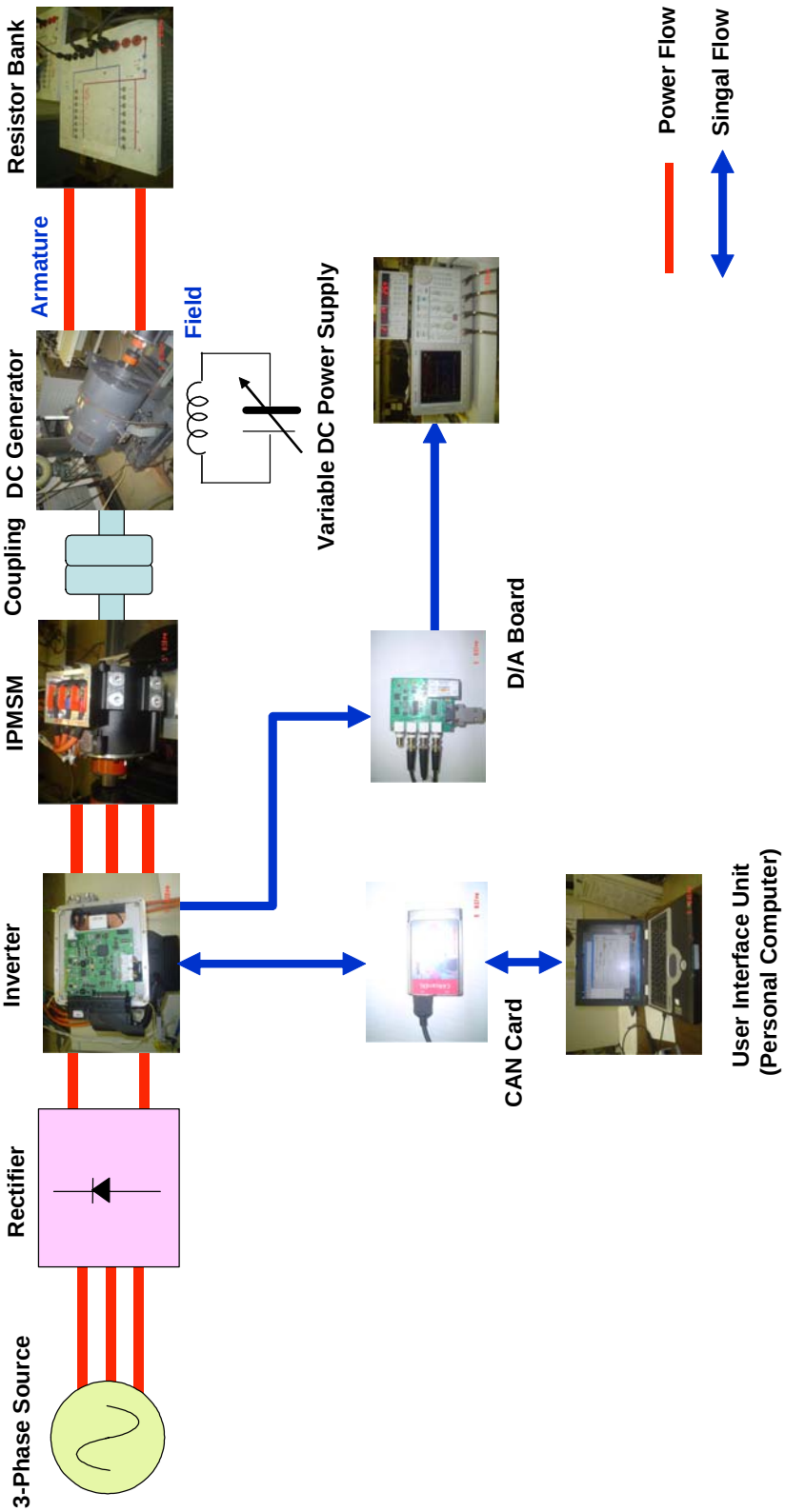

Figure 8.1. Overall Experimental setup.

Table 8.1. Specifications of the tested IPMSM.

Class	Item	Unit	Value	Remark
General	Pole Number	[-]	8	
	Rated / Max. Power	[kW]	10 / 20	
	Rated / Max. Torque	[Nm]	40 / 80	
	Rated / Max. Speed	[rpm]	2450 / 8000	
Stator	Slot Number	[EA]	12	
	Core Type	[-]	Separated	
	Core Thickness	[mm]	0.35t	
	Core Material	[-]	RM 8	
	Stator Core Length	[mm]	80	
	Winding Type	[-]	Concentric	
	Coils per Phase Winding	[EA]	4	
	Turns per Coil	[Turns]	24	
	Resistance	[mohm]	4.85	per phase
	Leakage Inductance	[uH]	33	per phase
	Magnetizing Inductance	[uH]	L1: 198 L2 : -73.3	per phase
	Rated / Max. Current	[Apeak]	120 / 250	per phase (30 A/coil)
	Winding Insulation	[-]	H	
Rotor	Magnet Material	[-]	Nd-Fe-Br	
	PM Flux	[Wb]	0.0534	
	Core Thickness	[mm]	0.35	
	Core Material	[-]	RM 8	
Position Sensor	Type	[-]	Resolver	
	Pole Number	[-]	4	
Cooling	-	-	Natural Convection	

Table 8.2. Specifications of the tested inverter.

Class	Item	Unit	Value	Remark
General	Control Algorithm	[-]	Vector control	MTPA
	DC-Link Voltage	[Vdc]	216	
	Max. Current	[Apeak]	300	
	Control Function	[-]	Speed / Torque	
	Current Control Rate	[kHz]	7	
	Switching Frequency	[kHz]	7	
	PWM Scheme	[-]	SVPWM	
Power Section	Switching Device	[-]	IGBT	
	Cooling	[-]	Forced-Air	

(a) IPMSM

(b) Inverter

Figure 8.2. Front views of the tested drive.

8.2.2 Drive User Interface System

The operation of the tested drive is controlled by the drive user interface software running on a personal computer. The controller area network (CAN) protocol provides the communication between the drive and the PC with a bit-rate of one megabit per second.

8.2.3 Load System

A dc machine is directly coupled to act as a dynamometer. The specifications of the dc machine are summarized in Table 8.3. Since the field circuit of the dc machine is separately excited, an independent dc-voltage supply is used to provide the excitation current. To apply variable loads to the tested motor, the armature circuit of the dc generator is connected to variable resistor banks. The load can be adjusted by changing the resistance of resistor banks and the applied field voltage.

8.2.4 Data Acquisition System

8.2.4.1 Current and Voltage Measurements

Currents are measured using current transducers and a digital oscilloscope. Voltages are measured with isolated voltage transducers and the digital oscilloscope.

Table 8.3. Specifications of the dc machine in the load system.

Item	Unit	Value	Remark
Rated Power	[kW]	7.5	Working as Generator
Rated Armature Voltage	[Vdc]	125	
Rated Field Voltage	[Vdc]	125	
Rated Armature Current	[Adc]	60	
Rated /Max. Speed	[rpm]	1750 / 3600	

8.2.4.2 Temperature Measurements

To measure the temperature rise at various spots on the tested motor, nine *K*-type thermocouples and a 16-channel thermocouple monitor are used. The placements of the thermocouples are summarized in Table 8.4. The placements of some of the thermocouples are shown in Figure 8.3. The measured voltages from the thermocouples are applied to a 16-channel thermocouple monitor to transform them into temperature readings. The temperature readings are logged at a sampling rated of 0.1 Hz to the personal computer through a general purpose interface bus (GPIB) communication.

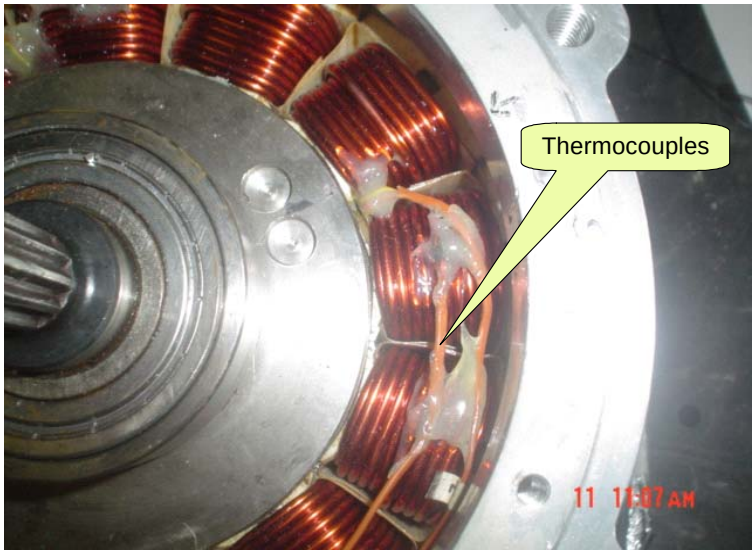

Figure 8.3. Thermocouples inside of the motor.

Table 8.4. Locations of the thermocouples.

No.	Locations	Remark
1	Shorted turns in a coil in the *b*-phase winding	End-winding
2, 3	Turns adjacent the shorted turns	End-winding
4, 5, 6	Healthy turns located at the different coils	End-winding
7, 8	Two positions on the frame	
9	Ambient	

8.2.4.3 Measurements and Acquisition of Drive Internal Variables

The drive's internal variables, such as the *q*- and *d*-axis voltage references, are acquired with the monitoring function provided in the drive user interface software. The acquired data can be transmitted to the digital oscilloscope through a four-channel, twelve-bit digital-to-analog conversion board or can be logged onto the PC in a data format that is accessible in Matlab™.

8.3 Implementation of a Stator Turn Fault

8.3.1 Creation of a Stator Turn Fault

Two taps are added onto a coil in the *b*-phase winding to access two adjacent turns for creating one-turn fault from outside of the machine. The implementation of the two taps on the two turns is shown in Figure 8.4.

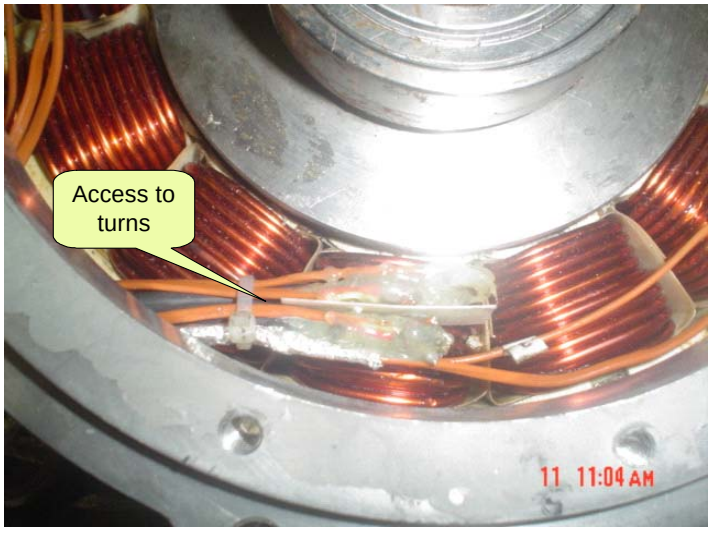

(a) View of the inside of the motor

Figure 8.4. Implementation of a stator turn fault.

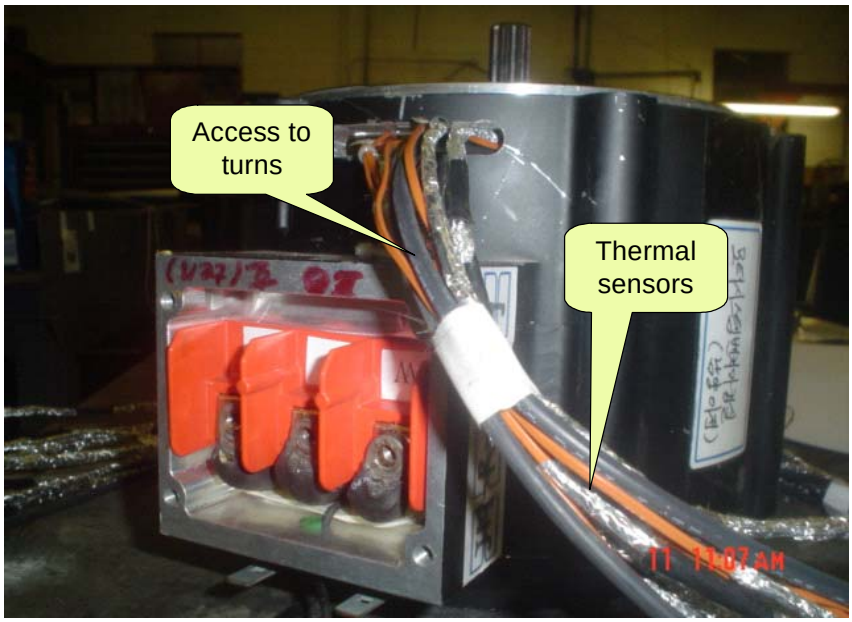

(a) View of the outside of the motor

Figure 8.4. Implementation of a stator turn fault.

8.3.2 Resistance of Copper Wires for Taps

Two 1-m 10 AWG copper wires are used to make the two taps. Even though the resistance of these wires is very small, it reduces the amplitude of the circulating current by acting as an external impedance (R_f). The dc resistance of the two wires can be determined by the following equation:

$$R_{Lead} = \rho \frac{l}{A_{wb}}, \tag{8.1}$$

where ρ is the resistivity of copper, l is the length of the two lead wires, A_{wb} represents the area of winding that can be calculated by

$$A_{wb} = \pi \left(\frac{d_{wb}}{2} \right)^2, \tag{8.2}$$

where, $d_{wb} = 8.24865\left(0.890526\right)^{G}$, and G is the size of the AWG cable. The increase in temperature is taken into account through the following relationship:

$$\rho(T) = \rho(T_0)\left[1 + \delta\left(T - T_0\right)\right], \tag{8.3}$$

where $\rho(20C^{\circ}) = 1.72 \times 10^{-8}$ and $\delta = 0.0038$ at $T_0 = 20^{\circ}C$.

The resistance of an individual turn in a coil can be obtained using (5.16) and (5.17).

Table 8.5 summarizes the calculated resistances of the shorted turns and the two wires. As presented in Table 8.5, the resistance of the two lead wires is much larger than that of the individual turn in the stator winding. The effects of the resistance of the two lead wires are investigated in Chapter 9.

8.4 Inductance Profiles of the Tested Motor Considering Magnetic Non-Linearity

The discussion of magnetic saturation and cross-coupling effects leading to variations in L_q and L_d of an IPMSM was presented in Chapter 4. A method for including the non-linear effects in the developed model of an IPMSM with stator turn faults, was also discussed.

Table 8.5. Resistances of the two copper wires and the shorted turns.

Item	Unit	Value	Remark
Resistance of the cables	[mohm]	6.54	
Resistance of the shorted turns	[mohm]	0.8083	One turn fault

The L_q and L_d profiles of the tested IPMSM obtained through experiments are presented in Figure 8.5 (a) and (b), respectively. As expected, it can be observed that L_q is more strongly affected by magnetic saturation than L_d. Furthermore, it can be seen that the tested IPMSM exhibits some degree of cross-coupling magnetization.

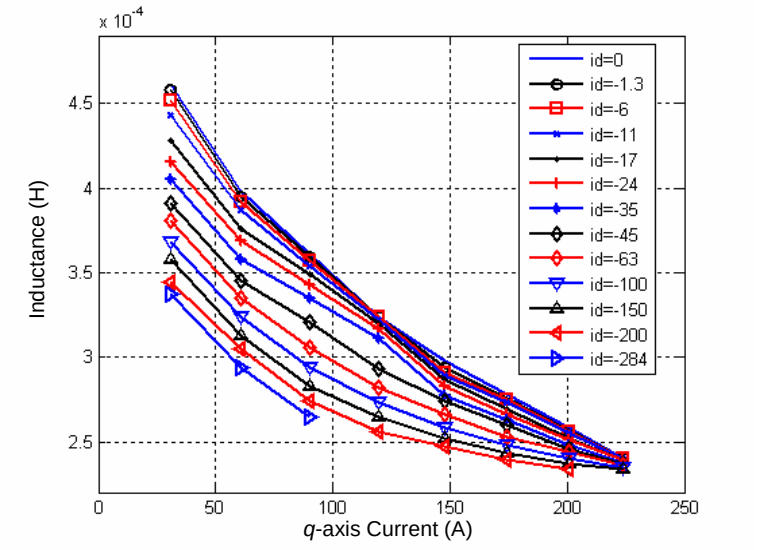

(a) L_q

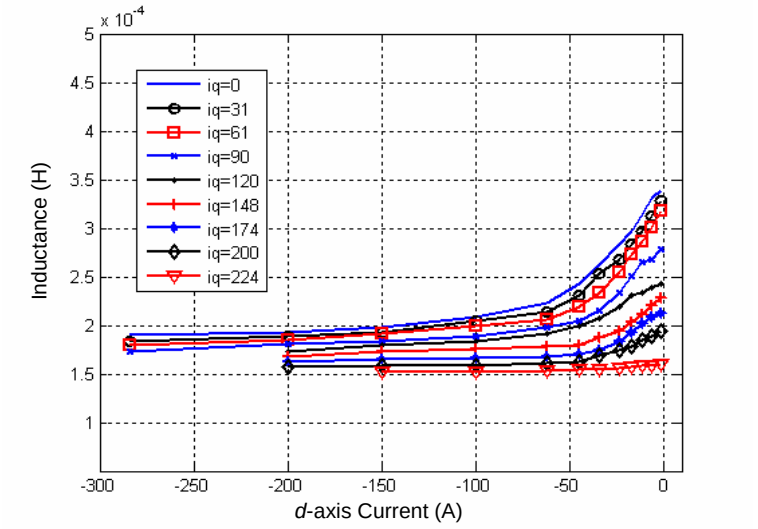

(b) L_d

Figure 8.5. The L_q and L_d profiles of the tested IPMSM [Courtesy of Hyundai Motor Company, Seoul, Korea].

8.5 Chapter Summary

In this chapter, the experimental setup and implementation of stator turn faults have been discussed. Furthermore, the additional resistance resulting from the two copper wires used to access two turns has been determined. The L_q and L_d profiles of the tested IPMSM while considering the magnetic non-linearity have been presented. These inductance profiles are applied to the simulations in the chapters that follow.

CHAPTER 9

VERIFICATION OF THE MODEL OF AN IPMSM DRIVE WITH STATOR TURN FAULTS

9.1 Overview

A simulation model of an IPMSM drive with stator turn faults was derived in Chapter 4. In this chapter, the model is validated by simulation and experiment. The inductance profiles presented in Chapter 8 are applied to the proposed model. The effects of the resistance of the two copper wires used to access two turns inside of the tested motor are also investigated.

9.2 Simulation Results

Simulations are carried out to show the characteristics of stator turn faults in an IPMSM drive. Particularly, the following issues are studied:

(1) Comparison of the characteristics of turn faults in a series and parallel windings

(2) The effects of rotating speed

(3) The effects of load level

(4) The effects of fault fraction (μ)

(5) The effects of the increased resistance caused by the two copper wires

9.2.1 Comparison of the Characteristics of Turn Faults in Series and Parallel Windings

To compare the characteristics of stator turn faults in series and parallel windings, the per-phase equivalent parameters of two IPMSMs, which have different coil connections, are assumed identical even though this would not generally be the case in practice. In addition, it is assumed that the two motors have the same number of series turns per phase.

The simulation conditions for comparing the amplitudes of the circulating currents ($|i_f|$) in series and parallel windings are defined in Table 9.1. The comparison of $|i_f|$ at each operating point within rated operation is provided in Figure 9.1. In the figure, the *x*- and *y*- axes represent the normalized values of the rotating speed and developed torque referred to their rated values, and the *z*-axis represents the normalized $|i_f|$ referred to the rated coil current. However, it should be noted that the rated coil current means the rated phase current in any series winding machine.

The machine variables of the two IPMSMs with the turn faults are compared at 1500 rpm rotating speed and rated load. The results are presented in Figure 9.2.

Table 9.1. Simulation conditions for comparing $|i_f|$ in series and parallel windings.

Item	Unit	Value	
		Series Winding	Parallel Winding
Coils Connected in Paralell	[-]	1	4
Fault Location	[-]	On a coil in the *a*-Phase	
Fault impedance	[ohm]	0 (a bolted turn fault)	
Fault Fraction	[%]	1.04	4.17
Rated Coil Current	[Apeak]	120	30
Load Torque	[Nm]	0~40 (from no load to the rated load)	
Rotating speed	[rpm]	0~2450 (from zero to the rated speed)	

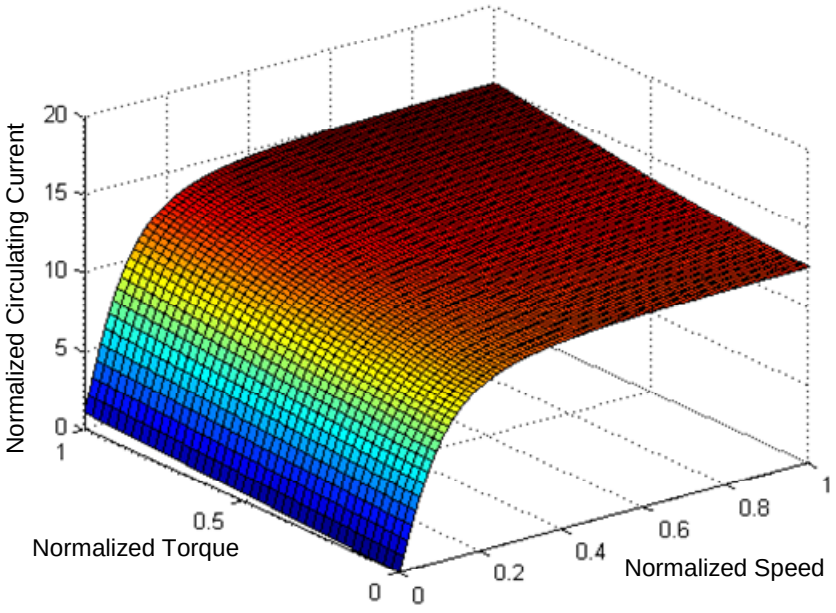

(a) In the series winding

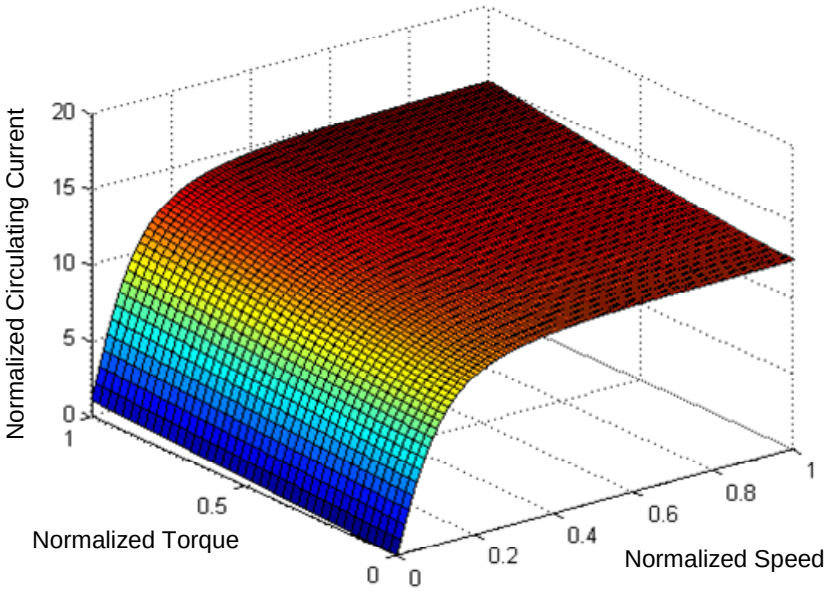

(b) In the parallel winding

Figure 9.1. Comparison of the normalized $|i_f|$ in the series and parallel windings at each operating point within rated operation.

As shown in Figure 9.1, the ratio of $|i_f|$ to the rated coil current in the series and parallel windings are almost same. This implies that the circulating currents in the series and parallel windings will generate almost the same copper losses in the shorted turns. This can be verified by the following relationship:

$$\frac{P_{T\_ser}}{P_{T\_par}} = \frac{R_{T\_ser} I_{f\_ser}^2}{R_{T\_par} I_{f\_par}^2} = \frac{\mu_{ser} R_s \left(A I_{s\_rated} \right)^2}{m\mu_{ser} m R_s \left(A \frac{I_{s\_rated}}{m} \right)^2} = 1, \tag{9.1}$$

where the subscripts, T_ser and T_par, represent the shorted turns of the series and parallel windings, respectively, I_{f_ser} and I_{s_par} are the rms values of the circulating currents in the shorted turns in both cases, R_s is the per-phase equivalent stator resistance, m is the number of coils in a phase winding connected in parallel, and A is the ratio of the circulating currents to the rated coil currents in both cases. From (9.1), it can be said that the type of coil connection of a machine is irrelevant when assessing the thermal stress caused by the circulating current.

As shown in Figure 9.1, i_f increases, but the rate of increase of i_f decreases as the rotating speed increases. This phenomenon can be explained by the fact that i_f at a low speed is mainly limited by the resistance of the shorted turns, while the leakage inductance (reactance) of the shorted turns limits i_f at a high rotating speed.

As presented in Figure 9.2, the stator turn faults in the series and parallel windings induce similar degrees of asymmetries in the machine variables except for the amplitudes of the circulating currents.

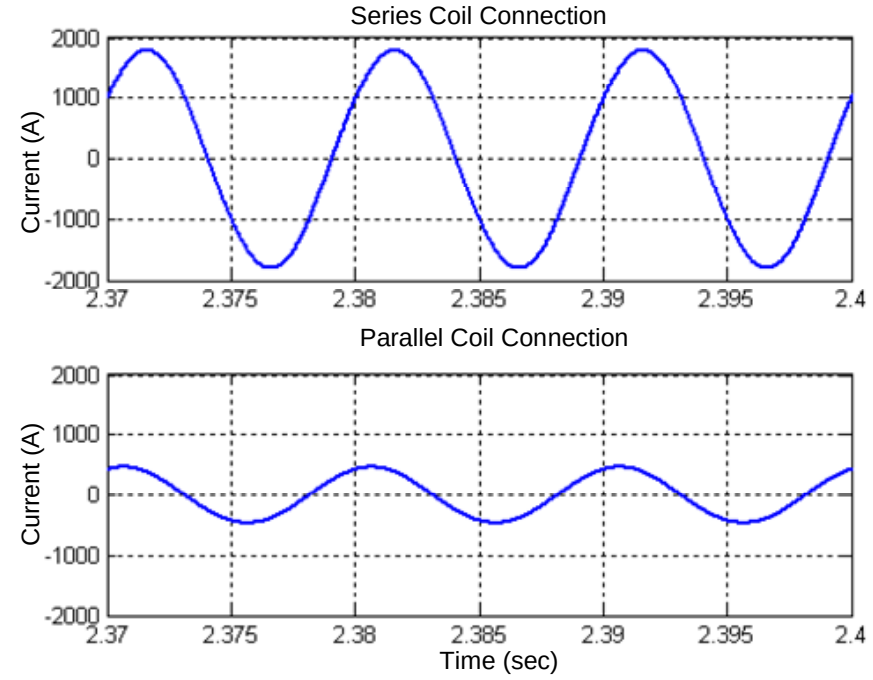

(a) Circulating currents

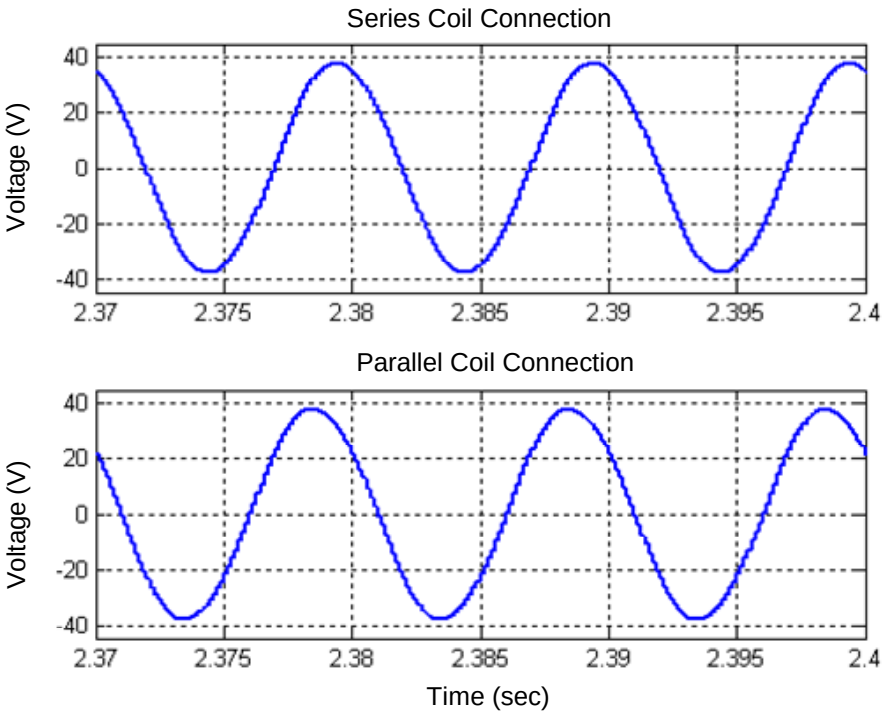

(b) *a*-phase line-neutral voltages

Figure 9.2. Comparisons of the machine variables in the series and parallel windings at 1500 rpm rotating speed and rated load.

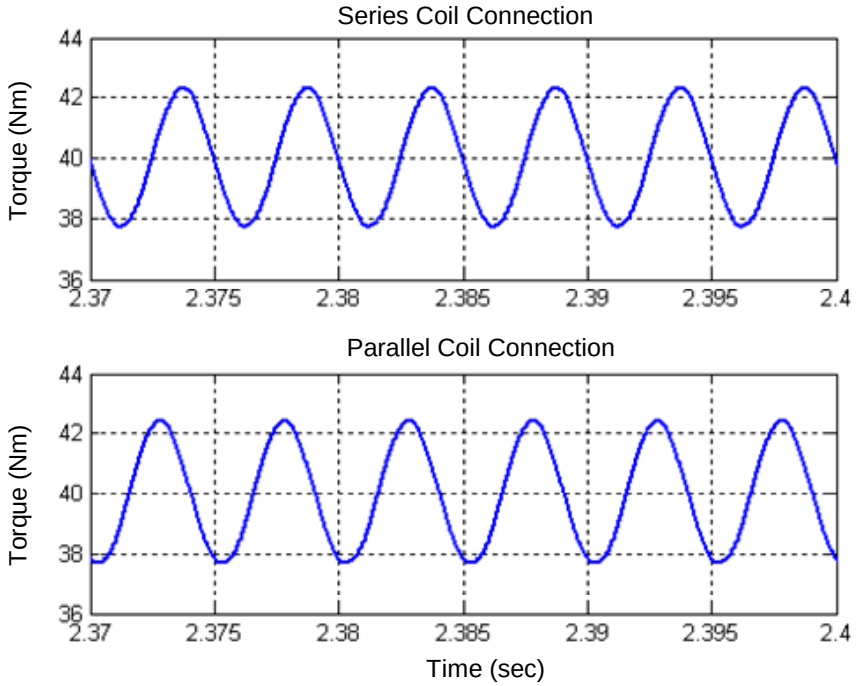

(c) Developed Torque

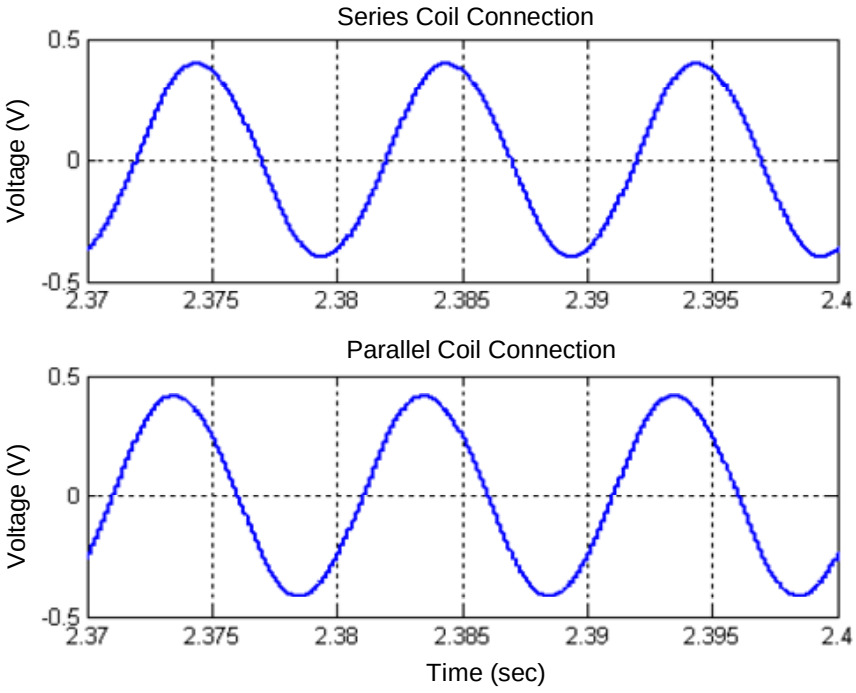

(d) Sum of the line-neutral voltages

Figure 9.2. Comparisons of the machine variables in the series and parallel windings at 1500 rpm rotating speed and rated load.

A turn fault in a symmetrical three-phase AC machine can induce unbalanced phase (or line) currents. These currents lead to uneven temperature rises in the phase windings. However, in the case of a CCVSI-driven machine, the controller actions of the CCVSI try to compensate for the asymmetry in the phase currents. This implies that when a series winding machine is driven by a CCVSI, the uneven winding temperature rises caused by the stator turn fault will not be significant. On the contrary, even the controller actions cannot make the coil currents in the faulty phase winding evenly distributed in the case of a parallel winding machine. This phenomenon is shown in Figure 9.3. In the figure, the currents flowing through the faulty coil and a healthy coil of the parallel winding IPMSM are compared at 1500 rpm rotating speed and rated load. As shown in Figure 9.3, the faulty coil current rises up to about 130 % of the rated coil current. This increased current generates more copper loss in the faulty coil. As a result, the faulty coil has more thermal stresses not only caused by the circulating current in the shorted turns, but also by the increased coil current.

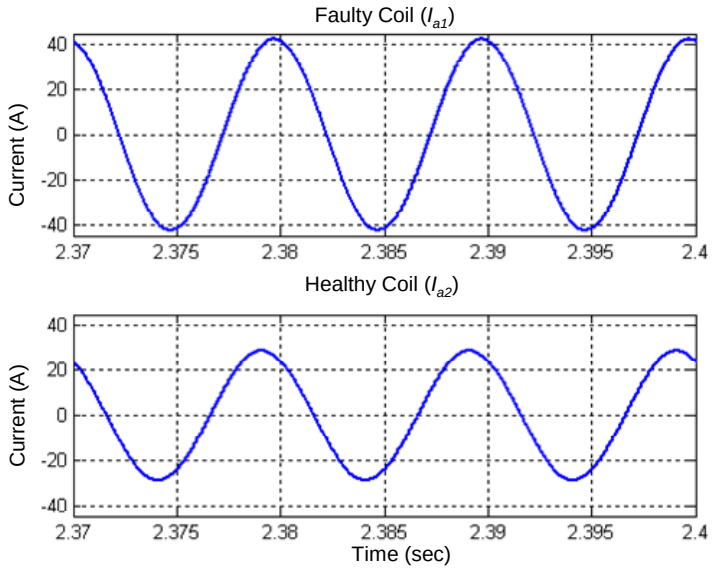

Figure 9.3. Comparison of the currents flowing through the faulty coil and a healthy coil in the parallel winding.

9.2.2 Effects of Rotating Speed

The simulations to show the effects of rotating speed on the behavior of an IPMSM drive with a stator turn fault are performed under the conditions defined in Table 9.2. The responses of the rotating speed and developed torque are presented in Figure 9.4(a) and (b), respectively. The *a*-phase line-neutral voltage and current, and circulating current (i_f) are presented in Figure 9.4(c). The simulation results in Figure 9.5 show the effects of rotating speed on the machine variables of the IPMSM with the turn fault. The results are summarized in Table 9.3. The machine variables observed in Figure 9.5 are related to a turn fault. Some of these variables have been suggested as the turn fault indicators in previously proposed detection methods.

As presented in Figure 9.4, the control performance of the drive is still satisfactory even in the presence of the turn fault. However, it can be easily inferred that the drive's control performance will degrade as the fault gets worse, eventually losing controllability completely. Figure 9.4(b) shows that the actual torque is less than the torque reference when the machine is accelerated to a speed range above the rated speed. However, this is not due to the fault, but rather due to field-weakening operation.

Table 9.2. Simulation conditions for showing the effects of rotating speed.

Item	Unit	Value
Coils Connection	[-]	Series
Load Torque	[Nm]	20
Fault Location	[-]	on the *a*-phase
Fault impedance	[ohm]	0 (a bolted turn fault)
Fault fraction	[%]	1.04
Rotating speed	[rpm]	1500 / 2450 / 3500

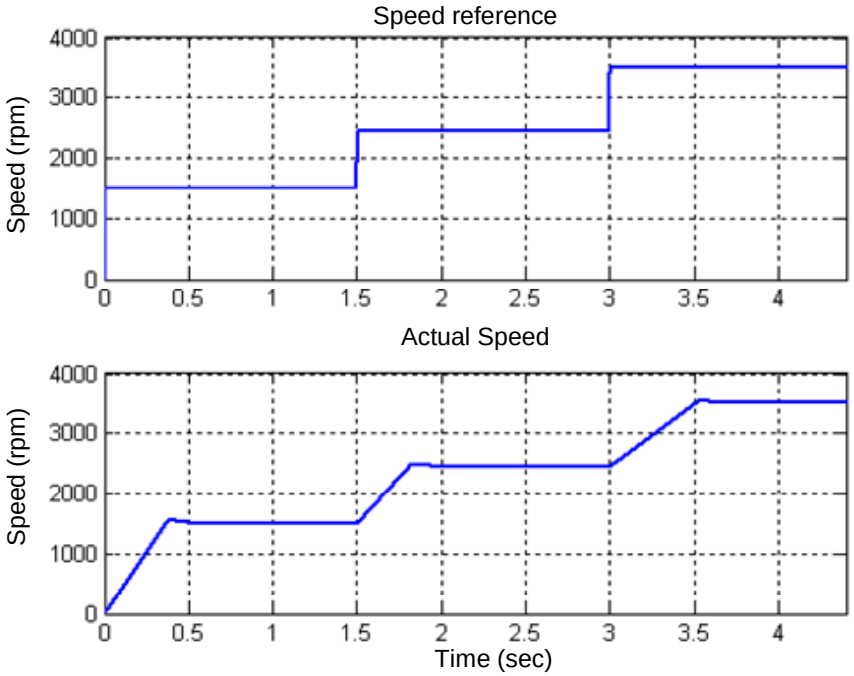

(a) Rotating speed

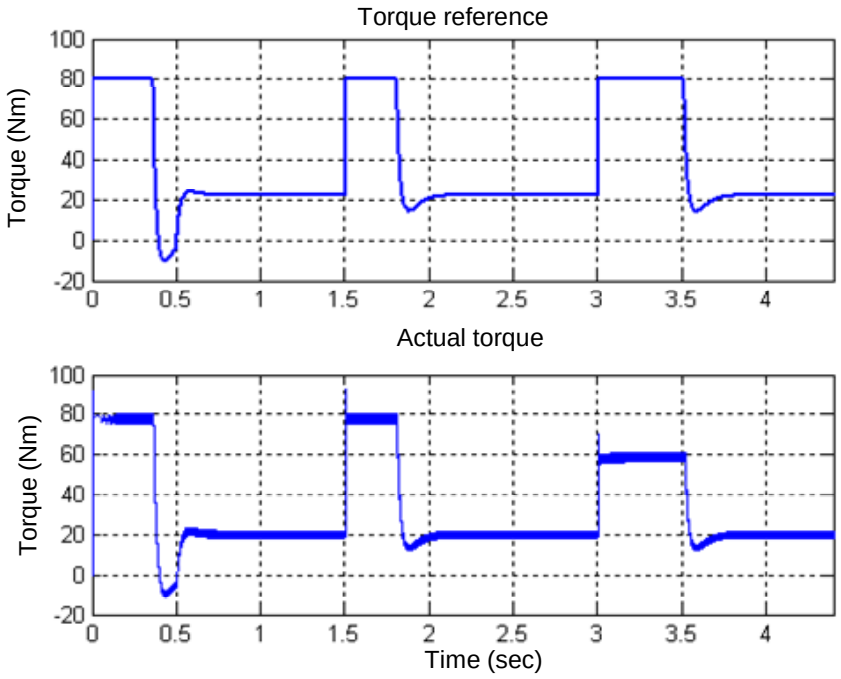

(b) Developed torque

Figure 9.4. Drive variables under various rotating speeds.

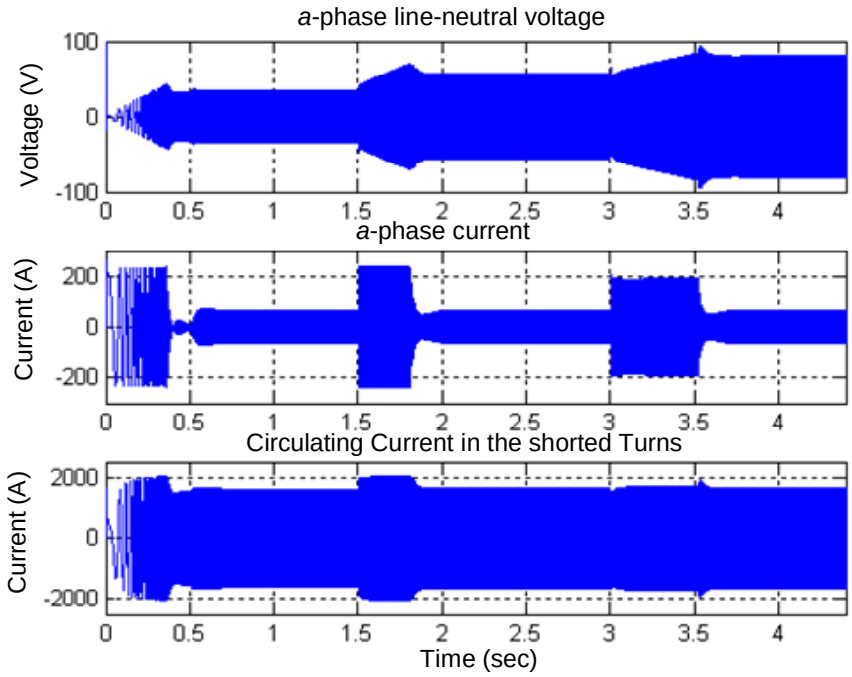

(c) *a*-phase line-neutral voltage, *a*-phase current and circulating current

Figure 9.4. Drive variables under various rotating speeds.

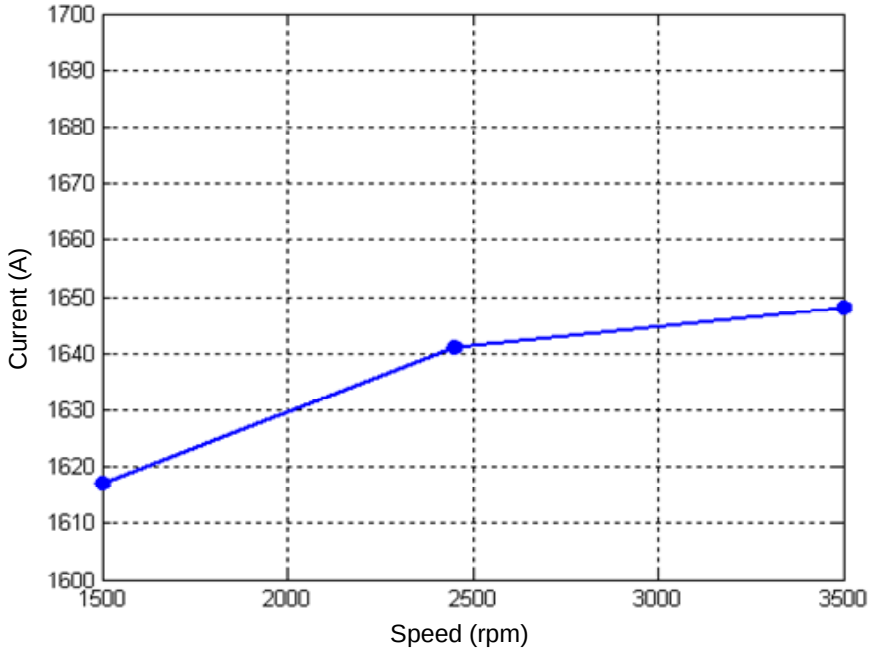

(a) Circulating current

Figure 9.5. Effects of rotating speed on the machine variables.

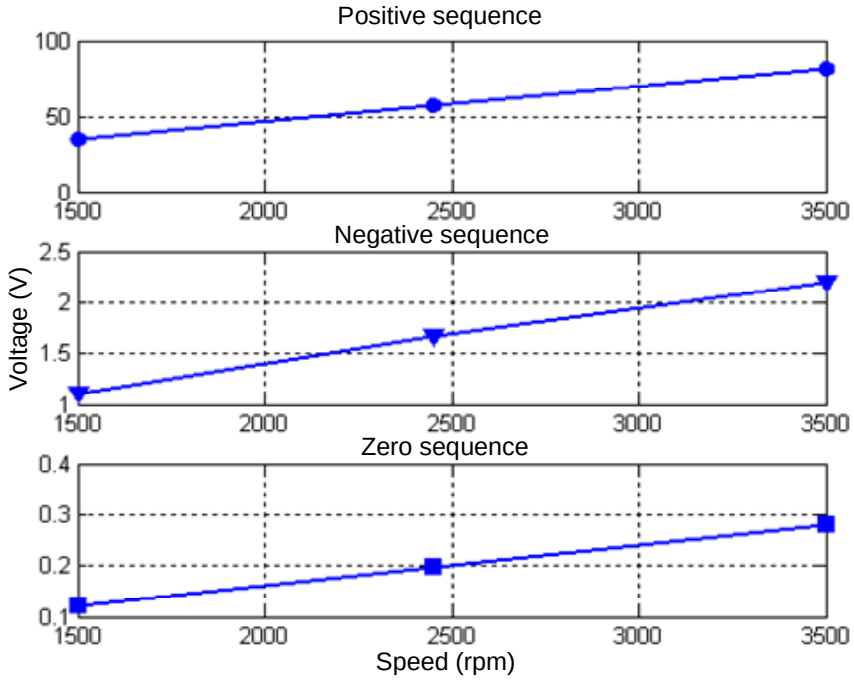

(**b) Sequence components in the line-neutral voltages**

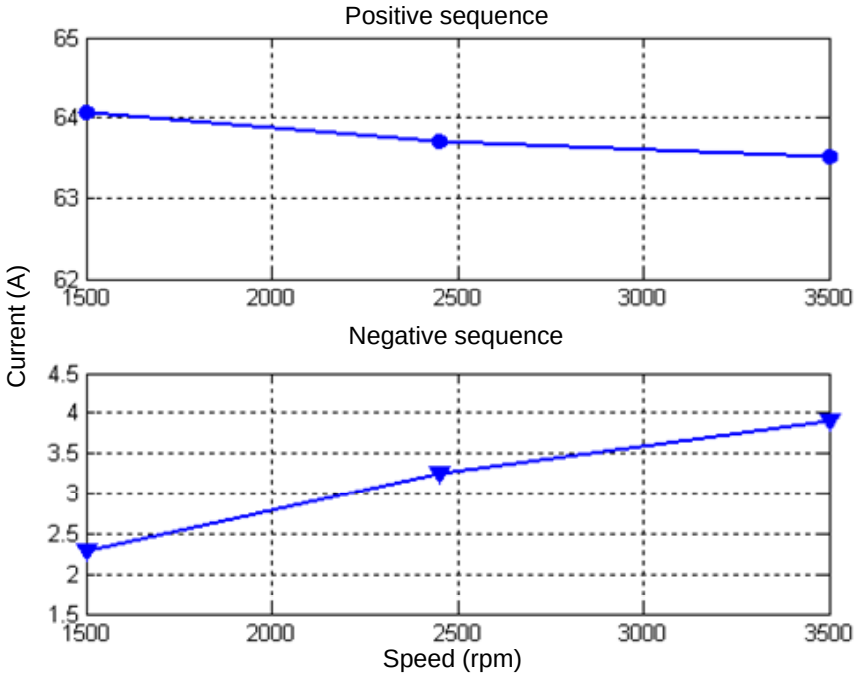

(**c) Sequence components in the line currents**

Figure 9.5. Effects of rotating speed on the machine variables.

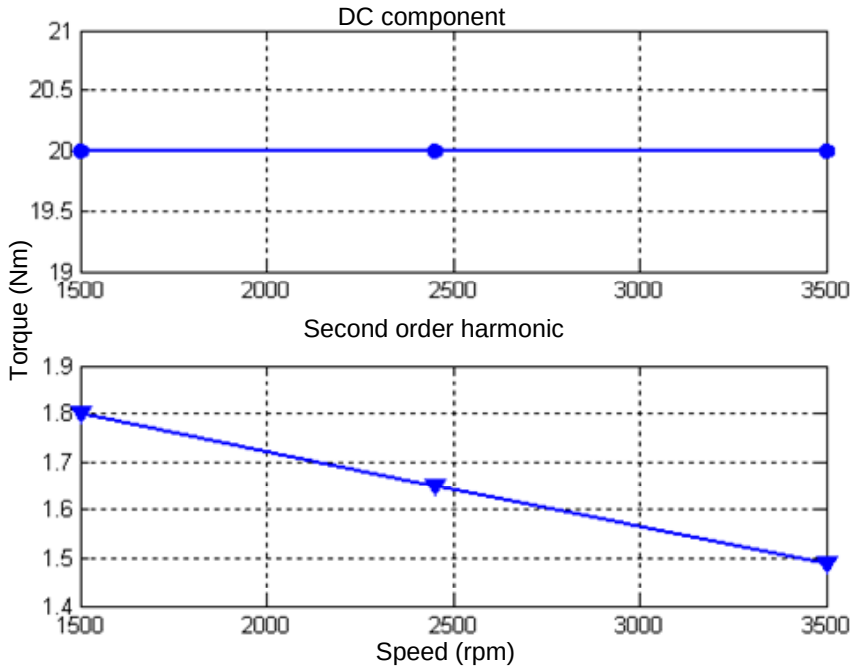

(d) DC component and second-order harmonics in the developed torque

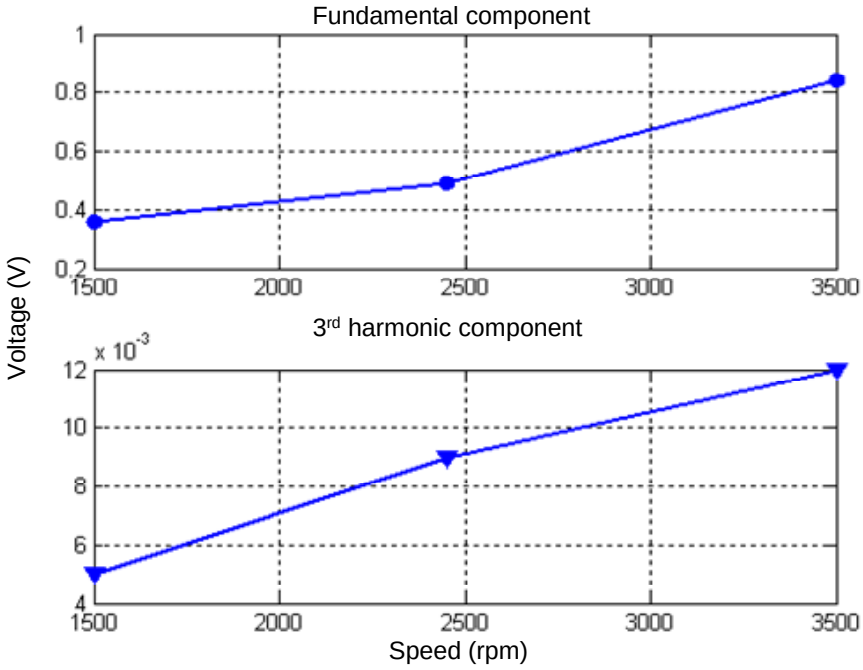

(e) Fundamental component and third-order harmonic in the sum of the line-neutral voltages

Figure 9.5. Effects of rotating speed on the machine variables.

Table 9.3. Summary of the simulation results showing the effects of rotating speed on the machine variables.

Item		Unit	Value		
Rotating Speed		[rpm]	1500	2450	3500
Circulating Current		[A]	1617	1641	1648
Sequence Components in Line-Neutral Voltages	Positive	[V]	35.34	57.42	81.51
	Negative	[V]	1.1	1.66	2.20
	Zero	[V]	0.12	0.20	0.28
Sequence Components in Line Currents	Positive	[A]	64.07	63.71	63.52
	Negative	[A]	2.28	3.25	3.90
Developed Torque	Fund	[Nm]	20	20	20
	2^{nd} Har.	[Nm]	1.80	1.65	1.49
Sum of the Line-Neutral Voltages	Fund	[V]	0.36	0.5	0.84
	3^{rd} Har.	[V]	0.005	0.009	0.012

As shown in Figure 9.5(a), i_f increases as the rotating speed increases. This result agrees with the result in Figure 9.1. However, as explained earlier, the rate of increase of i_f decreases as the rotor speed increases.

As investigated in Chapter 4, the zero sequence voltage resulting from a stator turn fault is proportional to i_f, the fault fraction (μ), and the impedance of the shorted turns. Therefore, the zero sequence voltage increases with increasing rotating speed.

In addition, the simulation results show that the negative sequence voltage and current increase as the rotating speed increases, while the positive sequence current and the second-order harmonic in the developed torque decrease as the rotating speed increases. At first glance, these two phenomena seem to be in conflict, but they are not. In the simulations shown here, the applied load and fault fraction are fixed, but the rotating speed changes. This indicates that the changes in the asymmetry of the machine impedances and rotor-induced voltages are mainly related to the rotating speed. Thus, the negative sequence impedance and the negative sequence rotor-induced voltage

increase as the rotating speed increases, and consequently, the negative sequence voltage and current increase. Furthermore, the increased negative sequence voltage and current produce an increased dc component in the instantaneous power (or developed torque). This can result in a slight decrease in the positive sequence current and consequently, a small decrease in the second-order harmonic in the developed torque that is induced by the interactions between the positive sequence voltage and the negative sequence current.

9.2.3 Effects of Load Level

The simulation conditions for showing the effects of load level on the machine variables of an IPMSM drive with a stator turn fault are summarized in Table 9.4. The corresponding results are presented in Figure 9.6 and summarized in Table 9.5.

Table 9.4. Simulation condition for showing the effects of load level.

Item	Unit	Value
Coils Connection	[-]	Series
Load Torque	[Nm]	0 / 40 /70
Fault Location	[-]	on the *a*-phase
Fault impedance	[ohm]	0 (a bolted turn fault: the effects of the lead wires are ignored)
Fault fraction	[%]	1.04
Rotating speed	[rpm]	1500

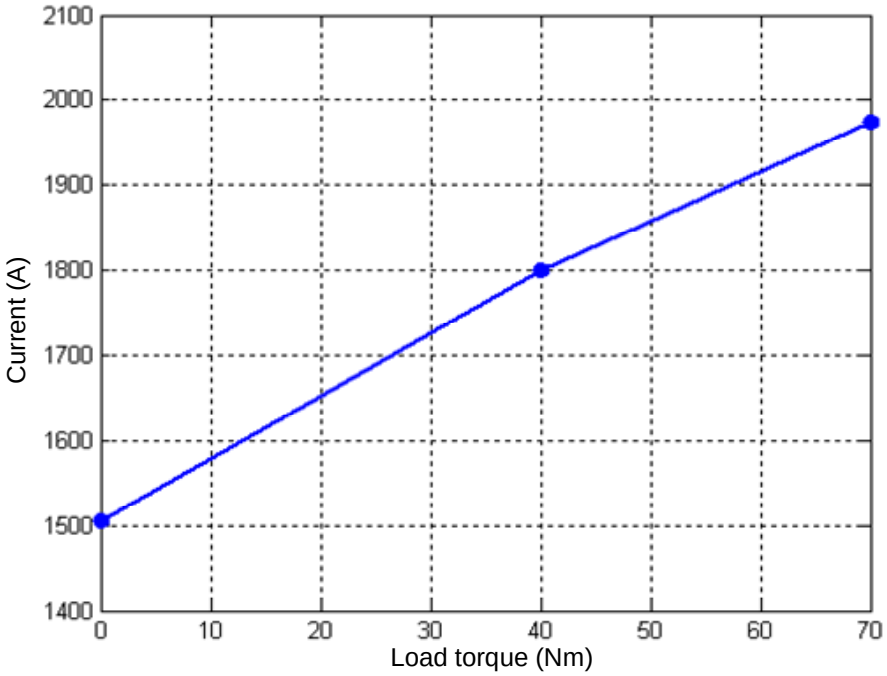

(a) Circulating current

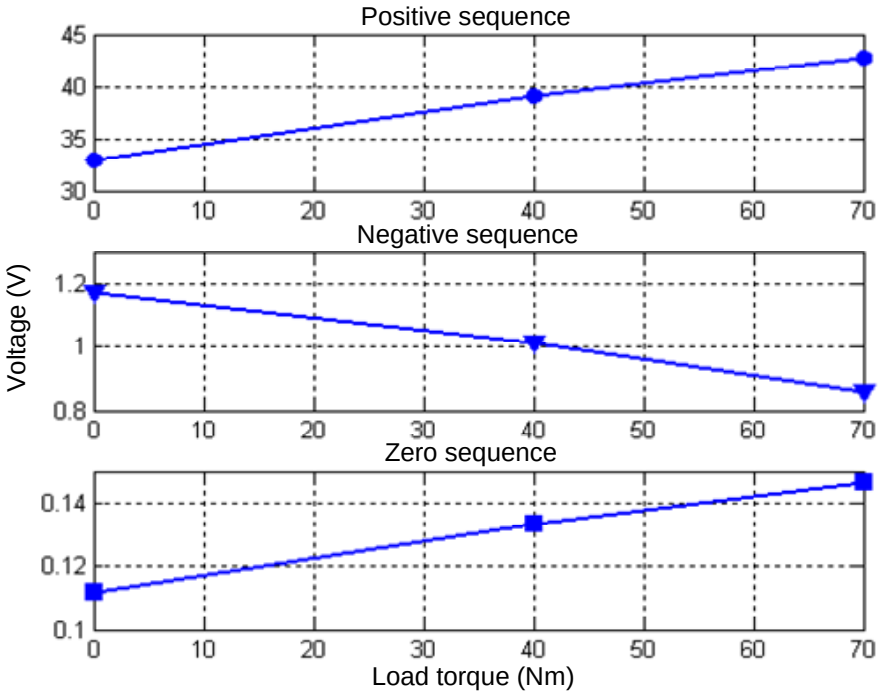

(**b) Sequence components in the line-neutral voltages**

Figure 9.6. Effects of load level on the machine variables.

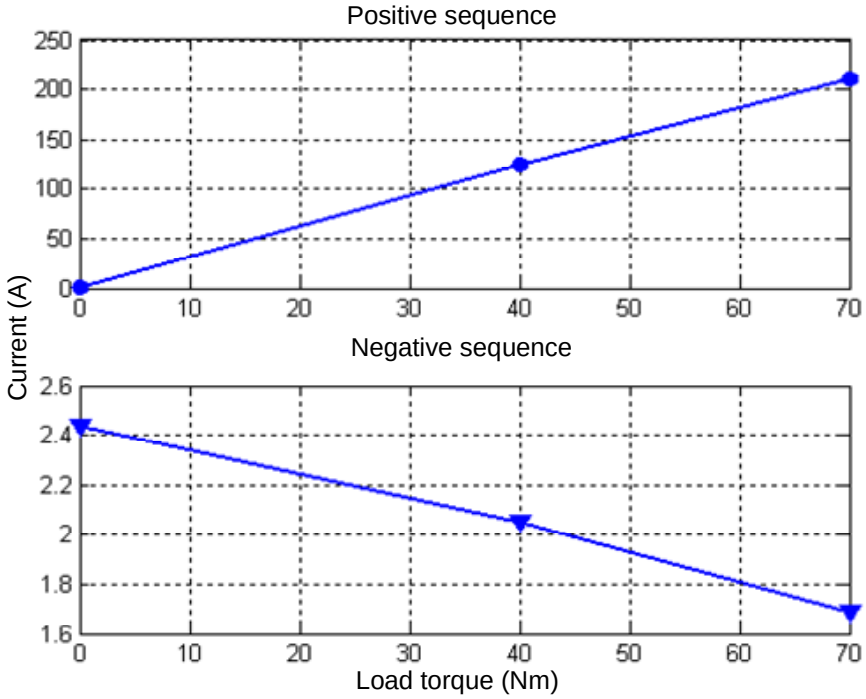

(c) Sequence components in the line currents

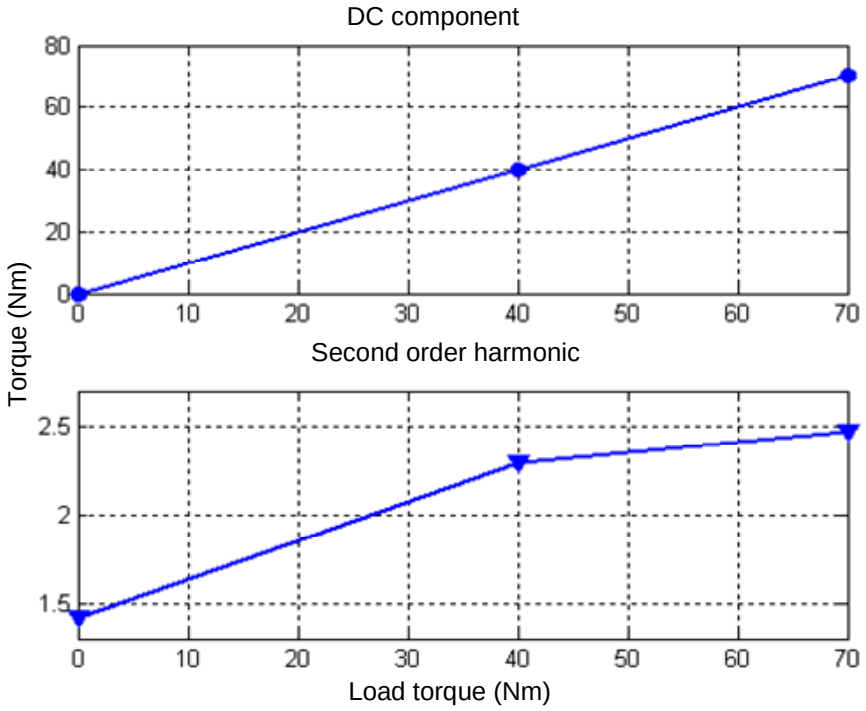

(d) DC component and second-order Harmonic in the developed torque

Figure 9.6. Effects of load level on the machine variables.

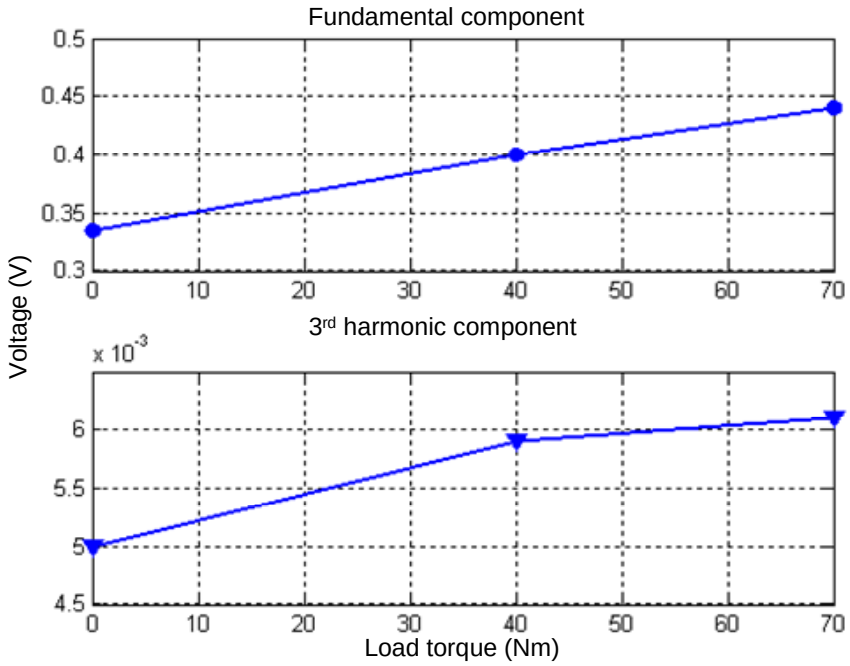

(e) Fundamental component and third-order harmonic in the sum of the line-neutral voltages

Figure9.6. Effects of load level on the machine variables.

Table 9.5. Summary of the simulation results showing the effects of load level on the machine variables.

Item		Unit	Value		
Load Torque		[Nm]	0	40	70
Circulating Current		[A]	1506	1801	1974
Sequence Components in Line-Neutral Voltages	Positive	[V]	32.99	39.16	42.75
	Negative	[V]	1.17	1.01	0.86
	Zero	[V]	0.11	0.13	0.15
Sequence Components in Line Currents	Positive	[A]	1.26	124.4	210.57
	Negative	[A]	2.434	2.05	1.69
Developed Torque	Fund	[Nm]	0	40	70
	2nd Har.	[Nm]	1.42	2.29	2.47
Sum of the Line-Neutral Voltages	Fund	[V]	0.33	0.40	0.44
	3rd Har.	[V]	0.005	0.0059	0.0061

As shown in the simulation results, i_f and the zero sequence voltage increase as the load increases, while the negative sequence voltage and current decrease as the load

increases. As investigated in Chapter 4 and Chapter 7, the amplitude of i_f is nearly proportional to the amplitude of the stator line-neutral voltage. The simulation results clearly show that the stator line-neutral voltage increases as the load increases. Thus, the amplitude of i_f increases as the load increases. In addition, the zero sequence voltage is only proportional to the amplitude of i_f because the rotating speed and fault fraction are fixed.

The magnetizing inductance is strongly affected by magnetic saturation, and decreases with increasing load. In addition, the rotating speed and fault fraction are constant. This implies that the negative sequence voltage is mainly determined by the magnetizing inductances. Consequently, the negative sequence voltage will decrease as the magnetizing inductance decreases. The reduction in negative sequence current can be explained via the same reasoning.

9.2.4 Effects of Fault Fraction

The simulation conditions for showing the effects of fault fraction (μ) on the machine variables of an IPMSM drive with a stator turn fault are defined in Table 9.6. The corresponding results are shown in Figure 9.7 and summarized in Table 9.7.

Table 9.6. Simulation condition for showing the effects of fault fraction.

Item	Unit	Value
Coils Connection	[-]	Series
Load Torque	[Nm]	40
Fault Location	[-]	on the *a*-phase
Fault impedance	[ohm]	0 (a bolted turn fault)
Fault fraction	[%]	0 / 1.04 / 3.13 / 5.21
Rotating speed	[rpm]	1500

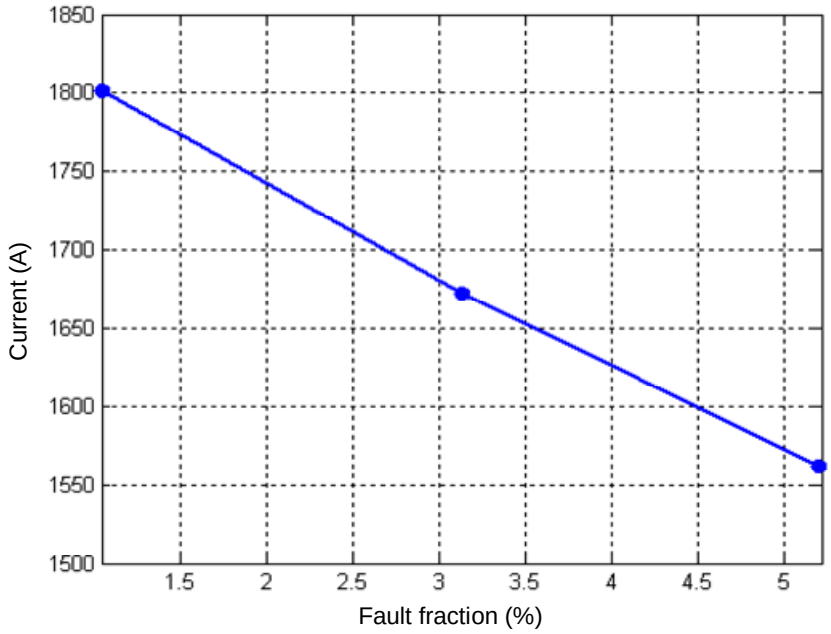

(a) Circulating current

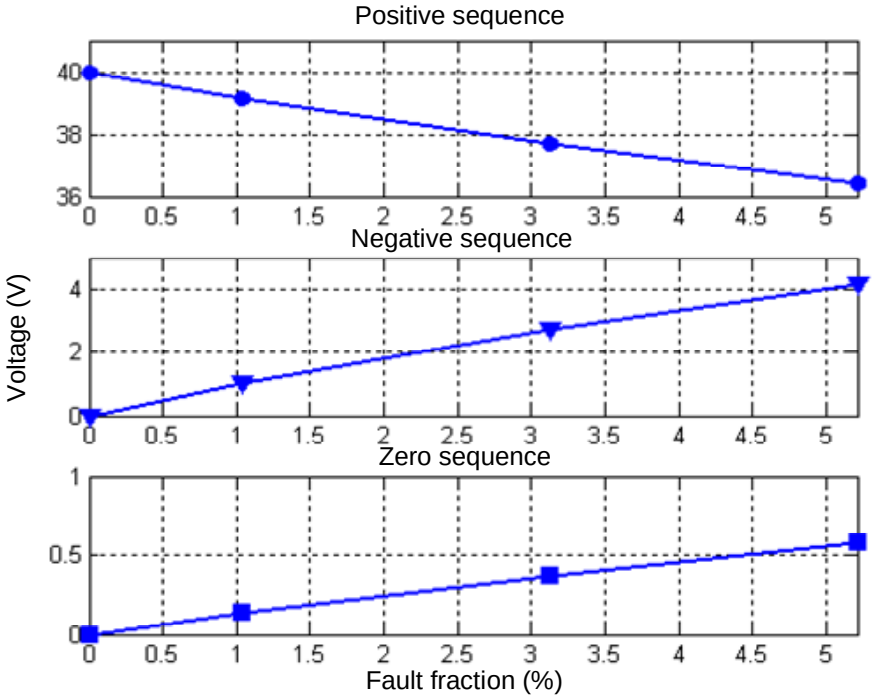

(b) Sequence components in the line-neutral voltages

Figure 9.7. Effects of fault fraction on the machine variables.

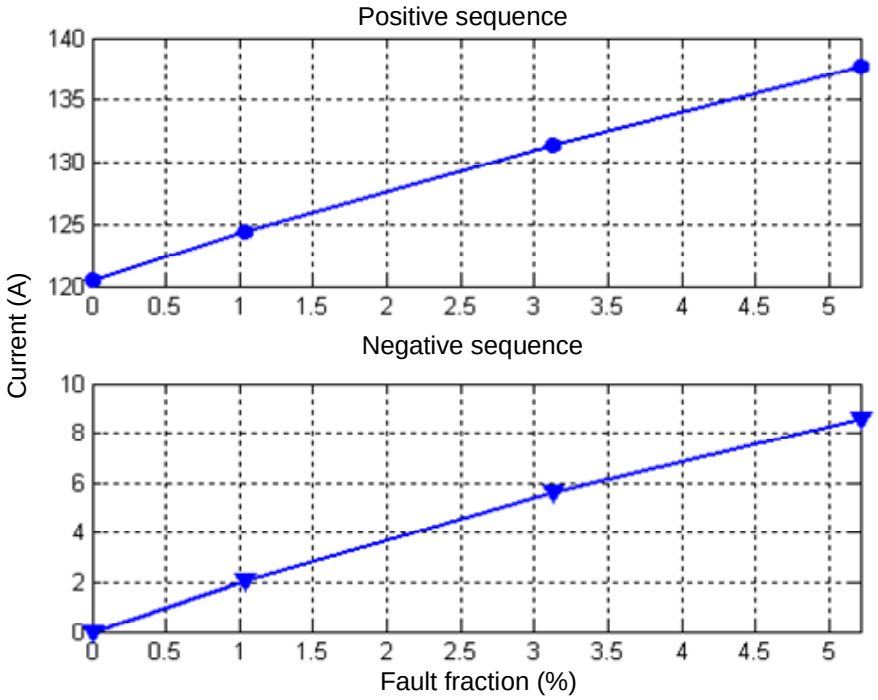

(c) Sequence components in the line currents

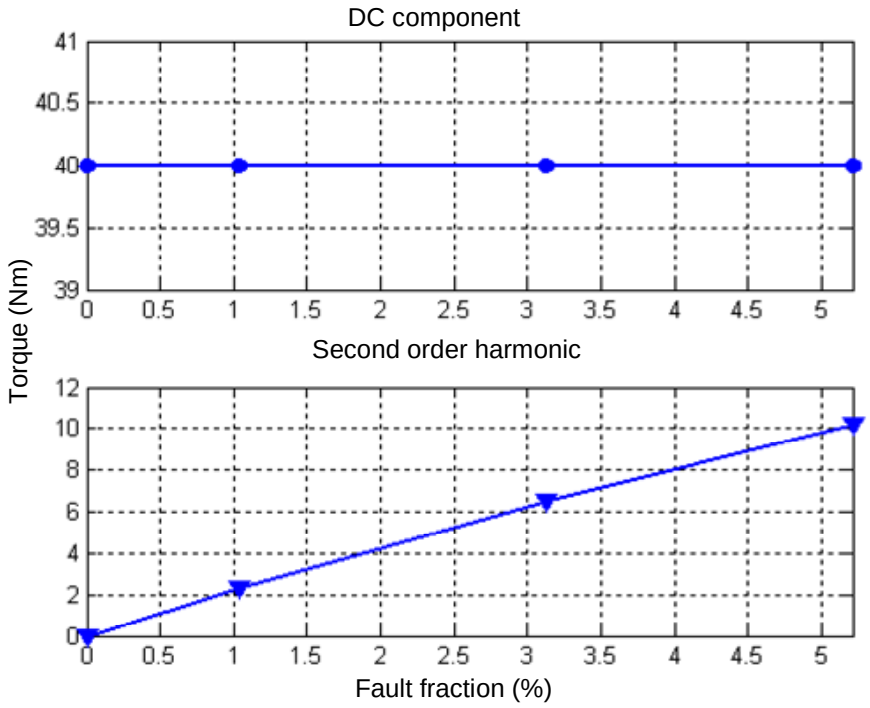

(d) DC component and second-order harmonics in the developed torque

Figure 9.7. Effects of fault fraction on the machine variables.

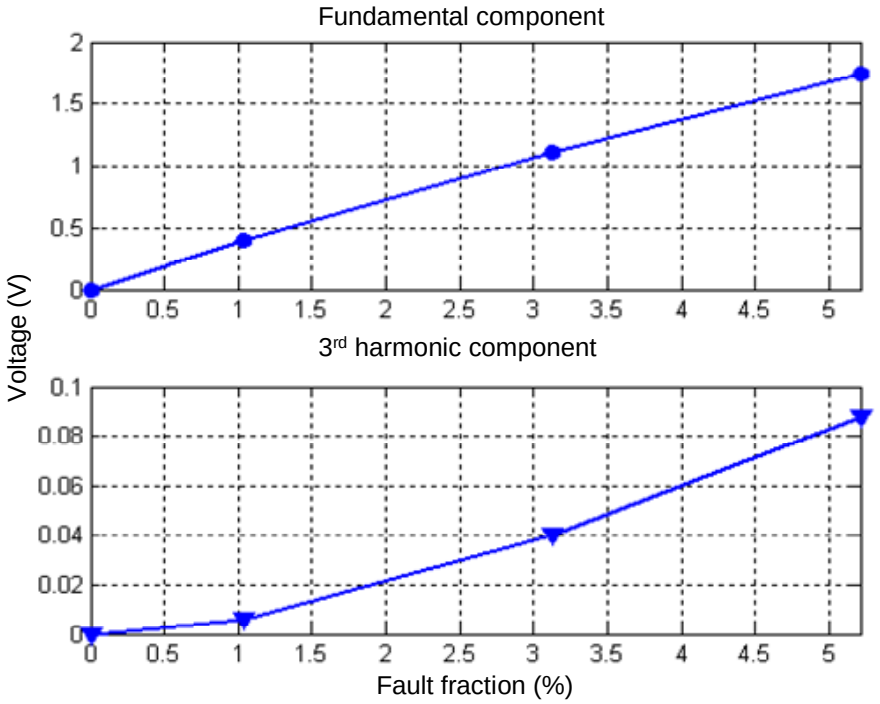

(e) Fundamental component and third-order harmonic in the sum of the line-neutral voltages

Figure 9.7. Effects of fault fraction on the machine variables.

Table 9.7. Summary of the simulation results showing the effects of fault fraction on the machine variables.

Item		Unit	Value		
Fault Fraction		[%]	1.04	3.13	5.21
Circulating Current		[A]	1801	1672	1562
Sequence Components in Line-Neutral Voltages	Positive	[V]	39.16	37.68	36.42
	Negative	[V]	1.01	2.74	4.16
	Zero	[V]	0.13	0.37	0.58
Sequence Components in Line Currents	Positive	[A]	124.4	131.45	137.63
	Negative	[A]	2.05	5.6	8.57
Developed Torque	Fund	[Nm]	40	40	40
	2nd Har.	[Nm]	2.29	6.49	10.19
Sum of the Line-Neutral Voltages	Fund	[V]	0.40	1.12	1.74
	3rd Har.	[V]	0.0059	0.04	0.09

As shown in Table 9.7 and Figure 9.7, the negative sequence current, zero sequence voltage, and double-synchronous frequency components in the power and developed

torque increase as the fault fraction increases. In addition, positive sequence voltage and i_f are decreasing as the fault fraction increases, while the positive sequence current increases. This phenomenon may not be easy to see at first, but is clear after a more intense investigation. The mathematical representation of $|i_f|$ in Chapter 7 shows that $|i_f|$ is not strongly related to the fault fraction (μ), but nearly proportional to the amplitude of the stator-line neutral voltages. In Chapter 6, it was shown that a stator turn fault in a CCVSI-driven IPMSM results in a reduced positive sequence voltage, but it is still much larger than the negative sequence voltage. Thus, the amplitude of the stator line-neutral voltages under a turn fault condition will decrease as the fault gets worse. Consequently, $|i_f|$ also decreases as the fault gets worse.

The mathematical representation of the zero sequence voltage resulting from a stator turn fault is given by (4.15) or (4.22). The equations show that the zero sequence voltage is proportional to the multiplication of the amplitude of i_f and the fault fraction when the rotating speed is constant. The simulation results clearly show that the value of the amplitude of i_f multiplied by the fault fraction, increases as the fault fraction increases. Thus, the zero sequence voltage increases as the fault fraction increases.

As described by (4.11) or (4.19), a stator turn fault introduces an ac torque component related to the value of multiplication of the amplitude of i_f and the fault fraction. Furthermore, this ac torque component decreases the overall developed torque. This implies that more current will be required to maintain a given rotating speed and load as the fault gets worse. This explains why the positive sequence current increases as the fault fraction increases.

9.2.5 Effects of the Experimental Fault Resistance

The effects of the wires used to access two turns inside of the motor are investigated in this section. Figure 9.8 presents the normalized $|i_f|$ at every operating point within rated operations when the resistance of the wires is considered. The other conditions for this simulation are the same as those for the parallel winding in Table 9.1.

As shown in Figure 9.8, even though a small resistance is added to the shorted turns, the amplitude of i_f is reduced significantly. As discussed before, the resistance of the two copper wires acts as the external impedance (R_f), which reduces the circulating current significantly. It can be inferred that other machine variables, which are related to i_f will be slightly different as compared to those under a bolted turn fault condition.

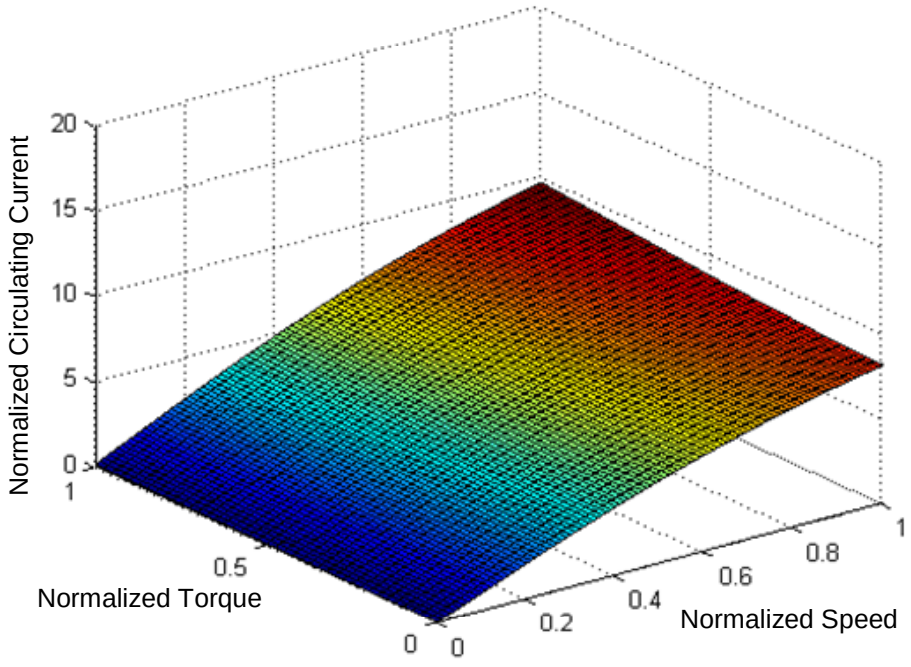

Figure 9.8. Effect of the two copper wires on $|i_f|$ at every operating point within rated operation.

9.3 Experimental Results

Experiments have been performed to show the effects of a stator turn fault on the behaviors of the tested IPMSM drive. Particularly, the experimental results showing the followings are provided:

(1) Open-circuit line-line and tap-tap back-emf voltages at different rotating speeds

(2) The amplitudes of the circulating currents at various rotating speeds

(3) The behaviors of the tested IPMSM drive with and without a stator turn fault

9.3.1 Open-Circuit Line-Line and Tap-Tap Back EMF Voltages at Various Rotating Speeds

The open-circuit line-line (E_{ab}) and tap-tap (E_{Tap}) back emf voltages are measured at three different rotating speeds. The measured waveforms are presented in Figure 9.9. The comparison of the measured data and calculated values is presented in Table 9.8 and Figure 9.10.

Table 9.8. Comparison of the measured and calculated open-circuit line-neutral and tap-tap back emf voltages.

Items	500 rpm	1000 rpm	1500 rpm	Remark
Measured Line-to Line EMF [Vpeak]	20.5	39	60	
Measured Line-Neutral EMF [Vpeak]	11.84	22.52	34.64	$\lvert E_{an}\rvert = \frac{\lvert E_{an}\rvert}{\sqrt{3}}$
Calculated Line-Neutral EMF [Vpeak]	11.37	22.75	34.12	$\lvert E_{an\_cal}\rvert = \omega_e \lambda_{PM}$
Measured Turn-Turn EMF [Vpeak]	0.45	0.82	1.35	
Calculated Turn-Turn EMF [Vpeak]	0.47	0.95	1.42	$\lvert E_{Turn\_cal}\rvert = \frac{\lvert E_{an\_cal}\rvert}{N_{coil}}$

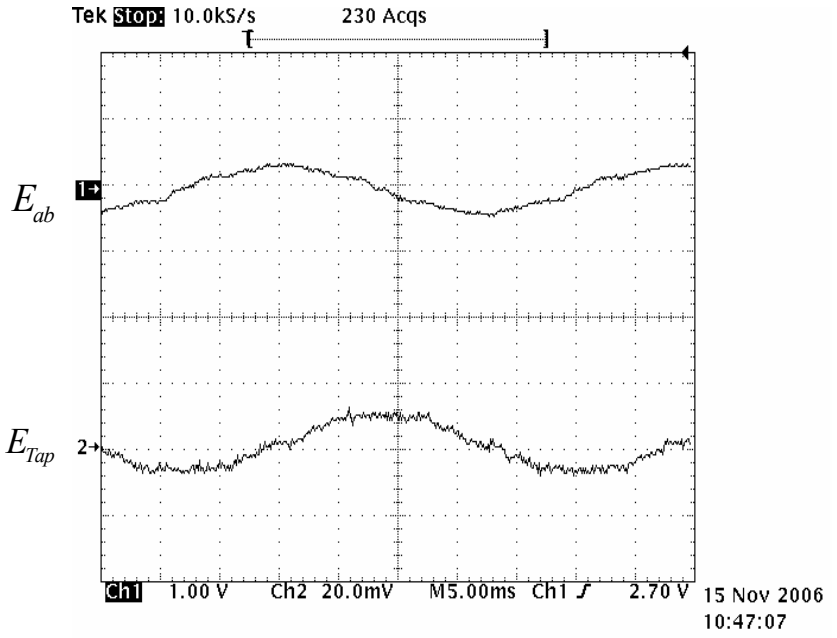

Ch.1: E_{ab} (50 V/div.), Ch. 2: E_{Tap} (1 V/div.), Time (5 ms/div.)

(a) At 500 rpm rotating speed

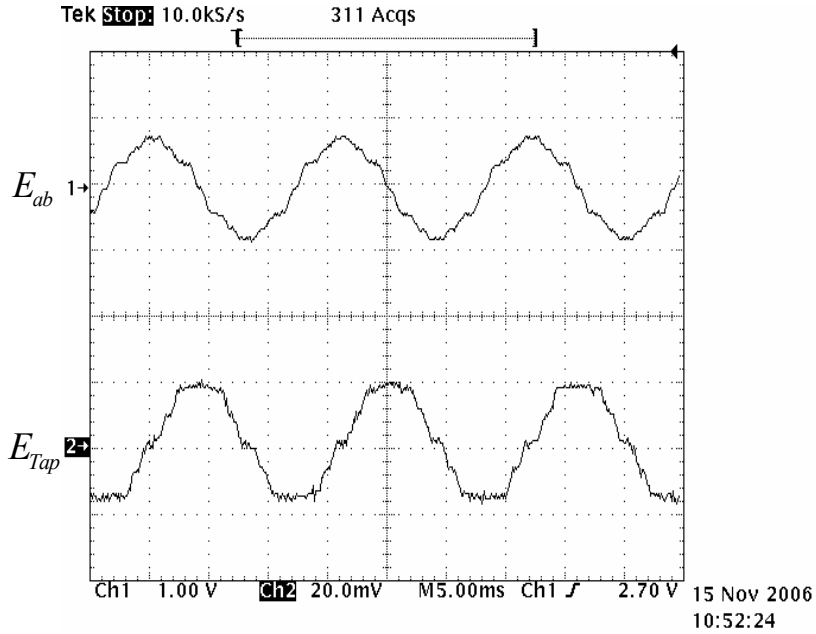

Ch.1: E_{ab} (50 V/div.), Ch. 2: E_{Tap} (1 V/div.), Time (5 ms/div.)

(b) At 1000 rpm rotating speed

Figure 9.9 Measured open-circuit line-line and tap-tap emf voltages at different rotating speeds.

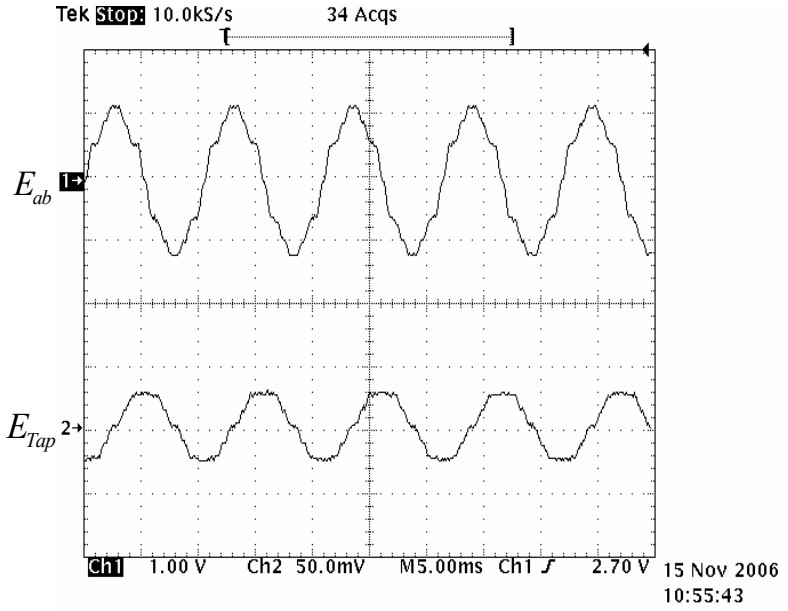

Ch.1: E_{ab} (50 V/div.), Ch. 2: E_{Tap} (2.5 V/div.), Time (5 ms/div)

(c) At 1500 rpm rotating speed

Figure 9.9. Measured open-circuit line-line and tap-tap emf voltages at different rotating speeds.

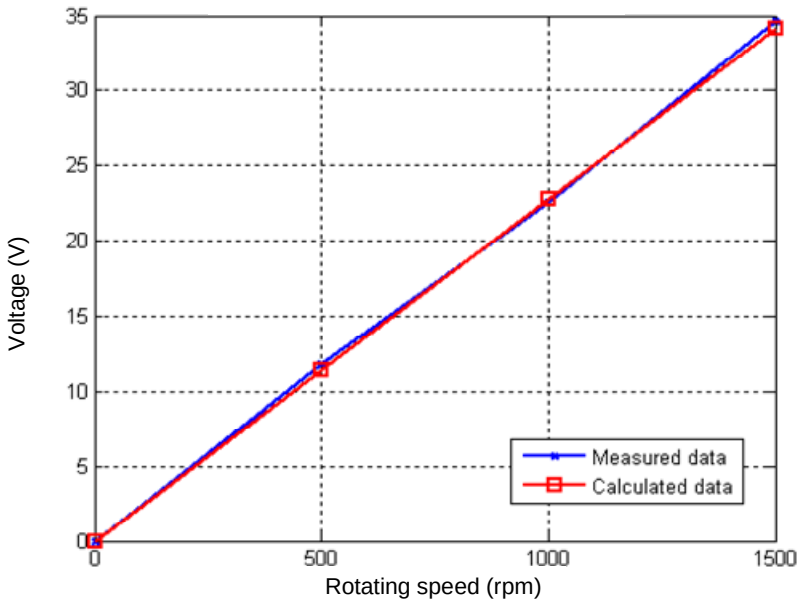

(a) Line-neutral emf voltages

Figure 9.10 Comparison of the measured and calculated open-circuit line-neutral and tap-tap emf voltages at different rotating speeds.

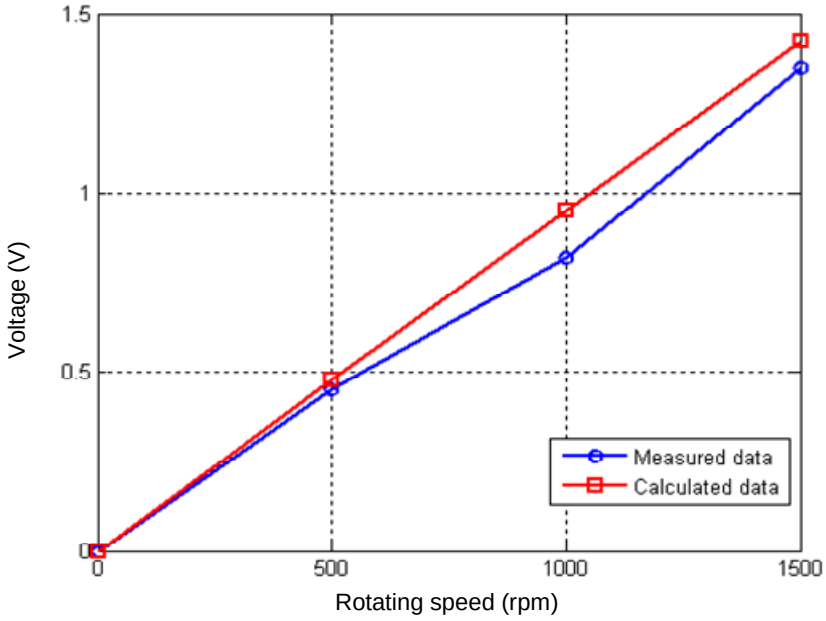

(b) Tap-Tap emf voltages

Figure 9.10 Comparison of the measured and calculated open-circuit line-neutral and tap-tap emf voltages at different rotating speeds.

The measured waveforms show that the line-line and tap-tap emf voltages contain the fifth and seventh space harmonics. Furthermore, the third-order harmonic can be observed in the tap-tap emf voltage. Therefore, the space harmonics affect the waveform of the circulating current. The comparison of the measured and calculated emf voltages confirms that the two taps on two turns in a coil are made properly.

9.3.2 Amplitude of Circulating Current

The circulating current in the shorted turns (i_f) are measured at rotating speed from 100 to 1000 rpm with an interval of 100 rpm at no applied load condition. The waveforms of the *a*-phase and circulating currents at rotating speeds of 500 and 1000 rpm are presented in Figure 9.11. Table 9.9 and Figure 9.12 compare the measured and

simulated $|i_f|$. The experimental results show that the resistance of the two copper wires has a significant effect on $|i_f|$. Furthermore, this external resistance makes the impedance of the shorted turns nearly resistive. Even though the circulating current is significantly reduced, the current at 1000 rpm rotating speed goes up to about four times the rated coil current. The comparison in Figure 9.12 shows that the measured and simulated data have a good agreement with only a small difference. This difference is accounted for by the negligence of the inductance of the two copper wires in the simulation. The comparison in Figure 9.12 also verifies the two basic assumptions of the IPMSM model with turn faults: 1) the circulating current in the shorted turns is proportional to the stator line-neutral voltage and 2) the circulating current is mainly limited by the resistance and leakage inductance of the shorted turns.

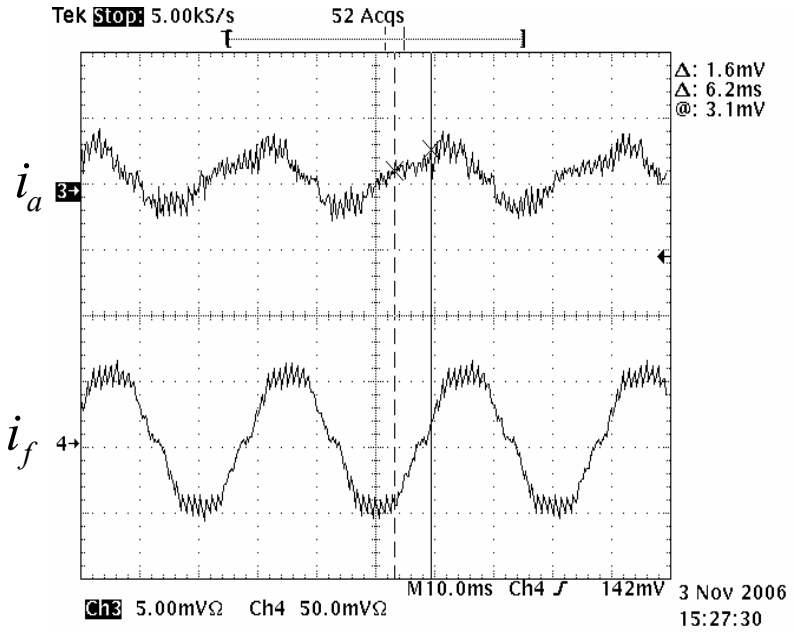

Ch.3: i_a (5 A/div.), Ch. 4: i_f (50 A/div.), Time (10 ms/div)

(a) At 500 rpm rotating speed

Figure 9.11. Measured phase and circulating currents at 500 and 1000 rpm with no applied load.

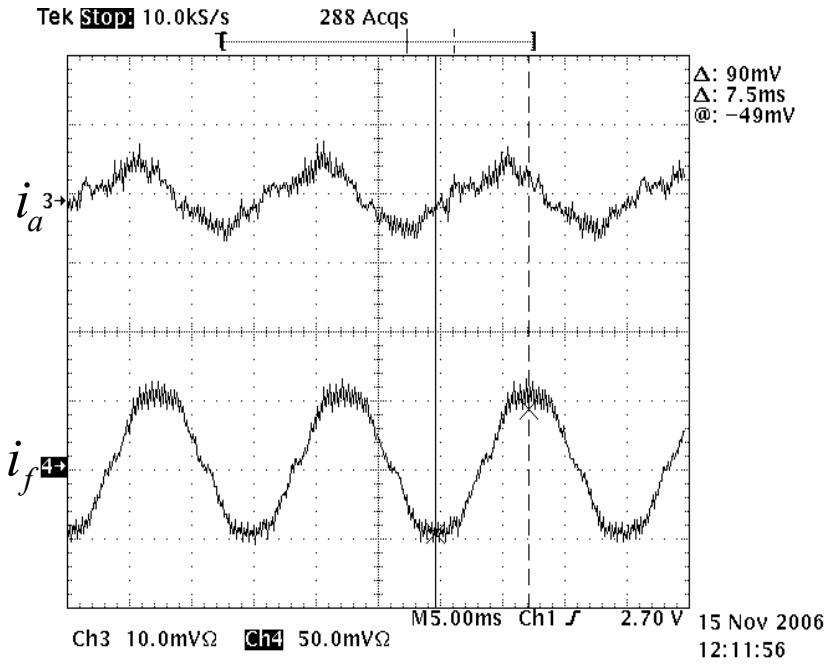

Ch.3: i_a (10 A/div.), Ch. 4: i_f (100 A/div.), Time (5 ms/div)

(b) At 1000 rpm rotating speed

Figure 9.11. Measured phase and circulating currents at 500 and 1000 rpm with no applied load.

Table 9.9. Comparisons of the measured and simulated $|i_f|$ at various rotating speeds with no-applied load.

Speed [rpm]	Amplitude of the Circulating Current			
	Measured		Simulated	
	Peak Value [Apeak]	Per unit Value	Peak Value [Apeak]	Per unit Value
100	11.6	0.39	12.8	0.43
200	22.4	0.75	25.7	0.85
300	32	1.07	38.5	1.28
400	38.4	1.28	51.1	1.70
500	53	1.77	63.6	2.12
600	65.5	2.18	75.8	2.52
700	77	2.57	87.9	2.93
800	85.5	2.85	99.6	3.32
900	96.7	3.22	111	3.70
1000	108	3.60	122	4.07

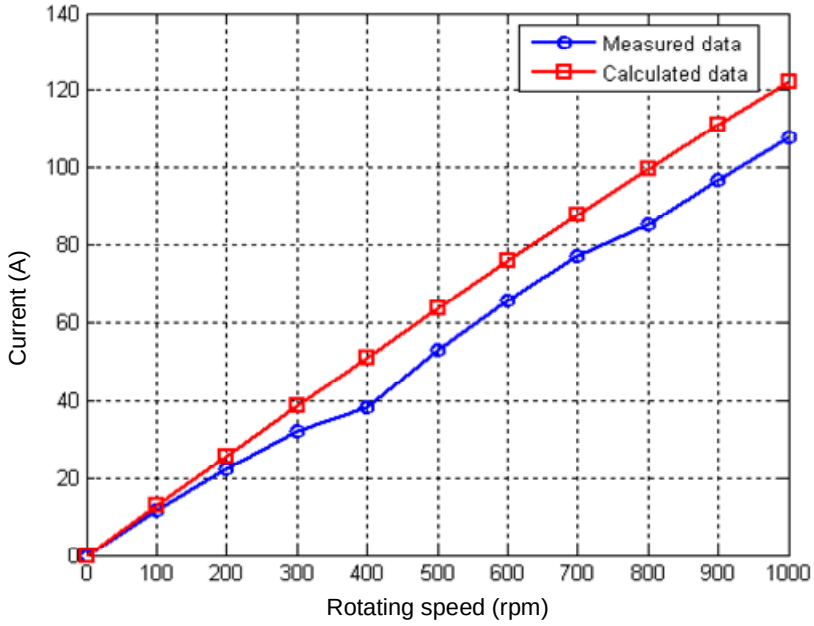

Figure 9.12. Comparison of the measured and simulated $|i_f|$ at various rotating speeds with no applied load.

9.3.3 Behavior of the Tested IPMSM Drive, With and Without a Turn Fault

The experimental conditions for showing the behavior of the tested IPMSM with and without a stator turn fault are summarized in Table 9.10. The corresponding results are presented in Figure 9.13 and Figure 9.14. The data presented in Figure 9.14 are sampled at every 100 ms period, and filtered by a low-pass filter with a cut-off frequency of 2 Hz.

Table 9.10. Experimental conditions for showing the behavior of the tested IPMSM drive with and without a stator turn fault.

Item	Unit	Value
Coils Connection	[-]	Parallel
Load Torque	[Nm]	9
Fault Location	[-]	on a coil in the *b*-phase
Fault impedance	[ohm]	6.54×10^{-3} : 6.54 [mohm]
Fault fraction	[%]	4.17
Rotating speed	[rpm]	500

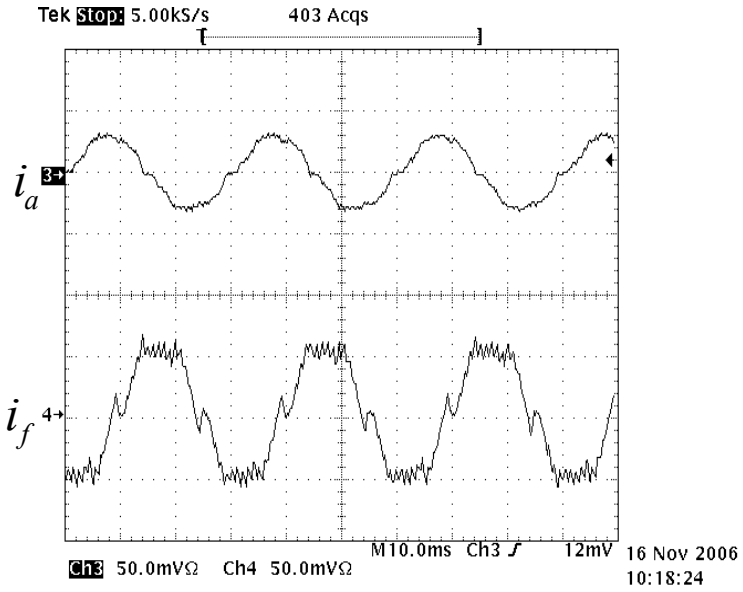

Ch.3: i_a (50 A/div.), Ch. 2: i_f (50 A/div.), Time (10 ms/div)

Figure 9.13. Measured *a*-phase and circulating currents with one turn fault at 500 rpm and 9 Nm load.

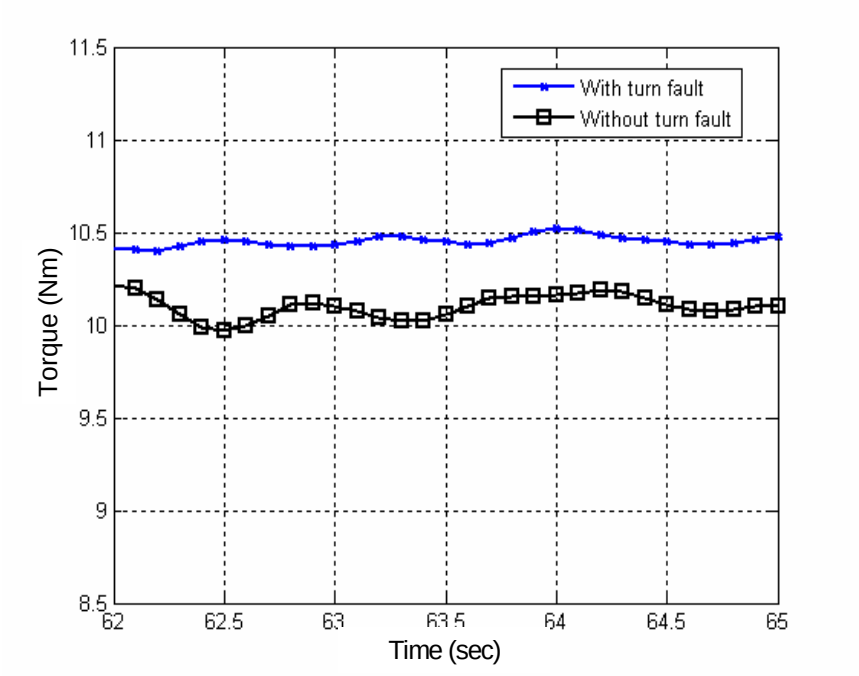

(a) Torque references

Figure 9.14. Comparison of the behaviors of the tested drive with and without one turn fault at 500 rpm rotating speed and 9 Nm load.

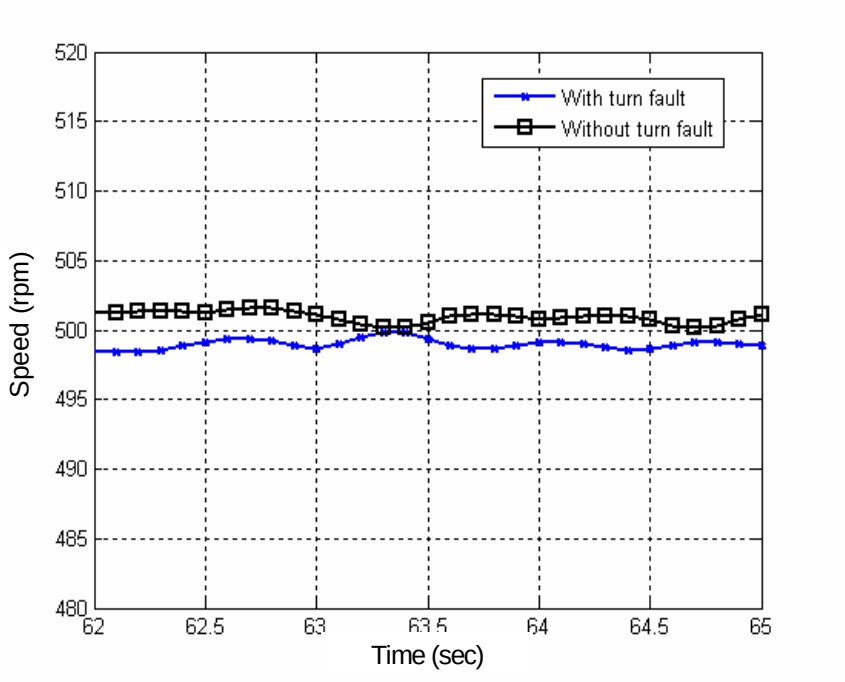

(b) Rotating speeds

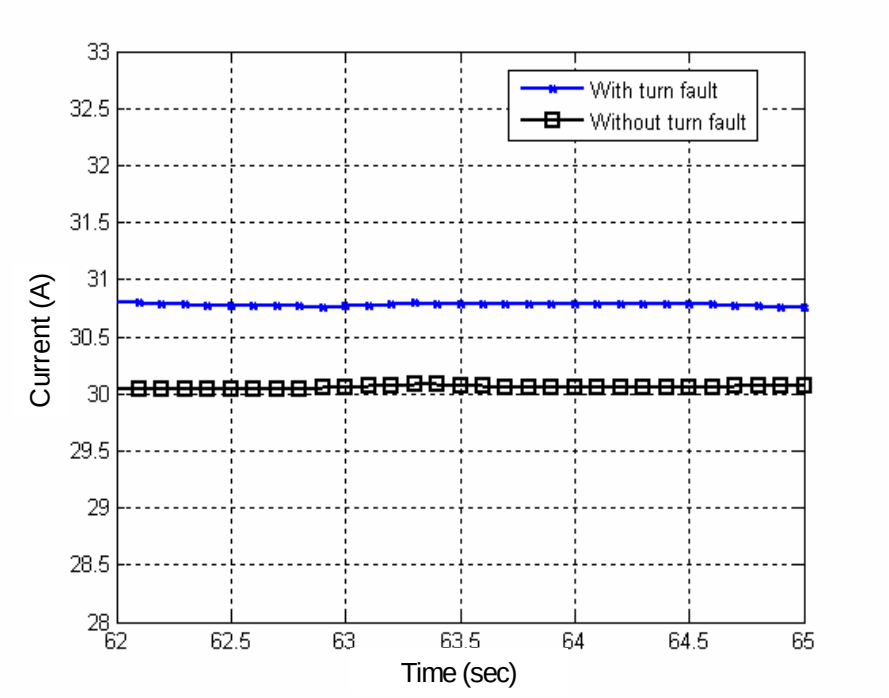

(c) *q*-axis current references

Figure 9.14. Comparison of the behaviors of the tested drive with and without one turn fault at 500 rpm rotating speed and 9 Nm load.

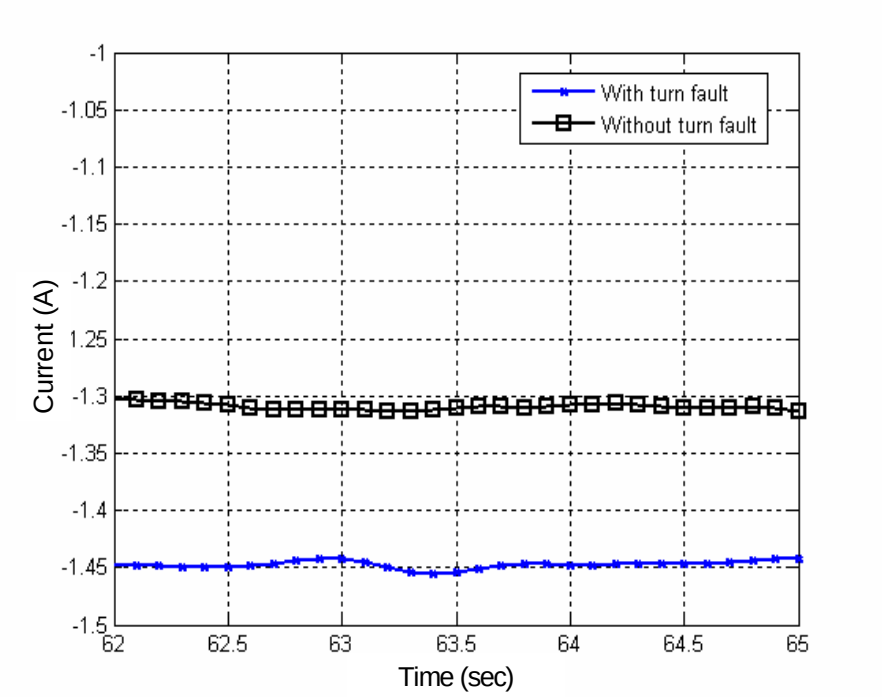

(d) *d*-axis current references

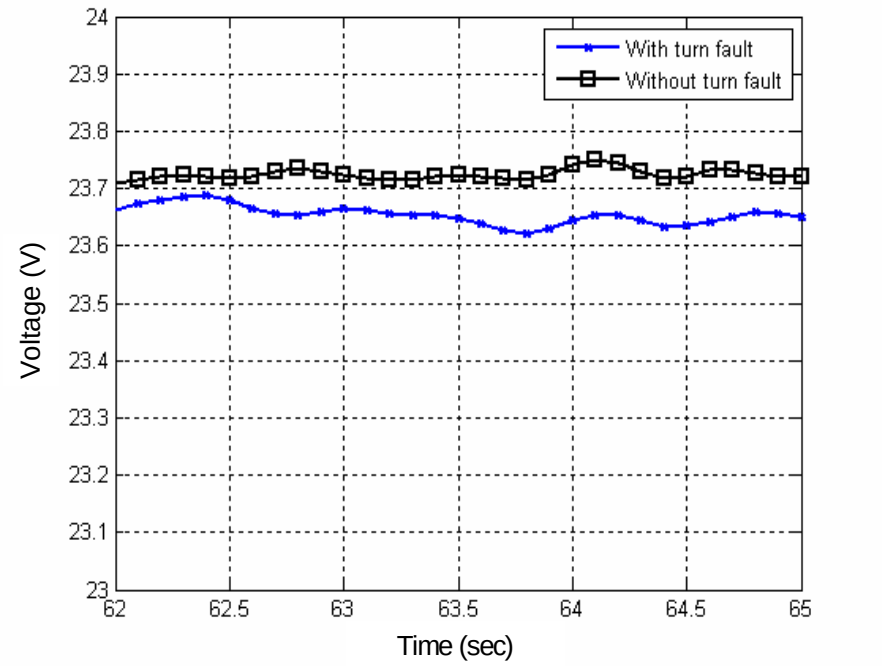

(e) *q*-axis voltage references

Figure 9.14. Comparison of the behaviors of the tested drive with and without one turn fault at 500 rpm rotating speed and 9 Nm load.

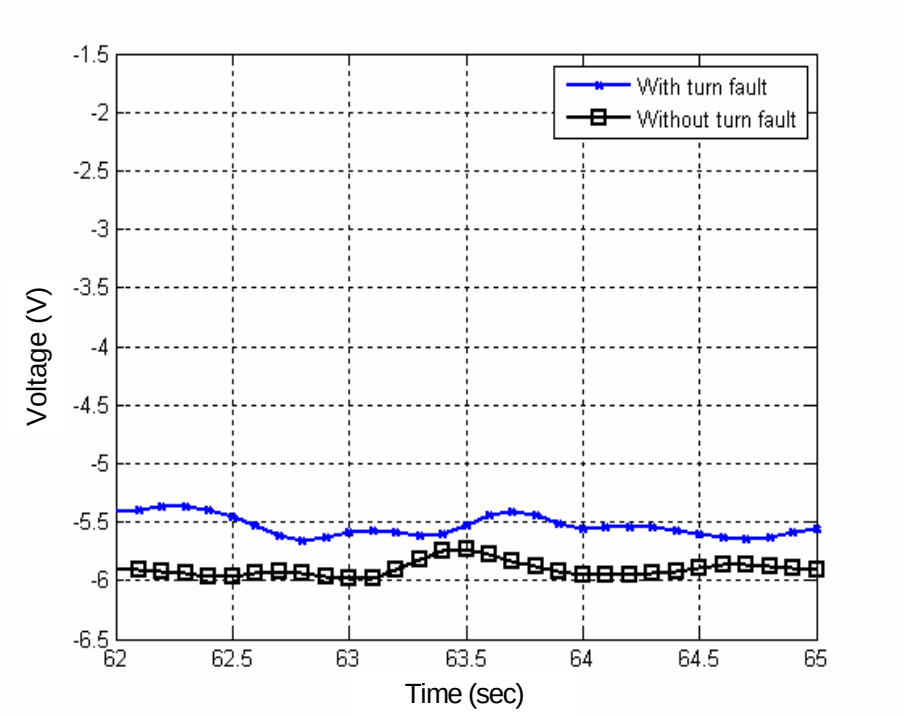

(f) *d*-axis voltage references

Figure 9.14. Comparison of the behaviors of the tested drive with and without one turn fault at 500 rpm rotating speed and 9 Nm load.

The experimental result in Figure 9.13 shows that the circulating current at the given operating condition has almost the same amplitude as that at the same rotating speed but no load condition. Even though the applied load levels are different, the amplitudes of the stator line-neutral voltages at the two operating conditions s are not quite different because the difference in the applied loads is not large enough to make a significant difference in the stator line-neutral voltages.

Figure 9.14(a) shows that the torque reference under the stator turn fault condition is slightly increased when compared to that for the fault-free IPMSM. This is explained by the fact that the torque component, generated from the circulating current, acts against the developed torque. Thus, it can be inferred that the difference in the torque references

between a turn fault and fault-free conditions will increase as the circulating current increases, or the turn fault gets worse.

In addition, the experimental results in Figure 9.14(e) and (f) show that the stator turn fault results in reductions in the amplitudes of the *q*-and *d*-axis voltage references when compared to those for the fault-free IPMSM even though the turn fault increases the amplitudes of the *q*-and *d*-axis current references. This phenomenon is well recognized, and provides the basis of the turn fault detection method proposed in this work. A more detailed discussion on this phenomenon is provided in Chapter 11. However, it should be pointed out that the differences in the machine variables between a stator turn fault and fault-free conditions will be more clearly observed when the machine has a bolted turn fault.

9.4 Chapter Summary

In this chapter, the proposed simulation model of an IPMSM with stator turn fault has been validated by the simulation and experimental results. Furthermore, the behavior of an IPMSM drive with stator turn fault has been thoroughly investigated with simulations and experiments under various operating conditions. Several noticeable phenomena, which have not been fully investigated in previous research, have been observed and analyzed. The phenomena are summarized as follows:

(1) A stator turn fault induces a large circulating current (i_f), whose amplitude ($|i_f|$) is strongly related to the rotating speed and load level, while the fault fraction (μ) has very little effect on $|i_f|$ [59]. However, a closer look at the

simulation and experimental results show that that $|i_f|$ is nearly proportional to the amplitude of the stator line-neutral voltage. It is also observed that i_f is mainly limited by the resistance and leakage inductance of the shorted turns [59].

(2) The circulating current in the shorted turns (i_f) generates a torque component that opposes the developed torque of the machine. Therefore, for a given rotating speed and applied load, the presence of a turn fault results in an increased torque reference when compared to that for a healthy machine.

(3) The circulating current in the shorted turns (i_f) generates a magnetic flux that acts against the air-gap magnetic flux. When a small number of turns are shorted, the additional flux is not large enough to demagnetize the permanent magnets. On the contrary, when a large number of turns are involved in a stator turn fault, the additional flux resulting from the turn fault can demagnetize the permanent magnets, and consequently, can result in an irreversible damage to the machine.

(4) In a CCVSI-driven application, the drive tries to control the variables to follow their reference values. This implies that the degrees of the asymmetries in the machine variables resulting from a stator turn fault will be reflected in different manners from those in a mains-fed application. Furthermore, the degrees of the asymmetries will be strongly affected by the configuration of the controllers, such as type, bandwidth, and so on [32], [36].

(5) The presence of controller actions of a drive reduces the unbalance in the phase (or line) currents. This means that the controller actions try to maintain evenly

distributed phase currents of a series winding machine even when the machine has a stator turn fault. However, in the case of a parallel winding machine, the controller actions cannot prevent unevenly distributed coil currents in the faulty winding. Therefore, the faulty coil current is generally larger than the currents in the healthy coils. For this reason, the faulty coil will experience more thermal stresses not only by the circulating current, but also by the increased coil current.

As verified in this chapter, the developed simulation model describes accurately the behavior of an IPMSM drive with stator turn fault. Thus, the developed model provides a powerful tool to investigate the characteristics of a stator turn fault in an IPMSM drive. Moreover, the developed model can be also used as a reliable test bench for the evaluation of any method for turn fault diagnosis or fault-tolerant operating strategy. Thus, the developed model can prevent a possible large toll in terms of cost and time that can be caused by a minor deficiency in the method.

CHAPTER 10

VERIFICATION OF THE THERMAL MODEL OF AN IPMSM WITH STATOR TURN FAULTS

10.1 Overview

Lumped-parameter thermal models of an IPMSM with and without stator turn faults were proposed in Chapter 5. The verifications of the proposed models are carried out through simulations and experiments in this chapter.

10.2 Verification of the Thermal Model without a Turn Fault

The schematic of the lumped-parameter thermal model of a fault-free IPMSM is shown again in Figure 10.1. The thermal model of the tested IPMSM under fault-free conditions is identified in the following section.

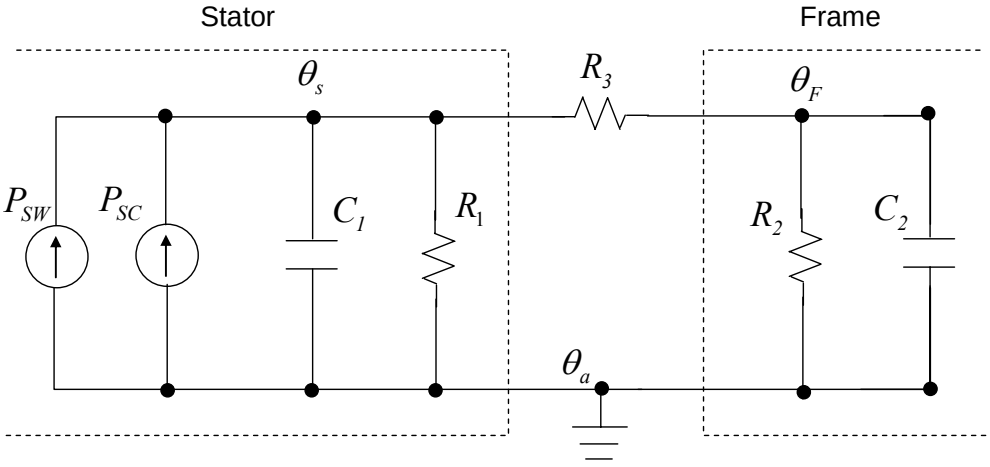

Figure 10.1. Schematic of the simplified thermal model of a fault-free IPMSM.

10.2.1 Identification of the Thermal Model under Fault-Free Conditions

To identify the thermal parameters, the temperature rises above the ambient temperature at the stator winding and frame (θ_S and θ_F) are measured at three different operating conditions. The test conditions and measured data are summarized in Table 10.1.

The dimensions of the frame of the tested motor are given in Table 10.2. The tested motor does not have any forced cooling system (fan or water jacket). Thus, the heat transfer to the ambient is mainly related to natural heat convection.

The identification of the thermal parameters is performed according to the procedure discussed in Section 5.4. The identified thermal parameters are summarized in Table 10.3.

Table 10.1. Summary of the test conditions and measured data for identifying the thermal model of the tested IPMSM under fault-free conditions.

Item	Unit	Operation 1	Operation 2	Operation 3
Rotating Speed	[rpm]	500	500	1000
Load	[Nm]	0	9	0
q-axis Current	[A]	2.5	25.4	3.0
d-axis Current	[A]	-0.1	-1.05	-0.1
Stator Copper Loss (Steady-State)	[W]	0.048	5.034	0.072
Fundamental Flux Linkage	[Wb]	0.0543	0.0555	0.0543
Temperature Rise at the Stator (Steady-State)	[$^\circ C$]	9.9	13.0	20.1
Temperature Rise at the Frame (Steady-State)	[$^\circ C$]	7.8	9.2	15.8

Table 10.2. Dimensions of the frame of the tested motor.

Item	Unit	Specification
Material of Frame	[-]	A6061-T6 (Aluminum)
Density of Frame Material	$[kg/m^3]$	2700
Specific Heat of Frame Material	$[J/kg/^\circ C]$	637.83
Length of Frame Body	$[mm]$	167
Outer / Inner Radii of Frame Body	$[mm]$	110 / 93.5
Length of Front Cap	$[mm]$	5
Outer / Inner Radii of Front Cap	$[m]$	110 / 1.75
Length of End Cap	$[m]$	10
Outer / Inner Radii of End Cap	$[m]$	110 / 1.75
Heat Transfer Coefficient	[-]	10

Table 10.3. Identified parameters of the thermal model under fault-free conditions.

Item	Symbol	Unit	Value
Hysteresis Loss Coefficient	k_h	$[W/Wb^2/(rad/\sec)]$	27.614
Eddy-Current Loss Coefficient	k_e	$[W/Wb^2/(rad/\sec)^2]$	0.0028
Thermal Resistance of the Stator	R_1	$[^\circ C/W]$	2.933
Thermal Capacitance of the Stator	C_1	$[J/^\circ C]$	5250
Thermal Resistance of the Frame	R_2	$[^\circ C/W]$	0.522
Thermal Capacitance of the Frame	C_2	$[J/^\circ C]$	3990
Contact Thermal Resistance between the Stator and Frame	R_3	$[^\circ C/W]$	0.176

The thermal model of the tested IPMSM under fault-free conditions is implemented in Matlab Simulink™ using the thermal parameters shown in Table 10.3. The measured and simulated θ_S and θ_F at the three different operating conditions are compared in Figure 10.2.

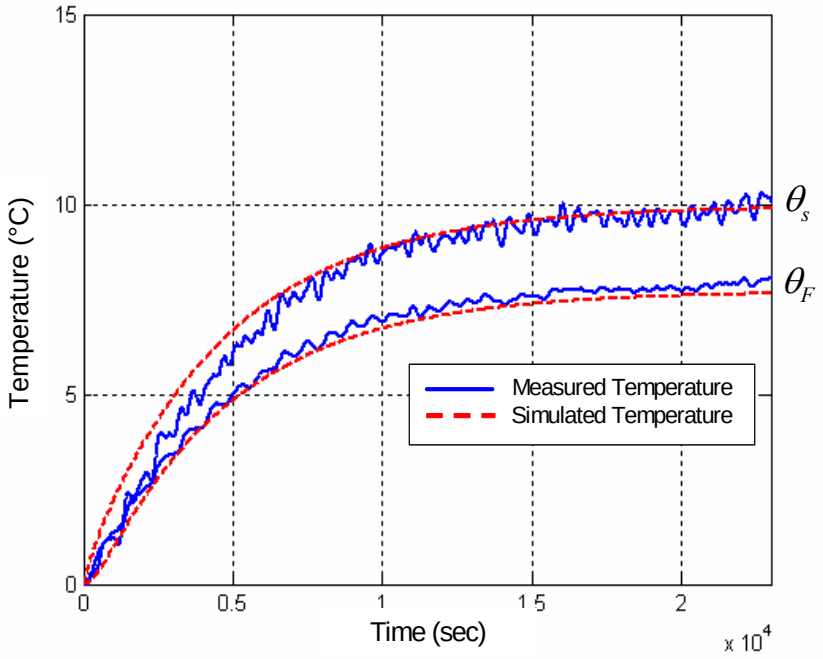

(a) At 500 rpm rotating speed and no load

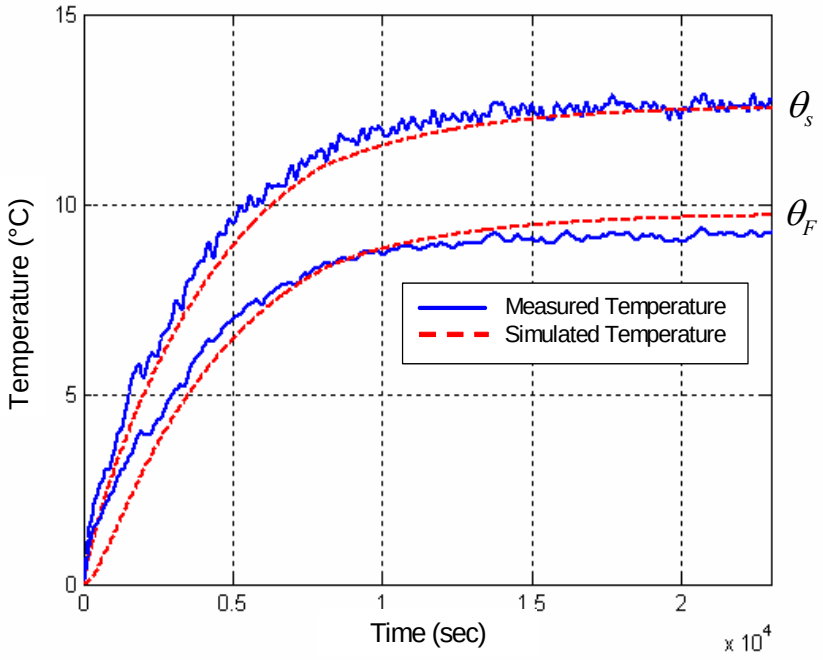

(b) At 500 rpm rotating speed and 9 Nm load

Figure 10.2. Measured and simulated θ_S and θ_F at the three different operating conditions.

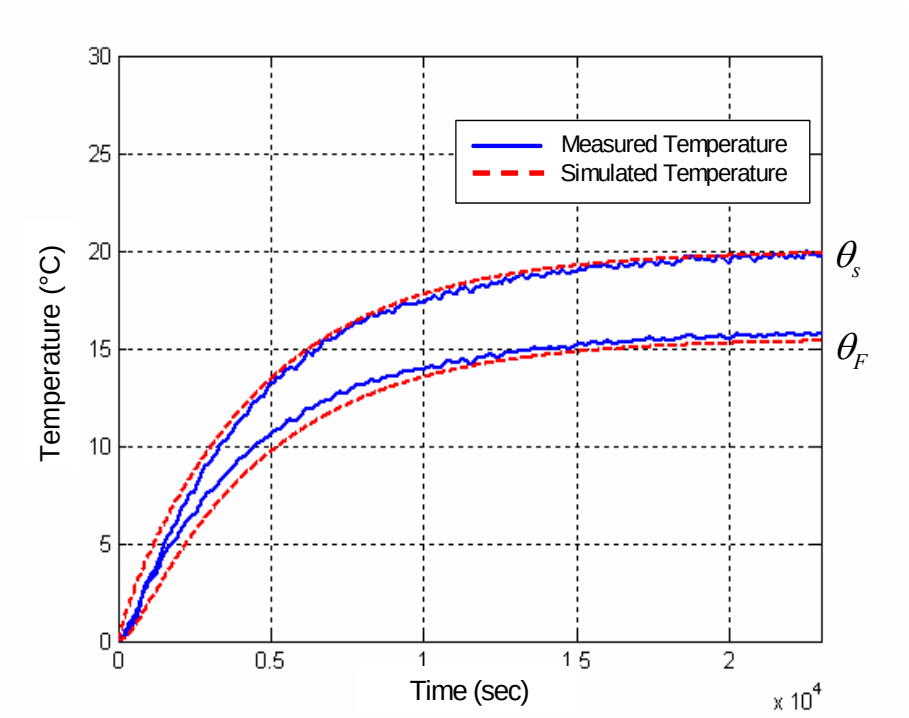

(c) At 1000 rpm rotating speed and no load

Figure 10.2. Measured and simulated θ_S and θ_F at the three different operating conditions.

10.2.2 Estimation of the Stator and Frame Temperature Rises

In the previous section, the thermal model of the tested IPMSM under fault-free conditions was identified. And the simulated θ_S and θ_F are compared with the measured data in Figure 10.2. In this section, the derived thermal model is validated by comparing the measured and estimated θ_S and θ_F at another operating condition. Table 10.4 summarizes the test conditions and estimated power losses. Figure 10.3 shows the corresponding results. The estimated values of θ_S and θ_F have a discrepancy of less than one $^{\circ}C$ when compared to the measured data.

Table 10.4. Summary of the test conditions and estimated power losses for validating the derived thermal model.

Item	Unit	Value
Rotating Speed	[rpm]	1000
Load	[Nm]	10
q-axis Current	[A]	32.6
d-axis Current	[A]	-1.8
Stator RMS Current	[Arms]	23.09
Hysteresis Loss	[W]	35.99
Eddy-Current Loss	[W]	1.53

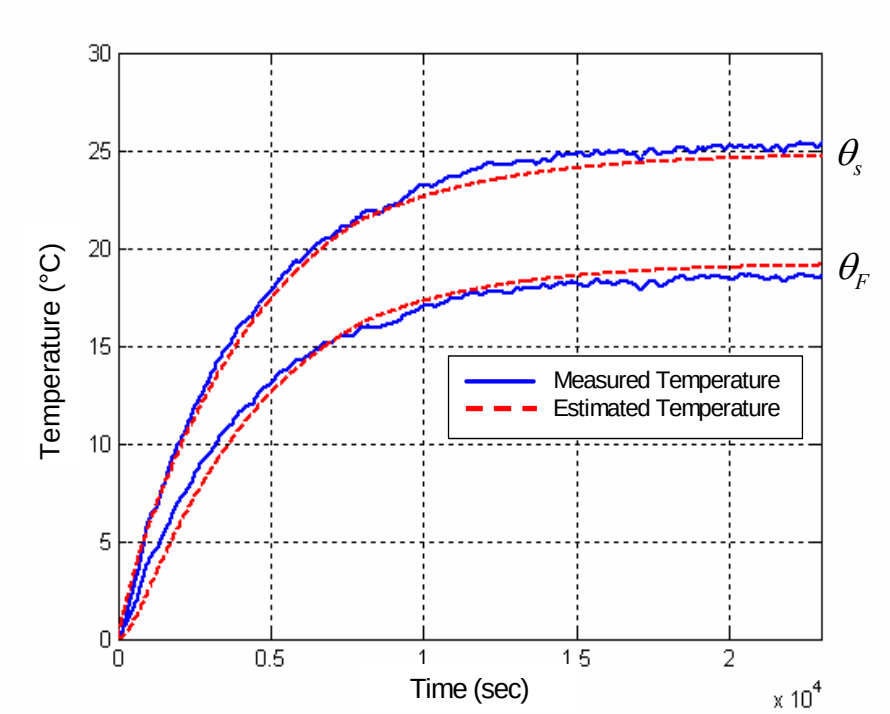

Figure 10.3. Measured and estimated θ_S and θ_F at 1000 rpm rotating speed and 10 Nm load.

10.3 Verification of the Thermal Model with Turn Faults

The schematic of the lumped-parameter thermal model of an IPMSM with a stator turn fault is given again in Figure 10.4.

10.3.1 Identification of the Thermal Model with a Turn Fault

To identify the thermal parameters, the temperature rises above the ambient temperature at the shorted turns, adjacent turns, healthy turns, and frame (θ_T, θ_A, θ_H and θ_F) are measured under three different operating conditions. The test conditions and measured data are summarized in Table 10.5. As indicated in Table 10.5, the circulating currents in the shorted turns are conversant to the steady-state values that are smaller than the initial values. This is due to the increase of the resistance of the shorted turns with increasing temperature. To identify the thermal parameters, the procedure proposed in Section 5.5 is adapted. The contact thermal resistance, R_{TA}, at each test operation is calculated by (5.32), and the average value of the three calculated values is used as the final value of R_{TA}. The same method is applied for determining the contact thermal resistance, R_{AH}. The identified thermal parameters are summarized in Table 10.6. Using the identified parameters, the thermal model of the tested IPMSM with a turn fault is defined. Comparisons of the measured and simulated temperature rises at the three different operating conditions are presented in Figure 10.5.

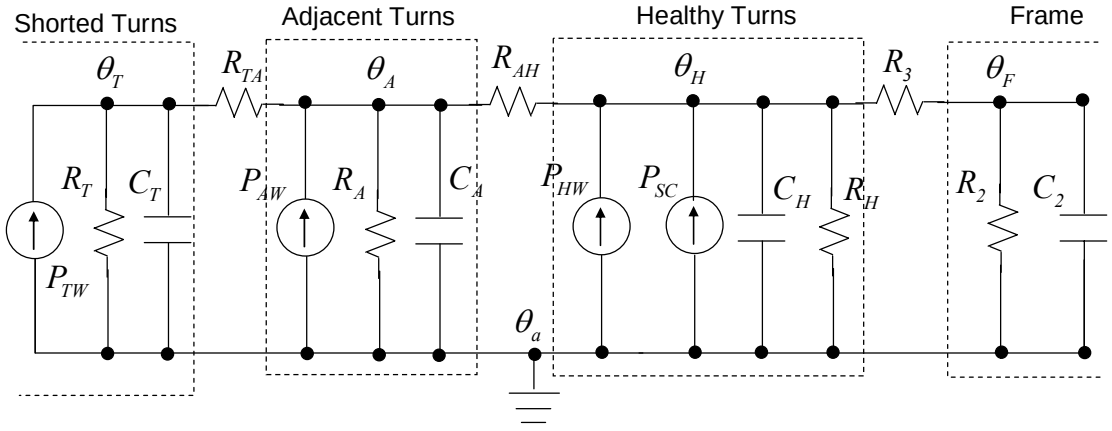

Figure 10.4. Schematic of the simplified thermal model of an IPMSM with a turn fault.

Table 10.5. Summary of the test conditions and measured data for identifying the thermal model of the tested IPMSM with a stator turn fault.

Item	Unit	Operation 1	Operation 2	Operation 3
Rotating Speed	[rpm]	500	500	1000
Load	[Nm]	0	9	0
Number of Coils per Phase (Parallel Winding)	[-]	4	4	4
Number of Turns per Coil	[-]	24	24	24
Number of the Shorted Turns (Fault Fraction)	[-]	1 (4.17 %)	1 (4.17 %)	1 (4.17 %)
Fault Impedance	[mohm]	6.54	6.54	6.54
Number of the Adjacent Turns	[-]	4	4	4
Circulating Current (Initial / Final)	[A]	53 / 50	58 / 56	108 / 100
q-axis Current	[A]	3.2	27.5	4.2
d-axis Current	[A]	-0.1	-1.14	-0.1
Coil Current (RMS)	[Arms]	0.566	4.87	0.743
Estimated Stator Core Losses	[W]	17.41	18.12	35.57
Temperature Rise at the Shorted Turns (Steady-State)	[$^{\circ}C$]	13.3	19.0	36.8
Temperature Rise at the Adjacent Turns (Steady-State)	[$^{\circ}C$]	12.7	18.4	34.2
Temperature Rise at the Other Healthy Turns (Steady-State)	[$^{\circ}C$]	10.5	14.2	22.2
Frame Temperature Rise (Steady-State)	[$^{\circ}C$]	8.4	10.0	16.7

Table 10.6. Identified parameters of the thermal model of the tested IPMSM with a turn fault.

Item	Symbol	Unit	Value
Thermal Resistance of the Shorted Turns	R_T	$[^\circ C/W]$	844.81
Thermal Capacitance of the Shorted Turns	C_T	$[J/^\circ C]$	18.23
Contact Thermal Resistance between the Shored and Adjacent Turns	R_{TA}	$[^\circ C/W]$	0.5565
Thermal Resistance of the Adjacent Turns	R_A	$[^\circ C/W]$	211.2
Thermal Capacitance of the Adjacent Turns	C_A	$[J/^\circ C]$	72.92
Contact Thermal Resistance between the Adjacent and other Healthy Turns	R_{AH}	$[^\circ C/W]$	2.77
Thermal Resistance of the Other Healthy Turns	R_H	$[^\circ C/W]$	2.99
Thermal Capacitance of the Other Healthy Turns	C_H	$[J/^\circ C]$	5158.9
Thermal Resistance of the Frame	R_2	$[^\circ C/W]$	0.522
Thermal Capacitance of the Frame	C_2	$[J/^\circ C]$	3990
Contact Thermal Resistance between the Stator and Frame	R_3	$[^\circ C/W]$	0.176

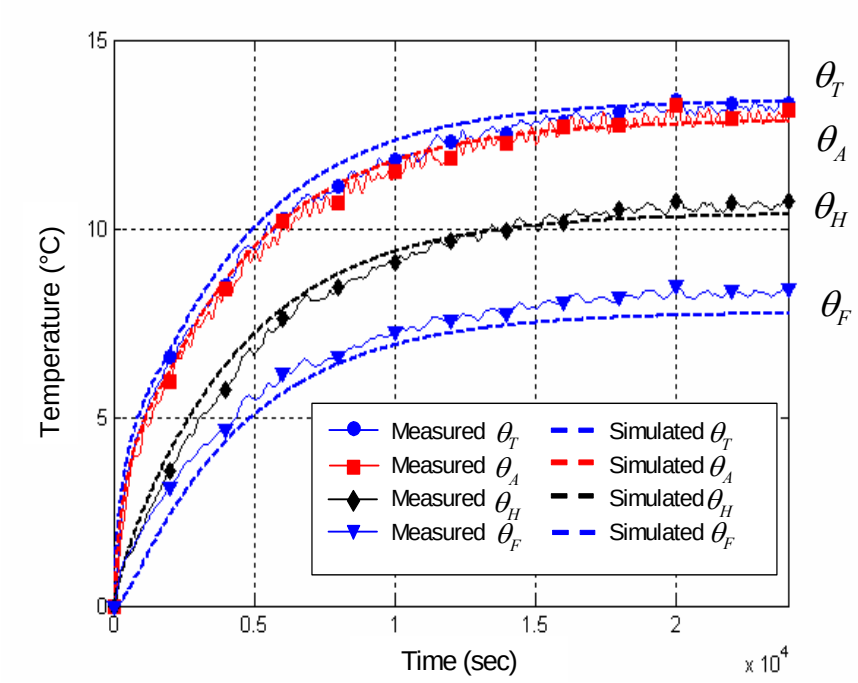

(a) At 500 rpm rotating speed and no load

Figure 10.5. Measured and simulated θ_T, θ_A, θ_H and θ_F at the three different operating conditions.

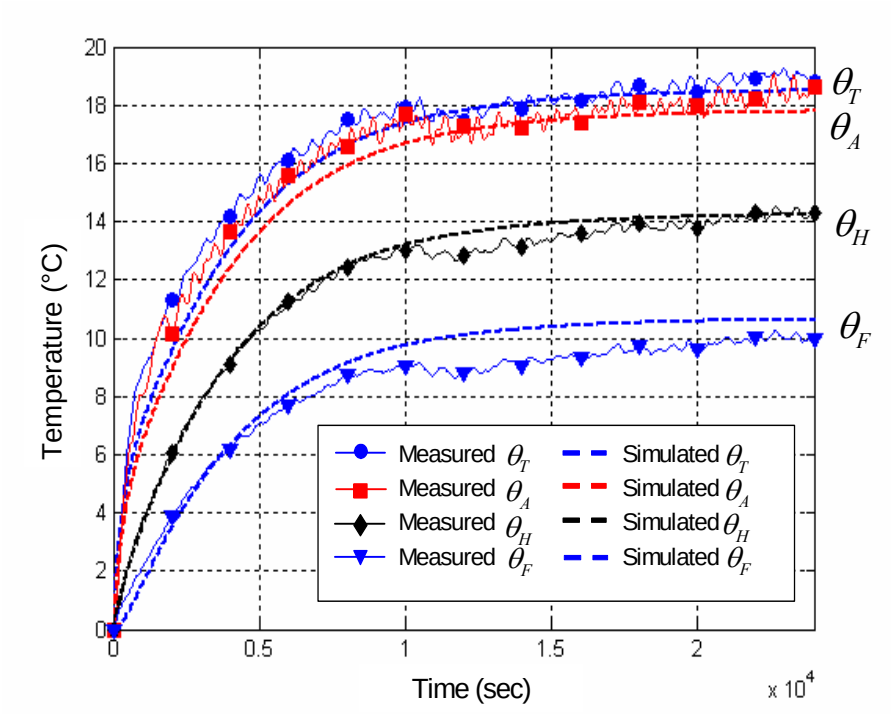

(b) At 500 rpm rotating speed and 9 Nm load

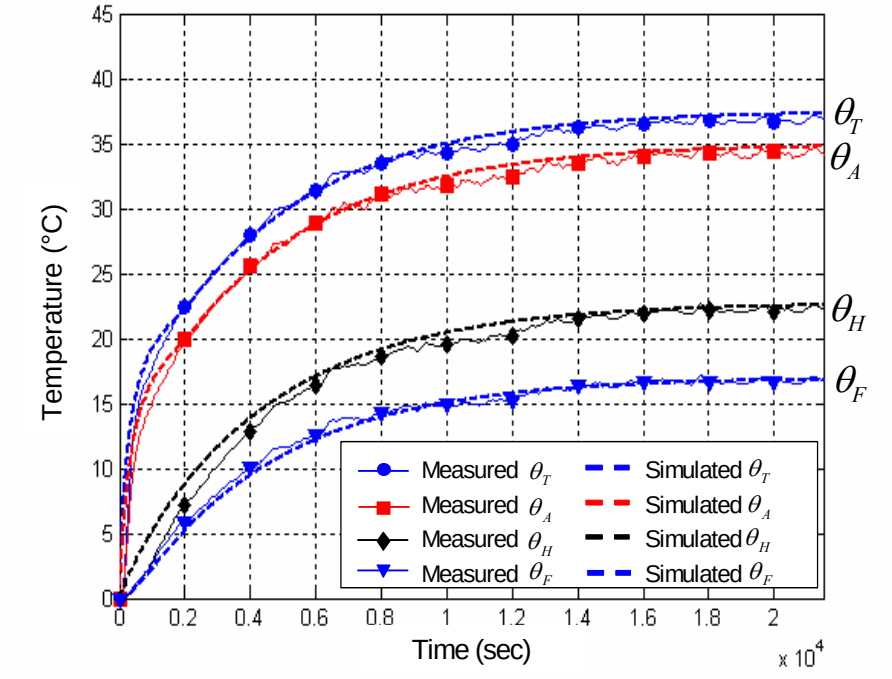

(c) At 1000 rpm rotating speed and no load

Figure 10.5. Measured and simulated θ_T, θ_A, θ_H and θ_F at the three different operating conditions.

10.3.2 Estimation of Temperature Rises

The temperature estimation performance of the implemented thermal model is validated by comparing the measured and estimated θ_T, θ_A, θ_H and θ_F at yet another operating condition. Table 10.7 summarizes the operating condition and the corresponding measured data. The corresponding results are presented in Figure 10.6. It should be noted that the turn fault conditions are identical to those in the previous tests.

Table 10.7. Test conditions for validating the derived thermal model with turn faults.

Item	Unit	Value
Rotating Speed	[rpm]	1000
Load	[Nm]	9
Circulating Current (Initial / Final)	[A]	110 / 97
q-axis Current	[A]	27.2
d-axis Current	[A]	-1.13
Coil Current (RMS)	[Arms]	4.81
Estimated Stator Core Losses	[W]	36.96

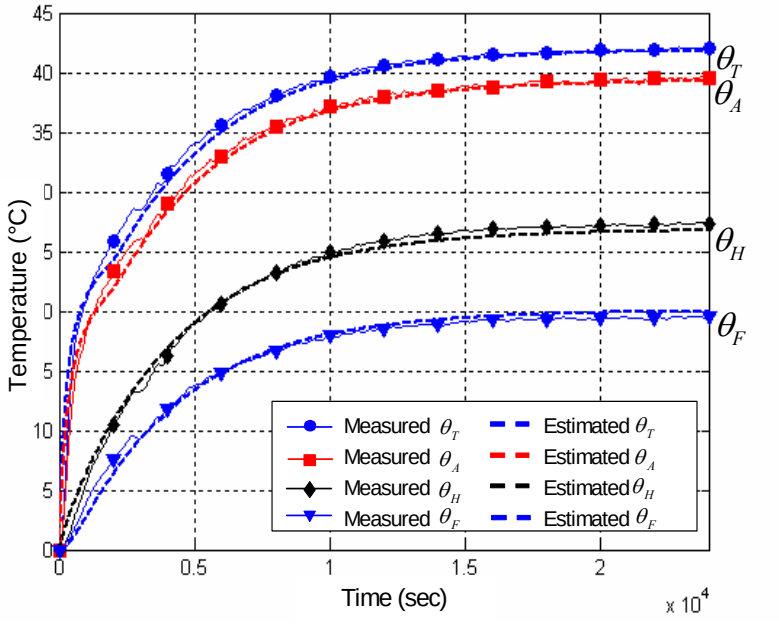

Figure 10.6. Measured and estimated θ_T, θ_A, θ_H and θ_F at 1000 rpm rotating speed and 9 Nm load with a turn fault.

As shown in Figure 10.6, the estimated and measured θ_T, θ_A, θ_H and θ_F have a quite good agreement with a difference of less than one $^\circ C$. This means that it is possible to investigate the thermal behavior of a stator turn fault under various operating conditions.

10.4 Estimation of Temperature Rises under Bolted Turn Fault Conditions

In the previous section, a thermal model of the tested IPMSM with stator turn faults was implemented. The performance of the model was verified by the simulation and experimental results. However, the turn fault in the tests is not a real bolted turn fault due to the resistance of the two external copper wires. In this section, the propagation speed of a bolted turn fault to the adjacent turns is estimated at three different operating conditions, summarized in Table 10.8. Operation 1 and 2 are selected to show the effect of rotating speed, and operation 2 and 3 are selected for investigating the effects of load level.

Table 10.8. Simulation conditions for estimating the propagation speed of a bolted turn fault.

Item	Unit	Operation 1	Operation 2	Operation 3
Control Method	[-]	MTPA	MTPA	MTPA
Rotating Speed	[rpm]	500	1000	1000
Load	[Nm]	0	0	40
Number of the Shorted Turns (Fault Fraction)	[-]	1 (4.17 %)	1 (4.17 %)	1 (4.17 %)
Fault Impedance	[mohm]	0	0	0
q-axis Current	[A]	0	0	119.43
d-axis Current	[A]	0	0	-17.07
Coil Current (RMS)	[Arms]	0	0	21.33
Estimated Stator Core Losses	[W]	17.42	35.56	49.31

10.4.1.1 RMS Current Flowing through the Shorted Turns

As discussed in Section 5.5.1, the rms value of the current flowing through the shorted turn should be determined to estimate the copper loss in the shorted turns accurately. For this, the phase angle difference between the circulating current and coil current should be considered. The actual current flowing through the shorted turns is defined by (5.21), and the circulating current in the shorted turns can be determined by (5.22). For convenience, these two equations are shown again as,

$$i_T = i_{coil} - i_f , \tag{10.1}$$

$$i_f \approx \frac{\mu v_{as}}{\mu\{mR_s(\theta_T + \theta_a) + j\omega_e[mL_{ls} + \mu(L_1 - 3L_2)]\}} , \tag{10.2}$$

where i_{coil} represents the coil current.

It can be inferred from (10.2) that i_f is almost in phase with the stator line-neutral voltage when the leakage reactance is much smaller than the stator winding resistance. In operating an IPMSM, the stator current is controlled so that the current is almost in phase with the stator voltage for MTPA operation although the voltage is slightly leading the current. It can be easily seen that these two conditions are satisfied in the tests performed in the previous section. Thus, the phase angle difference between i_f and i_{coil} can be safely ignored when the rms value of i_T is determined in the test performed in the previous section.

However, under a real bolted turn fault condition, ignoring the phase angle difference between i_f and i_{coil} can yield a somewhat large error in estimating the copper

loss in the shorted turns. The amplitudes of i_f and i_{coil} can be easily determined by (10.2) and (5.20), respectively. Assuming the voltage drop at the stator winding resistance is negligible, then the phase angle of the stator voltage vector ($\tilde{v}_s^e$) in the synchronously rotating reference frame is approximated using (7.6) as,

$$\alpha_{v_s} = \tan^{-1}\left(-\frac{v_{ds}^e}{v_{qs}^e}\right) = \tan^{-1}\left(\frac{L_q i_{qs}^e}{L_d i_{ds}^e + \lambda_{PM}}\right). \tag{10.3}$$

In a similar manner, the phase angle of the stator current vector ($\tilde{i}_s^e$) in the synchronously rotating reference frame is obtained as,

$$\alpha_{i_s} = \tan^{-1}\left(-\frac{i_{ds}^e}{i_{qs}^e}\right). \tag{10.4}$$

From (10.3) and (10.4), the relative phase angle of $\tilde{i}_s^e$ referred to that of $\tilde{v}_s^e$, can be obtained as,

$$\alpha_{i_s - v_s} = \alpha_{i_s} - \alpha_{v_s}. \tag{10.5}$$

However, it should be noted that the phase angle difference in (10.5) will be the same as that of the voltage and current in the same phase winding.

From (10.2), the relative phase angle of i_f referred to v_{as} can be approximated as,

$$\alpha_{i_f - v_{as}} = -\tan^{-1}\left(\frac{\omega_e L_{ls}}{R_s(\theta_T + \theta_a)}\right). \tag{10.6}$$

From (10.5) and (10.6), the phase angle difference between i_f and i_{coil} can be approximated as,

$$\alpha_{i_{coil}-i_f} = \alpha_{i_s-v_s} - \alpha_{i_f-v_{as}} \,. \tag{10.7}$$

By inserting the resultant value of (10.7) into (5.24), the rms value of the current flowing through the shorted turns can be determined. Consequently, the copper loss in the shorted turns can be estimated more accurately.

10.4.1.2 Temperature Rise Estimation

θ_T, θ_A, θ_H and θ_F are estimated at the three different operating conditions defined in Table 10.8,. The corresponding results are provided in Figure 10.7.

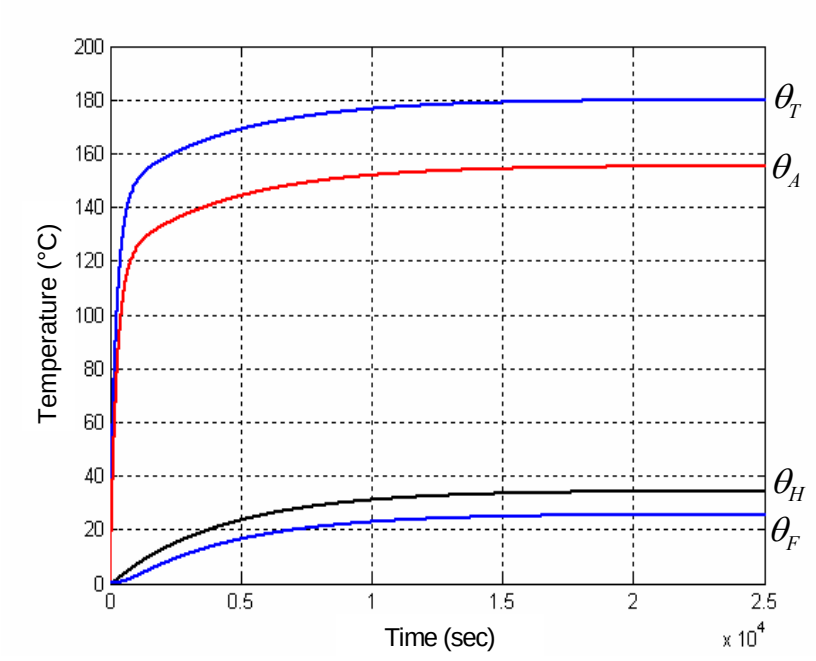

(a) At 500 rpm rotating speed and no load

Figure 10.7. Estimated θ_T, θ_A, θ_H and θ_F under a bolted turn fault condition.

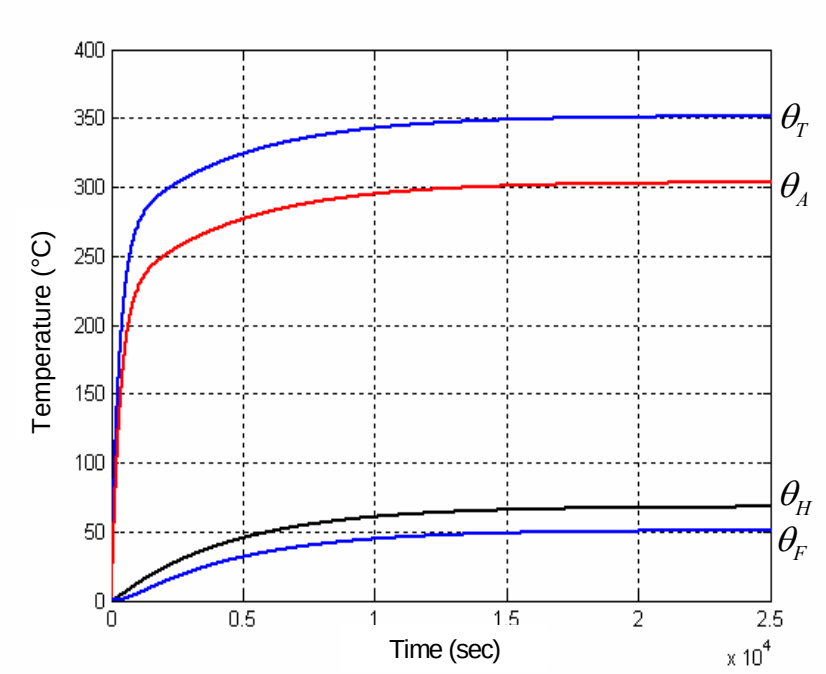

(b) At 1000 rpm rotating speed and no load

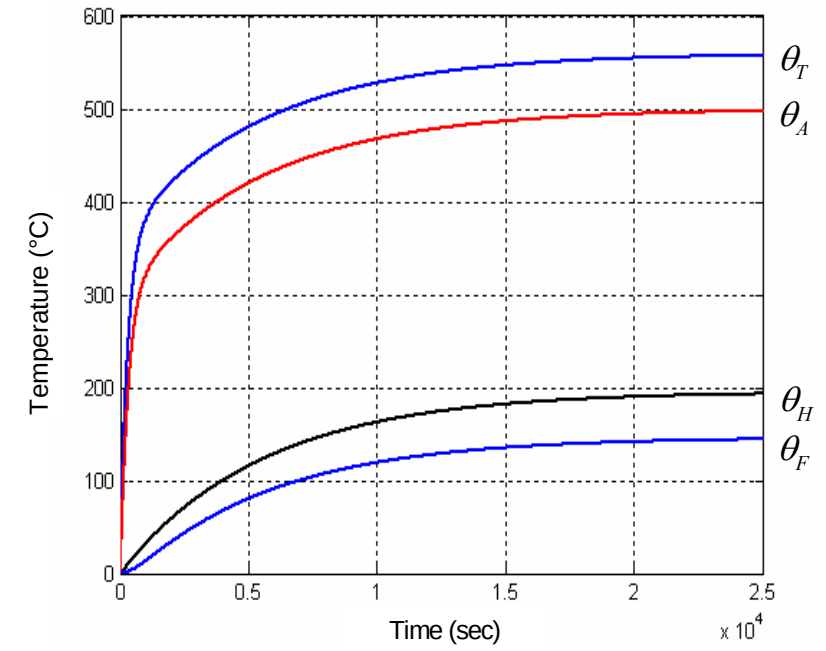

(c) At 1000 rpm rotating speed and rated load

Figure 10.7. Estimated θ_T, θ_A, θ_H and θ_F under a bolted turn fault condition.

The results of temperature estimation in Figure 10.7 shows that θ_T, θ_A, θ_H and θ_F are saturated at certain values. However some of the estimated temperatures are not realistic. The θ_T and θ_A in Figure 10.7(b) and (c) exceed $300^\circ C$, and thus, the stator windings will be burned up before the temperatures are saturated in a real situation. The insulation class of the tested IPMSM is class H. The allowed maximum hot spot temperature rise in a class H winding is $140^\circ C$ above an ambient temperature of $40^\circ C$. This means that the operation of the tested IPMSM with a bolted turn fault should be stopped before θ_A reaches the allowed maximum hot spot temperature rise. The simulation results in Figure 10.8 show the time before θ_A reaches $140^\circ C$ at the three different operating conditions.

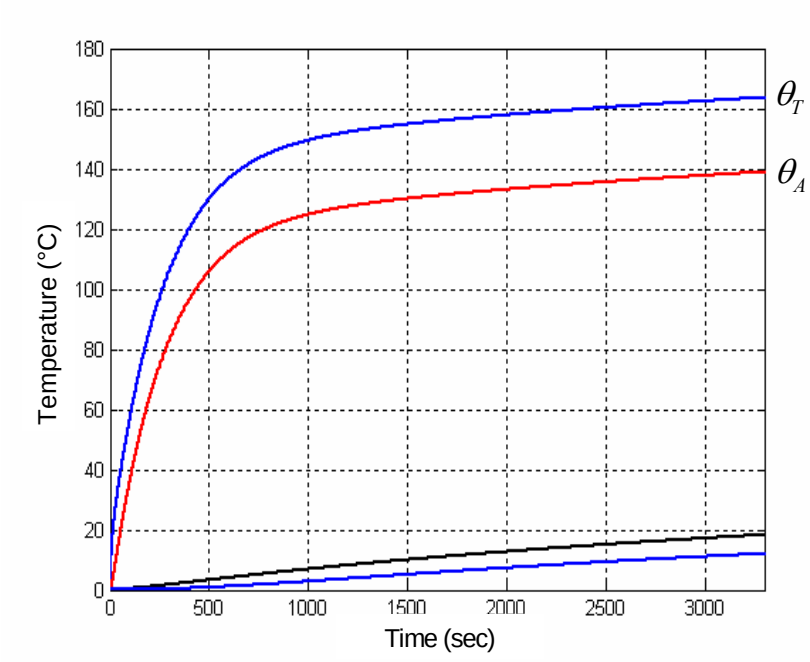

(a) At 500 rpm rotating speed and no-load

Figure 10.8. Temperature transient before θ_A reaches $140^\circ C$ at the three different operating conditions.

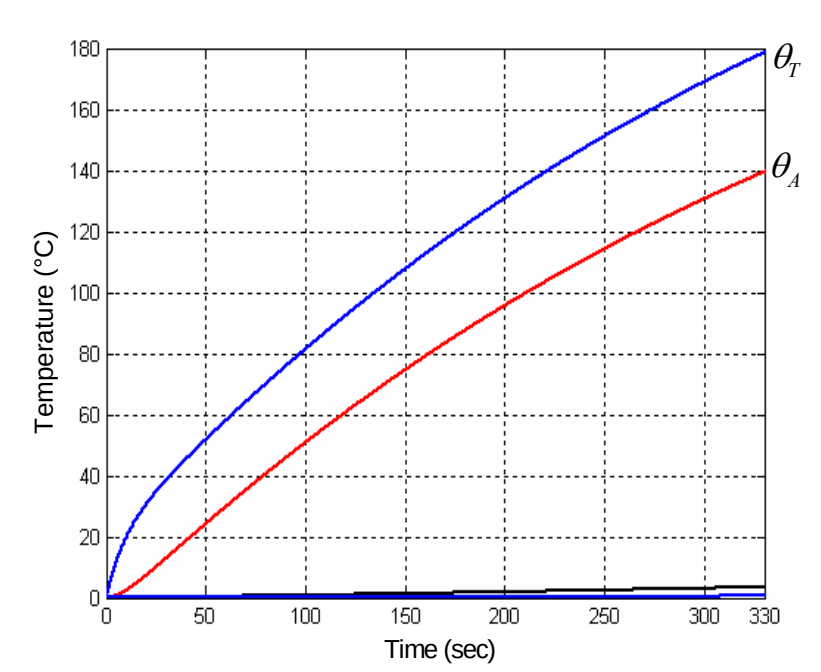

(b) At 1000 rpm rotating speed and no-load

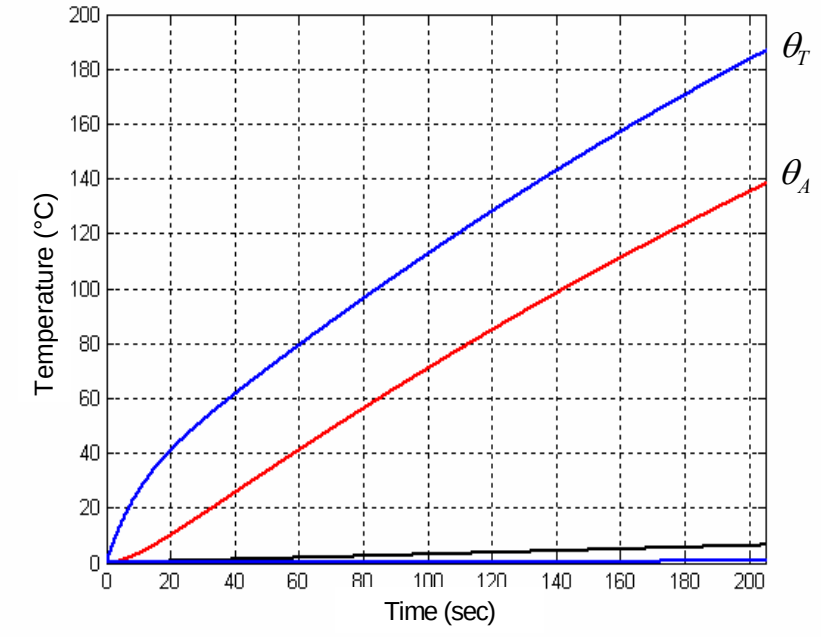

(c) At 1000 rpm rotating speed and rated load

Figure 10.8. Temperature transient before θ_A reaches 140$^\circ C$ at the three different operating conditions.

As shown in Figure 10.8(a) and (b), θ_A at 500 rpm rotating speed and no load goes up to $140^\circ C$ around one hour after the turn fault occurs, while the duration at 1000 rpm rotating speed and no load is reduced to less than six minutes. This is due to the increased i_f at 1000 rpm rotating speed and no load when compared to that at 500 rpm rotating speed and no load. Obviously, the situation at 1000 rpm rotating speed and rated load is the worst, because the amplitude of i_f is the largest, and the stator current (i_s) is also increased. In this situation, the duration before θ_A reaches $140^\circ C$ is less than four minutes, as shown in Figure 10.8(c). This result implies that even though the amplitude of i_f plays the dominant role in raising θ_A, while the amplitude of i_s also has a considerable effect on θ_A.

The amplitude of i_f, the resistance of the shorted turn (R_{TW}), and the copper losses at the shorted turns (P_{TW}) at the three different operating conditions are presented in Figure 10.9. The circulating currents are normalized referred to the rated coil current, and the resistances of the shorted turns are normalized to the resistance per turn at an ambient temperature of $40^\circ C$. The copper losses in the shorted turns are normalized to the copper loss per turn at rated load.

As shown in Figure 10.9(a) and (b), the circulating currents decrease as the resistance in the shorted turns increases during the temperature transients. However, the copper losses in the shorted turns increase during the temperature transients as shown in Figure 10.9(c). This is due to the fact that the copper loss in the shorted turns is related to the resistance of the shorted turns as well as the amplitude of the circulating current.

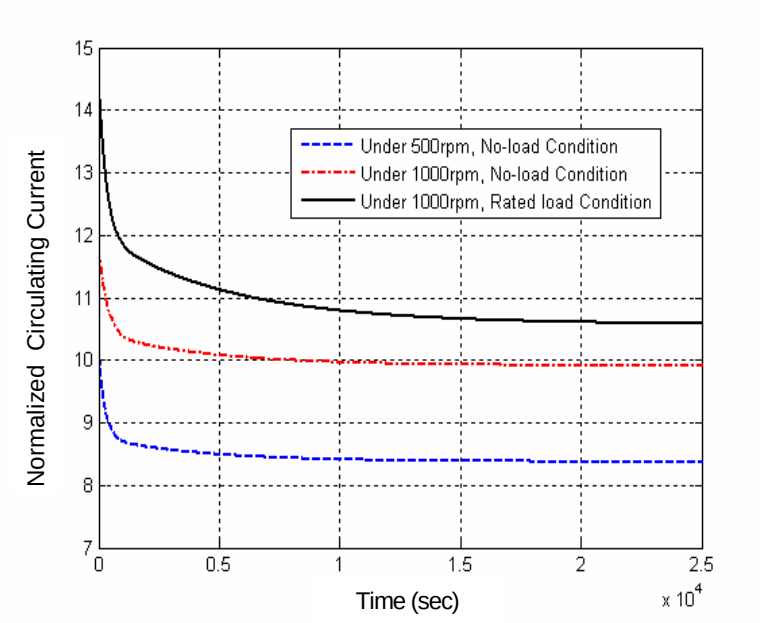

(a) Normalized circulating currents

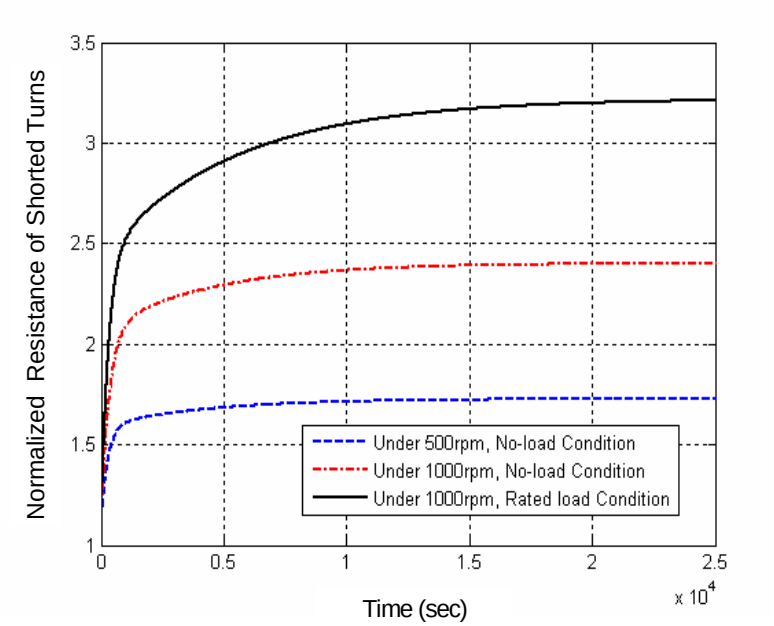

(b) Normalized resistance of the shorted turns

Figure 10.9. Normalized quantities in the shorted turns at three different operating conditions.

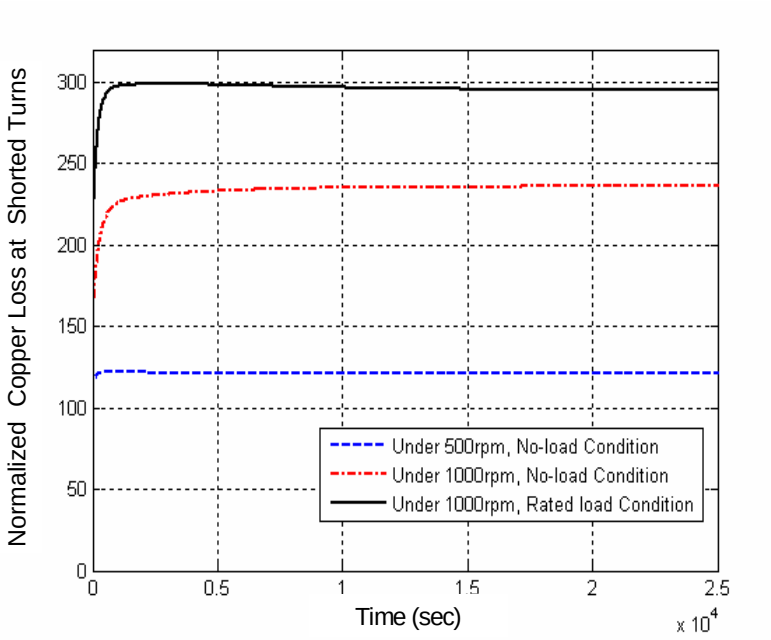

(c) Normalized copper losses in the shorted turns

Figure 10.9. Normalized quantities in the shorted turns at three different operating conditions.

From the simulation results in Figure 10.8 and Figure 10.9, it can be concluded that the copper loss in the shorted turns should be limited at a certain value to increase the allowable operating duration of a machine under a turn fault condition. However, it should be noted that the allowable operating duration is also related to the amplitude of the stator current required for maintaining the given operation.

10.5 Chapter Summary

The thermal models of an IPMSM without and with stator turn faults have been verified by showing that the estimation results have good agreement with the measured temperatures. In addition, an investigation on the thermal behavior of a bolted turn fault has been carried out under various operating conditions. This investigation shows how

fast a stator turn fault propagates to other healthy turns. Furthermore, it provides important information for reducing the propagation speed of a stator turn fault.

Actually, reducing the circulating current in the shorted turns is the only possible way to reduce the propagation speed of a stator turn fault. However, as investigated in Chapter 7, a larger stator current is required for reducing the circulating current, and thus, the increased stator current can raise the overall machine temperature. This means that the two thermal stresses caused by the reduced circulating current and increased stator current should be considered together to limit the temperatures within an acceptable level. The developed thermal model of an IPMSM with stator turn faults makes it possible to consider the effects of the two thermal stresses on the temperatures at the stator windings. This is the most valuable contribution of the developed thermal model.

CHAPTER 11

VERIFICATION OF THE TURN FAULT DETECTION METHOD

11.1 Overview

A turn fault detection method for IPMSM drives was proposed in Chapter 6. In this chapter, the proposed turn fault detection method is verified through simulations and experiments.

11.2 Simulation Results

In most industry applications, electric drives are commonly operated in speed control mode. However, in transit applications such as traction drives of electric or hybrid electric vehicles, torque control is the primary mode. For this reason, simulations are performed to show that the proposed turn fault detection method effectively works regardless of operation mode. The simulation conditions are summarized in Table 11.1.

Table 11.1. Simulation conditions for verifying the proposed turn fault detection method.

Item	Unit	Torque Control Mode	Speed Control Mode
Coil Connection	[-]	Series	Series
Fault Location	[-]	On the *a*-phase winding	On the *a*-phase winding
Fault Fraction	[%]	0 / 1/ 3/ 5	0 / 1/ 3/ 5
Fault Impedance	[ohm]	0 (a bolted turn fault)	0 (a bolted turn fault)
Torque Reference	[%]	0 / 40 / 80	0 / 40
Rotating Speed	[rpm]	500 / 1500	500 / 1500

The simulation results are presented in Figure 11.1 and Figure 11.2. In the figures, the x-axis represents the fault fraction (μ), the z-axis represents the fault estimation (F_{est}) defined in Chapter 6. Each y-axis in the figures represents the torque reference and load torque, respectively.

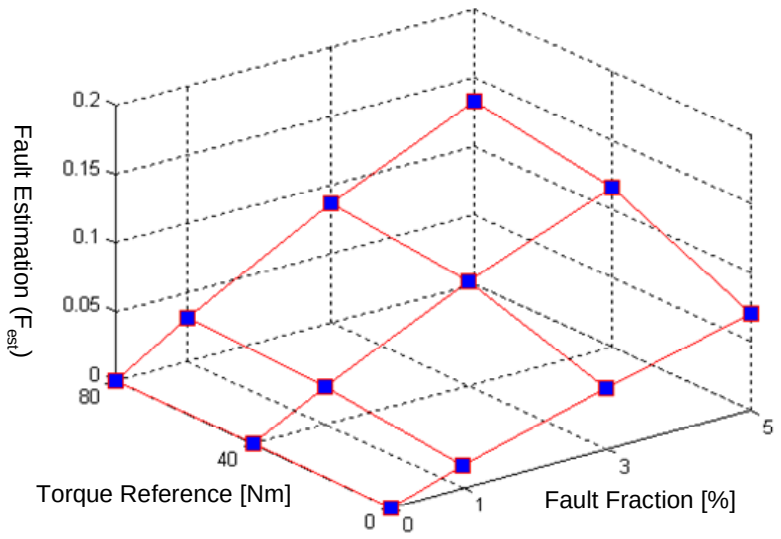

(a) At 500 rpm rotating speed

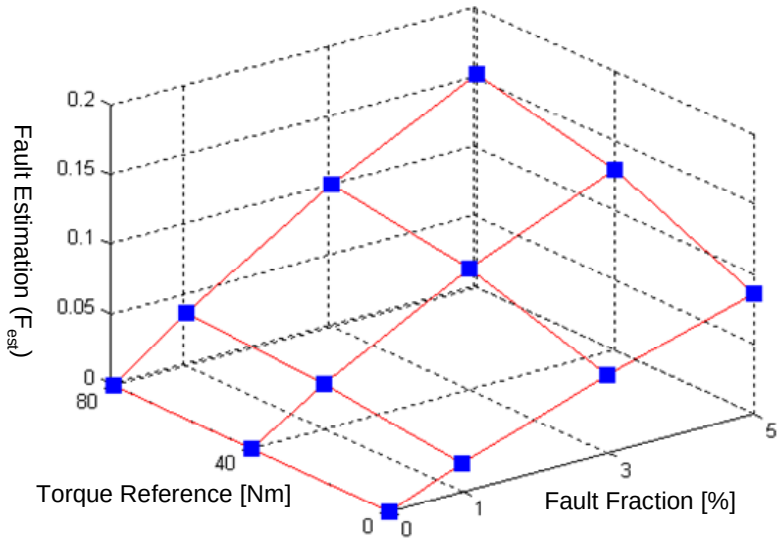

(b) At 1500 rpm rotating speed

Figure 11.1. Verification of the proposed turn fault detection method under torque control mode.

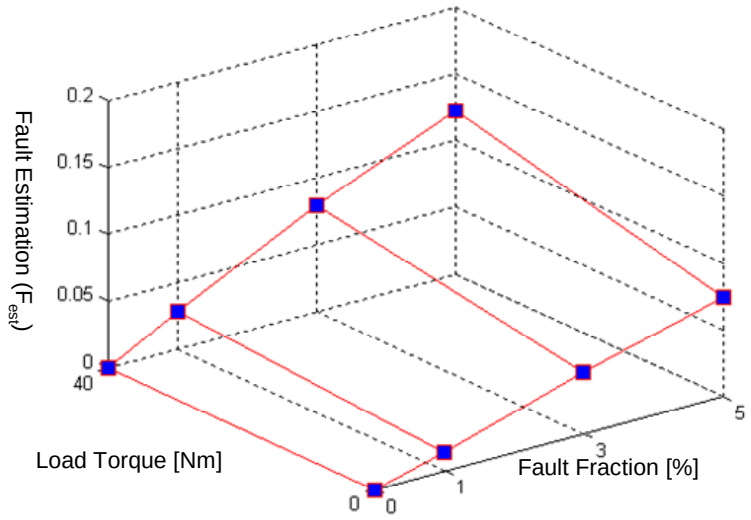

(a) At 500 rpm rotating speed

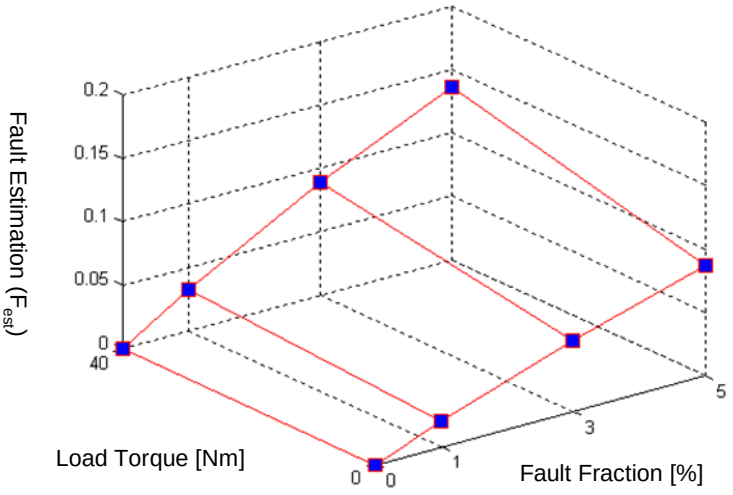

(b) At 1500 rpm rotating speed

Figure 11.2. Verification of the proposed turn fault detection method under speed control mode.

The simulation results clearly show that F_{est} increases as the fault gets worse. However, it is observed that F_{est} is dependent on the applied load and rotating speed since the reduction in the voltage references is a function of the applied load and rotating speed.

11.3 Experimental Results

As shown earlier, the degree of the change in voltage reference caused by a stator turn fault is dependent on the applied load and rotating speed. In other words, the degree will decrease as the rotating speed or applied load decreases. To show that the proposed detection method works well even at a low rotating speed and light load condition, two different load levels at a low rotating speed are selected. Under each load condition, three different operations are selected. In operation 1 and 3, there is no stator turn fault, while a turn fault is introduced in operation 2. Under operation 1 and 2, the same external load is applied, while the external load under operation 3 is adjusted to make the torque reference as close as to that under operation 2. The experimental conditions are summarized in Table 11.2. And the corresponding results are presented in Figure 11.3 and Figure 11.4, respectively. The machine variables are sampled at every 100 ms period, and filtered by a low-pass filter with a cut-off frequency of 2 Hz.

Table 11.2. Experimental conditions for verifying the proposed turn fault detection method.

Item	Unit	Operation 1	Operation 2	Operation 3
Coil Connection	[-]	Parallel	Parallel	Parallel
Control Mode	[-]	Speed	Speed	Speed
Speed Reference	[rpm]	500	500	500
Fault Location	[-]	No fault	A coil in the *b*-phase	No fault
Fault Fraction	[%]	-	4.17	-
Fault Impedance	[mohm]	-	6.54	-
Torque Reference 1	[Nm]	2.34	2.59	2.55
Torque Reference 2	[Nm]	10.19	10.4	10.5

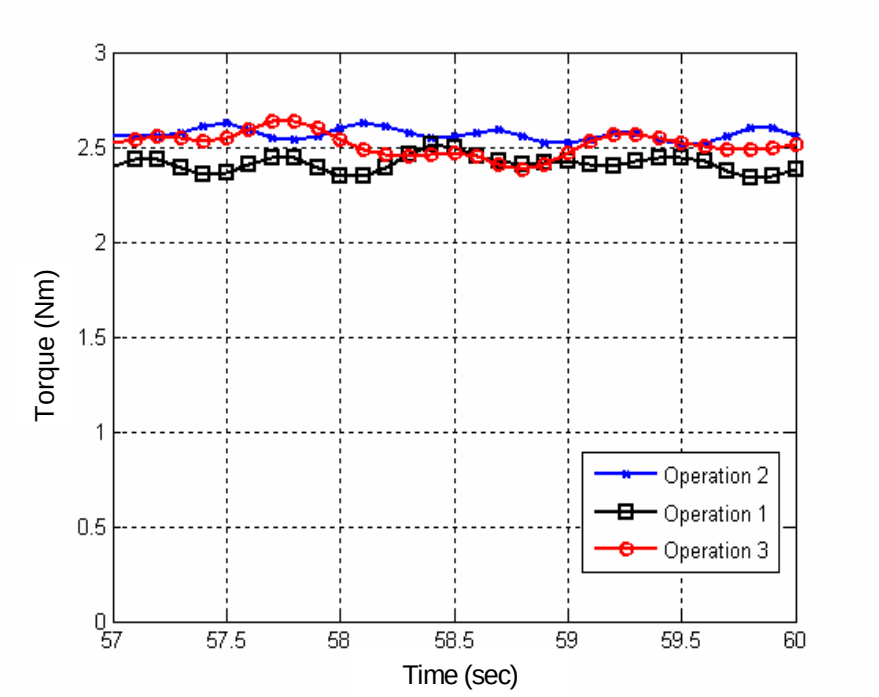

(a) Torque references

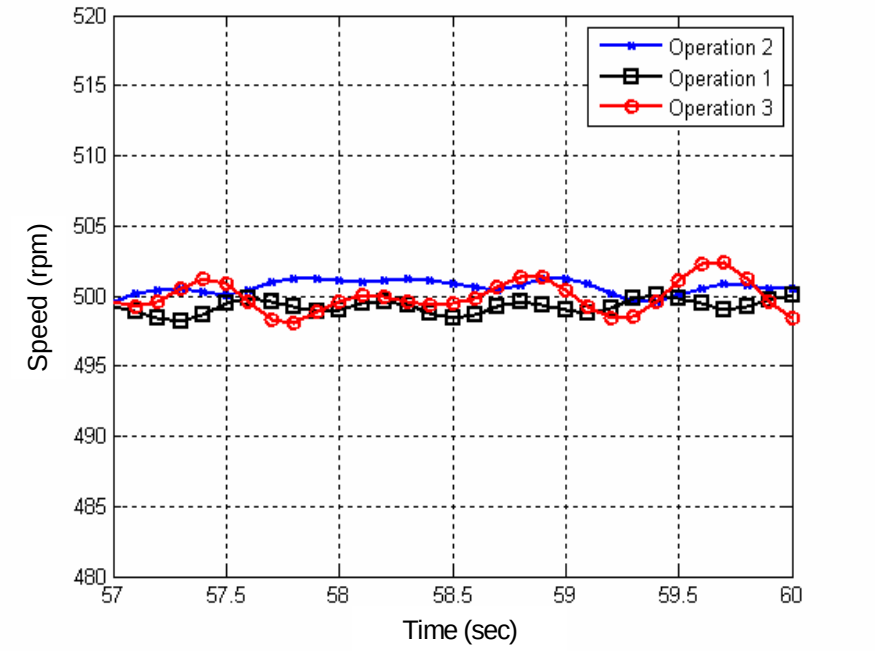

(b) Rotating speeds

Figure 11.3. Measured drive variables at load level 1.

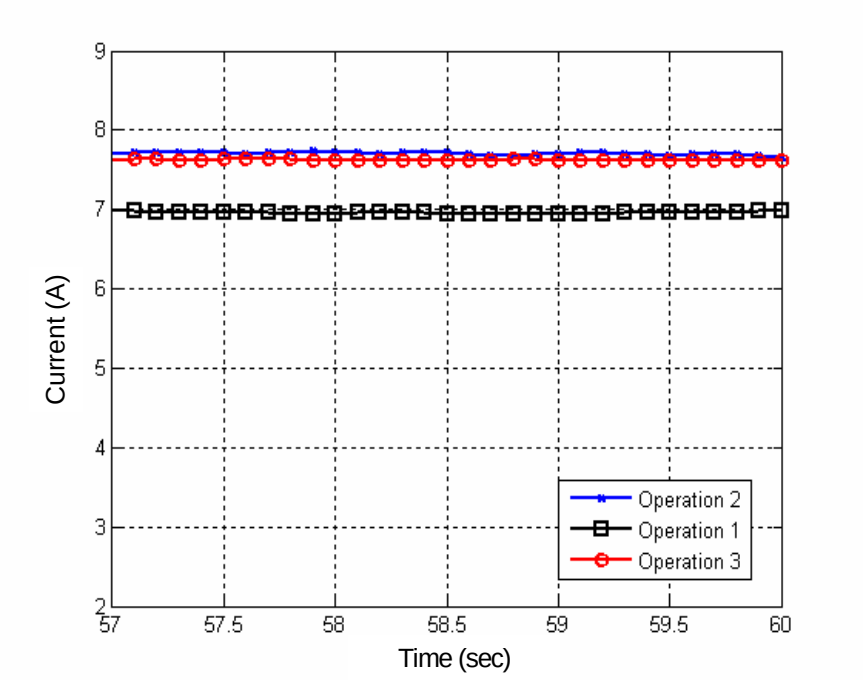

(c) *q*-axis current references

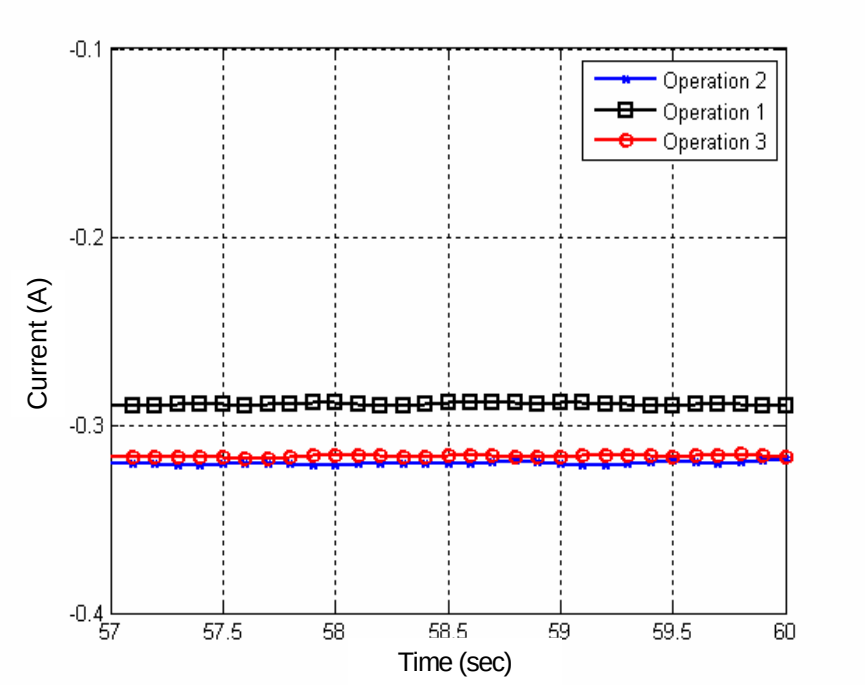

(d) *d*-axis current references

Figure 11.3. Measured drive variables at load level 1.

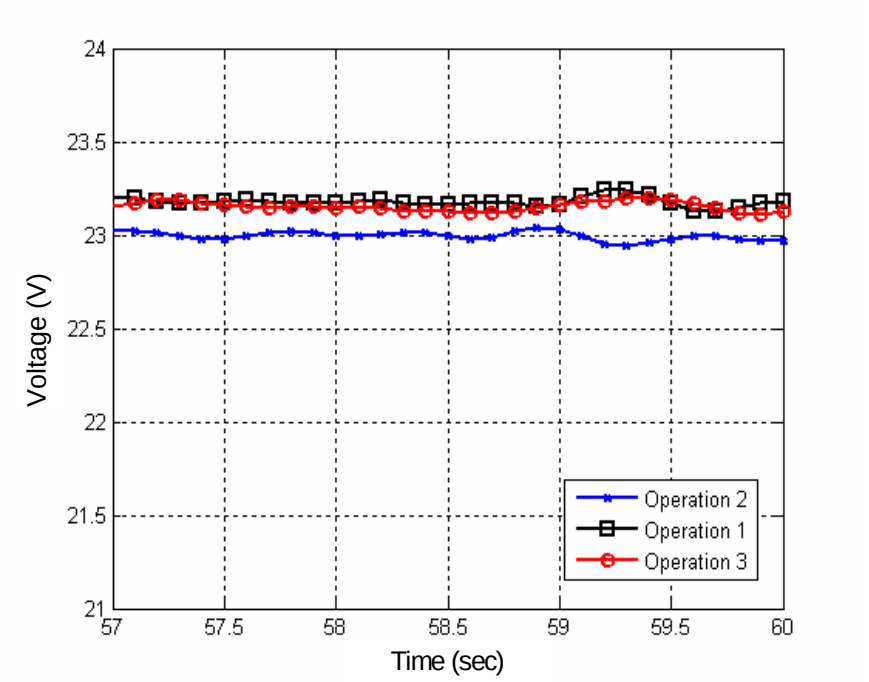

(e) *q*-axis voltage references

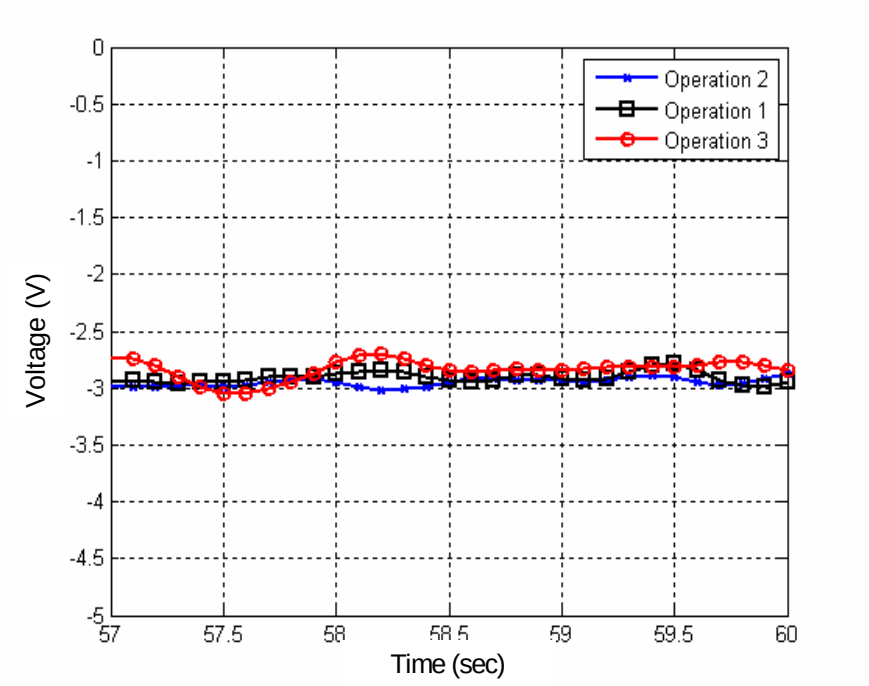

(f) *d*-axis voltage references

Figure 11.3. Measured drive variables at load level 1.

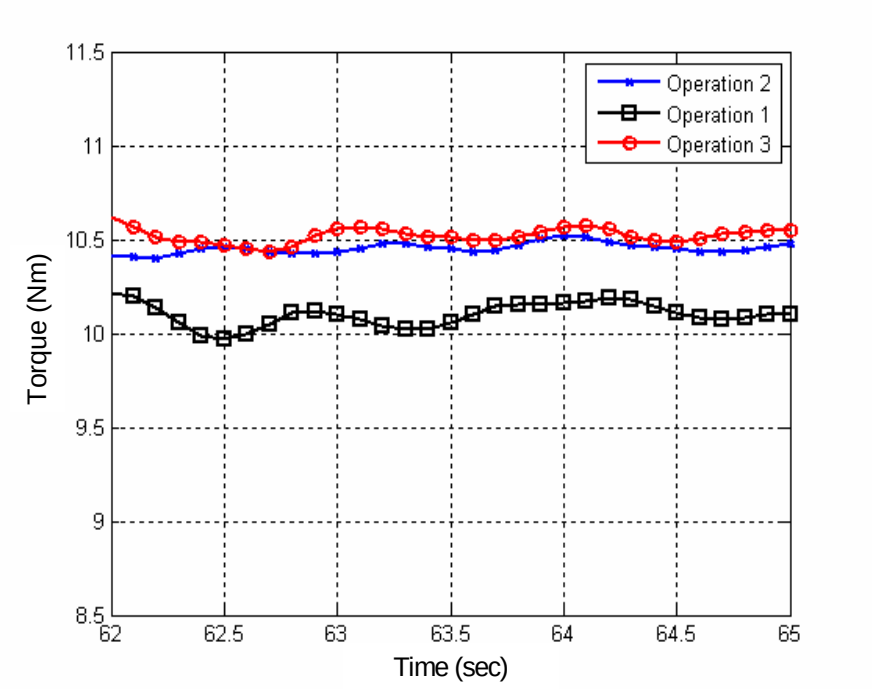

(a) Torque references

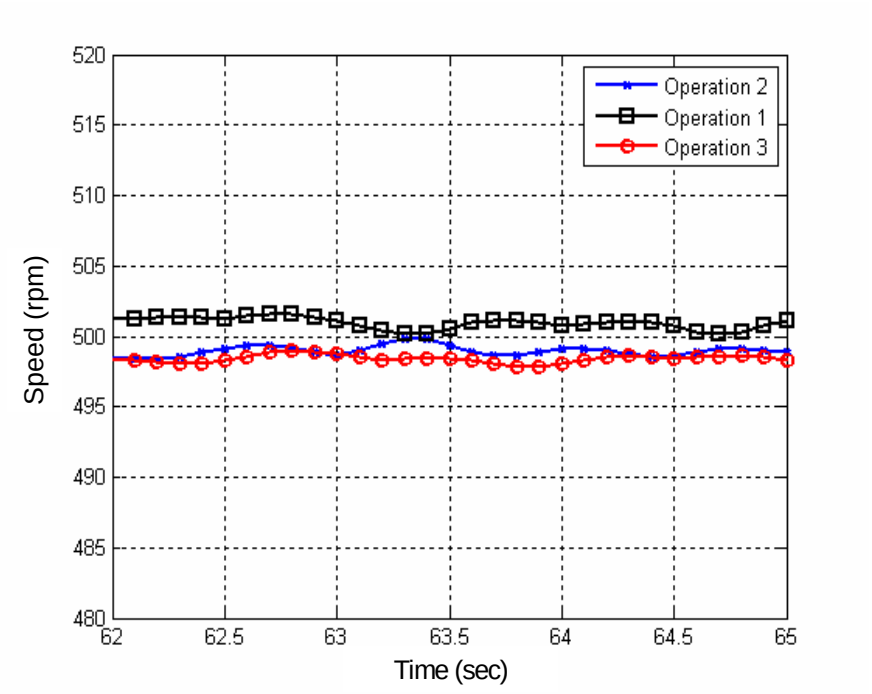

(b) Rotating speeds

Figure 11.4. Measured drive variables at load level 2.

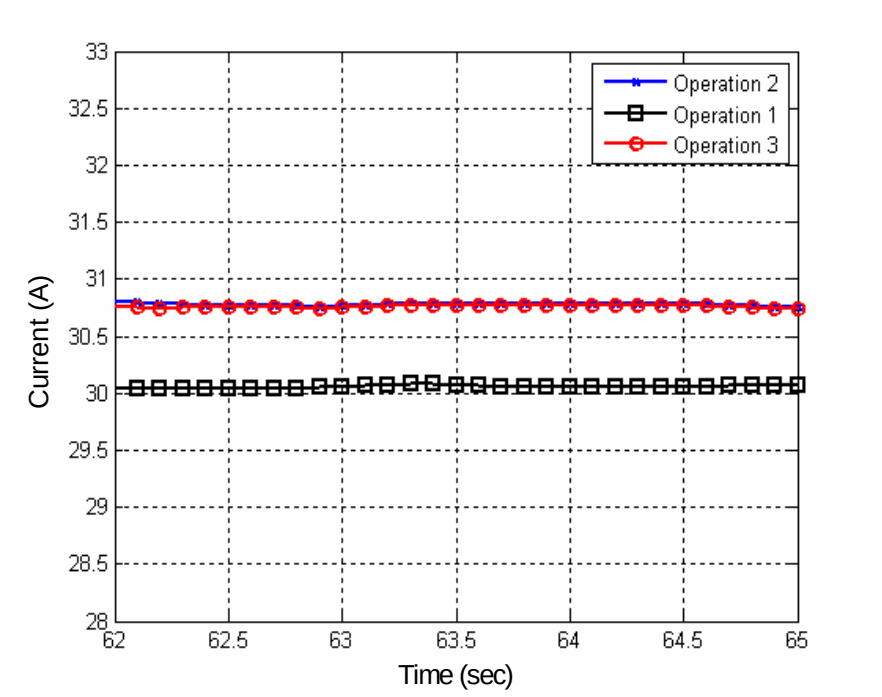

(c) *q*-axis current references

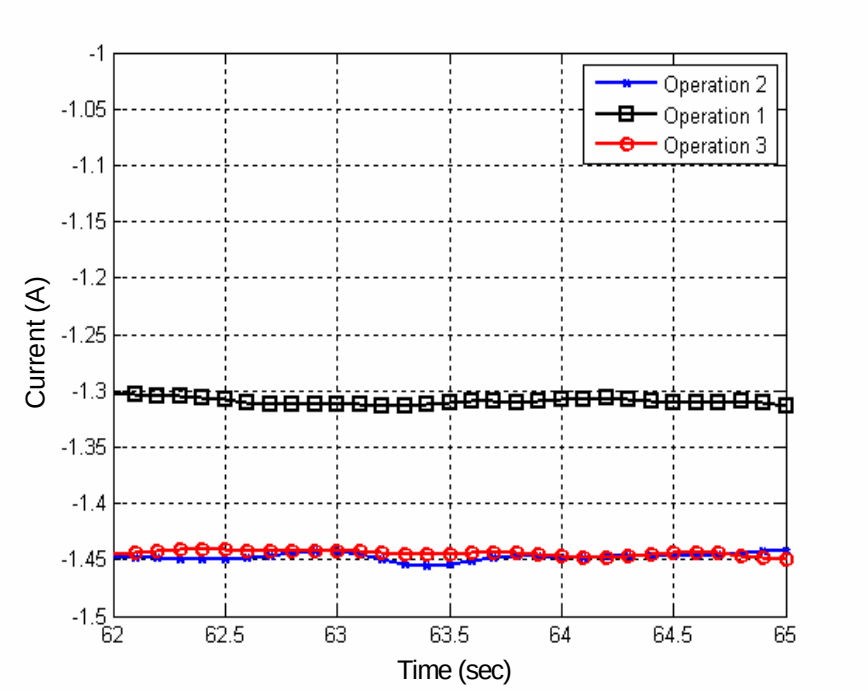

(d) *d*-axis current references

Figure 11.4. Measured drive variables at load level 2.

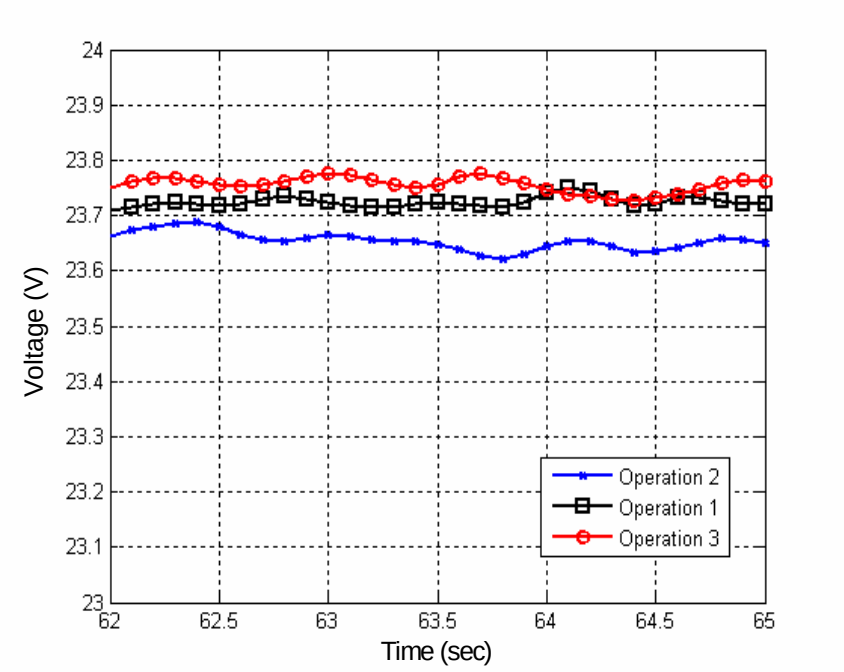

(e) *q*-axis voltage references

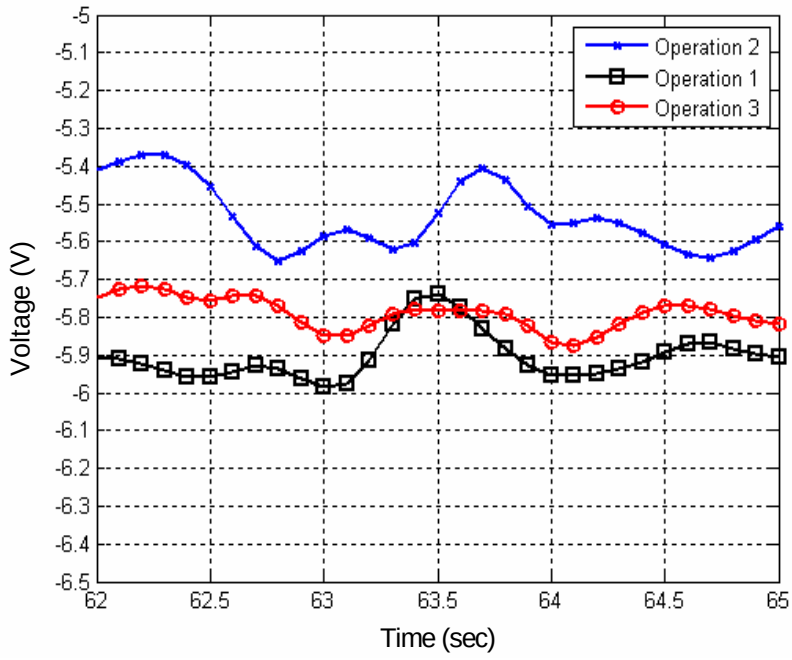

(f) *d*-axis voltage references

Figure 11.4. Measured drive variables at load level 2.

As shown in Figure 11.3 and Figure 11.4, the stator turn fault results in a slightly increased torque reference when compared to that for the IPMSM without a turn fault at the same rotating speed and applied load condition (operation 1 and 2). This phenomenon was already observed in Chapter 9, and explained. The increased torque reference leads to increased amplitudes of the *q*- and *d*-axis current references.

As shown in the waveforms of the *q*-axis voltage references in Figure 11.3(e) and Figure 11.4(e), the *q*-axis voltage references under operation 2 (with one turn fault) have the least value among the three voltage references regardless of the applied load level. Furthermore, the reduction in the *q*-axis voltage reference under operation 2 as compared to that under operation 3 is clearly seen even though the two operations are operated with the same *q*- and *d*-current references. On the contrary, the amplitude of the *d*-axis voltage reference under load level 1 seems to have little relationship with the stator turn fault as shown in Figure 11.3(f). However, it should be pointed out that load level 1 is a very light load. This implies that the reduction in the positive sequence voltage reference resulting from the stator turn fault under load level 1 is mainly contributed by the reduction in the positive sequence back-emf voltage that is independent of the applied load level. Consequently, the effect of the stator turn fault on the positive sequence voltage reference under load level 1 would be dominantly observed in the *q*-axis voltage reference. This reasoning makes sense since the reduction in the *d*-axis voltage reference as well as in the *q*-axis voltage reference is observable under load level 2 as shown in Figure 11.4(f). This discussion suggests that the proposed turn fault detection method can detect a stator turn fault quite independently of the applied load level by observing

the *q*-axis voltage reference under a light load condition and by observing both the *q*-and *d*-axis voltage references under a medium or heavy load condition.

From the experimental results, it can be said that the proposed turn fault detection method would be more reliable as rotating speed or applied load increases. Furthermore, it can be easily inferred that the proposed method will have the better performance when a machine has a bolted turn fault because a bolted turn fault will result in a larger stator current than that resulting from a non-bolted turn fault.

11.4 Chapter Summary

In this chapter, the on-line turn fault detection method, which was proposed in Chapter 6, has been verified through simulations and experiments. As proved by the simulation and experimental results, the proposed turn fault detection method has several distinct advantages over previously proposed methods. These advantages are summarized as follows:

(1) The use of voltage references for turn fault detection makes it unnecessary to measure the machine terminal voltages, and attenuates the effects of controller actions on turn fault detection.

(2) The observation of voltage references in the synchronously (rotor-aligned) rotating reference frame attenuates the effects of non-stationary operations of drives on turn fault detection. In addition, this observation method does not require additional computational efforts except for simple low-pass filtering.

(3) The look-up table-based fault decision algorithm provides a good immunity to the effects of the non-idealities in a given machine.

(4) The proposed turn fault detection method works nicely regardless of operating mode.

(5) The proposed turn fault detection method works independently of applied load level because the reduction in the q-axis voltage reference resulting from a turn fault is still observable even under a light load condition.

These distinct features make the proposed turn fault detection method reliable and cost effective. Thus, the proposed method can detect a stator turn fault in IPMSM drives at its initial stage, and consequently, can prevent it from developing into the catastrophic phase.

CHAPTER 12

VERIFICATION OF THE TURN FAULT-TOLERANT OPERATING STRATEGY

12.1 Overview

The practicality of the stator turn fault-tolerant operating strategy of Chapter 7 is verified by simulations and experiments in this chapter. This verification focuses on showing how much the circulating current in the shorted turns (i_f) can be reduced by the proposed strategy and subsequently, how much the allowable operating area and time in the presence of a fault can be extended. For this, the stator winding temperatures are estimated under the operation of the proposed strategy. In addition, the effects of machine specifications on the performance of the proposed strategy are investigated. Based on the observations from simulation and experimental results, a general IPMSM design guideline for increased stator turn fault tolerance is provided.

12.2 Simulation Results

Simulations are carried out to evaluate the performance of the proposed strategy. In particular, simulation results showing the following are provided:

(1) Reduction in the circulating current and increase in the allowable operating area

(2) Comparison with symmetrical short-circuited operation

(3) The effects of machine thermal capacity

(4) The effects of machine specifications

12.2.1 Reduction in Circulating Current and Increase in Allowable Operating Area

Two simulations are performed to verify the principle of the proposed turn fault-tolerant operating strategy. The first simulation is to show how much i_f can be reduced by the proposed strategy. The second one is to provide an example showing how much the allowable operating area can be increased as a result of the proposed strategy. The conditions for these two simulations are summarized in Table 12.1. The inductance variation depending on the operating condition is considered in the simulations.

The trajectories of the *q*- and *d*-axis currents (i_{qs}^e and i_{ds}^e) whose combination minimizes the stator voltage vector ($\left|\tilde{v}_s^e\right|$) at every speed and torque combination within rated operation are presented in Figure 12.1. The three-dimensional comparison of the amplitude of i_f ($\left|i_f\right|$) under MTPA operation and the proposed strategy are illustrated in Figure 12.2. In these figures, the *x*-and *y*-axes represent the normalized values of the rotating speed and developed torque referred to their rated values. Each *z*-axis in Figure 12.1 and Figure 12.2 represents the normalized quantity to the rated current, respectively.

Table 12.1. Simulation conditions for showing the reduction in $\left|i_f\right|$ and the increase in the allowable operating area.

Item	Unit	Value
Coil Connection	[-]	Parallel
Fault Location	[-]	On the *a*-phase winding
Fault Fraction	[%]	4.17
Fault Impedance	[ohm]	0 (a bolted turn fault)
Max. Stator Current	[A]	300

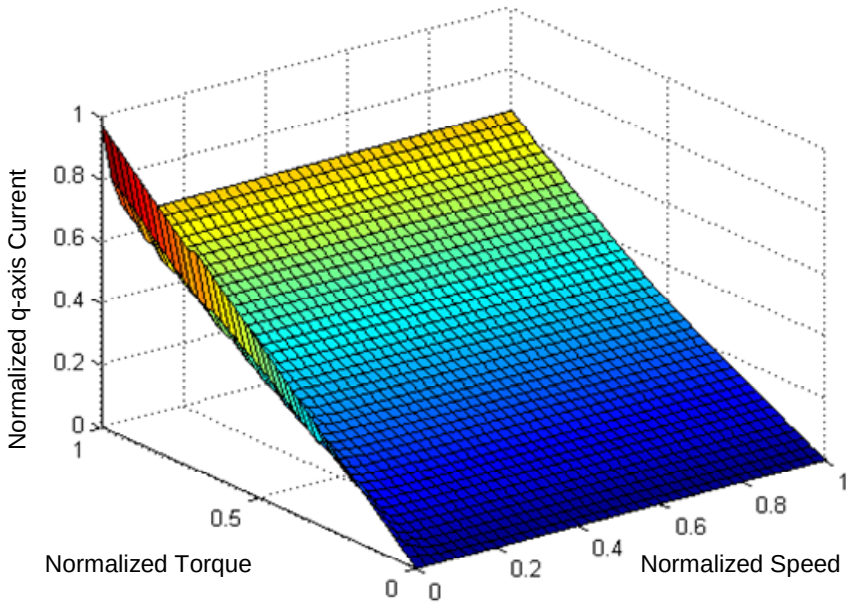

(a) i_{qs}^{e} trajectory

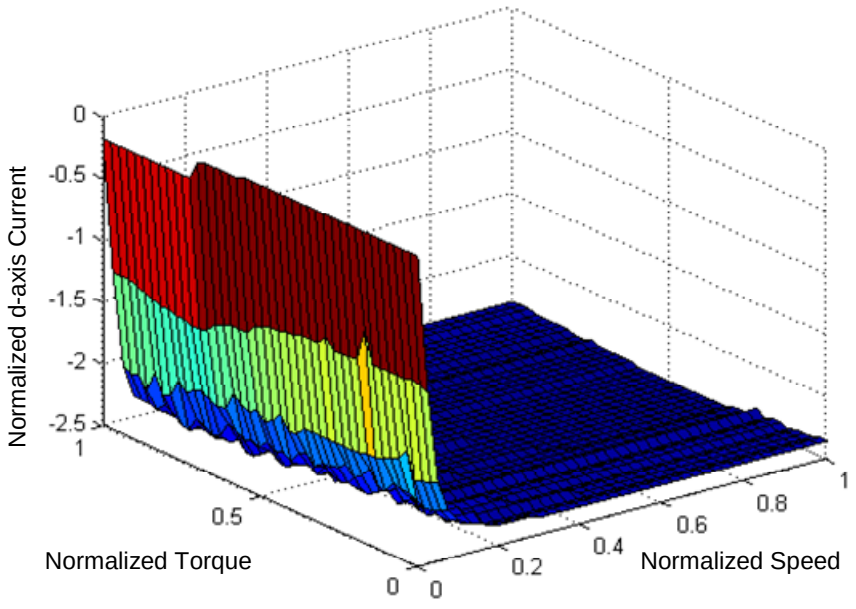

(b) i_{ds}^{e} trajectory

Figure 12.1. Trajectories of i_{qs}^{e} and i_{ds}^{e} whose combination minimizes $\left|\tilde{v}_{s}^{e}\right|$ at every operating point within rated operation.

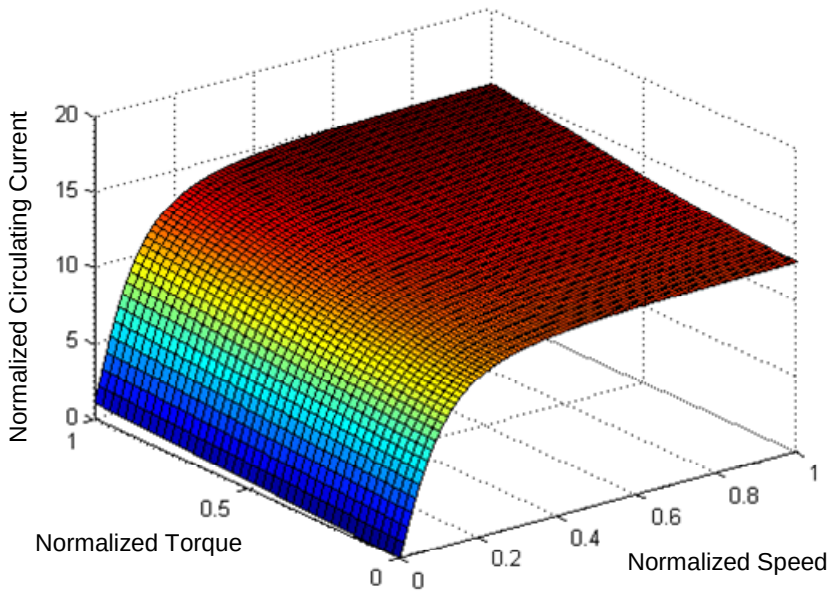

(a) Under MTPA operation

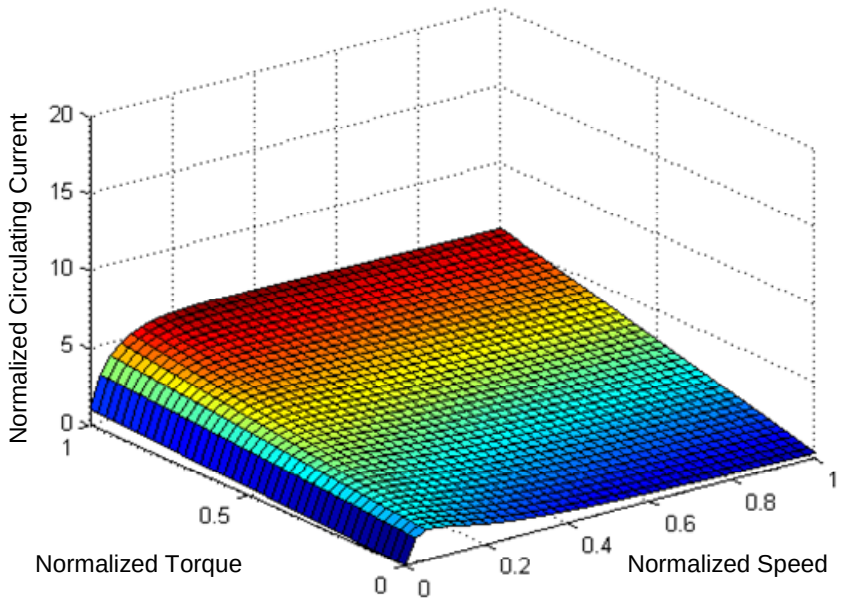

(b) Under the proposed strategy

Figure 12.2. Comparison of the normalized $|i_f|$ at every operating point within rated operation under MTPA and the proposed strategy.

As shown in Figure 12.1, while i_{ds}^{e} moves to the characteristic current as the torque and speed increase, i_{qs}^{e} is only proportional to the torque. As shown in Figure 12.2, significant reduction in $|i_f|$ is achieved by the proposed strategy. It is also observed that the proposed strategy yields a stronger effect at light loads.

As shown in Figure 12.2, even though significant reduction is achieved, $|i_f|$ at some operating points is unacceptable. Assuming the acceptable $|i_f|$ is three times the rated coil current, the allowable operating areas under MTPA operation and the proposed strategy, can be determined. The two allowable operating areas are compared in Figure 12.3.

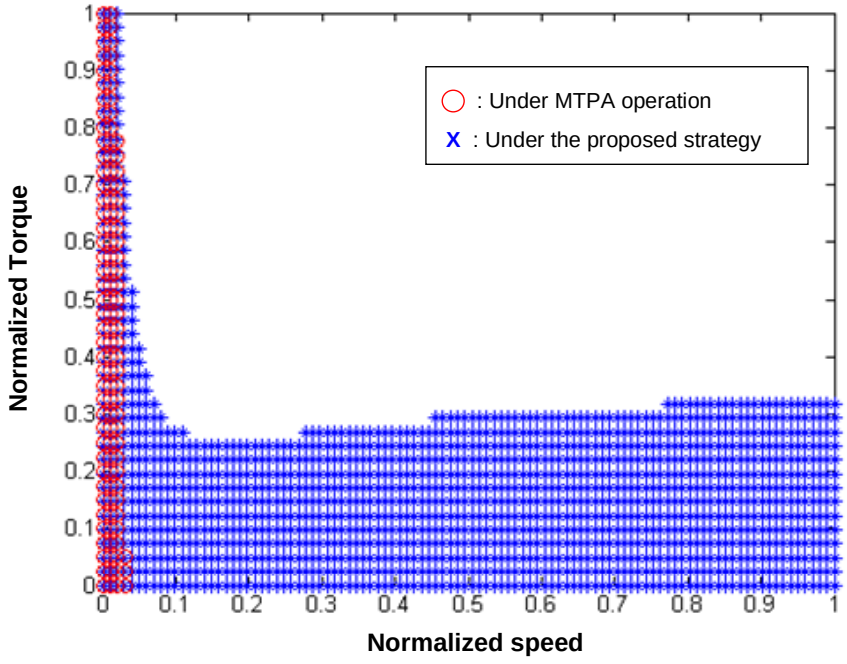

Figure 12.3. Comparison of the allowable operating areas where $|i_f|$ is limited to three times the rated coil under MTPA operation and the proposed strategy.

The simulation result in Figure 12.3 shows that the proposed turn fault-tolerant operating strategy tremendously increases the allowable operating area under a stator turn fault condition. However, it should be kept in mind that the allowable torque range under the proposed strategy is reduced when compared to that under the normal operation.

Although the simulation results in Figure 12.2 and Figure 12.3 clearly validate the performance of the proposed strategy, the results do not provide any information about the allowable operating *duration* of the proposed strategy. As discussed in Chapter 7 and 10, to estimate the allowable operating duration of the proposed strategy, the temperature rises at the shorted turns, adjacent turns, and healthy turns (θ_T, θ_A, and θ_H) need to be predicted. A more detailed investigation on this issue is carried out in later sections.

12.2.2 Comparison with Symmetrical Short-Circuit Operation

As investigated in Section 3.2.2, symmetrical short-circuit operation is also a possible post-turn fault way to reduce i_f. In this section, the performance of the proposed strategy is compared with that of symmetrical short-circuit operation via simulations. The conditions for this simulation are summarized in Table 12.2, and the corresponding results are provided in Figure 12.4.

Table 12.2. Simulation conditions for comparing the performances of the proposed strategy and symmetrical short-circuit operation.

Item	Unit	Proposed Strategy	Symmetrical Short-circuit
Coil Connection	[-]	Series	
Fault Fraction	[%]	1.04	
Fault Impedance	[ohm]	0 (a bolted turn fault)	
Load	[Nm]	0 (no load)	
Rotating Speed	[rpm]	1500 (Speed control)	1500

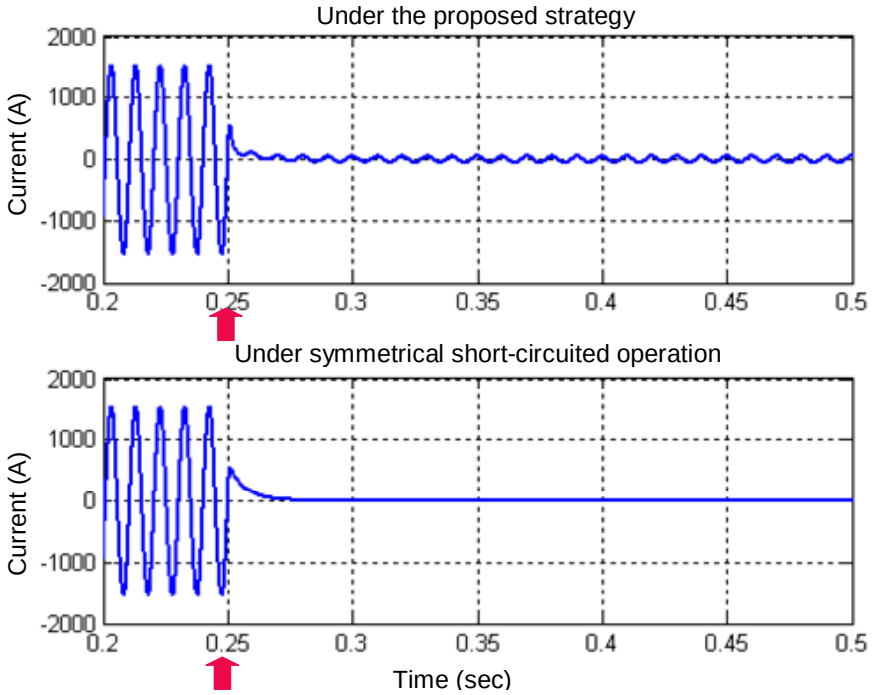

(a) Circulating current in the shorted turns

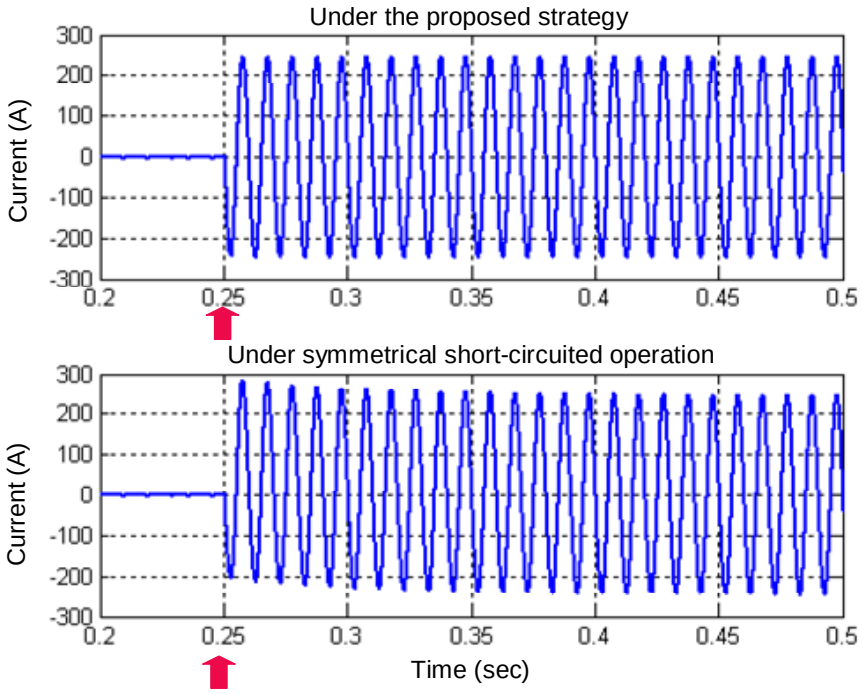

(b) *a*-phase current

Figure 12.4. Comparison of the performances of the proposed strategy and symmetrical short-circuit operation at 1500 rpm and no load.

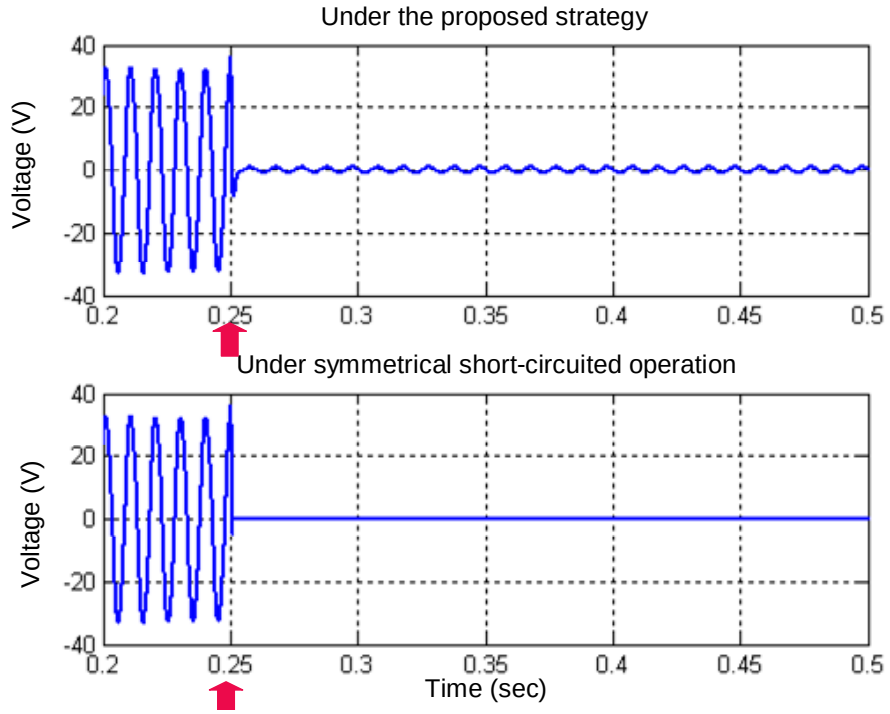

(c) a-phase line-neutral voltage

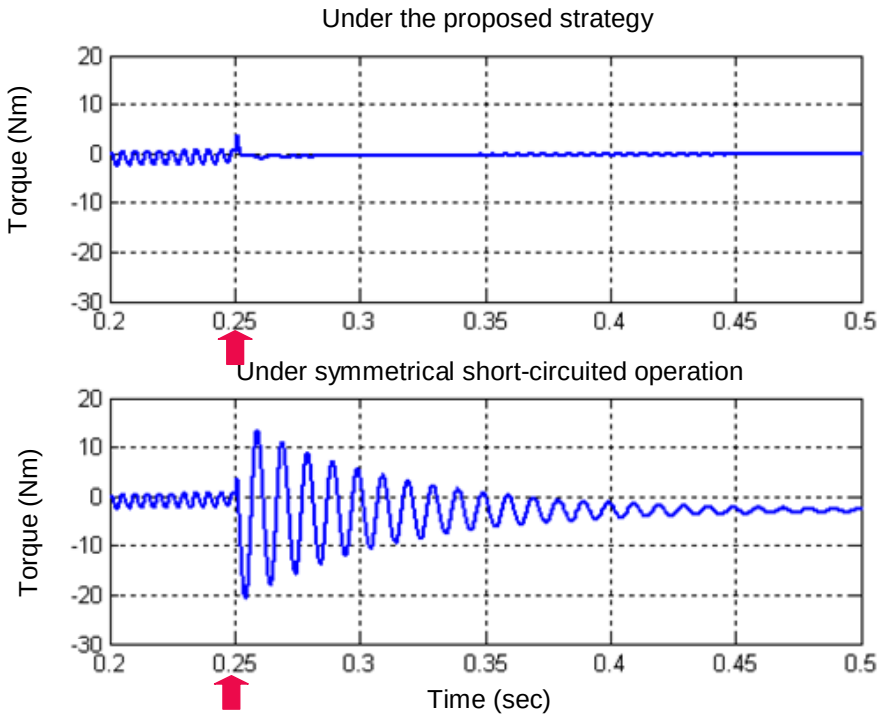

(d) Developed torque

Figure 12.4. Comparison of the performances of the proposed strategy and symmetrical short-circuit operation at 1500 rpm and no load.

Since control of the machine is not possible under symmetrical short-circuit operation, it is assumed that the rotating speed of the machine is maintained constant by a mechanical device connected to the machine. The arrow in Figure 12.4 indicates the instant when the two operations are activated.

The results in Figure 12.4(a) show that i_f under the symmetrical short-circuit operation gets close to zero, while i_f under the proposed strategy is reduced to less than 50 A (approximately 0.4 times the rated current). However, the line currents under both the operations rise up to around the characteristic current of the machine. The results in Figure 12.4(a) and (b) indicate that the two operations have almost the same performance in terms of reducing i_f. However, a noticeable superiority of the proposed strategy to symmetrical short-circuit operation is observed in the developed torque. As shown in Figure 12.4(d), the developed torque under the symmetrical short-circuit operation has a large torque pulsation right after activating the operation and slowly converges to a negative torque. The large torque pulsation can damage the mechanical coupling between the machine and mechanical device, and the negative torque acts as a load to the mechanical device. On the contrary, the developed torque under the proposed strategy has a very small transient, as well as a very small steady-state value. However, it should be noted that the proposed strategy continues to control the machine, while control over the machine is no longer available with the symmetrical short.

12.2.3 Effects of Machine Temperature Rise (or Machine Thermal Capacity)

The heat generated by the circulating current in the shorted turns and the required stator current will restrict the allowable operating duration of the proposed turn fault-

tolerant operating strategy. This means that the acceptable $|i_f|$ and $|i_s|$, which maximize the operating duration of the proposed strategy, should be determined. For this purpose, θ_T, θ_A, θ_H, and θ_F are estimated at various combinations of i_{ds}^e and i_{qs}^e for a given rotating speed and applied load using the developed IPMSM thermal model with stator turn fault. The conditions for this estimation are summarized in Table 12.3. The corresponding results are provided in Figure 12.5 and Figure 12.6. In Table 12.4, the estimated allowable operating durations of the proposed strategy are summarized.

The estimation results in Figure 12.5 show the durations before θ_A reaches the allowed maximum temperature rise ($140^\circ C$ in case of class H winding) at the five different combinations of i_{ds}^e and i_{qs}^e. The simulation results in Figure 12.6 show the normalized quantities in the shorted turns.

Table 12.3. Simulation conditions for estimating θ_T, θ_A, θ_H and θ_F under various combinations of i_{qs}^e and i_{ds}^e for 1000 rpm rotating speed and 10 Nm load operation.

Items	Unit	#1	#2	#3	#4	#5
Coil Connection	[-]	Parallel				
Fault Fraction	[%]	4.17 (one turn fault)				
Fault Impedance	[ohms]	0 (a bolted turn fault)				
Rotating Speed	[rpm]	1000				
Applied Load	[Nm]	10				
Operating Mode	[-]	MTPA	Field Weakening (Proposed Strategy)			
q-axis Current	[A]	30.63	27.72	25.28	23.23	21.49
d-axis Current	[A]	-1.27	-58.77	-117.53	-176.30	-235.06
Stator Current	[Apeak]	30.65	64.98	120.22	177.82	236.05
Stator Current	[pu]	0.26	0.54	1.00	1.48	1.96
Field-Weakening rate	[%]	0	25	50	75	100

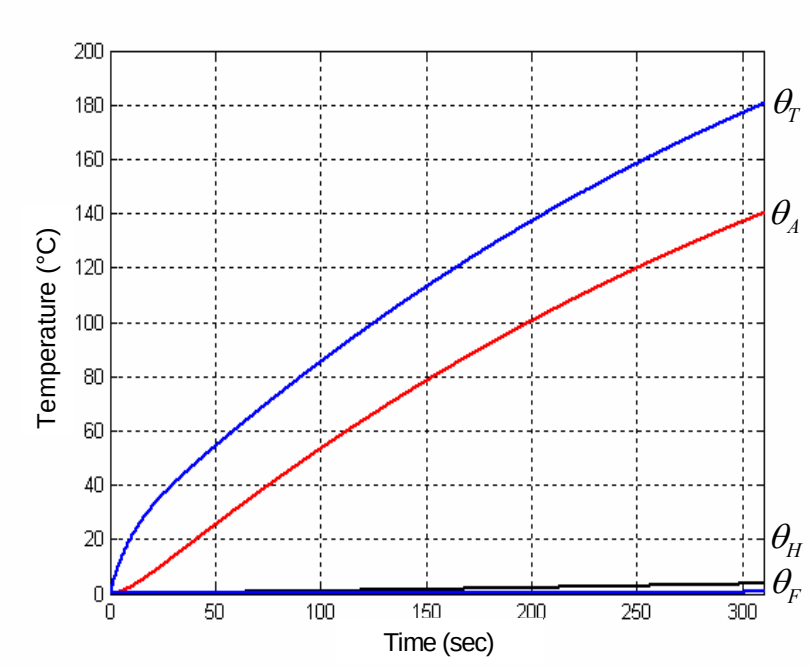

(a) Under condition 1 (MTPA)

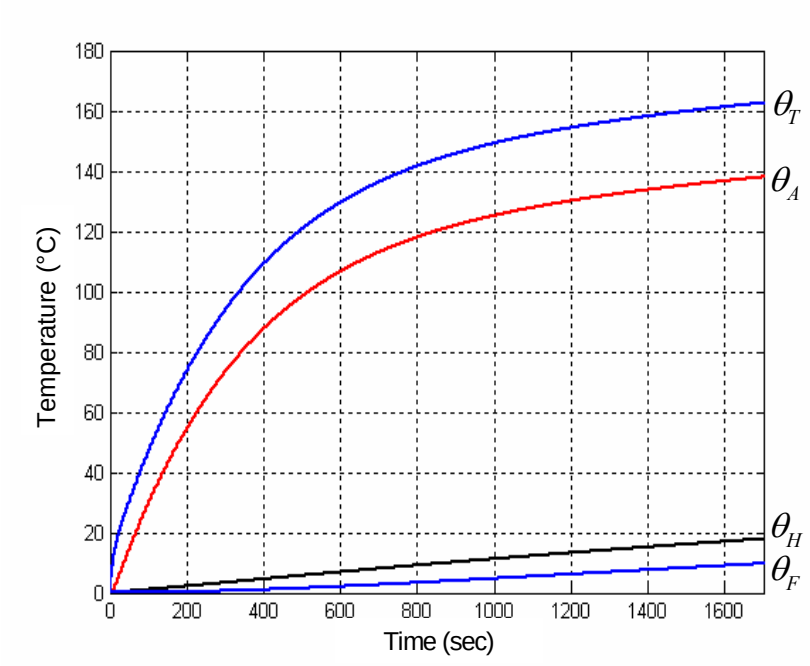

(b) Under condition 2 (25 % field-weakening)

Figure 12.5. Temperature estimation results showing the durations before θ_A reaches 140$^\circ C$ at five different combinations of i_{qs}^e and i_{ds}^e for 1000 rpm rotating speed and 10 Nm load operation.

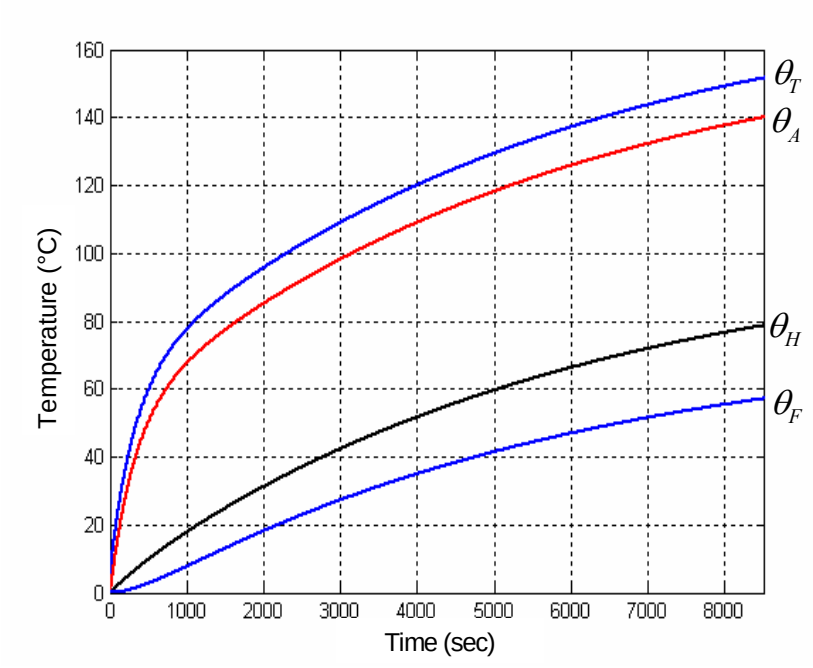

(c) Under condition 3 (50 % field-weakening)

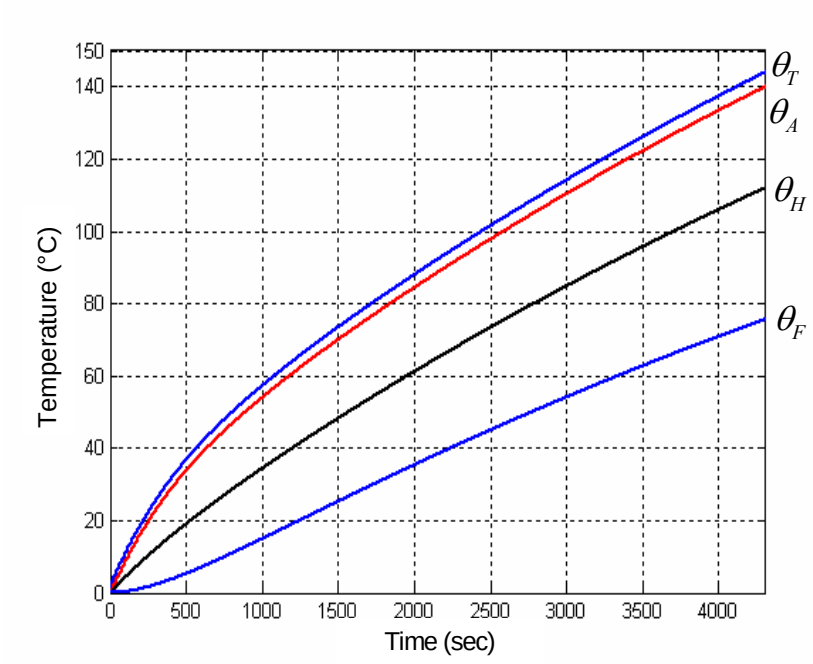

(d) Under condition 4 (75 % field-weakening)

Figure 12.5. Temperature estimation results showing the durations before θ_A reaches 140$^\circ C$ at five different i_{qs}^e and i_{ds}^e combinations for 1000 rpm rotating speed and 10 Nm load operation.

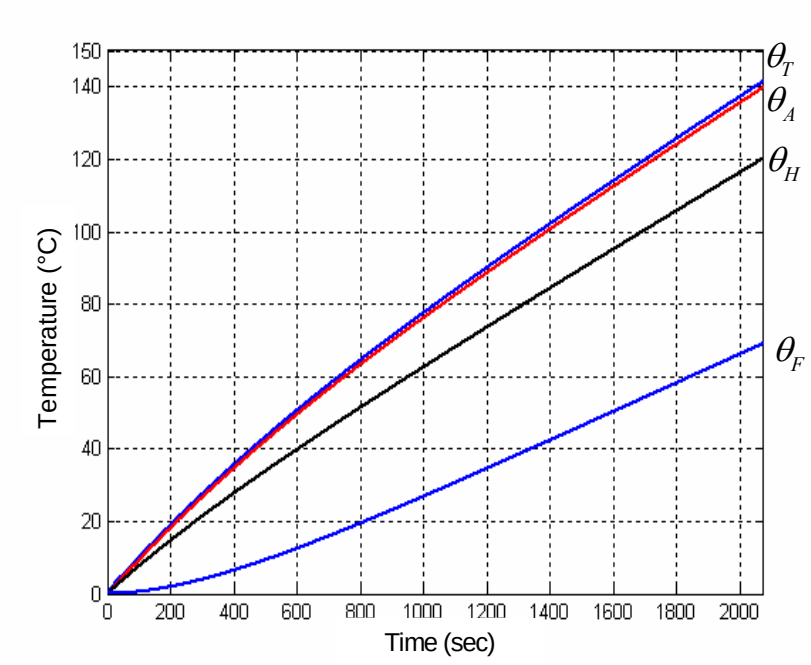

(e) Under condition 5 (100 % field-weakening)

Figure 12.5. Temperature estimation results showing the durations before θ_A reaches 140$^\circ C$ at five different combinations of i_{qs}^e and i_{ds}^e for 1000 rpm rotating speed and 10 Nm load operation.

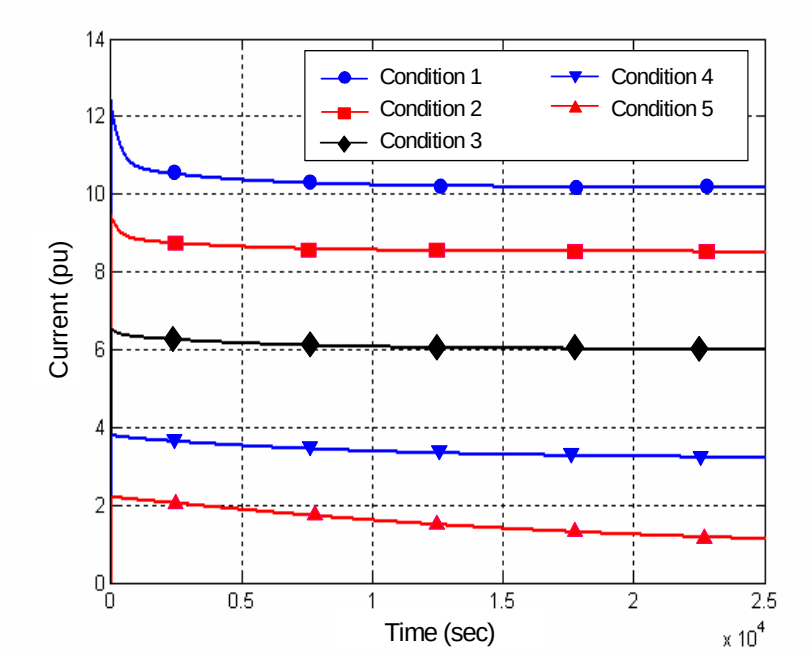

(a) Normalized circulating currents

Figure 12.6. Comparison of the normalized quantities in the shorted turns at five different combinations of i_{qs}^e and i_{ds}^e for 1000 rpm rotating speed and 10 Nm load operation.

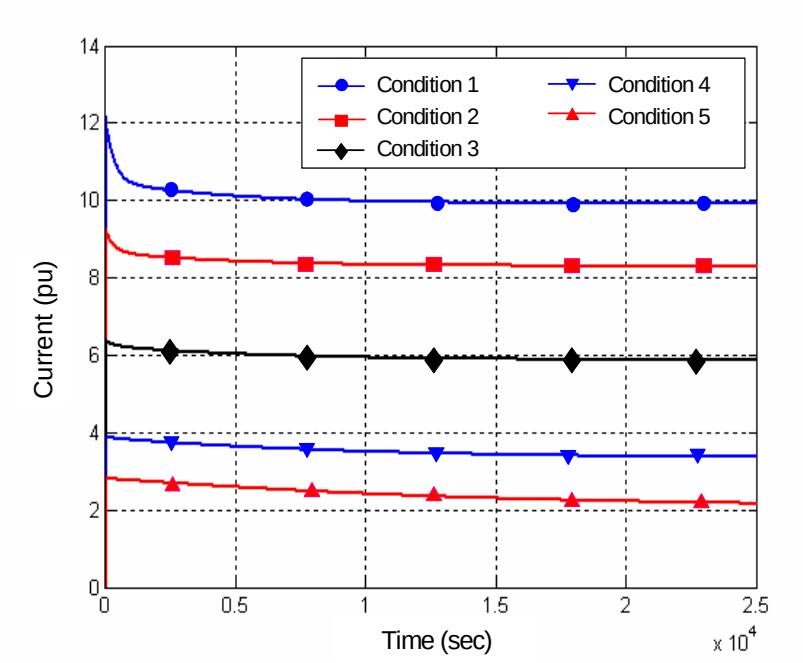

(b) Normalized current flowing through the shorted turns

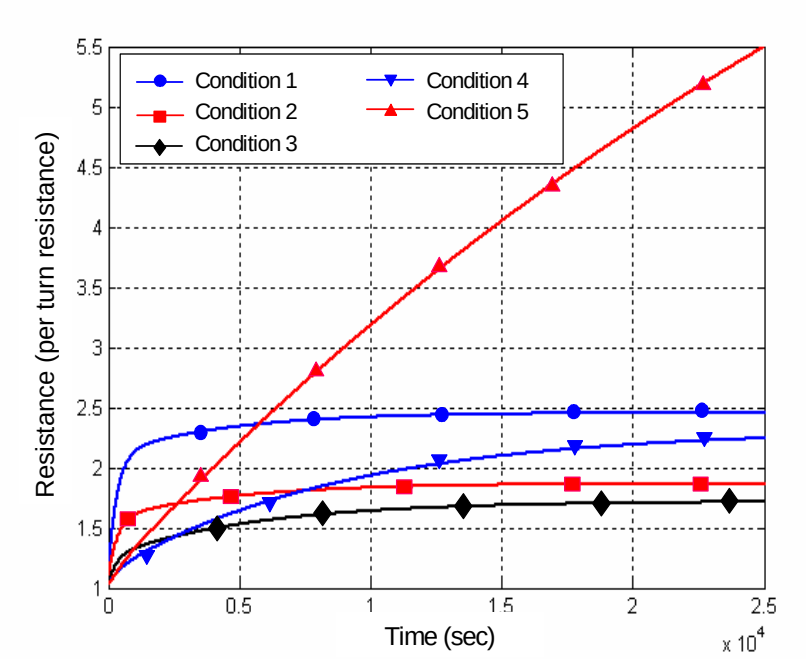

(c) Normalized resistance of the shorted turns

Figure 12.6. Comparison of the normalized quantities in the shorted turns at five different combinations of i_{qs}^{e} and i_{ds}^{e} for 1000 rpm rotating speed and 10 Nm load operation.

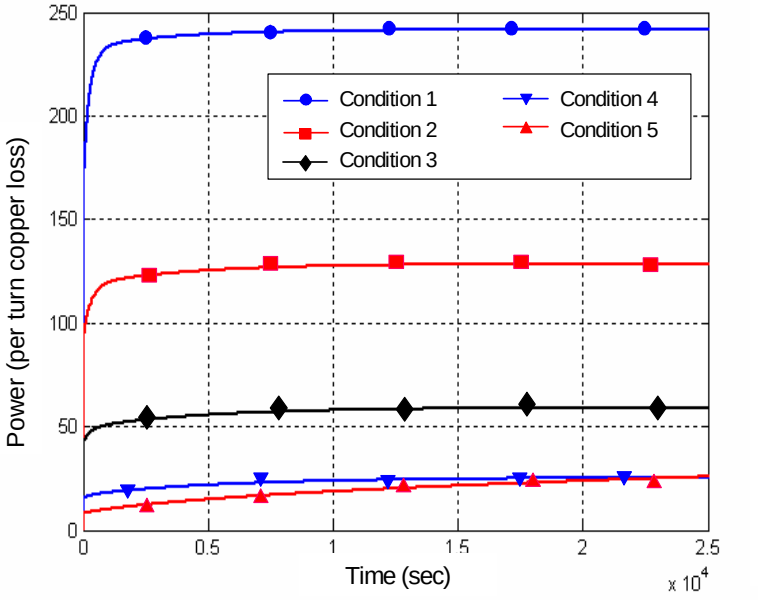

(d) Normalized copper loss in the shorted turns

Figure 12.6. Comparison of the normalized quantities in the shorted turns at five different combinations of i_{qs}^{e} and i_{ds}^{e} for 1000 rpm rotating speed and 10 Nm load operation.

Table 12.4. Estimated allowable operating durations at various combinations of i_{qs}^{e} and i_{ds}^{e} for 1000 rpm rotating speed and 10 Nm load operation.

Items	Unit	#1	#2	#3	#4	#5
Allowable Operating Duration	[sec]	310	1700	8500	4500	2070
Circulating Current (steady-state)	[pu]	10	8.5	6	3.5	1.3
Copper Loss at the Shorted Turns (steady-state)	[-]	230	125	59	25	25

As shown in Figure 12.5 and Table 12.4, the combinations of i_{qs}^{e} and i_{ds}^{e} for conditions 2, 3, 4, and 5 provide increased allowable operating durations as compared to that under MTPA operation (operation 1). However, the combination of i_{qs}^{e} and i_{ds}^{e} for condition 3 yields the longest allowable operating duration although the combination of i_{qs}^{e} and i_{ds}^{e} for condition 5 makes the circulating current smallest. In condition 5, the

stator current goes up to about two times the rated current to limit the circulating current to less than two times the rated coil current. This means that the stator current plays a more dominant role in the rises in θ_T, θ_A, and θ_H that the circulating current in the shorted turns under condition 5. On the other hand, under condition 1, wherein the stator current is the smallest, and the circulating current is the largest, the allowable operating duration is the shortest. This means that the circulating current dominantly increase θ_T and θ_A under condition 1. This observation implies a very important fact that *there is a specific combination of the amplitudes of the circulating current and stator current that maximizes the allowable operating duration of the proposed strategy for a given machine*. *The estimation results implies that for the case of the tested IPMSM, the allowable operating duration will be maximized up to at least two hours under the operation of the proposed strategy where the circulating current is limited within six times the rated coil current by a stator current around the rated machine current.* Based on this implication, the allowable operating area of the proposed strategy, where the tested IPMSM can operate during at least two hours without resulting in further insulation failures, is estimated in Figure 12.7. In the figure, the allowable operating area in the case of MPTA operation is also presented for comparison.

As shown in Figure 12.7, the proposed strategy tremendously increases the allowable operating area and duration of the tested IPMSM under a stator turn fault condition. However, it should be noted that the allowable operating area will change depending on the required operating duration of the proposed strategy. For example, the allowable operating area presented in Figure 12.3 can be maintained during at least twenty five minutes without resulting in the propagation of a stator turn fault.

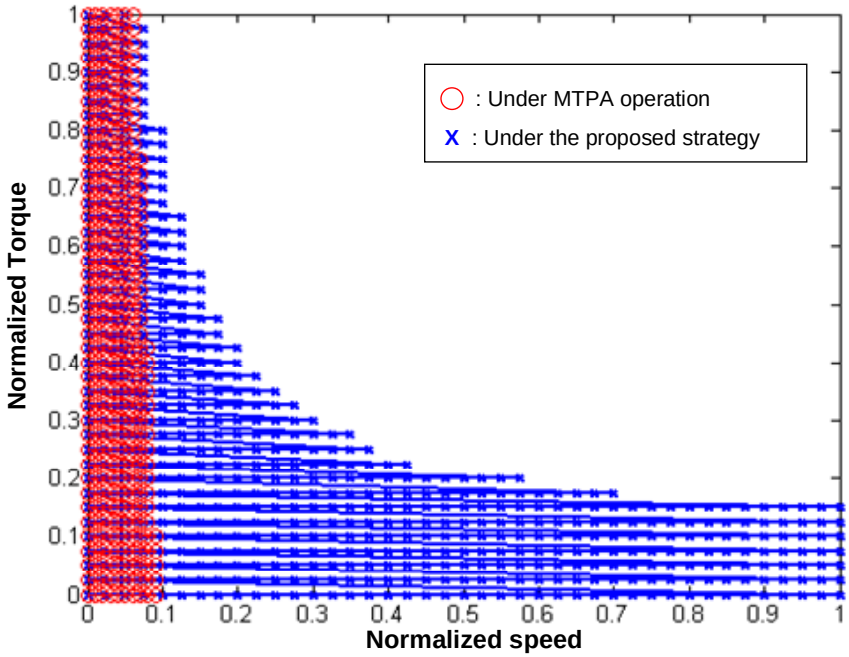

Figure 12.7. Comparison of the allowable operating areas where the operation can be maintained during at least two hours under MTPA operation and the proposed strategy.

12.2.4 Effects of Machine Specifications

As investigated in the previous section, the required stator current for the proposed strategy has considerable effect on the allowable operating area and duration of the proposed strategy. As discussed in section 7.2.1, if an IPMSM has a smaller characteristic current and a larger rotor saliency, a better performance of the proposed strategy is achievable.

In this section, the effects of the specifications of an IPMSM on the performance of the proposed strategy are investigated. For this investigation, three different sets of machine parameters are considered. The sets are selected to have similar values of maximum torques and rated currents with a given CCVSI. The lists of the three sets of machine parameters are summarized in Table 12.5.

Table 12.5. Parameter lists of three different machine designs.

Items	Unit	#1	#2	#3	Remark
Pole Number	[-]	8			
Max. Current	[A]	300			Inverter Max. Current
Rated Speed	[rpm]	2450			
DC-link Voltage	[Vdc]	216			
Stator Resistance	[mΩ]	4.85			
Leakage Inductance	[uH]	33			
d-axis Inductance	[uH]	220	311	127	
q-axis Inductance	[uH]	440	622	287	
Saliency Ratio	[-]	2	2	2.26	
PM Flux Linkage	[Wb]	0.0543	0.0384	0.0543	
Char. Current	[A]	247	123	428	

For this investigation, the magnetic non-linearity of the three different machine designs is ignored. As investigated earlier, the circulating current in the shorted turns (i_f) is a function of the stator resistance and leakage inductance. Thus, the stator resistances and leakage inductances of the three machine designs are assumed identical for only showing the effects of rotor saliency and characteristic current on the performance of the proposed strategy.

12.2.4.1 Comparison of the Performance Characteristics

The simulation results showing the performance characteristics of the three machine designs are provided in Figure 12.8. Figure 12.8(a) and (b) show the amplitude of the stator current and the trajectories of i_{qs}^e and i_{ds}^e for MPTA operation, respectively. And, Figure 12.8(c) and (d) compare the maximum torque-speed capabilities and the corresponding amplitude of the stator current for maintaining the maximum torque-speed operation, respectively.

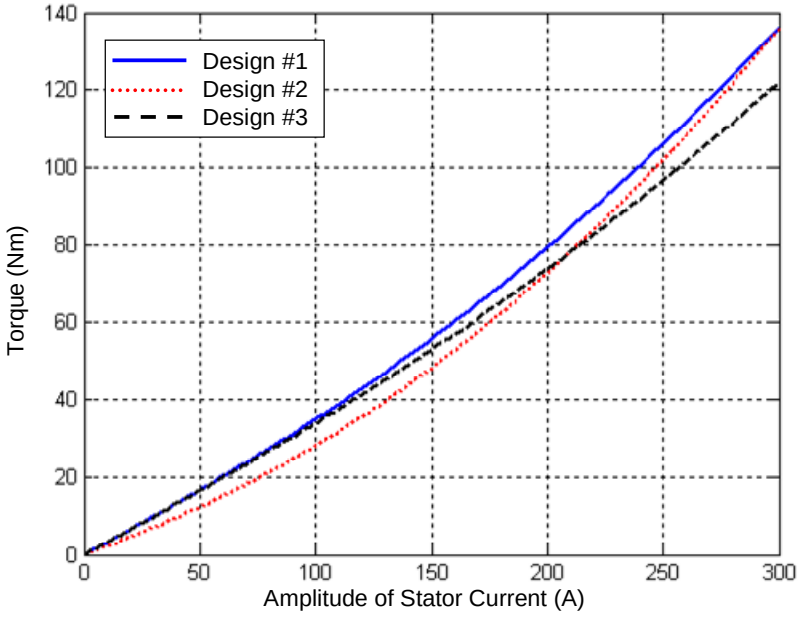

(a) Amplitude of the stator current for MTPA operation

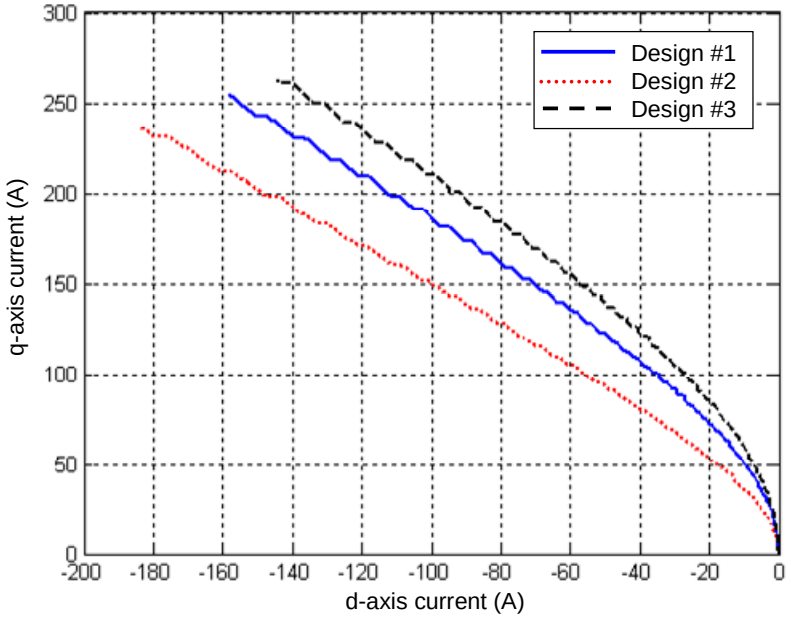

(b) Trajectories of the *q*-and *d*-axis currents for MTPA operation

Figure 12.8. Comparison of the performance characteristics of the three machine designs.

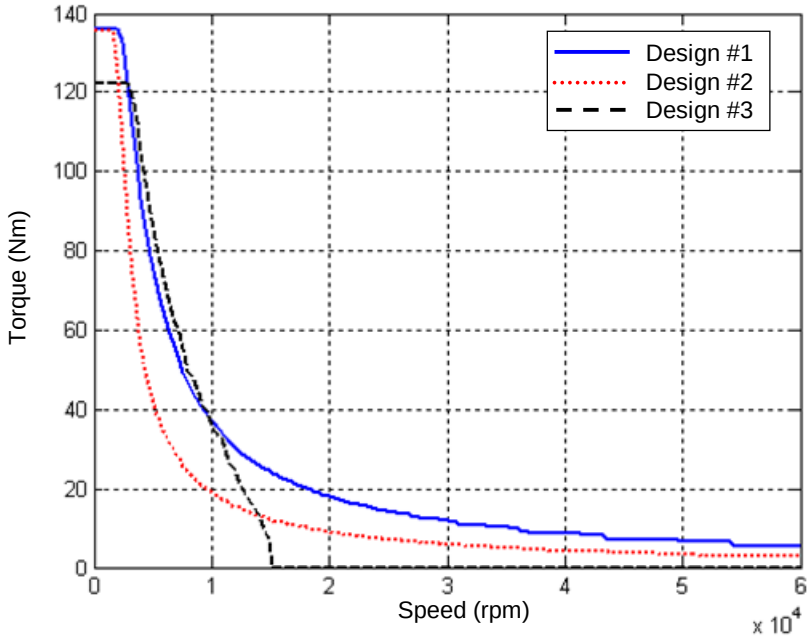

(c) Torque-speed Capability Curve

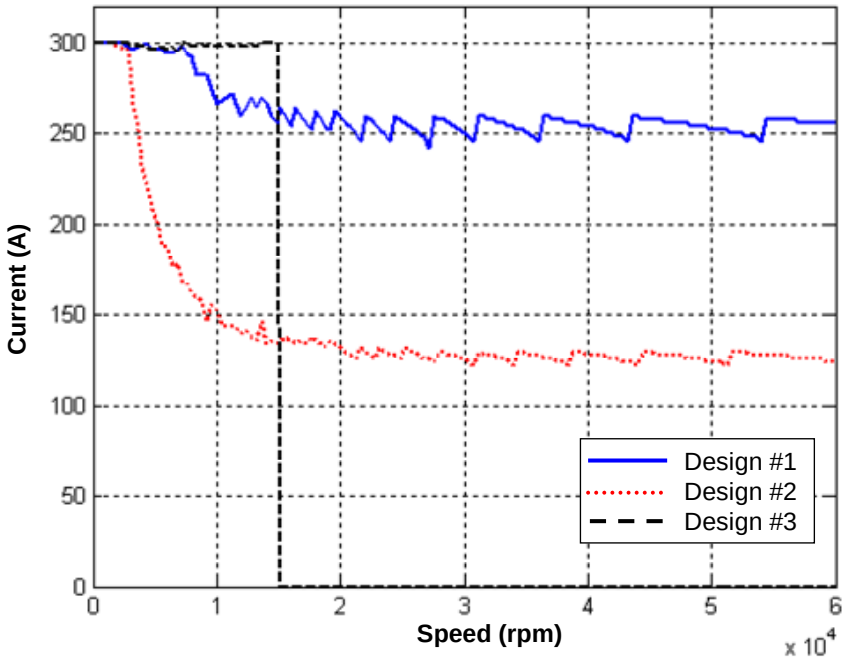

(d) Amplitude of stator current for maximum torque-speed operation

Figure 12.8. Comparison of the performance characteristics of the three machine designs.

As shown in Figure 12.8(c), the three machine designs yield similar ranges of maximum developed torque. However, it is shown in Figure 12.8(c) that design #3 has the narrowest constant-power speed ratio because the characteristic current of the design is the largest. Even though designs #1 and #2 have wide constant-power speed ratios, the amplitudes of the stator currents for field-weakening operation with maximum output power are quite different. As shown in Figure 12.8(d), in the case of design #1, the amplitude of the stator current is almost same as the maximum current rating, while that of design #2 is a half of the maximum current. This implies that design #2 requires a small current for field-weakening operation as compared to design #1, and consequently, the field-weakening operation of design #2 will be maintained for a longer duration than that of design #1.

12.2.4.2 Comparison of the Performance of the Proposed Strategy

To compare the performance of the proposed strategy for the three machine designs, their rated currents are set to the currents generating a developed torque of 40 Nm. The conditions for this comparison are summarized in Table 12.6. The corresponding results showing the amplitudes of the circulating currents under MTPA operation and the proposed tolerant operating strategy are presented in Figure 12.9 and Figure 12.10, respectively. In Figure 12.11, the amplitudes of the required stator currents of the three machine designs for the proposed strategy are provided. In these figures, *x*-axes represent the normalized values of the rotating speed referred to the rated speed (2450 rpm), and *y*-axes represent the normalized values of the developed torque referred to 40 Nm. Each *z*-axis in each figure represents the normalized quantity referred to the rated current of each design, respectively.

Table 12.6. Simulation conditions for comparing the performance of the proposed turn fault-tolerant operating strategy for the three machine designs.

Items	Unit	#1	#2	#3	Remark
Coils Connection	[-]	Series			
Fault Impedance	[mΩ]	0			a bolted turn fault
Rated Speed	[rpm]	2450			
Fault Fraction	[%]	1			
Max. Current	[A]	300			Max. Inverter Current
Rated Current	[A]	114	131	116.5	

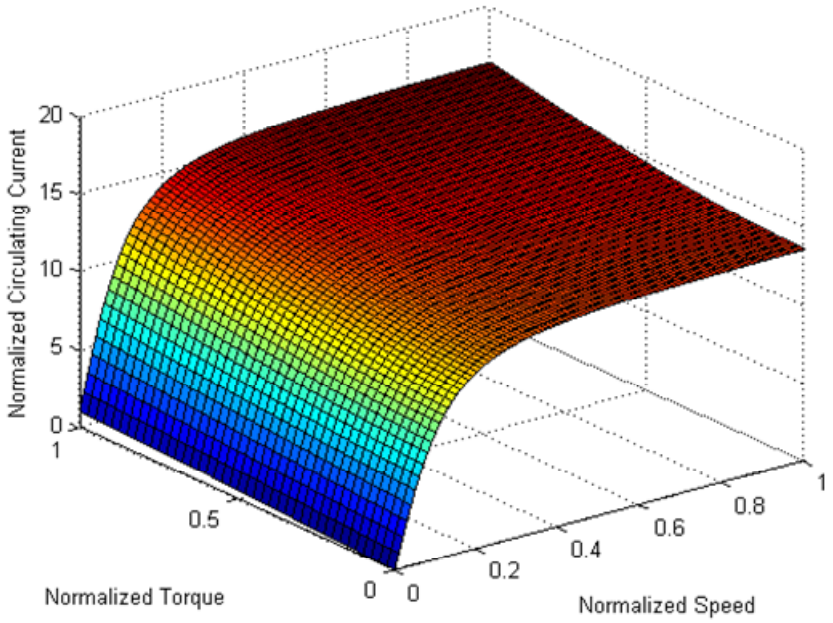

(a) In the case of design #1

Figure 12.9. Comparison of the normalized $|i_f|$ of the three machine design under MTPA operation.

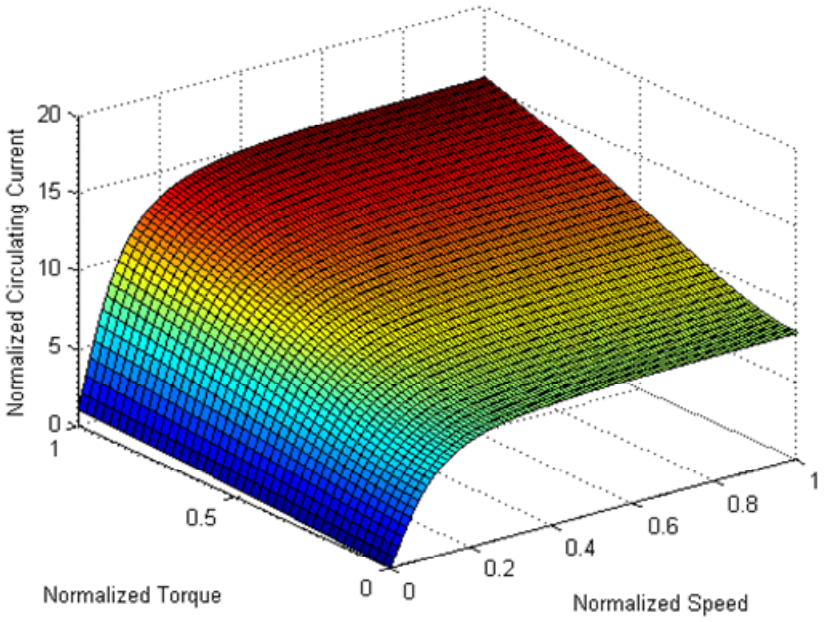

(b) In the case of design #2

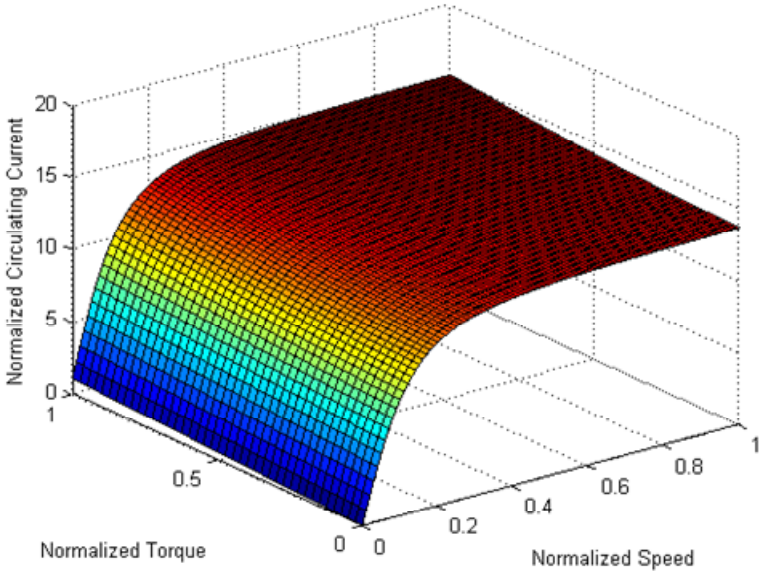

(c) In the case of design #3

Figure 12.9. Comparison of the normalized $|i_f|$ of the three machine design under MTPA operation.

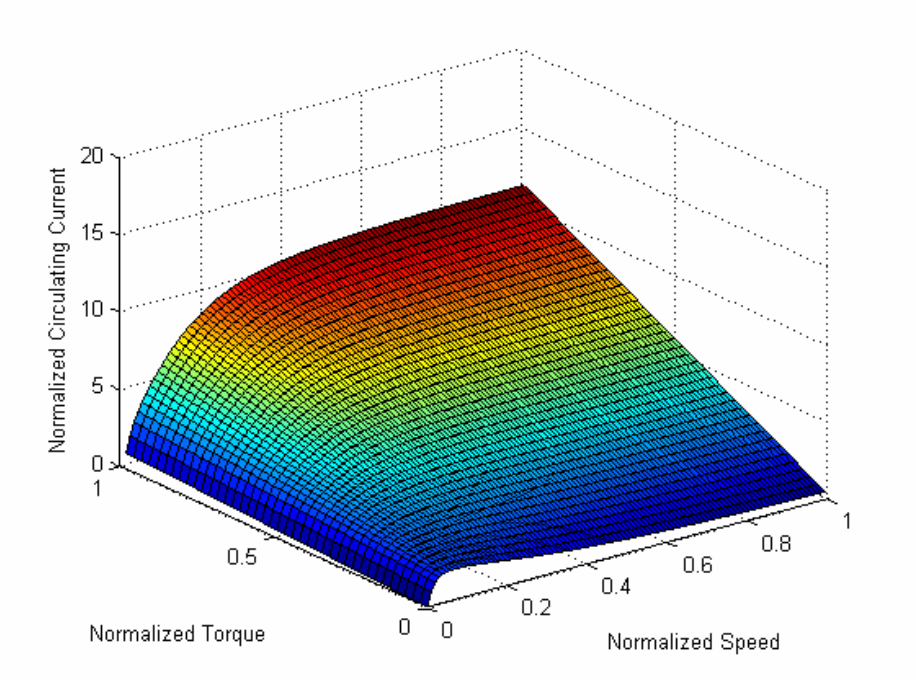

(a) In the case of design #1

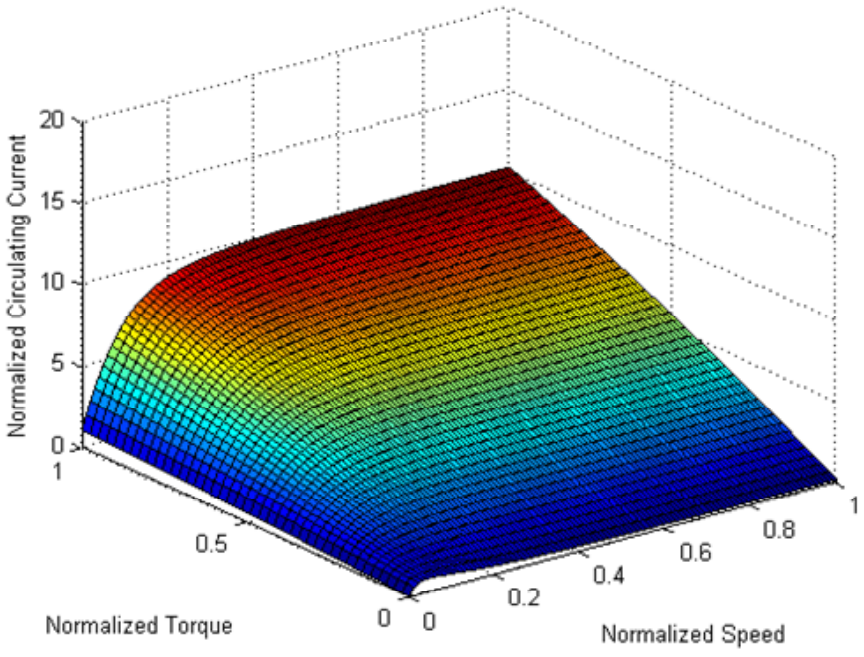

(b) In the case of design #2

Figure 12.10. Comparison of the normalized $|i_f|$ of the three machine design under the proposed tolerant strategy.

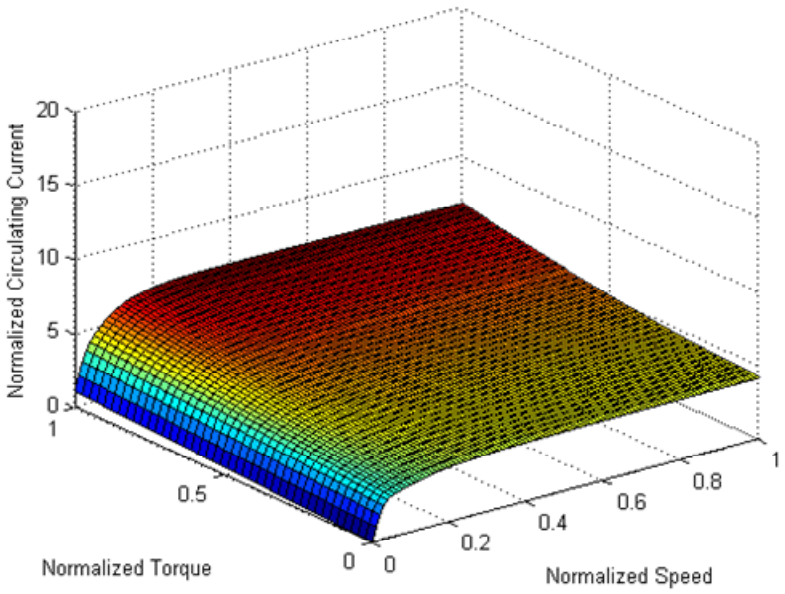

(c) In the case of design #3

Figure 12.10. Comparison of the normalized $|i_f|$ of the three machine design under the proposed tolerant strategy.

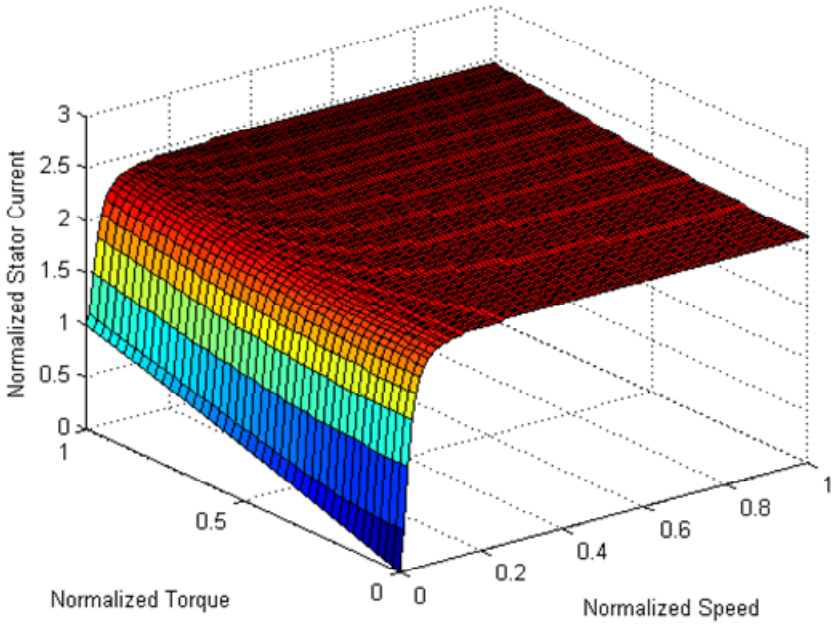

(a) In the case of design #1

Figure 12.11. Comparison of the amplitude of the required stator currents of the three machine designs under the proposed tolerant strategy.

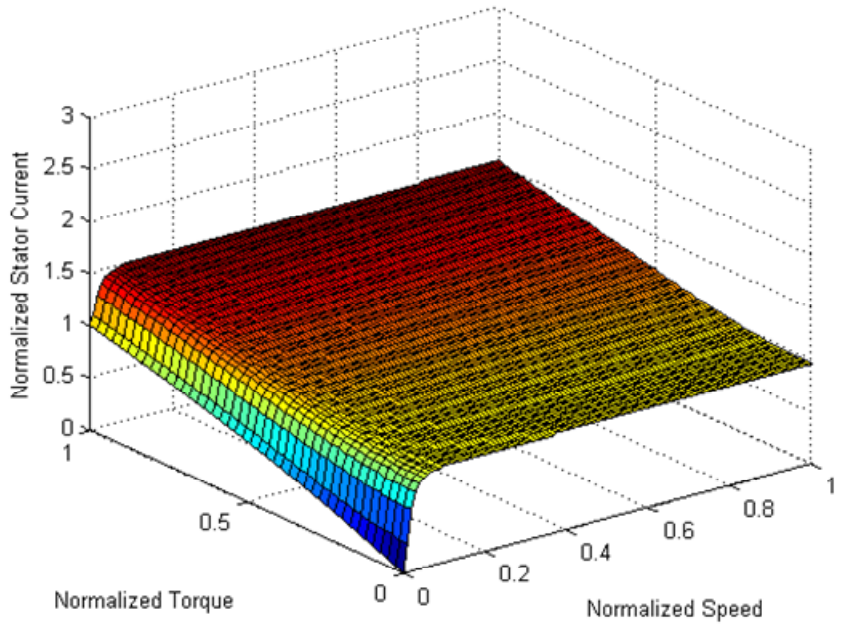

(b) In the case of design #2

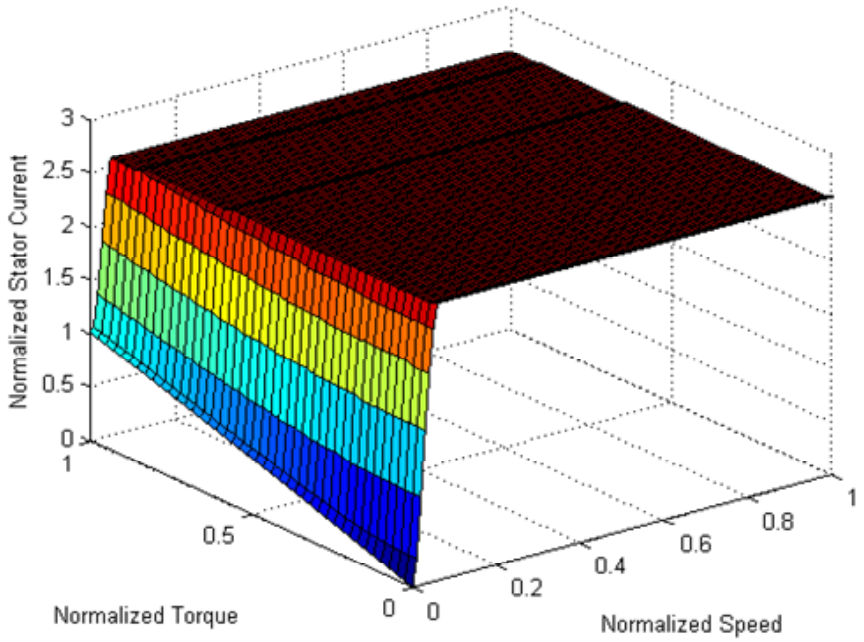

(c) In the case of design #3

Figure 12.11. Comparison of the amplitude of the required stator currents of the three machine designs under the proposed tolerant strategy.

The simulation results in Figure 12.9 show that the amplitudes of i_f under MTPA operation are in similar ranges regardless of the machine design. However, as shown in Figure 12.10, the amplitudes of i_f under the proposed strategy have quite different ranges depending on the machine design. The amplitudes of i_f of design #1 and #2 under the proposed tolerant strategy are almost same at entire operating points, but design #2 yields a slightly better performance in the reduction of i_f. On the contrary, the amplitudes of i_f of design #3 remains almost constant at around five times the rated current, regardless of operating point.

At first glance, design #3 seems to have the best performance under the proposed strategy, but a closer look at the results in Figure 12.11 reveals that this is not true. As shown in Figure 12.11, the required stator current of design #3 for the proposed strategy is the largest while being limited by the inverter maximum output current. This means that the increased stator current of design #3 will increase the winding temperature significantly. As a result, the allowable operating duration of the proposed strategy will be significantly decreased.

Although design #1 and #2 have similar performance in the reduction of i_f according to the results in Figure 12.10, the distinct superiority of design #2 to design #1 is found in Figure 12.11. The required stator current of design #1 for the proposed tolerant strategy is almost 2.5 times the rated current, while that of design #2 is at most 1.5 times rated current. This implies that the amount of stator copper loss of design #2 under the proposed tolerant strategy is only 36 % of the stator copper loss of design #1. This means that the allowable operating duration of the proposed strategy with design #2

will be much longer than that with design #1 when the two designs have the same thermal capacity.

The investigation performed in this section suggest that the performance of the proposed strategy will be enhanced when an IPMSM has a characteristic current whose amplitude is around the rated machine current. Furthermore, it is observed in the simulation results that a reduction of the characteristic current will not lead to any performance degradation of an IPMSM because the resultant reduction in the electromagnetic torque can be effectively compensated by adjusting to the rotor saliency.

12.3 Experimental Results

To verify the performance of the proposed strategy in reducing i_f, experiments are carried out at two different operation conditions. At each operating condition, the proposed strategy is applied with 49 % of the rated flux. The experimental conditions for the experiments are summarized in Table 12.7. The *b*-phase currents (i_b) and circulating currents (i_f) under the MTPA and the proposed strategy at the two experiments are compared in Figure 12.12 and Figure 12.13, respectively.

Table 12.7. Experimental conditions for verifying the proposed strategy.

Items	Unit	MTPA	Proposed Strategy
Coils Connection	[-]	Parallel	
Fault Location	[-]	A coil in the *b*-phase winding	
Fault Fraction	[%]	4.17 (one turn fault)	
Fault Impedance	[mΩ]	6.54	
Condition 1	[-]	500 rpm and no load	
Condition 2	[-]	1000 rpm and 10 Nm load	
Degree of Flux-Weakening	[%]	0	49

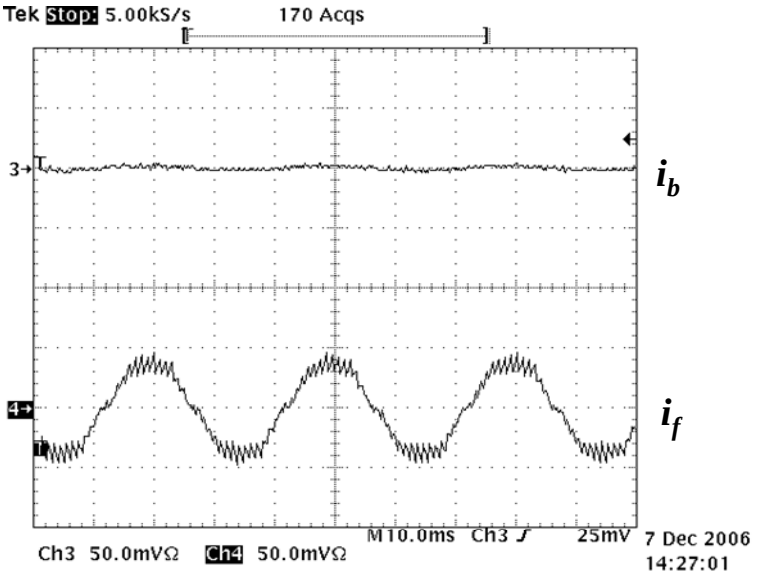

Ch.3: i_b (50 A/div.), Ch. 4: i_f (50 A/div.), Time (10 ms/div)

(a) Under MTPA operation

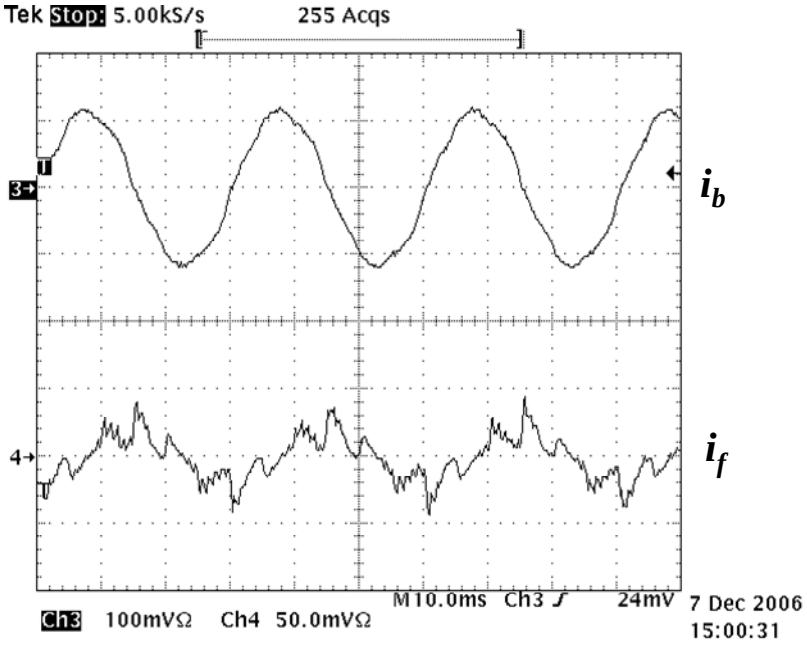

Ch.3: i_b (100 A/div.), Ch. 4: i_f (50 A/div.), Time (10 ms/div)

(b) Under the proposed strategy (49 % field weakening condition)

Figure 12.12. Comparison of i_b and i_f under the MTPA operation and the proposed strategy at 500 rpm rotating speed and no load.

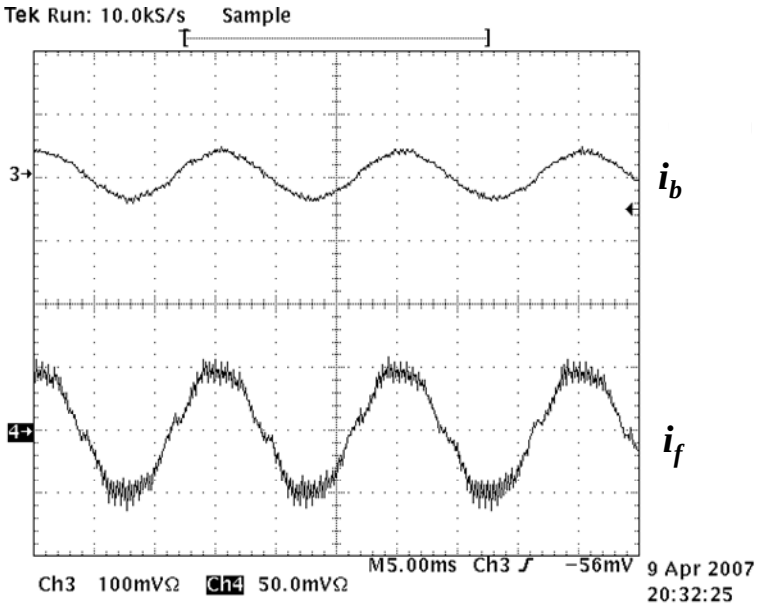

Ch.3: i_b (100 A/div.), Ch. 4: i_f (100 A/div.), Time (5 ms/div)

(a) Under MTPA operation

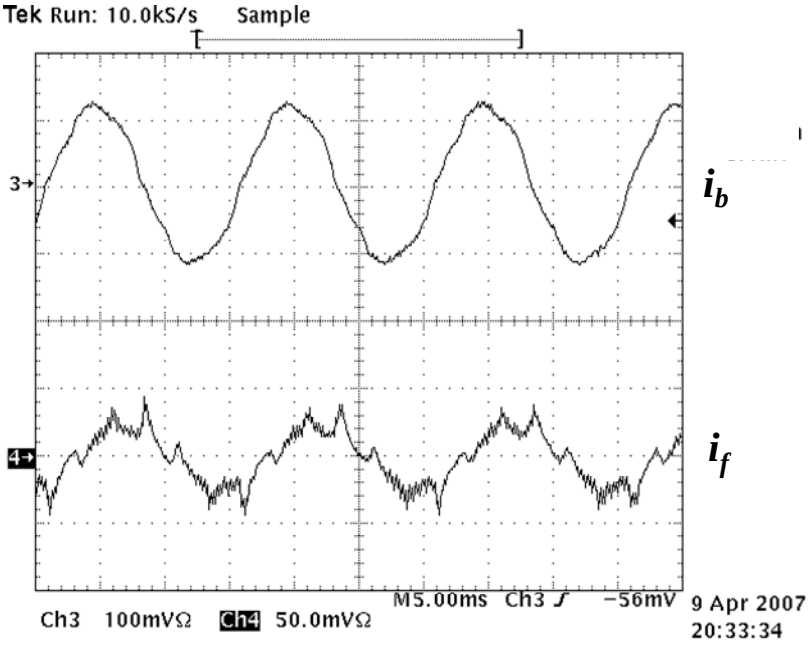

Ch.3: i_b (100 A/div.), Ch. 4: i_f (100 A/div.), Time (5 ms/div)

(b) Under the proposed strategy (49 % field weakening condition)

Figure 12.13. Comparison of i_b and i_f under the MTPA operation and the proposed strategy at 1000 rpm rotating speed and 10 Nm load.

The reductions in i_f resulting from the proposed strategy are clearly seen in Figure 12.12 and Figure 12.13. As investigated before, the stator currents are increased to maintain the given rotating speed and developed torque. But, the results show a phenomenon that has not been observed in the simulation results. In the waveforms of i_f, low order harmonic components are observed. Moreover, these harmonics are seen more clearly under the proposed strategy. The low order harmonics in i_f have contributions to the copper loss in the shorted turns because the loss is related to the rms value of i_f. However, the experimental results clearly show that the rms value of i_f is reduced as a result of the proposed strategy because the fundamental component of i_f is significantly reduced. This means that the proposed strategy reduces the copper loss, and consequently, slows down the propagation speed of the turn fault.

Although the experimental results clearly verify the performance of the proposed strategy, the results also suggest that the low order harmonics in i_f need to be reduced to achieve better performance. The presence of the low order harmonics can be explained as follows:

(1) As investigated earlier, the waveform of i_f is almost the same as that of the stator-line neutral voltage.

(2) As presented in Figure 9.9, the line-line back-emf voltage contains somewhat larger fifth- and seventh order harmonics, and the tap-tap back-emf voltage contains the third-order harmonic as well as the fifth- and seventh-order harmonics. Thus, the line-neutral back-emf voltage has the third-, fifth, and seventh-order harmonics.

(3) The third-order harmonic in the line-neutral back-emf has no effect on the line current because no third-order harmonic current can flow in a three-phase wye-connected machine having a floating neutral. Moreover, the inverter cannot compensate the third-order harmonic component in the stator line-neutral voltage because the floating neutral is not accessible. Therefore, the third-order harmonic line-neutral back-emf voltage induces the third-order harmonic component in i_f.

(4) On the other hand, the fifth- and seventh-order harmonics in the back-emf voltage will distort the line current when the inverter output voltage only contains the fundamental component. In this situation, if the line current is to be controlled sinusoidally, the inverter should inject the fifth- and seventh-order harmonics to the output voltage to eliminate the harmonics in the line current. The tested drive tries to control the line current sinusoidally based on this principle. This explains the presence of the fifth- and seventh-order harmonics in i_f. If this harmonic injection to the inverter output voltage is not carried out in phase with the harmonics in the back-emf voltage, the harmonic components in i_f can be increased under the proposed strategy. In addition, the implemented algorithm for this harmonic injection has a poor performance when the rotating magnetic flux is much weakened.

(5) The proposed strategy only considers the fundamental component in the rotating magnetic flux. Thus, the space harmonics in the rotating magnetic flux are not weakened by the proposed strategy.

Reduction of the low order harmonics is somewhat challenging. The fifth and seventh space harmonic in the rotating magnetic flux can be reduced by injecting fifth- and seventh-order harmonics to the *d*-axis current. But this will distort the line current. However, the most difficulty is that the third-order space harmonic in the rotating magnetic flux, which has the largest amplitude among the harmonic components, cannot be weakened at all. Only the possible way is to design an IPMSM so that the third-order harmonic in the rotating magnetic flux is minimized. Further research on the reduction of the low order harmonics in i_f remains future work.

12.4 Guideline of IPMSM Design for High Stator Turn Fault Tolerance

In the previous section, it was observed that machine specifications have considerable effects on the performance of the proposed turn fault-tolerant operating strategy. In this section, a general guideline for IPMSM design for a higher stator turn fault tolerance is provided. An important aspect of this guideline is that it should not result in any significant degradation in the basic motor performance requirements such as developed torque and speed range.

12.4.1 Design Criteria of IPMSMs

Regardless of the type of electric machines, the important performance characteristics are generally:

(1) High starting torque or higher torque at low speeds

(2) Wide constant-power speed ratio (CPSR)

(3) High power density

(4) High efficiency

An attractive feature in designing an IPMSM is the ability to adjust the relative contributions of electromagnetic torque and reluctance torque components to the machine's overall torque production. This appealing feature gives designers a large degree of freedom in selecting the set of machine parameters for meeting given requirements. However, any IPMSM design must tradeoff the desirable performance characteristics. For instance, the performance of peak torque capability at low speed may compromise a wider constant-power speed ratio [106]. To optimize the design of an IPMSM, many studies have been done in [106]-[109]. In these studies, IPMSM designs were investigated with varying the characteristic current and the rotor saliency ratio. At first glance, it may not be easy to see how only two parameters can define the performance of an IPMSM design. However, these two parameters contain sufficient information to define the contributions of electromagnetic and reluctance torque components to the machine's overall torque production. Furthermore, the machine terminal voltages can be approximated with these two parameters.

12.4.2 Characteristic Current

The investigations performed in [106]-[108] showed a very interesting fact. The widest field-weakening (constant-power speed ratio) performance is obtained when an IPMSM has a characteristic current whose amplitude is the same as its rated current. The studies performed in [1], [41], [52], and [53] showed that this one-per unit inductance machine has a higher fault tolerance to a line-to-line fault or a short-circuit failure of an

inverter switching device. As investigated in Section 12.1.4, the proposed turn fault-tolerant operating strategy yields its best performance to an IPMSM having one-per unit characteristic current.

One expected disadvantage resulting from one-per unit characteristic current is a reduction in peak torque capability. Generally, for a higher maximum torque, a large magnetic flux linkage contributed by permanent magnets (λ_{PM}) is required. However, this requirement is opposite to that for one per unit characteristic current. However, the reduction in peak torque capability can be effectively compensated by adjusting to the rotor saliency ratio.

12.4.3 Rotor Saliency Ratio

Once characteristic current is determined, then rotor saliency ratio needs to be adjusted to satisfy the required torque capability. In general, increasing rotor saliency is more difficult than decreasing it. This is mainly due to the allowable minimum air-gap length. However, as reported in [108], rotor saliency ratio can be increased up to 10 when the rotor core is laminated in the axial direction. Furthermore, rotor saliency can be also adjusted to by changing the shape or arrangement of the permanent magnets.

12.4.4 Winding Configuration

As discussed in section 3.3.2, a form winding configuration reduces the likelihood of a stator turn fault. However, form windings are not commonly applied in low-voltage machines because the winding configuration requires a larger stator slot area and higher cost than random windings. Nowadays, for multi-pole and concentrated winding PM machines, separable stator core design is gaining popularity since the core design can

reduce the time to wind the machine. With this design, the stator winding can be wound closer to a form winding configuration.

12.4.5 Space Harmonics in Rotating Magnetic Flux

As discussed in Section 12.2, space harmonics in the rotating magnetic flux have an adverse effect on the performance of the proposed turn fault-tolerant operating strategy. This means that the performance of the proposed strategy will improve as the low order harmonics are reduced.

Space harmonics in the rotating magnetic flux are due to non-sinusoidal winding and rotor magnet distributions. In general, a concentrated winding machine has a larger amount of low order space harmonics in the rotating magnetic flux than a distributed winding machine. However, the shape and distribution of permanent magnets also have considerable effects on the low order space harmonics. Furthermore, these harmonics can be reduced by skewing the stator slots.

12.5 Chapter Summary

In this chapter, the proposed turn fault-tolerant operating strategy has been validated through simulations and experiments. As verified by the simulation and experimental results, the proposed strategy is helpful to slow down the propagation of a stator turn fault, and subsequently, to prevent a serious accident resulting from the fault. The important facts, which have been observed during the verification of the proposed strategy, are summarized as follows:

(1) The circulating current in the shorted turns is significantly reduced by reducing the stator line-neutral voltage. The reduction in the voltage can be effectively carried out by appropriately adjusting the rotating magnetic flux.

(2) The proposed strategy significantly increases the allowable operating area and duration of an IPMSM drive under a stator turn fault condition. As a result, a serious accident resulting from an abrupt shutdown of the drive's operation can be prevented. However, the allowable operating area and duration of the proposed strategy are strongly related to the amplitudes of the circulating current and the stator current. This implies that for a given machine, there exists a specific combination of the amplitudes of the two currents that maximizes the allowable operating area and duration. To determine the specific combination, the thermal behavior of the machine with a stator turn fault must be known.

(3) The machine specifications, especially the characteristic current and rotor saliency ratio, have considerable effect on the performance of the proposed strategy. In addition, low order space harmonics in the rotating magnetic flux also affect the performance of the proposed strategy. Based on these observations, a general IPMSM design guideline for higher stator turn fault tolerance was provided.

Even though further research on the reduction of the low order harmonics in i_f remains future work, the practicality of the strategy has been clearly verified. The contribution of the proposed strategy is to provide a simple and cost-effective turn fault-tolerant operating strategy for IPMSM drives that can prevent a stator turn fault from

developing into the catastrophic phase. However, it should be emphasized that the proposed strategy can prevent a serious accident involving the loss of human life, caused by an abrupt shutdown of the drive.

CHAPTER 13

A STATOR TURN FAULT-TOLERANT OPERATING STRATEGY FOR INDUCTION MOTOR DRIVES

13.1 Overview

As verified in Chapter 12, the circulating current in the shorted turns in an IPMSM drive is significantly reduced by an appropriate adjustment to the rotating magnetic flux. Consequently, the propagation of a stator turn fault can be significantly slowed down. However, this principle is also applicable to any kind of electric machine drive that utilizes the rotor-field flux to generate the developed torque. To verify the generality of the principle, a stator turn fault-tolerant operating strategy for induction motor drives is developed and validated in this chapter.

13.2 Modeling of an Induction Motor with Stator Turn Faults

A phase-variable model of an induction motor with stator turn faults can be derived through the same approach as is applied for the case of an IPMSM. The only difference between the models of an induction motor and IPMSM is in the rotor-related parts [59]. In the henceforth analysis, a wye-connected series winding induction motor is considered.

The stator and rotor voltages, and developed torque of a fault-free induction motor are expressed in terms of phase variables, respectively by [59],

$$\boldsymbol{v}_{sn} = \boldsymbol{R}_s \boldsymbol{i}_s + \boldsymbol{L}_s \frac{d\boldsymbol{i}_s}{dt} + \boldsymbol{L}_{sr}(\theta_r)\frac{d\boldsymbol{i}_r}{dt} + \omega_r \boldsymbol{i}_r \frac{d\boldsymbol{L}_{sr}(\theta_r)}{d\theta_r}, \tag{13.1}$$

$$\boldsymbol{v}_r = 0 = \boldsymbol{R}_r \boldsymbol{i}_r + \boldsymbol{L}_r \frac{d\boldsymbol{i}_r}{dt} + \boldsymbol{L}_{sr}^T(\theta_r)\frac{d\boldsymbol{i}_s}{dt} + \omega_r \boldsymbol{i}_s \frac{d\boldsymbol{L}_{sr}^T(\theta_r)}{d\theta_r}, \tag{13.2}$$

$$T_e = \frac{P}{2}\boldsymbol{i}_s^T \frac{d\boldsymbol{L}_{sr}}{d\theta_r}\boldsymbol{i}_r, \tag{13.3}$$

where $\boldsymbol{v}_{sn} = \begin{bmatrix} v_{an} & v_{bn} & v_{cn} \end{bmatrix}^T$; $\boldsymbol{i}_s = \begin{bmatrix} i_a & i_b & i_c \end{bmatrix}^T$; $\boldsymbol{i}_r = \begin{bmatrix} i_{ar} & i_{br} & i_{cr} \end{bmatrix}^T$; $\boldsymbol{R}_s$ and $\boldsymbol{R}_r$ represent the stator and rotor resistance matrices, respectively; $\boldsymbol{L}_s$, $\boldsymbol{L}_r$, and $\boldsymbol{L}_{sr}$ represent the stator, rotor, and mutual inductance matrices, respectively; θ_r represents the rotor position in electrical radians; ω_r represents the rotor frequency in electrical radians per second; P is the number of poles. The machine parameters in (13.1)-(13.3) are represented as follows:

$$\boldsymbol{R}_s = diag\begin{bmatrix} R_s & R_s & R_s \end{bmatrix},\ \boldsymbol{R}_r = diag\begin{bmatrix} r_r & r_r & r_r \end{bmatrix} \tag{13.4}$$

$$\boldsymbol{L}_s = \begin{bmatrix} L_{ls} + L_{sm} & M_s & M_s \\ M_s & L_{ls} + L_{sm} & M_s \\ M_s & M_s & L_{ls} + L_{sm} \end{bmatrix}, \tag{13.5}$$

$$\boldsymbol{L}_r = \begin{bmatrix} L_{lr} + L_{rm} & M_r & M_r \\ M_r & L_{lr} + L_{rm} & M_r \\ M_r & M_r & L_{lr} + L_{rm} \end{bmatrix}, \tag{13.6}$$

$$\boldsymbol{L}_{sr} = L_{sr}\begin{bmatrix} \cos(\theta_r) & \cos(\theta_r + \frac{2\pi}{3}) & \cos(\theta_r - \frac{2\pi}{3}) \\ \cos(\theta_r - \frac{2\pi}{3}) & \cos(\theta_r) & \cos(\theta_r + \frac{2\pi}{3}) \\ \cos(\theta_r + \frac{2\pi}{3}) & \cos(\theta_r - \frac{2\pi}{3}) & \cos(\theta_r) \end{bmatrix}, \tag{13.7}$$

where R_s and R_r represent the per-phase stator and rotor resistances, respectively; L_{ls} and L_{sm} are the per-phase stator leakage and self-magnetizing inductances; M_s represents the mutual inductance between the stator phases; L_{lr} and L_{rm} are the per-phase rotor leakage and self-magnetizing inductances; M_r represents the mutual inductance between the rotor phases; L_{sr} represents the mutual inductance between the stator and rotor. When a stator turn fault occurs in the *a*-phase winding, the stator and rotor voltages, and developed torque can be expressed by in terms of phase variables, respectively by [59],

$$\boldsymbol{v}_{\boldsymbol{sn}}^{'} = \boldsymbol{R}_{\boldsymbol{s}}^{'}\boldsymbol{i}_{\boldsymbol{s}}^{'} + \boldsymbol{L}_{\boldsymbol{s}}\frac{d\boldsymbol{i}_{\boldsymbol{s}}^{'}}{dt} + \boldsymbol{L}_{\boldsymbol{sr}}^{'}(\theta_r)\frac{d\boldsymbol{i}_{\boldsymbol{r}}}{dt} + \omega_r\boldsymbol{i}_{\boldsymbol{r}}\frac{d\boldsymbol{L}_{\boldsymbol{sr}}^{'}(\theta_r)}{d\theta_r}, \tag{13.8}$$

$$\boldsymbol{v}_{\boldsymbol{r}} = 0 = \boldsymbol{R}_{\boldsymbol{r}}\boldsymbol{i}_{\boldsymbol{r}} + \boldsymbol{L}_{\boldsymbol{r}}\frac{d\boldsymbol{i}_{\boldsymbol{r}}}{dt} + \boldsymbol{L}_{\boldsymbol{sr}}^{'\boldsymbol{T}}(\theta_r)\frac{d\boldsymbol{i}_{\boldsymbol{s}}^{'}}{dt} + \omega_r\boldsymbol{i}_{\boldsymbol{s}}^{'}\frac{d\boldsymbol{L}_{\boldsymbol{sr}}^{'\boldsymbol{T}}(\theta_r)}{d\theta_r}, \tag{13.9}$$

$$T_e = \frac{P}{2}\boldsymbol{i}_{\boldsymbol{s}}^{'\boldsymbol{T}}\frac{d\boldsymbol{L}_{\boldsymbol{sr}}^{'}}{d\theta_r}\boldsymbol{i}_{\boldsymbol{r}}, \tag{13.10}$$

where $\boldsymbol{v}_{\boldsymbol{sn}}^{'} = \begin{bmatrix} v_{as1} & v_{as2} & v_{bn} & v_{cn} \end{bmatrix}^T$; $\boldsymbol{i}_{\boldsymbol{s}}^{'} = \begin{bmatrix} i_a & i_a - i_f & i_b & i_c \end{bmatrix}^T$; $\boldsymbol{R}_{\boldsymbol{s}}^{'} = diag\begin{bmatrix}(1-\mu)R_s & \mu R_s & R_s & R_s\end{bmatrix}$; μ represents the fault fraction; i_f represents the circulating current in the shorted turns;

$$\boldsymbol{L}_{\boldsymbol{s}}^{'} = \begin{bmatrix} (1-\mu)L_{ls} + (1-\mu)^2 L_{sm} & \mu(1-\mu)L_{sm} & (1-\mu)M_s & (1-\mu)M_s \\ \mu(1-\mu)L_{sm} & \mu L_{ls} + \mu^2 L_{sm} & \mu M_s & \mu M_s \\ (1-\mu)M_s & \mu M_s & L_{ls} + L_{sm} & M_s \\ (1-\mu)M_s & \mu M_s & M_s & L_{ls} + L_{sm} \end{bmatrix};$$

$$\boldsymbol{L}_{\boldsymbol{sr}}^{'} = L_{sr}\begin{bmatrix} (1-\mu)\cos(\theta_r) & (1-\mu)\cos(\theta_r + \frac{2\pi}{3}) & (1-\mu)\cos(\theta_r - \frac{2\pi}{3}) \\ \mu\cos(\theta_r) & \mu\cos(\theta_r + \frac{2\pi}{3}) & \mu\cos(\theta_r - \frac{2\pi}{3}) \\ \cos(\theta_r - \frac{2\pi}{3}) & \cos(\theta_r) & \cos(\theta_r + \frac{2\pi}{3}) \\ \cos(\theta_r + \frac{2\pi}{3}) & \cos(\theta_r - \frac{2\pi}{3}) & \cos(\theta_r) \end{bmatrix}.$$

The representations of the voltages at the healthy turns (as_1) and the shorted turns (as_2) in the a-phase winding can be obtained from (13.8), respectively as,

$$\begin{aligned} v_{as1} &= (1-\mu)[R_s i_a + \mathbf{L_{as}} \frac{d\mathbf{i_s}}{dt} + \mathbf{L_{asr}}(\theta_r)\frac{d\mathbf{i_r}}{dt} + \omega_r \mathbf{i_r} \frac{d\mathbf{L_{asr}}(\theta_r)}{d\theta_r}] \\ &\quad - \mu(1-\mu)L_{sm}\frac{di_f}{dt} \end{aligned}, \tag{13.11}$$

$$\begin{aligned} v_{as2} &= R_f i_f \\ &= \mu[R_s i_a + \mathbf{L_{as}} \frac{d\mathbf{i_s}}{dt} + \mathbf{L_{asr}}(\theta_r)\frac{d\mathbf{i_r}}{dt} + \omega_r \mathbf{i_r} \frac{d\mathbf{L_{asr}}(\theta_r)}{d\theta_r}], \\ &\quad - \mu[R_s i_f + (L_{ls} + \mu L_{sm})\frac{di_f}{dt}] \end{aligned} \tag{13.12}$$

where R_f represents a possible external impedance between the shorted turns, $\mathbf{L_{as}} = \begin{bmatrix} L_{ls} + L_{sm} & M_s & M_s \end{bmatrix}$, and $\mathbf{L_{asr}} = L_{sr}\begin{bmatrix} \cos(\theta_r) & \cos(\theta_r + \frac{2\pi}{3}) & \cos(\theta_r - \frac{2\pi}{3}) \end{bmatrix}$.

Rearranging (13.12) yields

$$\frac{R_f}{\mu} i_f + [R_s i_f + (L_{ls} + \mu L_{sm})\frac{di_f}{dt}] = v_{an}^0, \tag{13.13}$$

where v_{an}^0 represents the instantaneous value of the line-neutral voltage at the faulty phase winding.

Equation (13.13) implies an important fact that the circulating current in the shorted turns in an induction motor with a stator turn fault has the same relationship with the stator line-neutral voltage as the circulating current in an IPMSM, and thus, the same principle of the proposed stator turn fault-tolerant operating strategy for IPMSMs is applicable to the cases of induction motors. In the following section, the issue of how to apply the principle to induction motor drives is discussed.

13.3 Stator Turn Fault-Tolerant Operating Strategy for Induction Motor Drives

Under indirect rotor field oriented vector control, an induction motor in steady-state conditions is controlled to satisfy the following relationships [63]:

$$i_{dr}^{e} = 0 \text{ and } i_{qr}^{e} = -\frac{L_m}{L_r} i_{qs}^{e}, \tag{13.14}$$

$$\begin{aligned} &\lambda_{dr}^{e} = L_m i_{ds}^{e} \text{ and } \lambda_{qr}^{e} = 0 \\ &\lambda_{ds}^{e} = L_s i_{ds}^{e} \text{ and } \lambda_{qs}^{e} = (L_s - \frac{L_m^2}{L_r}) i_{qs}^{e} = \sigma L_s i_{qs}^{e}, \end{aligned} \tag{13.15}$$

where L_m represents the magnetizing inductance, and σL_s is defined as stator transient inductance where σ represents the leakage factor.

The *q*- and *d*-axis stator voltages and the developed torque of a fault-free induction motor in a steady-state condition in terms of the *qd*-variables in the synchronously rotating reference frame are given, respectively by,

$$\begin{bmatrix} v_{qs}^{e} \\ v_{ds}^{e} \end{bmatrix} = \begin{bmatrix} R_s i_{qs}^{e} + \omega_e L_s i_{ds}^{e} \\ R_s i_{ds}^{e} - \omega_e \sigma L_s i_{qs}^{e} \end{bmatrix}, \tag{13.16}$$

$$T_e = \frac{3}{2}\frac{P}{2}\frac{L_m}{L_r}\lambda_{dr}^{e} i_{qs}^{e} = \frac{3}{2}\frac{P}{2}(1-\sigma) L_s i_{ds}^{e} i_{qs}^{e}, \tag{13.17}$$

The complex vector form of the stator line-neutral voltage in this defined rotating reference frame is expressed as,

$$\tilde{v}_s = R_s(i_{qs}^{e} - j i_{ds}^{e}) + j\omega_e \sigma L_s (i_{qs}^{e} - j i_{ds}^{e}) + \omega_e (1-\sigma) L_s i_{ds}^{e}, \tag{13.18}$$

As shown in (13.18), the stator line-neutral voltage in an induction motor consists of the voltage drops at the stator resistance and stator transient inductance, and the rotor

induced voltage (back-emf voltage). Under almost operating conditions except very low speed ranges, the voltage drops at the stator resistance and stator transient inductance are much smaller than the rotor induced voltage. Thus, the stator line-neutral voltage can be reduced easily by reducing the flux (the *d*-axis current) at a given rotating speed and applied load condition. If the *d*-axis current is changed under the requirement of maintaining the same rotating speed and developed torque as before, then the corresponding *q*-axis current can be obtained using (13.17) as,

$$i_{qs1}^{e} = \frac{T_0}{\frac{3P}{4}(1-\sigma)L_s i_{ds1}^{e}} = \frac{C_1}{i_{ds1}^{e}}, \tag{13.19}$$

where T_0 is the given developed torque, i_{ds1}^{e} represents the newly applied *d*-axis current, and C_1 is a constant. And the corresponding synchronous frequency can be obtained as a function of i_{ds1}^{e} as,

$$\omega_{e1} = \omega_{m0} + \omega_{sl1} = \omega_{m0} + \frac{r_r}{L_r}\frac{i_{qs1}^{e}}{i_{ds1}^{e}} = \omega_{m0} + \frac{C_2}{(i_{ds1}^{e})^2}, \tag{13.20}$$

where ω_{m0} is the given rotating speed and C_2 is a constant.

By inserting (13.19) and (13.20) into (13.18), the following equation can be obtained:

$$\left|\tilde{v}_s\right| = \sqrt{\left[R_s\frac{C_1}{i_{ds1}^{e}} + \left(\omega_{m0} + \frac{C_2}{(i_{ds1}^{e})^2}\right)L_s i_{ds1}^{e}\right]^2 + \left[-R_s i_{ds1}^{e} + \left(\omega_{m0} + \frac{C_2}{(i_{ds1}^{e})^2}\right)\sigma L_s \frac{C_1}{i_{ds1}^{e}}\right]^2}. \tag{13.21}$$

Based on the same reasoning for the case of an IPMSM, the *d*-axis current minimizing i_f in an induction motor at a given operating condition can be determined by solving the following equation:

$$\frac{\partial \left|\tilde{v}_s\right|^2}{\partial i_{ds1}^e} = 0, \tag{13.22}$$

A simplified expression of (13.22) can be obtained as,

$$Ai_{ds}^{e*8} + Bi_{ds}^{e*6} + Ci_{ds}^{e*4} - D = 0, \tag{13.23}$$

where A, B, C, D are positive real values as functions of the rotating speed and developed torque. Even though equation (13.23) seems complicated, it can be seen that at least one real positive valued solution exist. This means that there exists a specific *q*-and *d*- axis current combination minimizing $\left|\tilde{v}_s\right|$ at every rotating speed and developed torque combination. Since all the coefficients in (13.23) are only related to motor parameters and the operating condition, the optimal trajectory of *q*-and *d*- axis currents minimizing $\left|\tilde{v}_s\right|$ can be extracted. Consequently, by controlling an induction motor along the trajectory under stator turn fault conditions, the circulating current in the shorted turns can be minimized.

13.4 Simulation Results

Simulations have been performed to validate the proposed strategy. In particular, the simulation results showing the following are provided:

(1) Reduction of the circulating current and increase of the allowable operating area under stator turn fault conditions

(2) Transient performance

The key specifications of the concerned induction motor drive in this work are summarized in Table 13.1. In all the simulations, a bolted turn fault with a fault fraction

of 1.03 % in the *a*-phase winding is considered. Also, the stator current is limited by the inverter maximum current rating, which is set to twice the motor rated current.

13.4.1 Reduction in Circulating Current and Increase in Allowable Operating Area

Figure 13.1 shows the trajectories of the *q*-and *d*-axis current combinations minimizing $|\tilde{v}_s|$ at every speed and torque combination within rated operation. Figure 13.2 illustrates the three-dimensional comparison of $|i_f|$ under the conventional control and proposed strategy. In these figures, the *x*- and *y*-axes represent the normalized values of the rotating speed and developed torque referred to their rated values. Each *z*-axis in Figure 13.1 and Figure 13.2 represents the normalized quantity referred to the rated stator current, respectively.

Table 13.1. Key specifications of the tested induction motor drive.

Class	Item	Unit	Value	Remark
Motor	Pole Number	[-]	4	
	Rated Power	[kW]	3.7	
	Rated Speed	[rpm]	1755	
	Coils per Phase Winding	[EA]	2	
	Turns per Coil	[Turns]	97	
	Rated Voltage	[Vrms]	230	
	Rated Current	[Arms]	12.5	6.5 Arms per coil
	Stator Resistance	[ohm]	0.332	per phase
	Rotor Resistance	[ohm]	0.237	
	Stator Leakage Inductance	[mH]	3	
	Rotor Leakage Inductance	[mH]	4.5	
	Magnetizing Inductance	[mH]	71	
Inverter	DC-Link Voltage	[Vdc]	216	
	Max. Current	[Arms]	25	
	Current Control Rate	[kHz]	7	
	Switching Frequency	[kHz]	7	
	PWM Scheme	[-]	SVPWM	

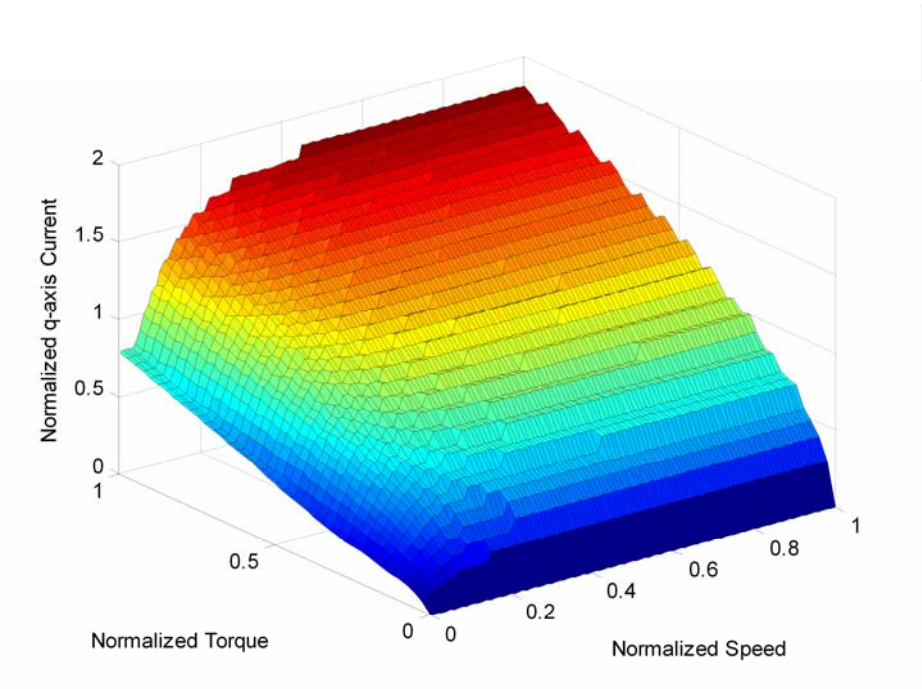

(a) *q*-axis Current

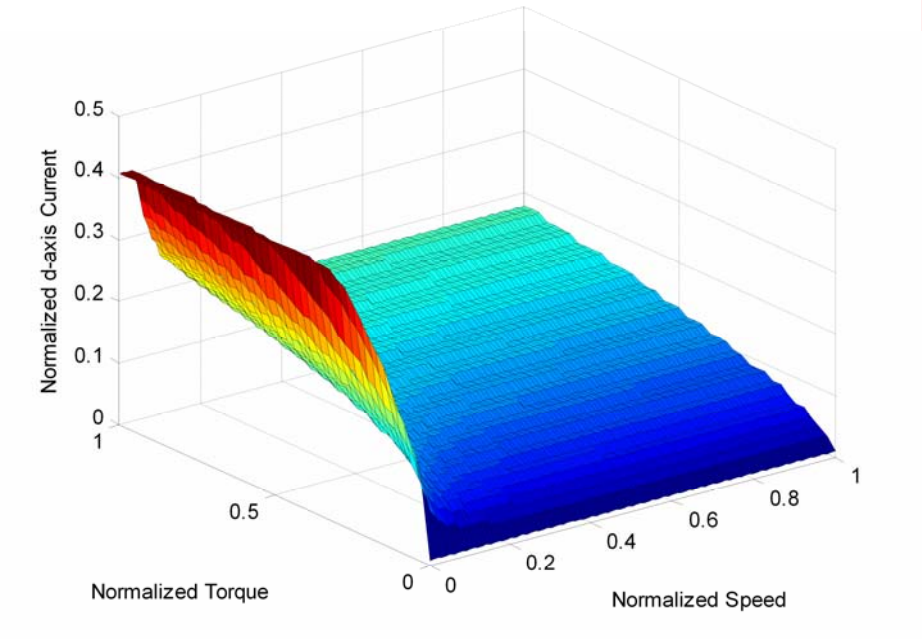

(b) *d*-axis Current

Figure 13.1. Simulation results showing the trajectories of the *q*- and *d*-axis current combination minimizing $\left|\tilde{v}_s\right|$ at every operating point within rated operations.

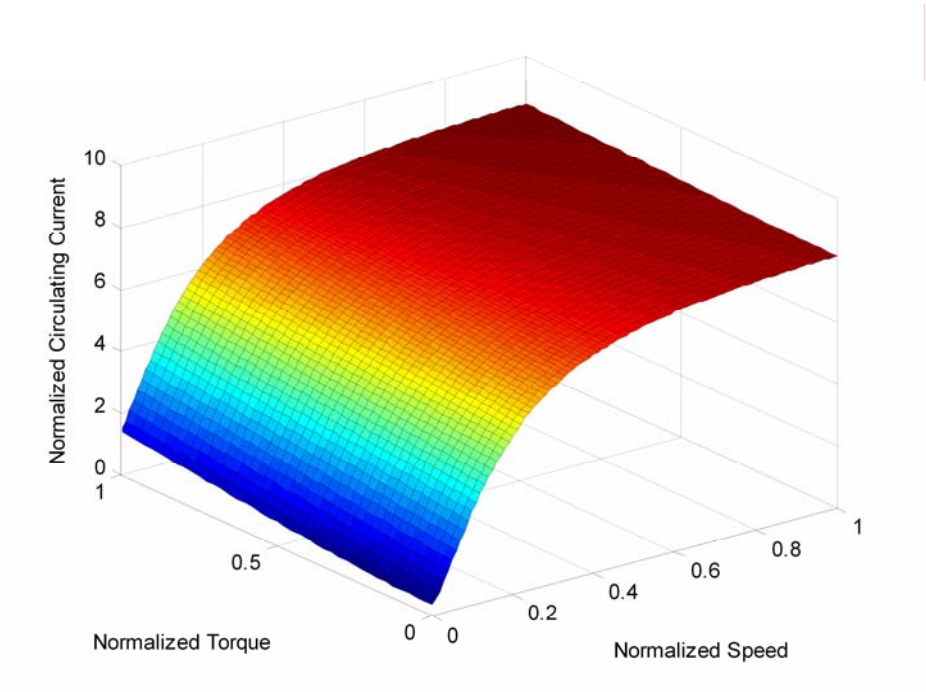

(a) Under the conventional control

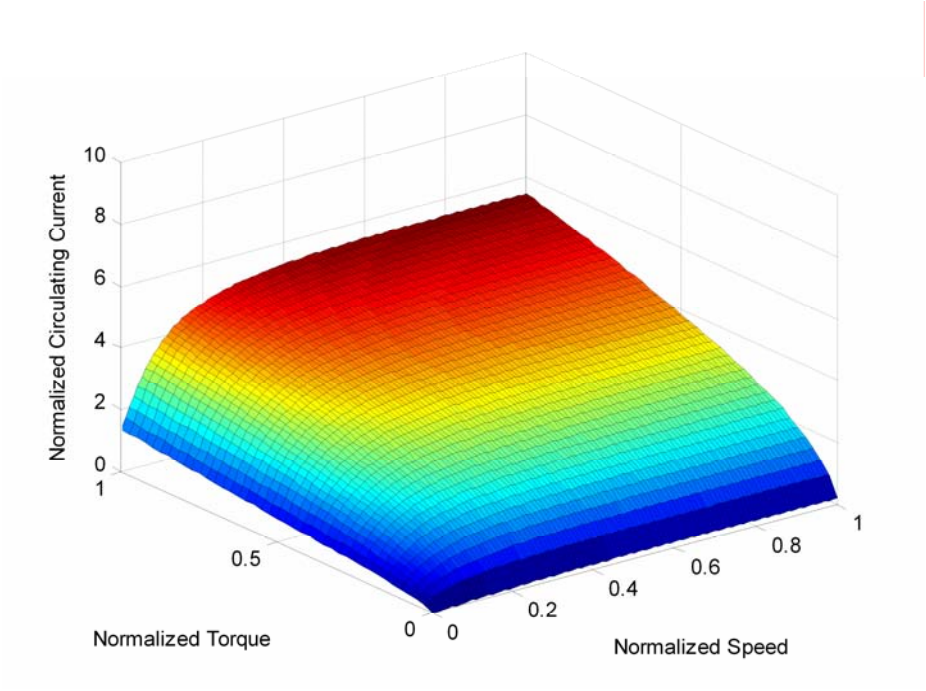

(b) Under the proposed strategy

Figure 13.2. Simulation results comparing the normalized $|i_f|$ at every operating point within rated operation under the conventional control and proposed tolerant strategy.

As shown in Figure 13.1, the *d*-axis current decreases to reduce the rotating magnetic flux, while the *q*-axis current increases in order to maintain a given developed torque. As a result, it can be seen that for a given rotating speed and developed torque, the stator current under the proposed strategy will be larger than that with conventional control. The same phenomenon was observed in the case of an IPMSM drive.

However, as in the case of IPMSM drives, the proposed turn fault-tolerant operating strategy for induction motor drives will significantly increase the allowable operating area of the drives under a stator turn fault condition. An example of this is provided in Figure 13.3. In the figure, the allowable operating areas, where $|i_f|$ is limited within three times the rated current, under the conventional vector control and proposed strategy, are compared.

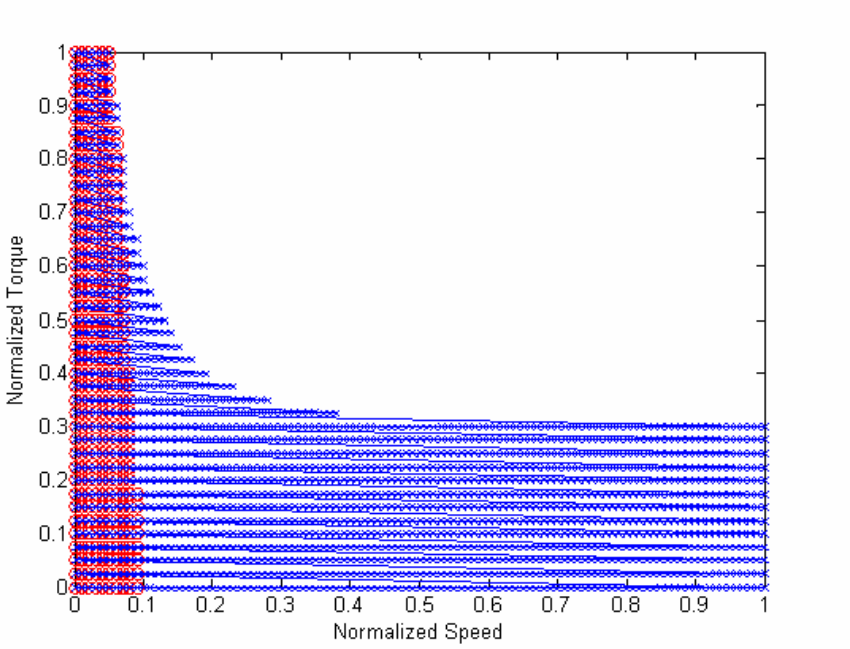

Figure 13.3. Simulation results comparing the allowable operating areas where $|i_f|$ is limited to three times the rated current under the conventional control (red circle-marked) and proposed strategy (blue x-marked).

13.4.2 Transient Performance of the Proposed Strategy

The transient performance of the proposed strategy is investigated by the simulation at 800 rpm rotating speed and 5 Nm load (0.25 times the rated torque). And the corresponding results are presented in Figure 13.4. In the figure, all the variables observed are normalized referred to their rated values. The arrow in the figure indicates the instant when the proposed strategy is activated.

The simulation results show clearly that the operation transition from the conventional vector control to the proposed strategy is performed smoothly without any significant fluctuations in the machine variables. Actually, the transient performance of the proposed strategy is mainly related to the control performance of the given drive because the operation transition only requires a change in the *q*- and *d*-axis current combination.

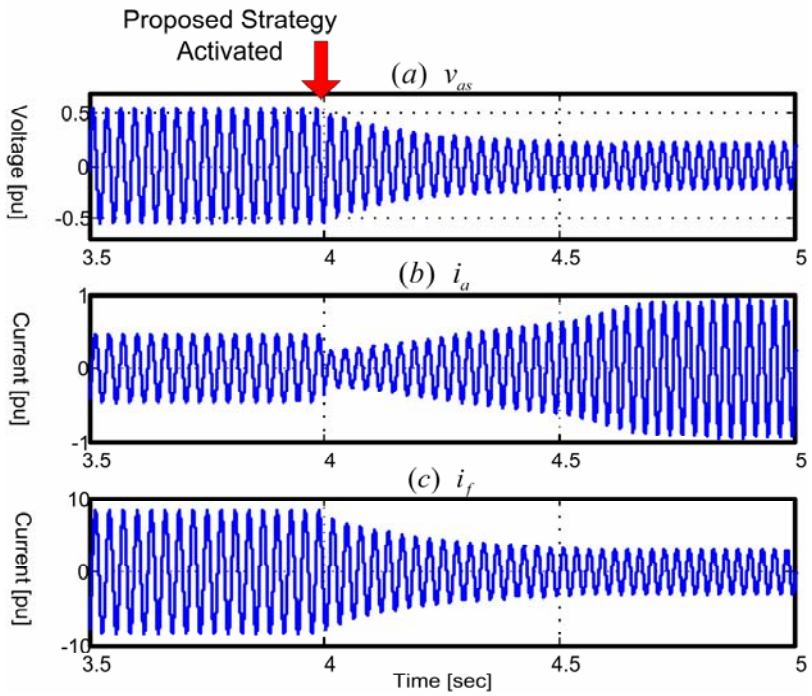

Figure 13.4. Simulation results at 800 rpm rotating speed and 0.25 rated torque load before and after activating the proposed strategy.

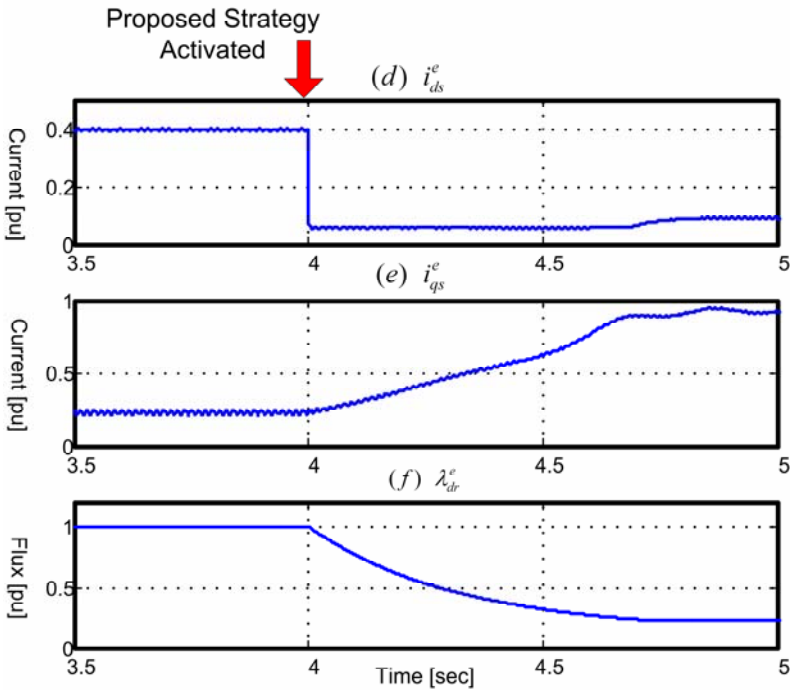

Figure 13.4. Simulation results at 800 rpm rotating speed and 0.25 rated torque load before and after activating the proposed strategy.

13.5 Experimental Results

The proposed stator turn fault-tolerant operating strategy has been tested on an induction motor drive. For the test, a specially prepared machine is used with access to 11 adjacent turns, for creating up to 10 turn faults. The picture of the special machine and schematic diagram of test bench are presented in Figure 13.5(a) and (b), respectively.

The experiment has been performed at 800 rpm rotating speed and 5 Nm load torque (0.25 times the rated torque) operating with a bolted turn fault between two turns. Figure 13.6 shows the rotating speed, i_{ds}^{e}, i_{qs}^{e}, i_{f}, and i_{a} before and after activating the proposed strategy. In Figure 13.6, the proposed strategy is activated at the instant that the arrow indicates.

As shown in Figure 13.6(a), i_{ds}^{e} decreases after activating the proposed strategy, while i_{qs}^{e} is increasing to maintain the rotating speed and developed torque. It should be noted that the rotating speed is not fluctuating regardless of these changes in the currents. In the experiment, the flux is decreased to 0.225 times rated flux.

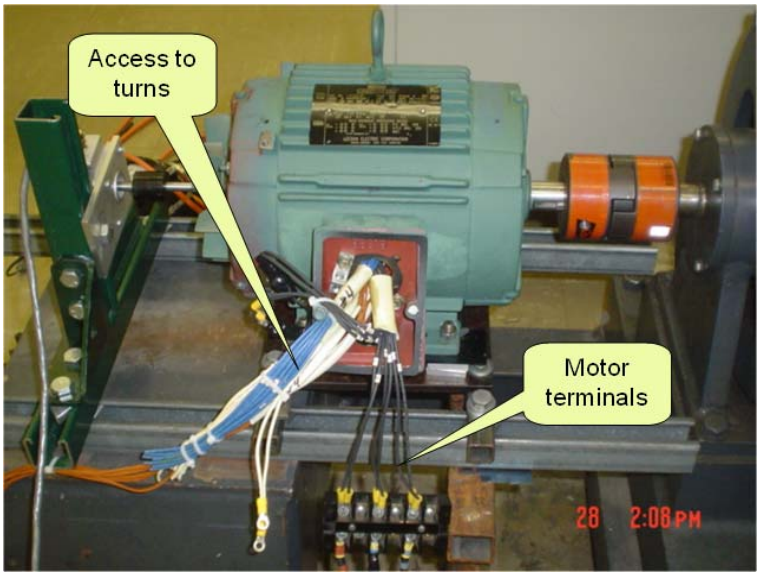

(a) Picture of the Tested Machine

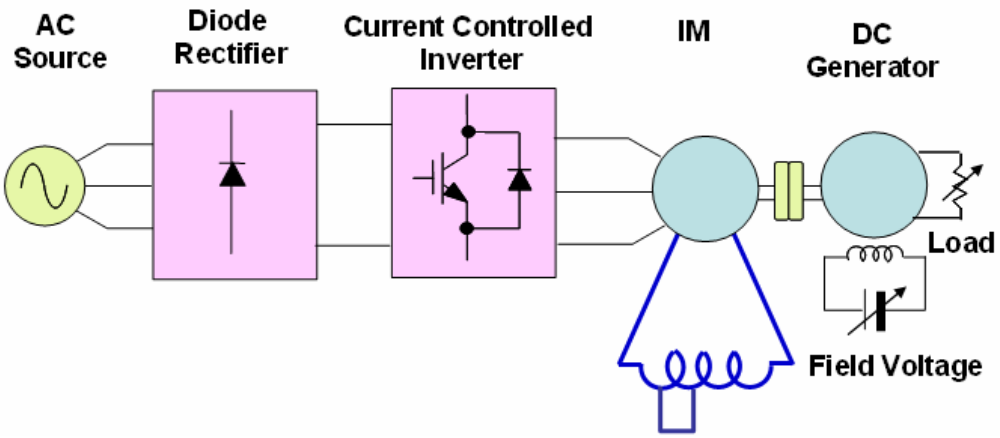

(b) Schematic of the Test Bench

Figure 13.5. Experimental Setup.

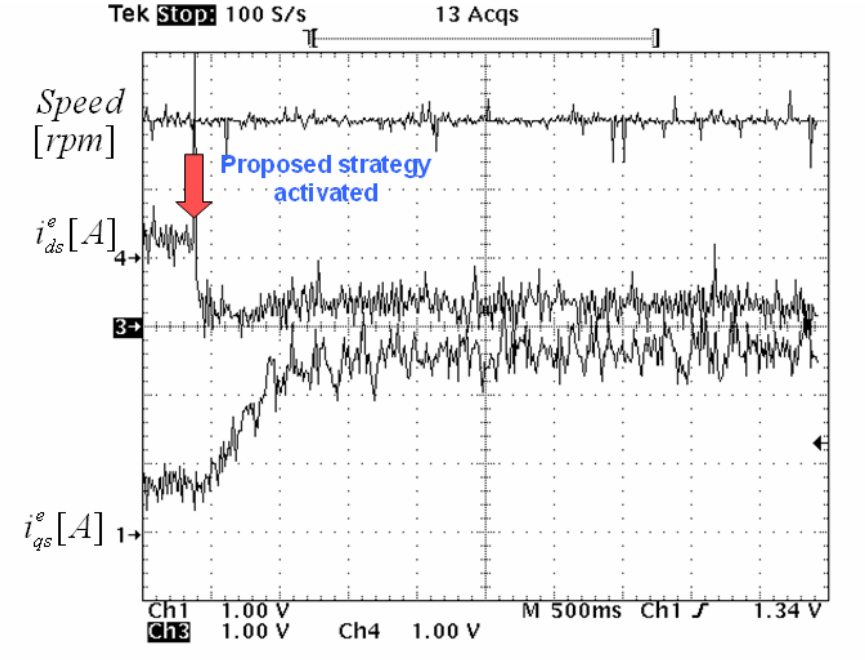

(a) Ch. 4: Rotating speed (400 rpm/V), Ch. 3: i_{ds}^{e} (5 A/V), Ch. 1: i_{qs}^{e} (5 A/V), Time (500 ms/div)

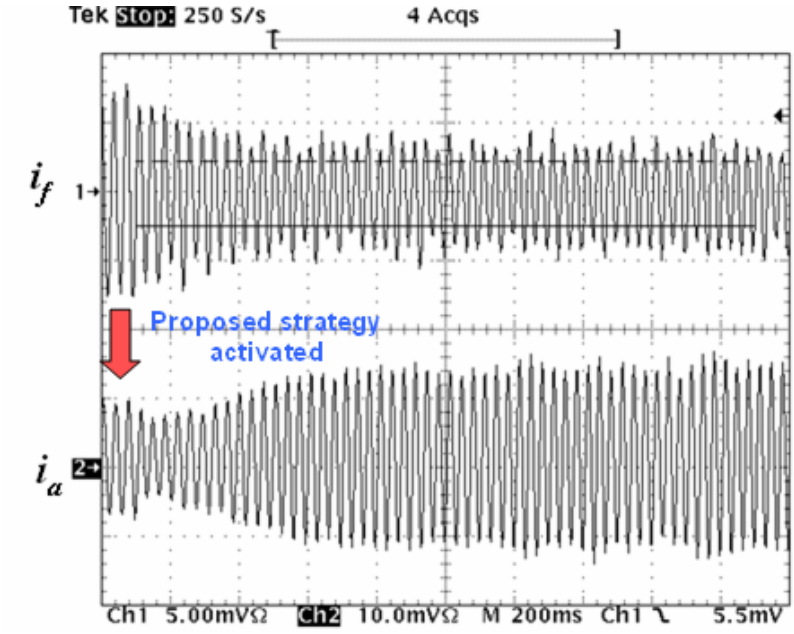

(b) Ch.1: i_f (50 A/10mV), Ch. 2: i_a (10 A/10mV), Time (200 ms/div)

Figure 13.6. Experimental results showing the transient performance of the proposed strategy at 800 rpm rotating speed and 5 Nm load.

The waveforms of i_f and i_a in a steady-state condition before and after activating the proposed strategy are presented in Figure 13.7(a) and (b), respectively.

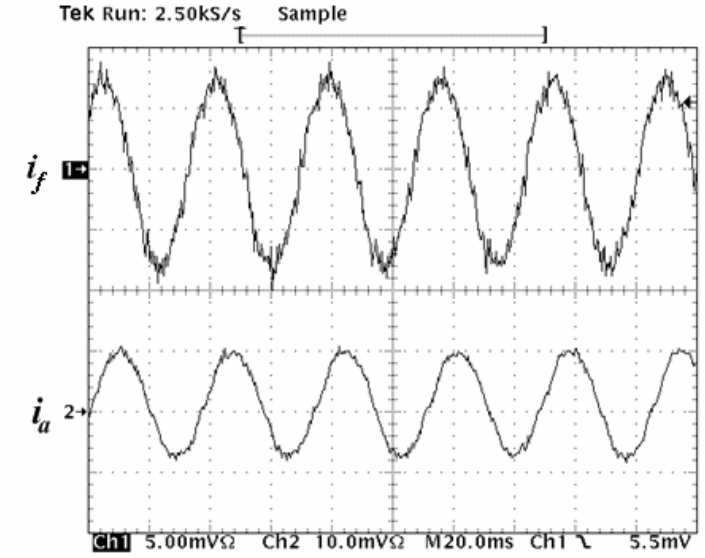

Ch.1: i_f (50 A/10mV), Ch. 2: i_a (10 A/10mV), Time (200 ms/div)

(a) Before activating the proposed strategy

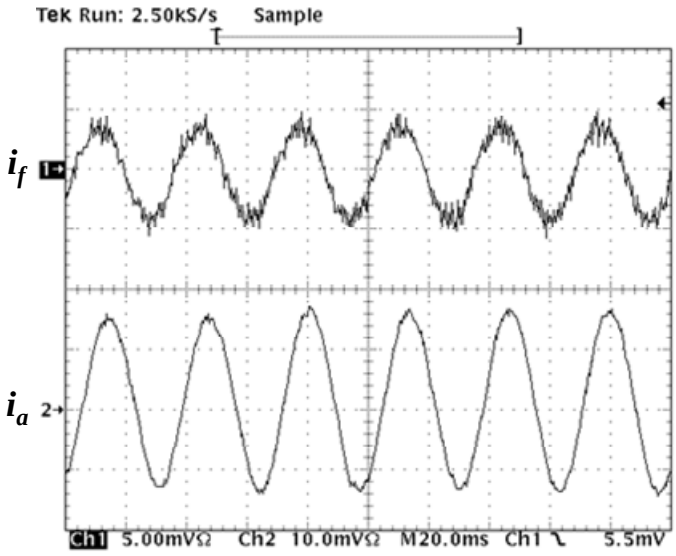

Ch.1: i_f (50 A/10mV), Ch. 2: i_a (10 A/10mV), Time (200 ms/div)

(b) After activating the proposed strategy

Figure 13.7. Experimental results showing the steady-state performance of the proposed strategy at 800 rpm rotating speed and 5 Nm load.

As shown in Figure 13.7, i_f is reduced from 5 times to 2.5 times the rated current with the aid of the proposed strategy, while i_a is increased from a half of the rated current to the rated current. It is observed that the experimental results are in accordance with the simulation results presented in Figure 13.4. Also, it can be found that that the synchronous frequency is increased due to the increased slip frequency. The smaller amount of discrepancy between the simulation and experimental results can be accounted for by inaccuracies in the values of the machine parameters. As mentioned before, the amplitude of the circulating current is strongly related to the stator resistance and leakage inductance as well as the stator line-neutral voltage. Furthermore, the externally added copper wires to access to turns in the stator winding will slightly increase the external impedance between the shorted turns.

When compared to the experimental results on the tested IPMSM in Figure 12.12 and Figure 12.13, the i_f in Figure 13.7 looks more sinusoidal. This comparison shows the effects of the low order space harmonic component of the rotating magnetic flux on the waveform of i_f. Moreover, the comparison implies the expected benefit when an electric machine has small amount of low order space harmonics in the rotating magnetic flux.

13.6 Chapter Summary

In this chapter, the generality of the principle of the stator turn fault-tolerant operating strategy developed in this work has been verified by showing the principle is applicable to induction motor drives. This implies that the principle will work for any

kind of electric machine drive that utilizes the rotor-field flux to generate the developed torque. However, as shown in the simulation and experimental results, the increased stator current for the proposed strategy will restrict the allowable operating area and duration of the proposed strategy. This means that the thermal behavior of an electric machine under the proposed strategy should be investigated to enhance the performance of the proposed strategy.

CHAPTER 14

CONCLUSIONS AND RECOMMENDATIONS FOR FUTURE WORK

14.1 Conclusions

The scope of this work was to achieve a high turn fault tolerance of an IPMSM drive in a safety-critical application for the prevention of a serious accident resulting from a stator turn fault. This objective was achieved by a reliable turn fault detection method and a simple turn fault-tolerant operating strategy.

A literature survey was presented to summarize the state of the art turn fault detection methods for CCVSI-driven machines. The use of CCVSIs increases the complexity of detecting stator turn faults. These difficulties are due to the controller actions, the drive's non-stationary operation, and the drive's non-idealities. To overcome these difficulties, several methods have been developed. But all the methods have trade-offs or limitations. Voltage-based methods are costly and inconvenient. Current-based methods are ineffective for CCVSI-driven IPMSMs. High frequency carrier signal injection-based methods are very complicated to implement. Furthermore, all the methods only consider turn faults in induction motors, while no turn fault detection method CCVSI-driven IPMSMs has been developed.

A thorough evaluation of the state of the art turn fault-tolerant operating strategies was provided. The evaluation clearly showed that all the previous strategies have unsatisfactory performance characteristics with respect to cost, efficiency, or availability.

However, the application of IPMSM drives is rapidly increasing in a wide variety of industrial areas. Thus, it is crucial to develop a turn fault-tolerant operating strategy for IPMSM drives that does not result in the complete loss of availability of the drives in the presence of a turn fault, and additionally, does not require any hardware modification to the standard drive configuration.

The first step towards the objective of this work was to investigate the characteristics of a stator turn fault in an IPMSM drive. For this purpose, a phase-variable drive-integrated model of an IPMSM with stator turn faults was developed. The use of equivalent circuit-based approach yields a much faster simulation speed than that of an FEA-based model. The inclusion of magnetic non-linearity made the simulation studies more realistic. Using the developed model, the characteristics of a stator turn fault in an IPMSM drive was extensively investigated with taking into account the effects of the drive's operation. The effectiveness of the developed model was verified by the simulation and experimental results. Also, it was shown that the observations in the simulations are in accordance with the findings in previous work.

The investigation using the developed model revealed two important facts for developing a turn fault detection method and a fault-tolerant operating strategy. The first was that a stator turn fault in an IPMSM drive reduces the positive sequence components of the machine impedances and back-emf voltages, and consequently leads to a reduced fundamental positive sequence voltage reference. The second fact is that the circulating current in the shorted turns is nearly proportional to the stator line-neutral voltage and is limited by the resistance and leakage inductance of the shorted turns.

The performance of the strategy should be particularly evaluated in terms of extending the allowable operating area and duration in the presence of a turn fault. For this evaluation, the investigation of the thermal behavior of a stator turn fault must be carried out. To this end, a thermal model of an IPMSM with stator turn faults was developed. The accuracy of the developed thermal model was verified by showing the estimated and measured temperatures have a quite good agreement with a difference of less than 1 $^{\circ}C$. The temperature estimation results with a one turn bolted fault at 1000 rpm and no load showed that the fault propagates to the adjacent turns within less than six minutes after the occurrence of the fault when no remedial action is taken. It can be easily inferred that the propagation speed of a turn fault will significantly increase as the rotating speed and applied load increases.

A voltage reference-based turn fault detection method was developed in this work. The use of voltage reference as the fault indicator does not result in any additional cost. The observation of the fault indicator in the synchronously rotating reference frame attenuates the effects of drive's non-stationary operation on turn fault detection with a small amount of computation. The employment of a look-up table based-turn fault decision algorithm makes the developed method convenient and reliable for IPMSM drives that control the machines with the rule of MTPA. The simulation results verified that the developed turn fault detection method works effectively whenever the drive operates in speed or torque control mode. The experimental results showed that the developed scheme is capable of detecting 1 turn fault out of 24 series turns in a single coil at 20 % of the rated speed and less than 6.25 % of the rated load.

A simple turn fault-tolerant operating strategy for IPMSM drives was developed based on the principle that the circulating current in the shorted turns can be significantly reduced by reducing the stator line-neutral voltage while maintaining the drive's uninterrupted operation. The investigation of the thermal behavior of a bolted turn fault using the developed thermal model revealed that there exists a specific combination of the amplitudes of the circulating current and the stator current that maximizes the allowable operating area and duration. The investigation also showed that the allowable duration of the tested IPMSM operation at 40 % of the rated speed and 25 % of the rated load is significantly extended from less than six minutes to at least two hours with the aid from the developed strategy. It was also shown that this extended operation can be maintained up to the rated speed and 15 % of the rated load. The investigation of the effects of the machine specifications on the performance of the developed strategy suggested that the performance of the developed strategy will be the best when an IPMSM has a characteristic current whose amplitude is around the rated machine current. The experimental results verified the principle of the developed strategy by showing that the amplitude of the fundamental component of the circulating current is reduced to about 50 % by reducing the fundamental component of the rotating air-gap flux to 49 % of the rated flux. However, it was observed that low order space harmonics in the rotating air-gap flux yield an adverse effect on the performance of the developed strategy. For better performance, these low order harmonics should be weakened in an appropriate manner. However, it should be emphasized that the extension in the operating area and duration of the developed strategy is achieved without any hardware modification to the standard drive configuration.

To verify the generality of the principle of the developed strategy, a stator turn fault-tolerant operating strategy for induction motor drives was developed and validated through simulations and experiments. The simulation and experimental results showed that the developed strategy for induction motor drives reduces the circulating current from 5 times to 2.5 times the rated current at 45 % of the rated speed and 25 % of the rated load.

14.2 Contributions

The research performed in this work on stator turn fault detection and turn fault-tolerant operating strategy includes the followings: 1) electrical modeling of an IPMSM drive with stator turn faults (Chapter 4 and 9), thermal modeling of an IPMSM with stator turn faults (Chapter 5 and 10), turn fault detection for IPMSM drives (Chapter 6 and 11), turn fault-tolerant operating strategy for IPMSM drives (Chapter 7 and 12), and turn fault-tolerant operating strategy for induction motor drives (Chapter 13). Many original contributions have been made in all five of the fore-mentioned areas, which are summarized as follows:

(1) A phase-variable based model of an IPMSM with stator turn faults was developed and integrated with a CCVSI model. In addition, the developed model was derived to be applicable to either series or parallel connected phase winding coils. For more realistic simulations, the magnetic non-linearity was also considered. These distinct features make it possible to investigate the behavior of a stator turn fault in an IPMSM drive with an appealing accuracy

and a fast simulation speed. Furthermore, the developed simulation model can be used as a reliable test bench for evaluating any method for turn fault diagnosis or turn fault-tolerant operating strategies.

(2) A methodology for studying the thermal behavior of a stator turn fault was proposed. Based on the proposed method, a thermal model of an IPMSM with stator turn faults was developed and verified experimentally. This developed thermal model provides valuable information to predict the remaining life of the motor or to establish an alarm level for the safe operation with a stator turn fault. This means that the developed thermal model will yield a significant contribution to the area of stator turn fault-tolerant operating strategy.

(3) A voltage reference-based turn fault detection method for IPMSM drives was developed and verified by experiments. The proposed method is capable of detecting a stator turn fault independently of applied load level. Furthermore, the method is immune to the influence of motor non-idealities. However, it is worth emphasizing that the appealing performances of the proposed turn fault detection method are achieved without any additional voltage sensors and significant burden to the drive's control tasks.

(4) A simple and effective stator turn fault-tolerant operating strategy for IPMSM drives was proposed and verified. The originality of the proposed strategy is that the proposed strategy can prevent a stator turn fault from developing into the catastrophic phase without resulting in the complete loss of the drive's availability; furthermore, it does not require any hardware modification to the

standard drive configuration. However, the most valuable contribution of the proposed strategy is that it can save human life by preventing a possible serious accident as a result of the abrupt shutdown of the drive's operation. Another contribution of the proposed stator turn fault-tolerant operating strategy is that the principle of the strategy is applicable to any type of electric drive that utilizes the rotating air-gap flux to generate the developed torque.

The work done in this thesis has resulted in several publications. Four conference papers have has been published [60], [110]-[112], and one journal paper has been submitted for review [113].

14.3 Recommendations for Future Work

Although this work has provided contributions to the areas of stator turn fault detection and turn fault-tolerant operating strategy, there are several directions in which further research could enhance the results presented in this work.

A stator turn fault adds two additional degrees to the magnetic non-linearity of an electric machine. This is due to the large circulating current in the shorted turns. First, the current flowing through the shorted turns generates a magnetic field that opposes the main air-gap flux. In the worst case, the permanent magnets can be demagnetized. Secondly, the increased leakage flux in the shorted turns, especially slot leakage flux, can effect on the magnetic saturation condition in tooth-tip region. But, in the developed simulation model, the effects of the magnetic non-linearity resulting from a stator turn fault were ignored based on the assumption that the effects of the non-linearity are not significant when a small number of turns are involved in a turn fault. However, the

magnetic non-linearity resulting from a stator turn fault obviously exist, and furthermore, the degree of the non-linearity increases as a stator turn fault gets worse. Thus, further research on this issue is required to describe the behavior of a stator turn fault more accurately.

Even though the developed thermal model of an IPMSM with stator turn fault accurately estimates the stator winding temperatures under a stator turn fault condition, the model does not provide the information about the rotor temperature, especially the temperatures of permanent magnets. It is a well-known fact that the performance of permanent magnet is strongly dependent on the operating temperature. If the effects of a stator turn fault on the permanent magnet temperature is investigated, a more reliable turn fault-tolerant operating strategy would be achieved.

Although the proposed turn fault detection method has a good immunity to drive's non-idealities, the method does not consider the effects of operating temperature. The back-emf voltage of a PM machine decreases, while the stator resistance increases as operating temperature increases. These changes in the back-emf voltage and stator resistance influence the voltage reference. Therefore, for more reliable turn fault detection, the effects of the operating temperature need to be compensated. Further research on this issue can develop upon the use of the voltage reference for turn fault detection.

As investigated, low order space harmonics in the rotating magnetic flux induce the same order harmonics in the circulating current in the shorted turns. These low order harmonics in the current increase the rms value of the current and consequently, increase the copper loss in the shorted turns. Further research on how to reduce low order space

harmonics in the rotating magnetic flux can extend the allowable operating duration of the proposed turn fault-tolerant operating strategy.

REFERENCES

[1] P. H. Mellor, T. J. Allen, R. Ong, and Z. Rahman, "Faulted behavior of permanent magnet electric vehicle traction drives," *in Conf. Rec. of IEEE IEMDC'03,* vol. 1, pp. 554-558, Madison, Wisconsin, USA, June, 2003.

[2] IAS Motor Reliability Working Group, "Report of large motor reliability survey of industrial and commercial installation, part I," *IEEE Trans. Industry Applications,* vol. IA-21, pp. 853-864, July/Aug., 1985.

[3] B. K. Gupta and W.T. Fink, "A proposed type test for interturn insulation in multi-turn coils," *in Conf. Rec. of IEEE International Symposium on Electrical Insulation,* pp. 235-238, Montreal, Quebec, Canada, June, 1996.

[4] S. B. Lee, R. M. Tallam, and T. G. Habetler, "A robust, on-line turn-fault detection technique for induction machines based on monitoring the sequence component impedance matrix," *IEEE Trans. Power Electronics,* vol. 18, no. 3, pp. 865-872, May, 2003.

[5] R. V. White and F. M. Miles, "Principles of fault tolerance," *in Conf. Rec. of APEC'96,* vol. 1, pp. 18-25, San Jose, CA, USA, March, 1996.

[6] F. W. Fuchs, "Some diagnosis methods for voltage source inverters in variable speed drives with induction machines A Survey," *in Conf. Rec. IECON'03,* vol. 2, pp. 1378-1385, Roanoke, Virginia, USA, November, 2003.

[7] A. H. Bonnet and G. C. Soukup, "Cause and analysis of stator and rotor failures in three-phase squirrel case induction motors," *IEEE Trans. Industry Application,* vol., 28, no., 4, pp. 921-937, July/August, 1992.

[8] T. A. Lipo, *Introduction of AC machine design, Wisconsin Power Electronics Research Center,* 2nd edition, 2004.

[9] S. F. Farag, R. G. Bartheld, and W. E. May, "Electronically enhanced low voltage motor protection and control," *IEEE Trans. Industry Applications,* vol. 29, no. 1, pp. 45-51, Jan./Feb., 1994.

[10] J. T. Boys and M. J. Miles, "Empirical thermal model for inverter-driven cage induction machines," *IEE Proc., Electr. Power Appl.,* vol. 141, pp. 360-372, 1994.

[11] K. D. Hurst and T. G. Habetler, "A thermal monitoring and parameter tuning scheme for induction machines," *in Conf. Rec. IEEE IAS'97*, pp. 136-142, New Orleans, LA, USA, October, 1997.

[12] S. B. Lee and T. G. Habetler, "An online stator winding resistance estimation technique for temperature monitoring of line-connected induction machines," *IEEE Trans. Industry Applications,* vol. 39, no. 3, pp. 685-694, May/June, 2003.

[13] W. L. Roux, R. G. Harley, and T. G. Habetler, "Detecting rotor faults in permanent magnet synchronous machines," *in Conf. Rec. SDEMPED'03,* pp. 198-203, Atlanta, GA, USA, August, 2003.

[14] D. G. Dorrell, W. T. Thomson, and S. Roach, "Analysis of airgap flux, current vibration signals as a function of the combination of static and dynamic airgap eccentricity," *IEEE Trans. Industry Applications,* vol. 33, no. 1, pp. 24-34, Jan./Feb., 1994.

[15] J. R. Stack, T. G. Habetler, and R. G. Harley, "Bearing fault detection via autoregressive stator current modeling," *IEEE Trans. Industry Applications,* vol. 40, no. 3, pp. 740-747, May/June, 2004.

[16] G. C. Stone and H. G. Sedding, "In-service evaluation of motor and generator stator windings using partial discharge tests," *IEEE Trans. Industry Applications,* vol. 31, no. 2, pp. 299-303, March/April, 1995.

[17] G. C. Stone, H. G. Sedding, and M. J. Costello, "Application of partial discharge testing to motor and generator stator winding maintenance," *IEEE Trans. Industry Applications,* vol. 32, no. 2, pp. 459-464, March/April, 1996.

[18] G. C. Stone and V. Warren, "Effect of manufacturer, winding age and insulation type on stator winding partial discharge levels," *IEEE Electrical Insulation Magazine ,* vol. 20, no. 5, pp. 13-17, Sept./Oct., 2004.

[19] M. Kaufhold, G. Borner, M. Eberhardt, and J. Speck, "Failure mechanism of the interturn insulation of low voltage electric machines fed by pulse-controlled inverters," *IEEE Electrical Insulation Magazine ,* vol. 12, no. 5, pp. 9-16, Sept./Oct., 1996.

[20] A. H. Bonnet, "Available insulation systems for PWM inverter-fed motors," *IEEE Industry Applications Magazine,* pp. 14-26, Jan./Feb., 1998.

[21] A. H. Bonnet, "Analysis of impact of pulse-width modulated inverter voltage waveforms on AC induction motors," *IEEE Trans. Industry Applications,* vol. 32, no. 2, pp. 368-392, March/April, 1996.

[22] M. A. Cash, "Detection of turn faults arising from insulation failure in the stator windings of AC machines," *Doctoral Dissertation,* Dept. of Electrical and Computer Engineering, Georgia Institute of Technology, USA, 1998.

[23] D. E. Schump, "Predict motor failure with insulation testing," *Pulp and Paper Industry Technical Conference'97,* pp.48-50, Cincinnati, OH, USA, June, 1997.

[24] D. E. Schump, "Reliability testing of electric motors," *IEEE Trans Industry Applications,* vol. 25, no. 3, pp. 386-390, May/June, 1989.

[25] R. Maier, "Protection of squirrel-cage induction motor utilizing instantaneous power and phase information," *IEEE Trans. Industry Applications,* vol. 28, no. 2, pp. 376-380, March/April, 1992.

[26] J. S. Hsu, "Monitoring of defects in induction motors through air-gap torque observation," *IEEE Trans. Industry Applications,* vol. 31, no. 5, pp. 1061-1021, Sept./Oct., 1995.

[27] G. B. Kliman, W. J. Premerland, R. A. Koegl, and D. Hoeweler, ”A new approach to on-line turn fault detection in AC motors,” *in Conf. Rec. IEEE IAS’96,* vol. 1, pp.687-693, San Diego, CA, USA, October, 1996.

[28] J. Sottile and J. L. Kohler, “An on-line method to detect incipient failure of turn insulation in random-wound motors,” *IEEE Trans. Energy Conversion,* vol. 8, no. 4, pp. 762-768, December, 1993.

[29] F. C. Trutt, J. Sottile, and J. L. Kohler, “Online condition monitoring of induction motors,” *IEEE Trans. Industry Applications,* vol. 38, no. 6, pp. 1627-1632, Nov./Dec., 2002.

[30] J. Penman, H. G. Sedding, B. A. Lloyd, and W. T. Fink, “Detection and location of interturn short circuits in the stator windings of operating motors,” *IEEE Trans. Energy Conversion,* vol. 9, no. 4, pp. 652-658, December, 1994.

[31] S. M. A. Cruz and A. J. M. Cardoso, “Stator winding fault diagnosis in three-phase synchronous and asynchronous motors, by the extended park’s vector approach,” *IEEE Trans. Industry Applications,* vol. 37, no. 5, pp. 1227-1233, Sept./Oct., 2001.

[32] R. M. Tallam, T. G. Habetler, and R. G. Harley, “Stator winding turn-fault detection for closed-loop induction motor drives,” *IEEE Trans. Industry Applications,* vol. 39, no. 3, pp. 720-724, May/June, 2003.

[33] M. A. Cash, T. G. Habetler, and G. B. Kliman, “Insulation failure prediction in AC machines using line-neutral voltages,” *IEEE Trans. Industry Applications,* vol. 34, no. 6, pp. 1234-1239, Nov./Dec., 1998.

[34] P. Garcia, F. Briz, M. W. Degner, and A. B. Diez, "Diagnosis of induction machines using the Zero sequence voltage," *in Rec. of Conf. IEEE IAS'04,* pp 735-742, Seattle, Washington, USA, October, 2004.

[35] F. Briz, M. W. Degner, P. Garcia, and A. B. Diez, "Induction machine diagnosis using zero sequence voltage," *in Rec. of Conf. IEEE IAS'05,* pp 34-41, Hong Kong, China, October, 2005.

[36] A. Bellini, F. Filippetti, G. Franceschini, and C. Tassoni, "Closed-loop control impact on the diagnosis of induction motors fault," *IEEE Trans. Industry Applications,* vol. 36, no. 5, pp. 1318-1329, Sept./Oct., 2000.

[37] T. M. Wolbank, K. A. Loparo, and R. Wohrnschimmel, "Inverter Statistics for online detection of stator asymmetries in inverter-fed induction motors," *IEEE Trans. Industry Applications,* vol. 39, no. 4, pp. 1102-1108, July/August, 2003.

[38] F. Briz, M. W. Degner, A. Zamarron, and J. M. Guerrero, "Online stator winding fault diagnosis in inverter-fed AC machines using high-frequency signal injection," *IEEE Trans. Industry Applications,* vol. 39, no. 4, pp. 1109-1117, July/August, 2003.

[39] S. M. A. Cruz, H. A. Toliyat, and A. J. M. Cardoso, "DSP implementation of the multiple reference frames theory for the diagnosis of stator faults in a DTC induction motor drive," *IEEE Trans. Energy Conversion,* vol. 20, no. 2, pp. 329-335, June, 2005.

[40] N. Ertugrul, W. Soong, G. Dostal, and D. Saxon, "Fault tolerant motor drive system with redundancy for critical applications," *in Rec. of Conf. IEEE PESC'02*, pp. 1457-1462, Cairns, Queensland, Australia, June, 2002.

[41] B. A. Welchko, T.M. Jahns, W. L. Soong, and J. M. Nagashima, "IPM synchronous machine drive response to symmetrical and asymmetrical short circuit faults," *IEEE Trans. Energy Conversion,* vol.18, no. 2, pp. 291-298, June., 2003.

[42] A. G. Jack, B. C. Mecrow, and J. A. Haylock, "A comparative study of permanent magnet and switched reluctance motors for high-performance fault-tolerant applications," *IEEE Trans. Industry Applications,* vol. 32, no.4, pp. 889-895, July/August, 1996.

[43] B. C. Mecrow, A. G. Jack, J. A. Haylock, and J. Coles, "Fault-tolerant permanent magnet machine drives," *IEE Proc., Power Application,* vol. 143, no.62, pp. 437-442, November, 1996.

[44] J. A. Haylock, B. C. Mecrow, A. G. Jack, and D. J. Atkinson, "Operation of fault tolerant machines with winding failures," *IEEE Trans Energy Conversion,* vol. 14, no. 4, pp. 1490-1495, December, 1999.

[45] R. M. Tallam, SB Lee, G. Stone, G. B. Kliman, JY Yoo, T. G. Habetler, and R. G. Harley, "A survey of methods for detection of stator related faults in induction motors," *in Conf. Rec. SDEMPED'03,* pp. 35-46, Atlanta, GA, USA, August, 2003.

[46] A. Bracale, G. Carpinelli, D. Lauria, Z. Leonowicz, T. Lobos, and J. Rezmer, "On Some Spectrum Estimation Methods for Analysis of Non-stationary Signals in

Power Systems Part 1. Theoretical Aspects," *in Conf. , Rec. of IEEE International Conference on Harmonics and Quality of Power,* pp. 266-271, Lake Placid, New York, USA, September, 2004.

[47] T. Lobos, J. Rezmer, and T. Sikorski, "Advanced Signal Processing Methods for Analysis of Non-Stationary Signals in Power Systems," *in Conf., Rec. of IEEE International Symposium on Intelligent Signal Processing*, pp. 43-47, Budapest, Hungary, September, 2003.

[48] L. Satish, "Short-time fourier and wavelet transforms for fault detection in power transformers during impulse test," *IEE Proc. –Sci. Meas. Technol.,* vol. 145, no. 2, pp. 77-84, March, 1998.

[49] K. Kim and A. G. Parlos, "Induction motor fault diagnosis based on neuropredictors and wavelet signal processing," *IEEE Trans. Mechatronics,* vol. 7, no. 2, pp. 201-219 June, 2002.

[50] F. Filippetti, G. Franceschini, C. Tassoni, and P. Vas, "Recent developments of induction motor drives fault diagnosis using AI techniques," *IEEE Trans. Industry Electronics,* vol. 47, no. 5, pp. 994-1004, October, 2000.

[51] R. M. Tallam, T. G. Habetler, and R. G. Harley, "Self-commissioning training algorithms for neural networks with applications to electric machine fault diagnostics," *IEEE Trans. Power Electronics,* vol. 17, no. 6, pp. 1089-1095, November, 2002.

[52] T. M. Jahns and V. Caliskan, "Uncontrolled generator operation of interior PM synchronous machines following high-speed inverter shutdown," *IEEE Trans. Industry Applications,* vol. 35, no. 6, pp. 1347-1357, Nov./Dec., 1999.

[53] N. Bianchi, M. D. Pre, and S. Bolognani, "Design of a fault-tolerant IPM motor for electric power steering," *IEEE Trans. Vehicular Technology,* vol. 55, no. 4, pp.1102-1111, July, 2006.

[54] J. Cros and P. Viarouge, "Synthesis of high performance PM motors with concentrated windings," *IEEE Trans. Energy Conversion,* vol. 17, no. 2, pp. 248-253, June, 2002.

[55] O. Bottauscio, G. Pellegrino, P. Guglielmi, M. Chiampi, and A. Vagati "Rotor loss estimation in permanent magnet machines with concentrated windings," *IEEE Trans. Magnetics,* vol. 41, no. 10, pp. 3913-3915, October, 2005.

[56] Y. Honda, T. Nakamura, T. Higaki, and Y. Takeda, "Motor Design Considerations and Test Results of an Interior Permanent Magnet Synchronous Motor for Electric Vehicles," *in Conf. Rec. IEEE IAS'97,* pp. 75-82, New Orleans, LA, USA, October, 1997.

[57] KATO Engineering Inc., "Form-wound coils, random-wound coils," *Engineering Report*, 2000.

[58] M. Dai, A. Keyhani, and T. Sebstian, "Fault analysis of a PM brushless DC motor using finite element method," *IEEE Trans. Energy Conversion,* vol. 20, no. 1, pp. 1-6, March, 2005.

[59] R. M. Tallam, T. G. Habetler, and R. G. Harley, "Transient model for induction machines with stator winding turn faults," *IEEE Trans. Industry Application,* vol., 38, no., 3, pp. 632-637, May/June, 2002.

[60] Youngkook Lee and T. G. Habetler, "A phase variable simulation model for interior PM synchronous motor drives with stator turn faults," *in Rec. of Conf. of EPE-PEMC06,* pp. 1074-1079, Portoroz, Slovenia, August, 2006.

[61] D. Hanselman, *Brushless Permanent Magnet Motor Design*, *The Writers' Collective,* 2nd edition, 2003.

[62] P. C. Krause, *Analysis of Electric Machinery*, *McGraw-Hill, Inc.,* 1986.

[63] D. W. Novotinty and T .A. Lipo, *Vector control and dynamics of AC drives*, *Clarendon Press Oxford,* 1996.

[64] V. Petrovic and A. M. Stankovic, "Modeling of PM synchronous motors for control and estimation tasks," *in Rec. of Conf. of IEEE Decision and Control,* pp. 2229-2234, Orlando, Florida, USA, December, 2001.

[65] S. Morimoto, M. Sanada, and Y. Takeda, "Wide-Speed Operation of Interior Permanent Magnet Synchronous Motors with High-Performance Current Regulator," *IEEE Trans. Industry Applications,* vol. 30, no. 4, pp. 920-926, July/August, 1994.

[66] B. K. Bose, "Wide-Speed Operation of Interior Permanent Magnet Synchronous Motors with High-Performance Current Regulator," *IEEE Trans. Industry Applications,* vol. 30, no. 4, pp. 920-926, July/August, 1994.

[67] E. Levi, "Saturation modeling in D-Q axis models of salient pole synchronous machines," *IEEE Trans. Energy Conversion,* vol. 14, no. 1, pp. 44-50, March, 1999.

[68] J. Wai and T. M. Jahns, "A new control technique for achieving wide constant power speed operation with an interior PM alternator machine," *in Conf. Rec. IEEE IAS'01*, pp. 807-814, Chicago, Illinois, USA, October, 2001.

[69] C. Mademlis and V. G. Agelidis, "On considering magnetic saturation with maximum torque to current control in interior permanent magnet synchronous motor drives," *IEEE Trans. Energy Conversion,* vol. 16, no. 3, pp. 246-252, September, 2001.

[70] P. J. Tavner, "Cross-magnetisation effects in electrical machines," *IEE Proc. Electr. Power Appl.,* vol. 151, no. 3, pp. 249-259, May, 2004.

[71] E. Levi and V. A. Levi, "Impact of dynamic cross-saturation on accuracy of saturated synchronous machine models," *IEEE Trans. Energy Conversion,* vol. 15, no. 2, pp. 224-230, June, 2000.

[72] B. Stumberger, G. Stumberger, D. Dolinar, A. Hamler, and M. Trlep, "Evaluation of saturation and cross-magnetization effects in interior permanent-magnet synchronous motor," *IEEE Trans. Industry Applications,* vol. 39, no. 5, pp.1264-1271, Sept./Oct., 2003.

[73] S-Y. Kwak, J-R. Kim, and H-J. Jung, "Characteristic analysis of multilayer-buried magnet synchronous motor using fixed permeability method," *IEEE Trans. Energy Conversion,* vol. 20, no. 3, pp.549-555, September, 2005.

[74] O. A. Mohammed, S. Liu, and Z. Liu, "A phase variable PM machine model for integrated motor drive systems," *in Rec. of Conf. of IEEE PESC'04,* pp.4825-4829, Aachen, Germany, June, 2004.

[75] K. Nakamura, K. Saito, and O. Ichinokura, "Dynamic analysis of interior permanent magnet motor based on a magnetic circuit model," *IEEE Trans. Magnetics,* vol., 39, no., 5, pp. 3250-3252, Sept., 2003.

[76] C. Gerada, K. Bradley, and M. Sumner, "Winding turn-to-turn faults in permanent magnet synchronous machine drives," *in Conf. Rec. IEEE IAS'05*, pp. 1029-1036, Hong Kong, China, October, 2005.

[77] K. Shima, K. Ide, M. Takahashi, and Y. Yoshinari, "Calculation of leakage inductances of a salient-pole synchronous machine using finite elements," *IEEE Trans. Energy Conversion,* vol. 14, no. 4, pp. 1156-1161, December, 1999.

[78] K. Shima, K. Ide, and M. Takahashi, "Analysis of leakage flux distributions in a salient-pole synchronous machine using finite elements," *IEEE Trans. Energy Conversion,* vol. 18, no. 1, pp. 63-70, March, 2003.

[79] P. H. Mellor, D. Roberts, and D. R. Turner, "Lumped parameter thermal model for electrical machines of TEFC design," *IEE Pro. Electr. Power Appl.,* vol. 138, pp. 205-218, 1991.

[80] O. I. Okoro, "Steady and transient states thermal analysis of a 7.5-kW squirrel-cage induction machine at rated-load operation," *IEEE Energy Conversion,* vol. 20, no. 4, pp. 730-736, December, 2005.

[81] A. M. EL-Refaie, N. C. Harris, T. M. Jahns, and K. M. Rahman, "Thermal analysis of multibarrier interior PM synchronous machine using lumped parameter model," *IEEE Trans. Energy Conversion,* vol. 19, no. 2, pp. 303-309, June, 2004.

[82] Z. Gao, T. G. Habetler, and R. G. Harley, "An online adaptive stator winding temperature estimator based on a hybrid thermal model for induction machines," *in Conf. Rec. IEEE IEMDC'05*, pp. 754-761, San Antonio, Texas, USA, May, 2005.

[83] J. F. Moreno, F. P. Hidalgo, and M. D. Martinez, "Realization of tests to determine the parameters of the thermal model of an induction machine," *IEE Proc. Electr. Power Appl.,* vol. 148, no. 5, pp.393-397, September, 2001.

[84] P. Milanfar and J. H. Lang, "Monitoring the thermal condition of permanent-magnet synchronous motors," *IEEE Trans. Aerospace and Electronic Systems,* vol. 32, no. 4, pp. 1421-1429, October, 1996.

[85] J. R. Hendershot and T. Miller, *Design of Brushless Permanent-Magnet Motors*, *Clarendon Press Oxford,* 1994.

[86] C. Mi, G. R. Slemon, and R. Bonert, "Modeling of iron losses of permanent- magnet synchronous motors," *IEEE Trans. Industry Applications,* vol. 39, no. 3, pp. 734-742, May/June, 2003.

[87] G. R. Slemon and X. Liu, "Core losses in permanent magnet motors," *IEEE Trans. Magnetics,* vol. 26, no. 5, pp. 1653-1655, September, 1990.

[88] F. Deng, "An improved iron loss estimation for permanent magnet brushless machines," *IEEE Trans. Energy Conversion,* vol. 14, no. 2, pp. 1391-1395, December, 1999.

[89] G. Bertotti, "General properties of power losses in soft ferromagnetic materials," *IEEE Trans. Magnetics,* vol. 24, no. 1, pp. 621-630, January, 1988.

[90] K. Yamazaki and Y. Seto, "Iron loss analysis of interior permanent magnet synchronous motors-variation of main loss factors due to driving condition," *IEEE Trans. Industry Applications,* vol. 42, no. 4, pp. 1045-1052, July/August, 2006.

[91] K. Atallah, D. Howe, P. H. Mellor, and D. A. Stone, "Rotor loss in permanent-magnet brushless AC machines," *IEEE Trans. Industry Applications,* vol. 36, no. 6, pp. 1612-1618, Nov./Dec., 2000.

[92] A. Cassat, C. Espanet, and N. Wavre, "BLDC motor stator and rotor iron losses and thermal behavior based on lumped schemes and 3-D FEM analysis," *IEEE Trans. Industry Applications,* vol. 39, no. 5, pp. 1314-1322, Sept./Oct., 2003.

[93] N. Schofield, K Ng, Z. Q. Zhu, and D. Howe, "Parasitic rotor losses in a brushless permanent magnet traction machine," *in Rec. of Conf. IEE Electrical Machines and Drives,* pp. 200-204, Cambridge, UK, September, 1997.

[94] K. Yamazaki and S. Watari, "Loss analysis of permanent-magnet motor considering carrier harmonics of PWM inverter using combination of 2-D and 3-D finite-element method," *IEEE Trans. Magnetics,* vol. 41, no. 5, pp. 1980-1983, May, 2005.

[95] D. A. Ionel, M. Popescu, S. J. Dellinger, T. J. E. Miller, R. J. Heideman, and M. I. McGilp, "On the variation with flux and frequency of the core loss coefficients in electrical machines," *IEEE Trans. Industry Applications,* vol. 32, no. 3, pp. 658-667, May/June, 2006.

[96] C. Mademlis, I Kioskeridis, and N. Margaris, "Optimal efficiency control strategy for interior permanent-magnet synchronous motor drives," *IEEE Trans. Energy Conversion,* vol. 19, no. 4, pp. 715-724, December, 2004.

[97] A. Boglietti, P. Ferraris, M. Lazzari, and M. Pastorelli, "Influence of the inverter characteristics on the iron losses in PWM inverter-fed induction motors," *IEEE Trans. Industry Applications,* vol. 32, no. 5, pp. 1190-1194, Sept./Oct., 1996.

[98] R. Kaczmarek, M. Amar, and F. Protat, "Iron loss under PWM voltage supply on Epstein frame and in induction motor core," *IEEE Trans. Magnetics,* vol. 32, no. 1, pp. 189-194, January, 1996.

[99] Z. Q. Zhu, Y. S. Chen, and D. Howe, "Iron loss in permanent-magnet brushless AC machines under maximum torque per ampere and flux weakening control," *IEEE Trans. Magnetics,* vol. 38, no. 5, pp. 3285-3287, Spetember, 2002.

[100] Jong-Woo Choi and Seoung-Ki Sul, "Inverter output voltage synthesis using novel dead time compensation," *IEEE Trans. Power Electronics,* vol. 11, no. 2, pp. 221-227, March, 1996.

[101] N. Urasaki, T. Senjyu, K. Uezato, and T. Funabashi, "An adaptive dead-time compensation strategy for voltage source inverter fed motor drives," *IEEE Trans. Power Electronics,* vol. 20, no. 5, pp. 1150-1160, September, 2005.

[102] R. Peuget, S. Courtine, and J. P. Rognon, "Fault detection and isolation on a PWM inverter by knowledge-based model," *IEEE Trans. Industry Applications,* vol. 34, no. 6, pp. 1318-1326. Nov. /Dec., 1998.

[103] Y. S. Jeong, S. K. Sul, S. E. Schulz, and N. R. Patel, "Fault detection and fault-tolerant control of interior permanent-magnet motor drive system for electric vehicle," *IEEE Trans. Industry Applications,* vol.41, no.1, pp 46-51, Jan./Feb., 2005.

[104] W. le. Roux, R. G. Harley, and T. G. Habetler, "Converter control effects on condition monitoring of rotor faults in permanent magnet synchronous machines," *IEEE Trans. Industry Applications,* vol. 36, no. 5, pp.1318-1329, Sept./Oct., 2000.

[105] T. Sebastian, "Temperature effects on torque production and efficiency of PM motors using NdFeB magnets," *IEEE Trans. Industry Applications,* vol. 31, no. 2, pp. 353-357, March/April, 1995.

[106] R. F. Schiferi and T. A. Lipo, "Power capability of salient pole permanent magnet synchronous motors in variable speed drive applications," *IEEE Trans. Industry Applications,* vol. 26, no. 1, pp.115-123, Jan./Feb., 1990.

[107] W. L. Soong and T. J. E. Miller, "Field-weakening performance of brushless synchronous AC motor drives," *IEE Proc. Electr. Power Appl.,* vol. 141, no. 6, pp.331-340, November, 1994.

[108] W. L. Soong and N. Ertugrul, "Field-weakening performance of interior permanent-magnet motors," *IEEE Trans. Industry Applications,* vol. 38, no. 5, pp.1251-1258, Sept./Oct., 2002.

[109] Y. Honda, T. Higaki, S. Morimoto, and Y. Takeda, "Rotor design optimization of a multi-layer interior permanent-magnet synchronous motor," *IEE Proc.-Electr. Power Appl.,* vol. 145, no. 2, pp.119-124, March, 1998.

[110] Youngkook Lee and T. G. Habetler, "A stator turn fault-tolerant strategy for induction motor drives in safety-critical applications," *in Rec. of Conf. of IEEE PESC'06,* pp. 2522-2528, Jeju, Korea, June, 2006.

[111] Youngkook Lee and T. G. Habetler, "A stator turn fault-tolerant strategy for interior PM synchronous motor drives in safety-critical applications," *in Rec. of Conf. of ICEM'06,* paper ID 244, Crete Island, Greece, September, 2006.

[112] Youngkook Lee and T. G. Habetler, "An on-line stator turn fault detection method for interior PM synchronous motor drives," *in Rec. of Conf. of IEEE APEC'07,* pp. 825-831, Anehaim Portoroz, Slovenia, August, 2006.

[113] Youngkook Lee and T. G. Habetler, "Modeling and analysis of stator turn faults in interior PM synchronous motor drives," *submitted for review in IEEE Trans. Energy Conversion*.

VITA

Youngkook Lee was born September 3 1970 in Seoul, Korea. He received his Bachelor and Master of Electrical Engineering degrees from Hanyang University, Seoul, Korea, in 1994 and 1996, respectively.

In January 1996, he was employed by Hyundai Motor Company, Seoul, Korea as a research engineer and currently, is a senior research engineer working on developing electric power train systems for electric or hybrid-electric vehicles.

In August 2003, he enrolled at the Georgia Institute of Technology, Atlanta, GA, where he is pursing his doctoral studies in Diagnostics and Control of Electrical Machines. While at Georgia Tech, he worked as a Research Assistant from January 2006 to May 2007 for the School of Electrical and Computer Engineering. He married Dukehee Kim in January 2000. They have two children Hyungi and Seohee.